2019

Improving Turbine Performance: A Contribution to the Understanding of Heat Transfer and Vortical Structures in Staggered Pin Fin Arrays

Marcel Otto
University of Central Florida

IMPROVING TURBINE PERFORMANCE: A CONTRIBUTION TO THE UNDERSTANDING OF HEAT TRANSFER AND VORTICAL STRUCTURES IN STAGGERED PIN FIN ARRAYS

by

MARCEL OTTO
B.S. Mechanical Engineering, TU Berlin, 2010
M.S. Mechanical Engineering, TU Berlin, 2013
M.S. Mechanical Engineering, University of Central Florida, 2015

A dissertation submitted in partial fulfillment of the requirements
for the degree of Doctor of Philosophy
in the Department of Mechanical and Aerospace Engineering
in the College of Engineering and Computer Science
at the University of Central Florida
Orlando, Florida

Fall Term
2019

Major Professor: Jayanta S. Kapat

ABSTRACT

Through the comparison of flow structures, velocity contours, turbulence statistics, and additional flow quantities, the error sources of RANS are qualitatively described. The findings in this work will help gas turbine design engineers to tweak their turbulence models and give guidance on the interpretation of their results. The novelty is the application of the transient TLC method on this type of geometry as well as the near-wall PIV measurements. The advancements in additive manufacturing disrupt the classic turbine cooling development for casted airfoils. More and more complicated shapes and cooling schemes are possible. Nonetheless, a detailed physical understanding of fundamental cases - as provided in this study - is required for physics-based optimization of cooling designs.

Meiner Familie - namentlich Eltern, Brüdern und Großeltern gewidmet - und natürlich

Dem, Der über allem steht.

ACKNOWLEDGMENTS

First of all, I want to thank my advisor and mentor Dr. Jayanta Kapat for his support, inspiration, and guidance throughout my time at UCF. Your help, input, and opinions were, are, and always will be highly appreciated. Furthermore, I would like to thank you for identifying and promoting hidden talents; their discovery will significantly impact and shape my future personal life and career.

Also, I would like to extend my gratefulness to my committee members. The help and support from Dr. Ahmed, Dr. Bhattacharya, Dr. Kinzel, and Dr. Wiegand significantly improved the quality of my research through their constant feedback. Alongside my committee, I would like to thank CATER and IST for their resources and great people.

I also want to thank my lab mates. Many are not only colleagues but have become friends over the course of time. In particular, it is an honor to acknowledge and highlight the impact of Andrea, Andres, Akshay, Bernie, Gaurav, Greg, Husam, Jorge, Justin, Kevin, Luisana, Patrick, Shinjan, and Zack on my life.

Thank you to all of the many great people that I have met during my time at UCF. Either church or soccer, you have all made me feel home in Florida. Not to forget my friends back home with whom I am happy to maintain a friendship over several thousand miles. Here, I would like to personally thank Nick, Sean, Rodrigo, David, Linda, Ansgar, Tanja, Daniel, Alex, Robert, and Novid.

I would not be here without the support of my parents Christian and Veronika. Thank you. Thank you for teaching me the importance of education and your selfless support of all my endeavors. I do not take it for granted. Thank you to my brothers Christopher and Julian for always being there when needed. Thank you Oma und Opa for all your love and support.

Maybe there are more elegant ways to express my thankfulness to everyone than this clumsily written acknowledgment section, but it is genuine and sincere.

TABLE OF CONTENTS

LIST OF FIGURES

LIST OF TABLES

NOMENCLATURE

$\dot{m}$	Mass Flow Rate $[kg/s]$
$\dot{Q}$	Transferred Heat Rate $[J/s]$
$\mathbf{A}$	Anisotropy Tensor
$\mathbf{R}$	Reynolds Stress Tensor
$\overline{U}$	Mean Velocity $[m/s]$
A_c	Cross Section Area $[m^2]$
C	Constant
c_p	Specific Heat Capacity $[J/(kg.K)]$
C_s	Smagorinsky Coefficient
D	Pin Diameter $[m]$
E	Energy $[J]$
e	Specific Enthalpy $[J/kg]$
F	Frequency $[Hz]$
f	Darcy Friction Factor
Fo	Fourier Number
h	Heat Transfer Coefficient $[W/(m^2K)]$

I Current $[A]$

I, II, III Principal Components of Turbulence Anisotropy

k Thermal Conductivity $[W/(mK)]$

k Turbulent Kinetic Energy $[J/(kg)]$

k Wavenumber $[1/m]$

L Half-thickness of the Material Slab coated with TLC paint $[m]$

l_s Smagorinsky Lengthscale

M M

N Number of Rows

N_r Number of Pins per Rows

p Pressure $[Pa]$

P_{wet} Wetted Perimeter $[m]$

Q Transferred Heat $[J]$

R Result

r Radial Direction

$R_{specific}$ Specific Gas Constant

Re Reynolds Number

s Specific Entropy $[J/(K.kg)]$

Sr Strouhal Number

T Temperature $[K]$

t Time $[t]$

T_∞ Free Stream Temperature $[K]$

T_f Film Temperature $[K]$

$T_{GreenPeak}$ Green Peak Temperature $[K]$

T_w Local Wall Temperature $[K]$

U Velocity $[m/s]$

u, v, w Velocity Components $[m/s]$

W Channel Width $[m]$

x Streamwise Coordinate Direction

X_i Measurable Property

y Wall-normal Coordinate Direction

z Spanwise Coordinate Direction

${}^{x}/_{D}$ Streamwise Pin Spacing

${}^{z}/_{D}$ Spanwise Pin Spacing

Greek Symbols

α Thermal Diffusivity $[m^2/s]$

β Thermal Performance Index

Δ Change in Value

δ Uncertainty of Value

Δ_{LES} LES Filter Width

ϵ Turbulence Energy Dissipation Rate $[m^2/s^3]$

η Efficiency

η_{th} Thermal Performance Index

∞ Free-Stream Conditions

λ Eigenvalue of Anisotropy Tensor

μ Dynamic Viscosity $[(Ns)/m^2]$

μ_k Turbulent Viscosity $[m^2/s]$

ν Kinematic Viscosity, Momentum Diffusivity $[m^2/s]$

Π Pressure Ratio

π Pressure Spectrum

ρ Density $[kg/m^3]$

σ Standard Deviation

Superscripts and Subscripts

$'$ Fluctuating Component Value

$^{-}$ Time-Mean Value

amb Ambient Conditions

avg Average Reading

$fluid$ Average Value of Fluid

i Initial Conditions

K Kolmogarov

max Computed maximum Value at smallest Cross Section between Pins

min Computed minimum Value at upstream and downstream of Pins without Blockage

$surface$ Acrylic Surface

Acronyms

BR Blockage Ratio

$CAGR$ Compound Annual Growth Rate

CFD Computational Fluid Dynamics

$CMOS$ Complementary Metal-Oxide-Semiconductor

DMD Dynamic Mode Decomposition

FAA Federal Aviation Administration

FFT Fast Fourier Transform

fps Frames Per Second

$HDMI$ High-Definition Multimedia Interface

HSV Horseshoe Vortex

KV von Kármán Vortex

LDV Laser Doppler Velocimetry

LES Large Eddy Simulation

LED Light Emitting Diode

PIV Particle Image Velocimetry

POD Proper Orthogonal Decomposition

PSD Power Spectral Density

$RANS$ Reynolds Averaged Navier-Stokes

RSM Reynolds Stress Model

SGS Subgrid Scale

SV Secondary Vortex

TBC Thermal Barrier Coating

TC Thermocouple

TIT Turbine Inlet Temperature $[K]$

TLC Thermochromic Liquid Crystal

TV Tertiary Vortex

$WALE$ Wall-Adapting Local Eddy-viscosity SGS Model

CHAPTER 1: INTRODUCTION

This chapter intends to convey a brief overview of the design, operation, and key parameters of modern gas turbines for power generation, propulsion, and industrial applications. In addition, an outline on key challenges related to safe operation and achieving high efficiencies is given which then directly connects to the last section of this chapter which addresses gas turbine cooling mechanisms and finally narrows down to cooling of the airfoil trailing edge.

Background

For decades, gas turbines have powered planes and connected the world. The world faces several major challenges over the next years, such as climate change and sustainable energy supply [6]. Gas turbines power plants, whether single cycle or combined cycle, produce less pollution compared to conventional coal power plants and have efficiencies beyond 60%, putting them in an important role in the transition to renewable energy [7]. Due to their dependency on sun and wind, photo voltaic power generation and wind turbines, respectively, are intermittent in their output. Highly flexible operation of gas turbine power plants can provide necessary grid stability. At this point, it is deemed appropriate to first of all answer the question: What are gas turbines? Gas turbines are a kind of internal combustion engine where the work generation is continuous. Due to the large power output per unit area and comparable high efficiencies, gas turbines are used for a large variety of applications as shown in Figure 1.1 - which links the main value drivers, compound annual growth rate, and market size data [1–4]. The first link at the top is gas turbines for power generation which usually ranges from 120 Megawatt to 600 Megawatt per unit in single-cycle operation. Larger units tend to be base

load power plants supplying energy continuously; they usually aim to generate electricity at high efficiencies and long maintenance intervals. Smaller units are mainly used for local power generation in remote locations or to compensate for the intermittent nature of renewables. In this case, gas turbines act as peakers and provide grid stability due to the quick ramping of the engines. Here, the main design parameters besides ramping are hot- and cold start abilities as well as turn-down behavior. The second group of land-based gas turbines are industrial applications. Industrial gas turbines are commonly differentiated by applications: upstream, midstream and downstream. Upstream gas turbines are found on on-shore and off-shore oil rigs. The main design goal here is reliability as money is lost when no oil can be pumped. Midstream gas turbines are used for recompression along pipelines with a compromise between efficiency, reliability, and long maintenance intervals. Downstream gas turbines are found at the end of these pipelines. They mainly generate electricity, as mentioned earlier, or generate mechanical work used for various industrial applications. The basic principles, nonetheless, are the same for all three areas of application. The third application field is aircraft propulsion. Since those engines are not land based, weight considerations, as well as fuel efficiency, are main design goals. However, the basic principles are the same for all three areas of application. The only difference is that propulsion engines are designed to generate thrust whereas the other two are meant to drive a shaft which is either connected to mechanical equipment or a generator. New gas turbine technologies are first introduced into aviation turbines (early adopters) and then tickle down to gas turbines for power generation and ultimately to oil and gas applications.

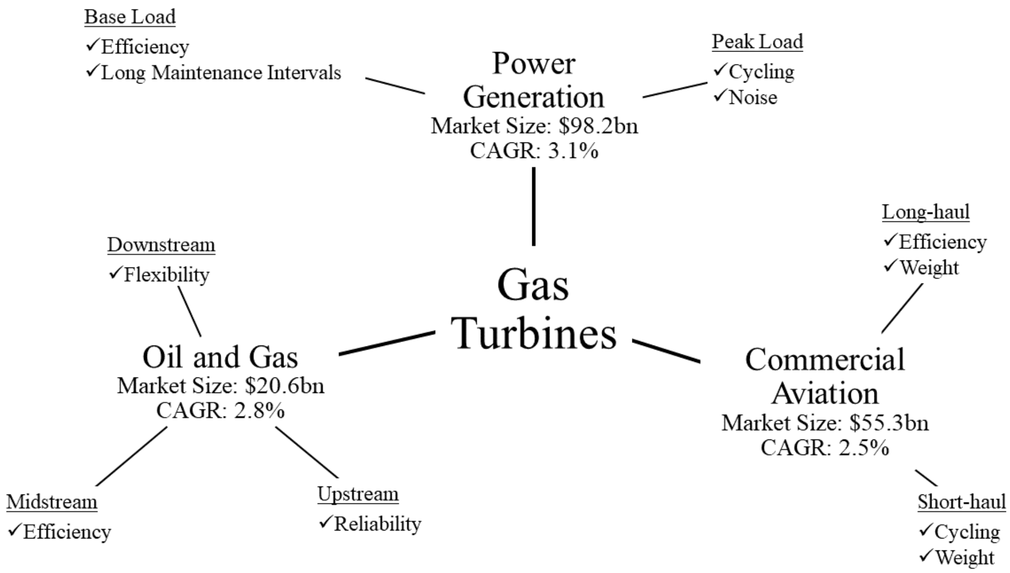

Figure 1.1: Market summary of gas turbines including main value drivers. Market size and growth rate data is reported in [1–4]

For this reason, it is not surprising that the early development of gas turbines were turbojet engines. They originate from H.J. von Ohain's (patented in 1935, tested in 1937) and F. Whittle's (patented 1930, tested 1937) parallel efforts in WW II to develop a predecessor for reciprocal jet engines [8]. With economic growth in the post-world war era, commercial flight become more and more affordable and promoted further research and development of turbojet and turbofan engines [8]. The decreasing price of gas compared to coal, the lower capital cost per installed kWh and higher efficiency promoted the adaption of gas turbines for power generation due to their unique value propositions. Large boilers and other high pressure, high-temperature equipment are required for steam power plants. The savings in initial cost are realized as this equipment is not required for gas turbine power plants.

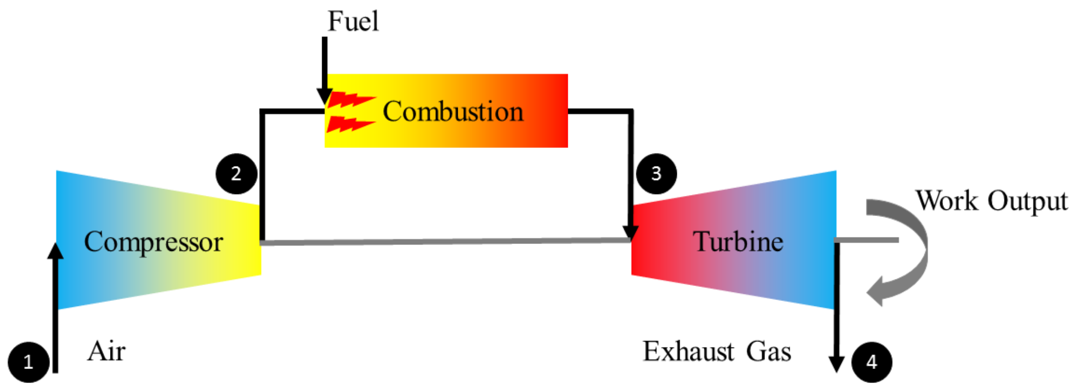

Figure 1.2: Basic functionality of a gas turbine

The three main components for a power generation gas turbine are compressor, combustor and turbine. The main components of a gas turbine system are outlined in Figure 1.2. Compressor and turbine are connected via a shaft. In the case of turbines for aviation, the compressor and turbine are usually split into a high pressure and low pressure sections. High pressure compressor and high pressure turbine are on separate shaft which allows the gas generator to rotate at higher speed, resulting in a more efficient propulsion system. Here, the system mainly drives a fan which generates thrust that propels the aircraft forward. The shaft of gas turbines for power generation is connected to a generator on the cold side of the system. The work output is used to spin the generator coming from the conversion of chemical energy to mechanical work to electrical power. The ultimate goal of a gas turbine is to convert chemical energy into mechanical work. Understood in conjunction with Figure 1.3 which graphically displays the Brayton cycle. The Brayton cycle is the idealized thermodynamic cycle of a gas turbine and is characterized by four processes:

- 1-2: isentropic compression

- 2-3: constant pressure heat addition
- 3-4: isentropic expansion
- 4-1: constant pressure heat rejection

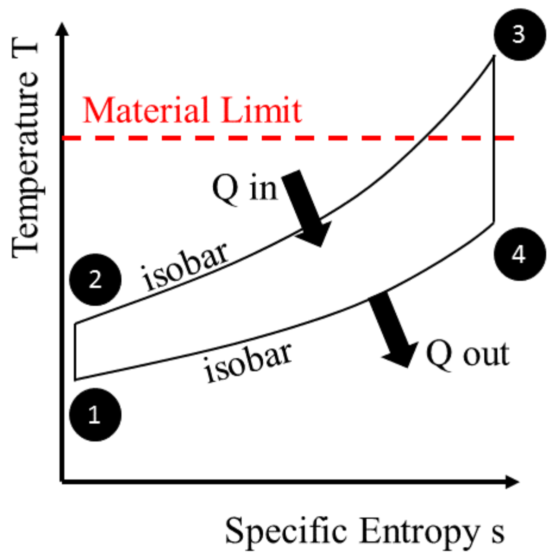

Figure 1.3: Qualitative sketch of Brayton cycle

Process 1-2 is cold air that is sucked into the compressor. The compressor, depending on design and manufacturer, usually consists of 12-14 stages (power generation) plus variable guide vanes at the inlet to optimize performance in part-load operation. One compressor stage consists of one rotating component and one stationary component. Work is added to the working fluid in the rotating stage. The flow path of the stationary portion is designed to decrease velocity while increasing static pressure. According to the ideal gas law in Equation 1.1, that links pressure P, temperature T and density ρ, density and temperature increase (indicated by the gradient in 1.2) through the various stages

of the compressor. Therefore, the cross-sectional area decreases downstream through the compressor between states 1 and 2 of the thermodynamic cycle.

$$P = \rho R_{specific} T \tag{1.1}$$

The work addition in the fluid is described by the specific enthalpy[1] difference between both states as follows:

$$W_{1-2} = -(e_2 - e_1) = c_p(T_2 - T_1) \tag{1.2}$$

Next, heat via combustion of gas or oil with the compressed air or by injection hot steam is added to the working fluid. Ideally, this heat addition is at constant pressure and occurs between state 2 and 3 of the Brayton cycle. In terms of specific enthalpy, heat addition can be written as the work augmented by the fluid as described below:

$$Q_{2-3} = -(e_3 - e_2) = c_p(T_3 - T_2) \tag{1.3}$$

In the next step, the fluid is expanded through a turbine (between state 3-4) where the energy of the working fluid is exchanged with the turbine in form of work W_{3-4}.

$$W_{3-4} = -(e_3 - e_4) = c_p(T_3 - T_4) \tag{1.4}$$

Since the pressure gradient is favorable in the turbine, the isentropic expansion and work extraction can be commonly achieved with 3-5 turbine stages only. Here, the order of the rotating and stationary stages is diametrical to the compressor. Due to the divergence of the isobars, the work extraction from the turbine stage is larger than the work added

[1]The typical symbol for specific enthalpy in Thermodynamic is usually h. However, the symbol h is required and reserved for the heat transfer coefficient. In order to avoid any confusion, the symbol e will be used to represent specific enthalpy.

during compression. Since turbine and compressor are on the same shaft, the net gain in work Q_{2-3} is diminished by the compressor work W_{1-2} as shown in Equation 1.5.

$$W_{net} = W_{3-4} - W_{1-2} = c_p(T_3 - T_4) - c_p(T_2 - T_1) \tag{1.5}$$

In today's gas turbines for power generation, the net work output of a turbine stage is about 1/3 where 2/3 of the work is used to drive the compressor. Therefore, by either increasing the pressure ratio between state 1 and 2 or increasing the temperature at 3, the net work output of the system can be increased. In furtherance, with increased net work output, the cycle efficiency increases. The cycle efficiency is expressed by:

$$\eta = \frac{W_{net}}{Q_{2-3}} = \frac{c_p(T_3 - T_4) - c_p(T_2 - T_1)}{c_p(T_3 - T_2)} \tag{1.6}$$

With the pressure ratio Π

$$\Pi = \frac{p_2}{p_1} = \frac{p_3}{p_4} \tag{1.7}$$

and the isentropic relation

$$\frac{T_2}{T_1} = \frac{T_3}{T_4} = \Pi^{\frac{\gamma - 1}{\gamma}} \tag{1.8}$$

the cycle efficiency from Equation 1.6 modifies to

$$\eta = 1 - \left(\frac{1}{\Pi}\right)^{\frac{\gamma - 1}{\gamma}} \tag{1.9}$$

which is in particular useful to visualize the aforementioned sensitivity of the cycle efficiency on pressure ratio. Resubstituting Equation 1.8 into 1.9 shows the cycle efficiency based on temperature ratios. The temperature at the inlet T_1 is the ambient temperature. Also, an increase in the maximum cycle temperature T_3, or also commonly referred to

as Turbine Inlet Temperature (TIT) or firing temperature can increase the cycle efficiency. The turbine exit temperature T_4 is thermodynamically constrained through the heat addition and the isobar $p_1 = constant$ and consequently cannot be manipulated for higher cycle efficiencies[2].

$$\eta = 1 - \left(\frac{1}{\Pi}\right)^{\frac{\gamma - 1}{\gamma}} = 1 - \frac{T_1}{T_2} = 1 - \frac{T_4}{T_3} \tag{1.10}$$

At this point, it shall be reiterated upon the fact that the noted efficiency is only for an ideal cycle efficiency which does not account for aerodynamic and/or thermodynamic losses. This fact is reinfored in Figure 1.4demonstrating the factors associated with efficiency loss for a simple cycle gas turbine.

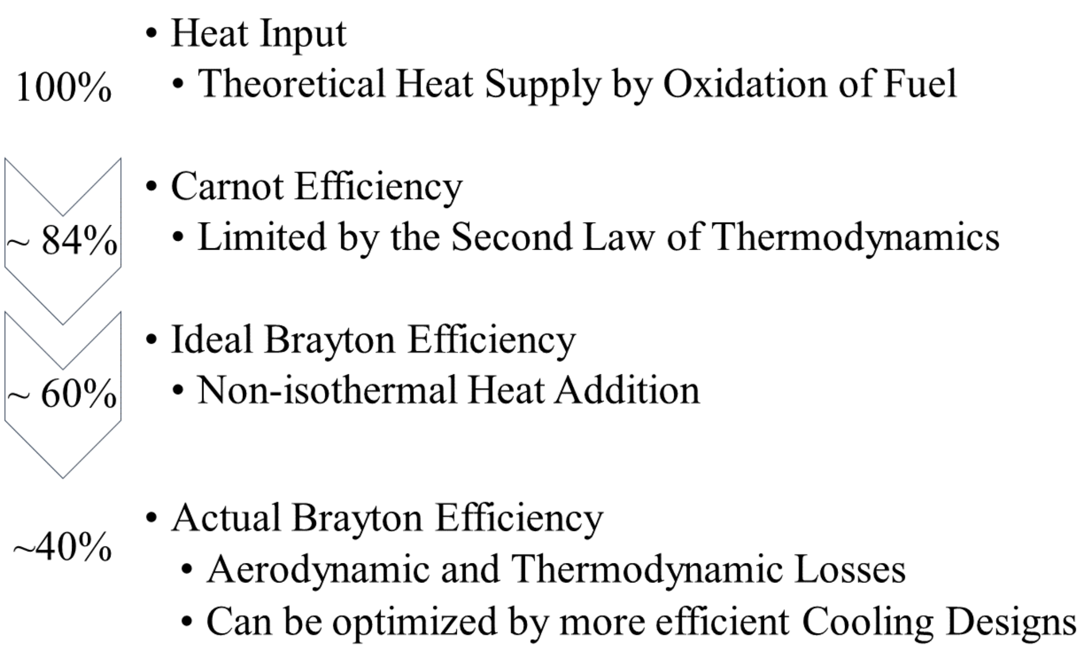

Figure 1.4: Visualization of Efficiency Losses in a Simple Cycle Gas Turbine

[2] The turbine exit temperature T_4 nevertheless is relatively high so it contains substantial unused energy. For this reason, it is common to route the exhaust gas through a heat exchanger. In the heat exchanger heat is transferred to steam which then powers a separate steam turbine. This configuration is also referred to as a combined cycle compared to the simple cycle which consists of a gas turbine only.

A closer look at Equation 1.9 and Equation 1.10 may suggest that increasing the compressor pressure ratio is an alternative approach to increase cycle efficiency. This limiting factor, however, typically is the ambient conditions that are independent of the system. When applying the isentropic relation in Equation 1.8 to the net power output, a non-dimensionalized specific work expression can be obtained:

$$\frac{W_{net}}{c_p T_1} = \frac{T_3}{T_1}\left(1 - \left(\frac{1}{\Pi}\right)^{\frac{\gamma-1}{\gamma}}\right) - \left(\Pi^{\frac{\gamma-1}{\gamma}} - 1\right) \tag{1.11}$$

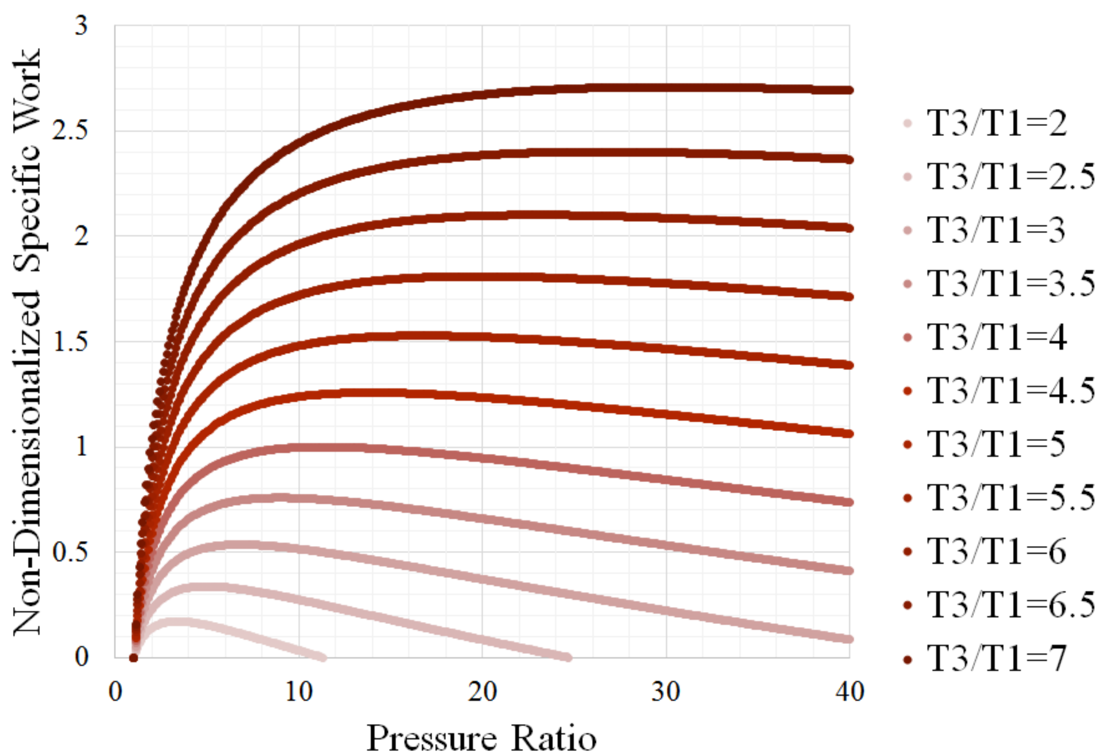

Figure 1.5: Dependency of specific work output on pressure ratio and firing temperature

From Figure 1.5 it can be seen that the specific work at a constant pressure ratio increases with increasing firing temperature T_3 represented by the gradient in red from lighter to darker colors. At the same time, given a constant temperature ratio, a peak value for specific work is observed. Further increasing the pressure ratio would increase the cycle efficiency but reduce specific work. This would in turn increase the mass flow rate through the system yielding to larger gas turbines in order to obtain a specific output. This is to be avoided.

In conclusion, it is a more common practice to increase the firing temperature or TIT to increase the cycle efficiency rather than the pressure ratio, even though both are not independent of each other. The basis of a cycle efficiency design is reliant on the customer's needs where it translates into two possible value schemes. First, increased firing temperature capabilities with the same amount of fuel resulting in more revenue due to higher power output per unit fuel. Second, increased firing temperature with fixed power output reducing the amount of fuel needed thus reduce the operational costs. The market imperative for increasing firing temperatures is undoubted[3]. A small increase in firing temperature by about 50K can raise efficiency between 2-4% and power output by 8-9% [10].

Yet, this sounds much easier than it is done. Modern gas turbines have temperature ratios ${}^{T_3}/_{T_1}$ between 6 to 7 with TIT's up to 1900K [11, 12]; this is equivalent to the temperature measured on a Space Shuttle during re-entry [13]. The temperatures found in gas turbines are beyond the temperature capabilities of superalloys and indicated by the red dashed line in Figure 1.3. Safe operation with respect to creep and other fatigue failure mechanisms is not guaranteed above this point and can incur catastrophic

[3]More so in Asia and Europe where the cost per unit fuel is significantly higher than in the United States of America [9].

failure or irreparable damage of the equipment[4]. However, the design engineer has the goal to optimize efficiency and increase component lifetime; an opposing design challenge. Protecting the hot gas path components of gas turbines requires several cooling techniques which are deployed to reduce the temperature-related damage and failure. Obviously, other challenges such as increased NO_x emissions are also an undesired effect of increased firing temperatures [10]. Accomplishing this vital role of turbine cooling for safe operating conditions has three major components:

- High temperature super alloys with sufficient mechanical properties at high temperatures;
- Active cooling - cold air from the compressor that is pumped through the blades and vanes of the hot section of a turbine;
- Thermal Barrier Coating (TBC), a ceramic protection layer on the outer metal surface that is exposed to the hot gas.

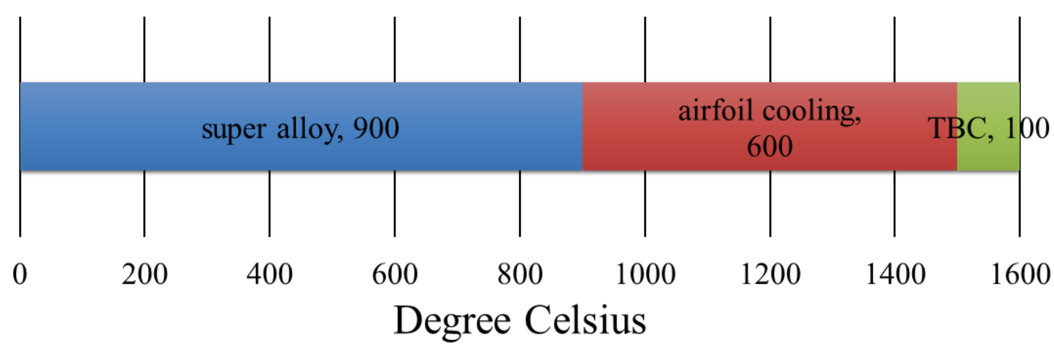

Figure 1.6: Distribution of each component on temperature resistance

[4]Probably the first fatal accident in aviation history dates back to ancient Greece and was caused by temperature-related material failure where it could have been avoided by proper cooling or a better choice of materials by Icarus.

Figure 1.6 lists the approximate contribution of each category. The sum is the reliability at high temperature. The first category, super alloys, can commonly withstand temperatures up to 1200K. Another temperature increase of 600K can be accounted for by integrating airfoil cooling into the blades and vanes. An additional 100K increase in firing temperature can be achieved by coating the airfoils with TBC [14].

Gas Turbine Cooling

The previous section emphasized how imperative turbine cooling is in order to achieve higher power output and higher efficiencies. Moving forward, it will be discussed several types of different cooling schemes that can be used to locally reduce the heat load on the metal of the airfoil hence increasing the life span of the component. The shape and functionality of certain regions of the airfoil will dictate the different mechanisms used for cooling.

Figure 1.7 depicts a generalized turbine blade as found in the first and second row of gas turbines. As hot gas approaches the airfoil, film cooling holes bleed cold air between the metal surface and the hot gas. The air acts as a shielding layer between both antagonists. Before the air is used for film cooling, it enters through coolant supply slots on the bottom of the blade. Here, as shown in Figure fig:TurbineCooling, the air is split into two or three regions based on the design of the internal cooling geometry: leading edge, mid-section and trailing edge where the latter ones can potentially be combined. The leading edge is cooled by impinging cold air onto the inner surface of the leading edge. The air then exits through film cooling holes as described earlier. The mid-section cooling is realized by serpentine channels. The coolant is routed two or three times up and down through this particular section. The internal cooling channels are additionally equipped with rib turbulators. These rib turbulators increase the turbulent transfer of

heat from the surface into the coolant and hence increase heat transfer. This coolant is commonly used also to cool the tip of the turbine blade and act as a kind of barrier to reduce tip leakage which in turn reduces the overall efficiency of the setup. The latter section of the turbine blade is referred to as the trailing edge section where the metal thickness of the blade is minimal to reduce the wake of the blade making cooling particularly important. Pin fin like structures are used to achieve mechanical strength and maintain high heat transfer in the region. The increase in surface area due to those pins and the additionally increased turbulence in this region contribute to better heat transfer. However, when introducing such restriction as impingement holes, features such as pin fins or rib turbulators, the pressure drop increases as additional restrictions are imposed on the flow. A higher pressure drop of the coolant directly relates to a larger amount of coolant that is needed to get the job done.

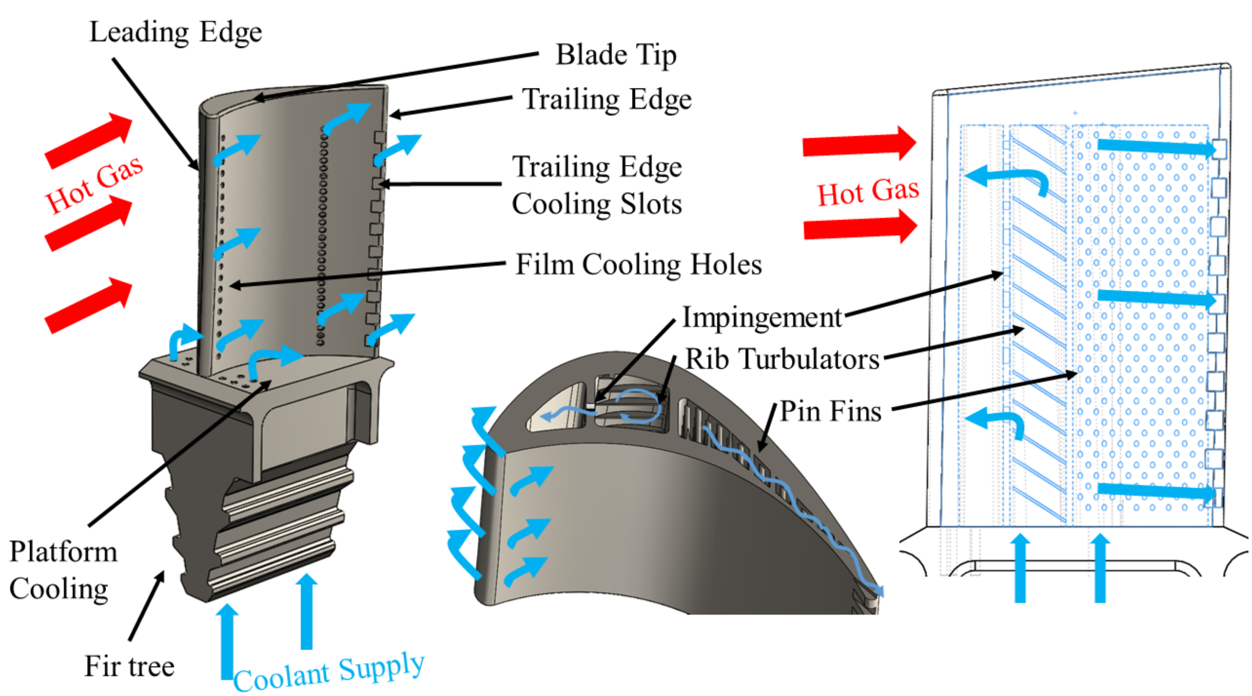

Figure 1.7: Different cooling schemes in a rotating airfoil including cross-sectional view

As always in life: "There ain't no such thing as a free lunch." Without optimization and thorough engineering, better turbine cooling can actually decrease the overall target of better engine performance. Inherently with better heat transfer, many times the pressure drop within the airfoil increases. Clearly the negative effect from the higher pressure drop has to be compensated by a higher mass flow rate of coolant which is provided as bleed air from the compressor. The trade-off is obvious thus a balance between pressure drop increase and heat transfer enhancement is heavily studied. Usually, this relationship between heat transfer enhancement and pressure drop increase (described in the form of friction factor augmentation) is summarized in the thermal performance index which is defined as

$$\eta_{th} = \left(\frac{Nu}{Nu_0}\right) / \left(\frac{f}{f_0}\right)^{\frac{1}{3}} \tag{1.12}$$

and was introduced by Webb and Eckert for a heat exchanger [15] and modified by Chyu for airfoil cooling [16]. Values larger than one indicate a better performance of the proposed cooling system as the gain in heat transfer compensates the additional coolant requirements with respect to the overall engine performance. Hence, thermal performance indices smaller than one indicate an inferior performance compared to the baseline case. The thermal performance index is widely recognized and used within the gas turbine industry to evaluate the cooling performance and is often used as a parameter to compare different geometrical approaches to airfoil cooling.

The ratio of actual Nusselt Number to baseline Nusselt Number is referred to Nusselt Number augmentation (if greater than 1); in the same manner, the ratio of friction

[5] Additive manufacturing is currently disrupting the way how internal cooling geometries are designed. Without the restrictions due to casting, additive manufacturing enables a multitude of new and different cooling mechanisms such as micro-channels. In these channels, the typical correlations such as Dittus Boelter and Blasius cannot be applied anymore as they do not account for the roughness from the manufacturing process. At this point, the development of new heat transfer correlations is subject to ongoing research. For this reason, there is a trend to determine the overall augmented heat transfer and friction factor in dependency of the projected area and surface rather than the actual internal dimensions.

factors with the same format is referred to as friction factor augmentation. The baseline for the augmentation in terms of Nusselt number is the Dittus Boelter correlation for rectangular duct and the Blasius correlation for the friction factor, respectively[5]. At this point, it is deemed to be appropriate to elaborate further on the detailed cooling of the trailing edge.

Trailing Edge

The trailing edge of an airfoil is the edge where the flow from the suction side and pressure side of the airfoil join. The region, as well as a typical cooling setup, are shown in Figure 1.7. Engineers aim to have a homogeneous velocity profile exiting one turbine stage before approaching the next stage of the turbine. This requires that the wake of the airfoil is minimal which can be partially achieved by minimizing the thickness of the airfoil in the trailing edge region. Thin metal thickness, however, reduces the mechanical strength and life of the component in this region. This challenge is addressed when internal cooling features are incorporated that increase the heat transfer while providing additional strength. Typical features are cylindrical pins, diamond-shaped pins or oblong-shaped pins in-line and perpendicular to the flow. Yet, combinations of pimples and dimples are also found in trailing edge applications [17], provided they are incorporated in micro-channels that provide the necessary mechanical strength. A typical non-proprietary geometry for the trailing edge section is banks of circular pins that can be in-line or staggered. The pins act twofold. On the one hand, the pins act as extended surfaces, hence also called pin fins, so that more area is available for heat removal. On the other hand, the pins introduce turbulence and vortical structures into the flow that increases heat transfer. A typical flow field in a bank of four staggered cylinders is shown in Figure 1.8. Flow enters the channel from the left and passes through the array of four pin

fin rows. The geometrical regions of pin-fin cooling can be divided into the pin and the endwall where the pins are perpendicular. These regions jointly contribute to the overall heat transfer.

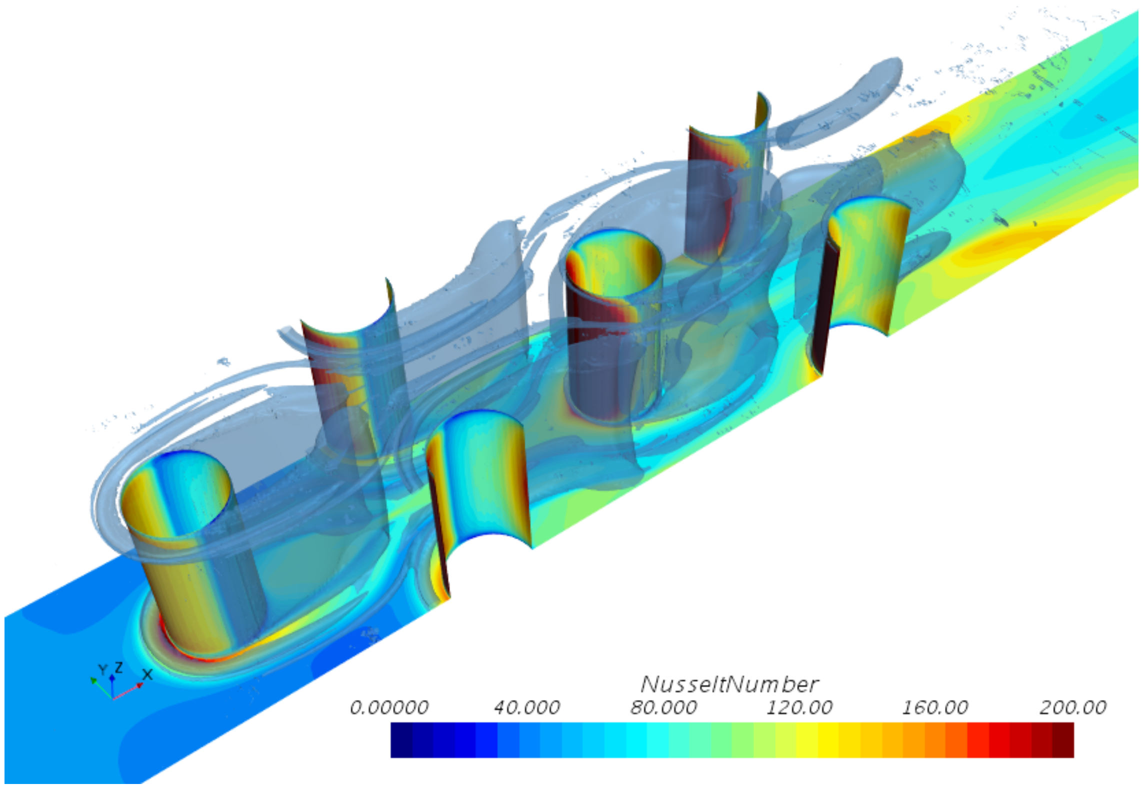

Figure 1.8: Time-averaged flow field in a typical pin fin array

In terms of heat transfer, these features within the cooling channel address to different parameters of the heat convection equation 1.13 where $\dot{Q}$ is the transferred heat between solid and fluid, h the heat transfer coefficient, A the area of the solid that is in contact with fluid, and the temperature difference between the fluid free stream and the surface $(T_\infty - T_w)$.

$$\dot{Q} = hA(T_\infty - T_w) \tag{1.13}$$

The heat transfer coefficient h and the wetted area A in Equation 1.13 are the independent variables that are adjusted. The features introduced into the flow directly increase the wetted area thus increasing the transferred heat rate. More heat can be transported from the hot metal, given similar flow conditions, if the surface area between coolant and metal is increased. At the same time, the features introduce turbulence into the flow as well as promote the formation of vortex structures. Both increase the local heat transfer so that the transferred heat rate increases even further by promoting mixing of the fluid in the channel. Furthermore, it is common to non-dimensionalize the heat transfer coefficient by defining the Nusselt number[6] as follows:

$$Nu = \frac{hD}{k_{fluid}} \tag{1.14}$$

The Nusselt number, as shown, is a way to present heat transfer in a non-dimensional form. The heat transfer coefficient, h, is related to a critical length scale, D, and divided by the thermal conductivity, k The respective test conditions shall be using air. The thermal conductivity of the fluid k_{fluid} is a function of temperature with a known correlation. The decision which temperature to use is not straightforward. Convective heat transfer only occurs if there is a driving temperature potential between the surface temperature and fluid bulk temperature. Therefore, a temperature gradient over the boundary layer is present. It is common to define a mean boundary layer temperature, called film temperature T_{film} (Equation 1.15), as the reference of the thermophysical properties of the fluid [18].

$$T_{film} = \frac{T_{wall} + T_{\infty}}{2} \tag{1.15}$$

[6]The pin fin geometries are unique in the way how the Reynolds number and Nusselt number is defined. The definition can be based on the hydraulic diameter D_h or the pin diameter D. This will be subject to a dedicated discussion later on. Both definitions are easily intertwined thus will be used interchangeably throughout the introduction chapter.

The introduction of cooling geometries alter the flow structure and heat transfer coefficient magnitude bringing about an affect in the local distribution. The introduced cooling geometries, furthermore, increase the turbulence levels within the airfoil's internal cooling passages. The general statement is higher turbulence levels yield higher heat transfer; this holds true since increased shear stress on a surface due to a turbulent flow increases the heat transfer locally. Contrary to a laminar flow, where the fluid is separated into several parallel layers without interaction, turbulent flow is of a chaotic nature with a fluctuation in velocity and pressure, yielding a high unsteadiness of the flow. Additionally, energy, equivalent to heat, is transferred in a normal direction of a turbulent flow. When expressing the velocity of a turbulent flow, a mean value in terms of a temporal average $\overline{u}$ and a fluctuation component u' has to be considered. The process of separating the velocity into its component is referred to as Reynolds decomposition and can be written in the following form according to Pope [19] and Tennekes and Lumley [20]:

$$u(x,t) = \overline{u(x,t)} + u'(x,y,z,t) \tag{1.16}$$

The Reynolds decomposition can be applied to the Navier-Stokes governing equation. If one considers a velocity U whose components are u, v, and w, a flow without body forces in a non-moving reference frame, the Navier-Stokes equation can be written as decomposition of mean and fluctuating components in the form of Equation 1.17.

$$\rho \frac{\partial \overline{u_i}}{\partial x_j} = \frac{\partial}{\partial x_i} \left[-\overline{p}\delta_{ij} + \mu \left(\frac{\partial \overline{u_i}}{\partial x_j} + \frac{\partial \overline{u_i}}{\partial x_i} \right) - \rho \overline{u_i' u_j'} \right] \tag{1.17}$$

where $\mathbf{R} = \tau_{ij} = \rho \overline{u_i' u_j'}$ is the Reynolds stress tensor with its respective components. The Reynolds stress tensor comprises of all velocity co-variances. With the principal stresses

along the tensor diagonal and the shear stresses the Reynolds stress tensor becomes

$$\mathbf{T} = \tau_{ij} = \rho \begin{pmatrix} \overline{u'u'} & \overline{u'v'} & \overline{u'w'} \\ \overline{v'u'} & \overline{v'v'} & \overline{v'w'} \\ \overline{w'u'} & \overline{w'v'} & \overline{w'w'} \end{pmatrix} \tag{1.18}$$

The tensor is symmetric about is diagonal so that $\overline{u_i'u_j'} = \overline{u_j'u_i'}$. Based on the prominent position of the Reynolds stress tensor within the governing Navier-Stokes equation, it is apparent that the detailed knowledge of the Reynolds stress tensor is required to accurately describe the flow field and even more so to accurately describe convective heat transfer, due to the relationship between turbulent transport and convective heat transfer.

The Reynolds analogy states a proportionality between momentum transport and heat transport. Since the goal is to increase heat transfer, analogously momentum transport must increase as well. The heat transfer away from the wall is realized by momentum transfer away from the wall, thus perpendicular to the main flow direction. Friction is then increased from this cross-flow due to the additional shear introduced into the flow. This sequentially requires additional pumping power and coolant consumption to overcome the additional frictional losses for overall improved heat transfer. The question then arises if there are other methods to increase heat transfer without causing frictional losses to rise. In other words, do means exist to increase heat transfer and local turbulent heat transfer of momentum and heat without an increase of global turbulence levels. This, for example, could be realized by intelligently shaped cooling geometries that promote local heat removal without overly increasing the local turbulence in the flow. In order to make such an assessment, it is imperative to understand the effect on local heat transfer as well as local and global turbulent transport. Intelligently shaped cooling geometries such that

increase local heat and mass transport from the wall by suppressing the global increase of turbulence.

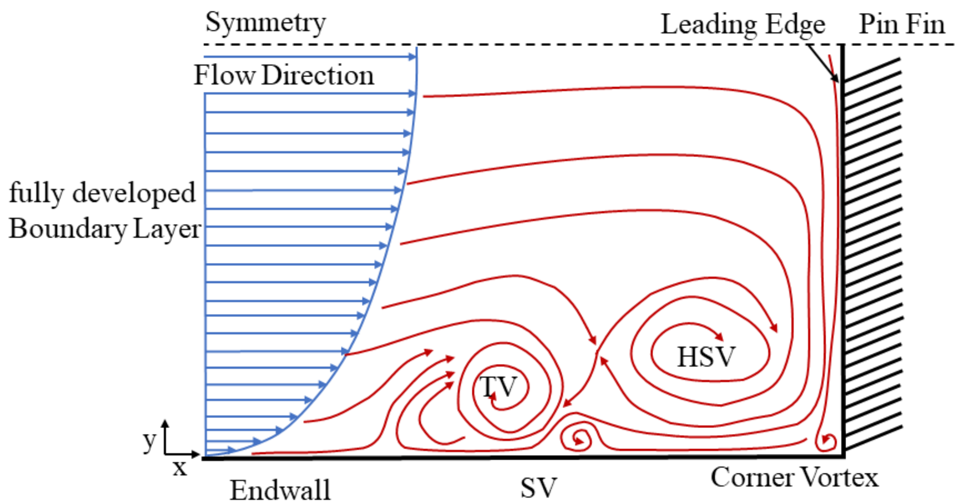

Figure 1.9: Horseshoe vortex system upstream of a blunt body as commonly found at the junction between pin fins and endwall

Two main vortical structures exist in arrays of staggered pin fins and are shown in the example flow field in Figure 1.8. The horseshoe vortex (HSV) system forms at the junction between pin and endwall. The forming vortex further wraps around the pin while spreading laterally and lifting off. Increased endwall heat transfer can be found in this region directly upstream of the pin on the endwall and adjacent to the pin. As the vortex travels further downstream, its turbulent kinetic energy dissipates more and more and the vortex diffuses into the bulk flow. The horseshoe vortex system is actually a system of four vortices where the HSV is the most dominant vortex and therefore name-giving. The other vortex components of the horseshoe vortex system are a corner vortex right at the junction between pin and endwall, a counter-rotating secondary vortex upstream of the horseshoe vortex (SV), and a tertiary vortex (TV) upstream of the secondary vortex.

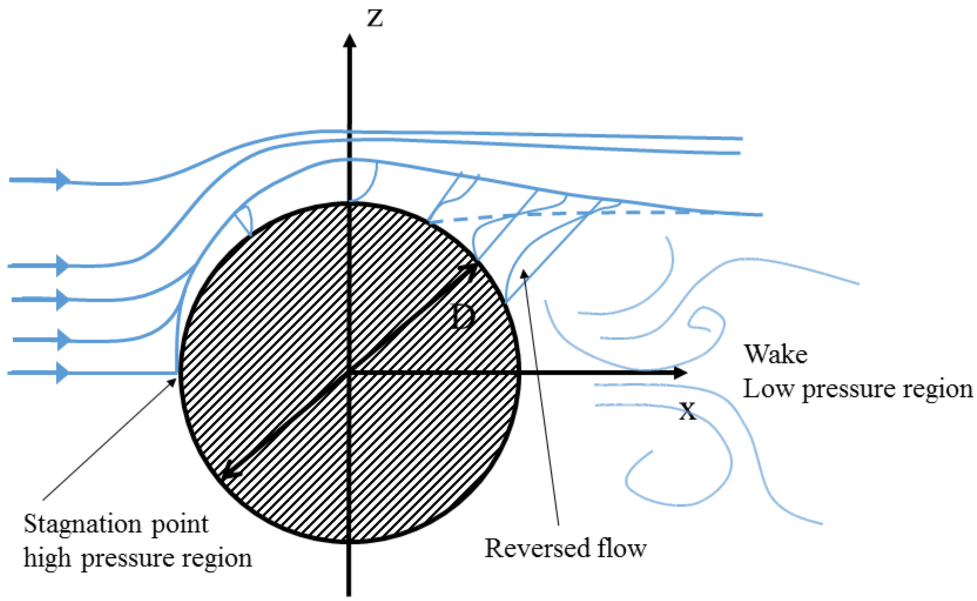

Figure 1.10: Flow around cylinder

The formation of the horseshoe is due to the velocity deficit within the boundary layer. The oncoming flow towards the pin encounters the obstacle due to the blunt body and gets deflected into the direction of lower pressure. Although the static pressure is constant over the height of the channel, the total pressure varies since the fluid in the boundary layer has a lower velocity. The fluid that stagnates on the pin surface gets deflected upwards and downwards towards either endwall. The steady resupply of fluid pushes the fluid on the endwall itself against the main flow direction in negative x direction as shown in Figure 1.9. Eventually the flow collides with the fluid approaching the pin further upstream. The collision causes an upwash of the fluid where it is redirected towards the pin: the horseshoe vortex is formed. The roll-up of the horseshoe vortex itself acts as a kind of blunt body for the flow even further upstream of the newly formed vortex. The outlined process repeats and results in the formation of the smaller tertiary vortex (TV). It goes without saying that the dynamics of the actual horseshoe vortex strongly af-

fect the dynamics of the smaller tertiary vortex. The cartoon depicts horseshoe vortex in a time-averaged manner. The vortex system is strongly unstable as it will be outlined in the following chapters.

The second vortex structures in the flow field are the von Kármán vortices (KV). Since no real-world fluid is inviscid, flow around the cylinder in Figure 1.10 occurs. The flow around the cylinder separates due to the adverse pressure gradient. At this point, a von Kármán vortex is shed from the cylinder. Von Kármán vortices are shed on either side of the cylinder and propagate further downstream along the centerline of the pin. Based on the incoming flow, also characterized as Reynolds number, which the pin is subjected to, the von Kármán vortices either shed alternating from either side or shed simultaneously. The vortex formation and transport are highly transient phenomena. The roll-up and shedding of the vortex cause a swiping motion along the endwall that helps to remove heat. In this context, it should be noted that the depiction in Figure 1.10 shows the time-averaged behavior and not an instantaneous snapshot of the von Kármán vortex street.

$$Sr = \frac{fD}{u_{max}} \tag{1.19}$$

The vortex shedding is characterized by the Strouhal number, a non-dimensional number relating the shedding frequency f with the pin diameter D and the approaching bulk flow velocity which is, in this case, u_{max} due to the blocking of the neighboring pins. The flow in the channel has the velocity u_{min}. Once the flow approaches the pins, the effective cross-sectional area of the channel is reduced. By employing the continuity equation for non-compressible fluids, the change in velocity based on the change of area can be written as:

$$\frac{A_{max}}{A_{min}} = \frac{u_{min}}{u_{max}} \tag{1.20}$$

A_{max} is the effective flow area between the pins with the corresponding velocity u_{max}. The minimum area A_{min} and free stream velocity u_{min} are to be understood in the same fashion.

The author is aware that the content towards the end of the trailing edge chapter might have become more and more confusing as the complexity of the presented material underwent a steep incline. The primary goal was to lay out a path from the overall engine perspective to the need for airfoil cooling to the narrow area of trailing edge cooling. Additionally, it has been shown that the nature of convective airfoil cooling ultimately culminates in a detailed understanding of local turbulent transport and larger scale vortical structures. A more in-depth discussion of the fundamentals and underlying physics will be found in the appropriate chapters.

CHAPTER 2: REVIEW OF LITERATURE

Pin fin arrays, also called pin fin banks or tubes, in crossflow have been subject to research for almost five decades with different application spectrums.

First, Žukauskas [21] work can be most likely seen as the first scientific study on pin fin tubes in a heat exchanger published in 1972 applicable to the scope of this dissertation. Later studies investigate the effect of Reynolds number on the heat transfer on such tube bundles. In the next phase of research, the geometric parameters were widely varied, including height to diameter ration, spanwise and streamwise spacing of the pins, in-line versus staggered setups, and duct shapes [22–25]. The main goal during the phase just mentioned was to understand the relationship between geometric parameters, heat transfer augmentation, and increase in pressure drop. The next logical step was to alter the shape of the pins itself. Triangular, rectangular, and various other shapes were tested and analyzed with respect to heat transfer and pressure drop [26, 27].

Secondly, whereas the early experimental data were obtained by heating a copper block and measuring the power needed to heat the flow with a heater to a specific temperature, advanced measurement techniques such as Naphthalene method (heat and mass transfer analogy) and thermochromic liquid crystals (TLC) were developed, utilized, and improved to provide information about local heat transfer rather than global values from previous measurement techniques [5, 28–31]. The non-uniformity seen in the local heat transfer distributions on the endwall motivated the next era in pin fin research. The flow field analysis. Researchers since then have aimed to understand the underlying flow field in these pin fin arrays. Various techniques have been employed such as Schlieren, PIV, and hotwire [32–34]. These measurements helped to identify flow structures and vortices that relate to the spatially resolved heat transfer measurements. These additional measurements were required by increasing demand for more efficient gas turbines. However,

when looking into literature for single wall-bounded cylinders in crossflow, structural and civil engineers are the dominant target audience as the vortical flow structures are crucial for building safe piers and bridges as the vortices tend to erode underwater foundations [35].

Thirdly, with microprocessor becoming more and more powerful, the impact on the advancement of pin fin cooling was twofold. One the one hand, the newly built data centers to perform highly demanding computations needed advanced cooling to remove the generated heat within the computer and the data center itself. Pin fins are commonly found as components of heat exchanger for forced convection and natural convection cooling systems within electronic systems [36–38]. On the other hand, and more importantly in terms of the scope of this work, the advancements in computational power enabled the broad adaption of Computational Fluid Dynamics (CFD). Plenty of studies using CFD for pin fins were performed ranging between conventional RANS simulations [39, 40] to LES [41, 42] with the goal to better understand the flow physics and predict the most important engineering quantities such as pressure drop and heat transfer. Often a mismatch is observed between numerical and experimental results [39]. For this reason, studies have been looking into the quality of the results provided by RANS and LES [43].

In summary, many sub-categories have to be considered to accurately reflect the developments in pin fin research over time. For this reason, the chapter reviewing the applicable literature and the state of the art is broken down into heat and pressure measurement research, research regarding the flow field analysis, and lastly the numerical studies. After this brief introduction and overview of literature, a more detailed discussion follows in the upcoming sections.

Heat Transfer and Pressure Drop

A comprehensive summary of previous heat transfer studies on pin fin arrays is shown in Table 2.1. The table is sorted by year of publication. Other listing criteria are the spanwise and streamwise spacing $^z/_D$ and $^x/_D$, respectively, as well as the style of the array whether inline or staggered, the Reynolds number range, and the shape of the pins. The definition of Reynolds number is inconsistent in the early years of pin fin research, therefore, comparisons should be made with caution.

Pin fins for turbine cooling were first described by Žukauskas [21] in 1972 with very large height to diameter ratios larger than 8. The research motivation is rooted in the improvement of nuclear heat exchanger not specifically geared towards airfoil cooling even though an airfoil is principally an heat exchanger as well. Further merits of this study are heat transfer and pressure drop correlations for a variety of Prandtl numbers and a large range of Reynolds numbers between 1,000,000 and 2,000,000. As the pins are eight times longer than in diameter, they can be treated as almost infinity cylinders. Therefore, the author's work focuses on the heat transfer on the pin fins alone and not the endwall.

Metzger et al. [44] investigated pin fin arrays with shorter pins as usually found in turbine airfoils. The pin height was equal to the diameter in their study. The test setup contained 10 segments, equal to the amount of rows, for which a Nusselt number is reported independently. An increase of Nusselt number is observed for the first 3 to 4 rows where the row-resolved Nusselt number peaks. Further downstream, the heat transfer steadies out at a slightly lower lever. Additionally, it is reported that the Nusselt number increases with Reynolds number so that higher flow rates produces higher heat transfer coefficients. The observed heat transfer, even including the heat transfer on the wall, is smaller than what found in banks of long tubes. Ultimately, a correlation for Nusselt

number based on Reynolds number and pin spacing is derived and presented as well as a correlation for friction factor as a function of pin spacing and Reynolds number. Those correlations are discussed in greater detailed and updated in [45]. A follow-up paper on the same geometry by Metzger and Haley [46] reports the heat transfer coefficient distribution around the pin in conjunction with flow visualization on the endwall. A highly three-dimensional flow field that strongly deviates from those of infinite cylinders is observed. The circumferential heat transfer around the pin shows augmented values in the stagnation region, a steep drop-off where the flow separates from the pin, and again higher values at the backside of the pin. Further downstream, the stagnation region is the most dominant heat transfer region around the cylinder.

Additional work by Metzger et al. [47] alters the shape of the pins. Here, oblong pins are used instead of cylindrical pins. As oblong-shaped pins are not perfectly symmetric, the effect of orientation of those was investigated as well by varying the angle of attack. It is reported that oblong pins in line with the flow decrease pressure drop as they act as a blunt body and delay flow separation. If inserted perpendicular to the flow, the pressure drop increases up to 100%. Not the shape of the pins but the shape of the duct was changed in another study by Metzger et al. [25] where the duct was assumed to be converging for downstream rows. The convergence reduces the effective cross-section which in turn causes an increase of flow velocity for downstream rows. In contrast to the findings in [44], the row-resolved heat transfer coefficient does not level for row numbers larger than 4. Instead, the heat transfer increases towards the end of the test section due to the acceleration of the flow.

VanFossen continued research on pin fin arrays specifically for gas turbine cooling applications. The trailing edge section of an airfoil is narrow so that no long pins relative to their diameter can be implemented as casting restricts the potential diameter. VanFossen [22] studied staggered pin fin arrays with height to diameter ratios between 0.5 and

2. It was observed that for small pins the heat transfer can be lower than for a plain channel without any additional features. Furthermore, it is reported that heat transfer of the pin itself is about a factor of two lower than what Žukauskas [21] reported for long pins. Brigham and VanFossen [23] looked at pins with four times the diameter as well as those in the previous study by VanFossen. It was reported that the total array heat transfer in an array of four pin rows is slightly lower than an array of eight pins and generally higher than for the shorter pins. Total array heat transfer consists of overall heat transfer of pin and endwall combined. Simoneau and VanFossen [24] looked at the heat transfer of a pin as a function of its location in the array. A heated pin was therefore located in one of the six rows. The observed heat transfer on the pin increased by up to 50% when one inline row was added upstream of the pin. However, the pin heat transfer did not change when moved further downstream. Opposing to the inline results, an increased heat transfer was observed for all locations when the pin location was varied within a staggered array.

Besides the research listed in this summary, a multitude of other pin fin literature was published as well. The framework was outlined above. The major variation was pin spacing. The variety of data inspired Armstrong and Winstanley [48] to publish a review paper on the data available and derive correlations for Nusselt number and friction factor. The correlations derived for array Nusselt number and array pressure drop by Armstrong and Winstanley are also used as reference in this study.

In terms of experimental setups, Lau et al. [49,50] used the naphthalene-sublimation method on the endwall. The test section was coated with a thin layer of naphthalene which is locally sublimated as flow passes through the test section. With measurements prior to and after the test, the local sublimation can be estimated which, in turn, can be correlated to local heat transfer. The group observed an almost periodic pattern of heat transfer once the pins are encountered.

Chyu and Goldstein [28] and Chyu and Natarajan [51] continued investigations of local heat transfer pattern on at the endwall of pin fin arrays for inline and staggered pin fin arrays, respectively. The method of choice was once again the naphthalene-sublimation method. The group identified the contribution of a strong horse shoe vortex system upstream of the obstacle. The horse shoe vortex increases the local Nusselt number directly upstream of the pin. It was reported how the findings were in agreement with work by Goldstein and Karni [52] for a single cylinder. Chyu and Goldstein [28] used the heat and mass transfer analogy between in-line and staggered arrays of pin fins to obtain spatially resolved Nusselt number distributions on the endwall. Local minima and maxima were found at one and two pin diameters downstream in the wake of the edge of the pin along the centerline for each cylinder. Another maximum was found just upstream of the pin which is attributed to the horse shoe vortex system forming at the junction between pin and endwall. As the horse shoe vortex wraps around the cylinder and propagates downstream, additional heat transfer enhancements were found adjacent to the pin. Also, by visualizing streaklines, it was found the that the flow pattern at the pin is significantly different in the wall-near region and in the mid-section with almost free-stream conditions.

Chyu and Natarajan [53] deployed the same method to investigate various shapes such as cubes, diamonds, pyramids, and hemispheres as replacements for pin fins. The goal was to establish a relationship between local heat transfer augmentation upstream and downstream of the element. The different shapes affect the horseshoe vortex build up and its spreading at the leading edge. It is concluded that different shapes need different spacings. Eventually, the method was applied to an array of cubes and diamonds [26]. It was found that cubes and diamonds result in higher array heat transfer compared with circular pin fins. The drawback is increased pressure drop up to a factor of two.

At this point, a controversy arose whether pin heat transfer or endwall heat transfer does contribute more to the overall array heat transfer [29]. Chyu et al. applied the naphthalene-sublimation method very carefully considering the thermal boundary conditions to an array of circular inline and staggered pins. Through the heat and mass transfer relationship, local heat transfer and array heat transfer distributions were obtained. It was discovered that the correlation by VanFossen [22] is reasonable accurate and the heat transfer on the pins is consistently 10 to 20% larger than the endwall. However, the author points out that this might be insignificant as the endwall commonly accounts for about 80% of the wetter channel area.

Hwang [54,55] studied the effect of trapezoidal ducts on heat transfer and pressure drop. The author reports that the staggered pins in a trapezoidal duct are advantageous over inline configurations and both increase averaged Nusselt number compared to a smooth channel. On account of the flow accelerating caused by the smaller area, higher endwall heat transfer was noticed at the trailing edge.

Won et al. [39] use infrared camera to understand the flow field upstream and downstream of the pins. Higher resolution compared to the previously introduced measurement methods enabled to capture the highest heat transfer location consisting of primary and secondary horse shoe vortices upstream of the pin. The infrared camera method was also used by Ames et al. [5] in a staggered pin fin array similar to the one used in this study; the authors report heat transfer coefficient for the endwall were the pins are kept adiabatic and vice versa. The heat transfer tests were conducted for a Reynolds number of 3,000, 10,000, and 30,000. The resulting local Nusselt number distribution varied for all three cases. This is attributed to the altering behavior of the wake region and turbulence levels between the pins.

Chyu et al. [56] used the thermochromic liquid crystal technique to obtain endwall Nusselt number information for changing height to diameter ratios of the pin. It

was observed that the overall array heat transfer increases with increasing length of the pins where the pins contribute more to the overall heat transfer than the endwall. The drawback is, that longer pins have a much higher pressure drop. The thermal performance index, as introduce in Equation 1.12, is the least significant for the longest pin. That means, that even though the heat transfer is the highest, the pressure drop increase outweighs the increase in heat transfer. The highest performance was found for a height to diameter ratio of two as it is also used in the present study.

Approximately 2011 marks the end of reported heat transfer measurements for pin fin array with extensive work by Lawson et al. [57]. The researchers used an IR camera for endwall heat transfer measurements and foil heaters around wooden cylinders for pin Nusselt numbers. In the study, the streamwise and spanwise spacing are varied. Shorter streamwise spacing yields higher heat transfer coefficients; a variation in spanwise spacing has a minor effect on heat transfer but more on pressure drop.

Research studies thereafter have focused more on a combination of existing features such as pin fins and rib turbulators together [58] or pimple and dimple geometries. Furthermore, flow measurements such as PIV and hot-wire have become more common. Those methods are used to explain the flow physics that eventually determine the local endwall and pin heat transfer.

Table 2.1: Overview of applicable literature on pin fin array heat transfer

Authors	Year	Array	Feature Shape	$^{y}/_{D}$	$^{x}/_{D}$	$^{H}/_{D}$	Heat Transfer Surface	Reynolds Number Range
Zukauskas [21]	1972	inline	circular	-	-	<8	pin	1,000,000 – 2,000,000
VanFossen [22]	1981	staggered	circular	4	4	0.5 - 2	both	15,000 – 100,000
Metzger et al. [44, 45]	1982	inline & staggered	circular	2.5 & 1.5	2.5 & 1.5	2	both	5,000 - 50,000
Metzger and Haley [46]	1982	inline & staggered	circular	2.5 & 1.5	2.5 & 1.5	2	pin	5,000 - 50,000
Brigham and VanFossen [23]	1984	staggered	circular	4	4	4	pin	15,000 – 100,000
Simoneau and VanFossen [24]	1984	inline & staggered	circular	2.67	2.67	3	pin	5,000 – 125,000
Metzger et al. [47]	1984	inline & staggered	circular & oblong	2.5 & 1.5	2.5 & 1.5	1	pin	5,000 – 50,000

Authors	Year	Array	Feature Shape	$^{y}/_{D}$	$^{x}/_{D}$	$^{H}/_{D}$	Heat Transfer Surface	Reynolds Number Range
Metzger et al. [25]	1986	inline & staggered	circular	2.5 & 1.5	2.5 & 1.5	2	both	5,000 - 50,000
Armstrong and Winstanley [48]	1988	Review						
Lau et al. [49, 50]	1989	inline & staggered	circular	2.5	2.5	1	endwall	6,000 – 60,000
Chyu and Goldstein [28]	1991	inline & staggered	circular	2.5	2.5	1	endwall	3,000 – 18,000
Goldstein et al. [59]	1994	staggered	circular & stepped	2.5	2.5	1	endwall	3,000 – 18,000
Chyu and Natarajan [53]	1996	single & element	cube & diamond	2.5	2.5	1	both	5,000 – 25,000
Chyu et al. [26]	1999	inline & staggered	circular & diamond	2.5	2.5	1	both	5,000 – 25,000
Chyu et al. [29]	1989	inline & staggered	circular	2.5	2.5	1	endwall	5,000 – 25,000

Authors	Year	Array	Feature Shape	y/D	x/D	H/D	Heat Transfer Surface	Reynolds Number Range
Hwang et al. [54]	1999	inline & staggered	circular	2.5	2.5	2	both	6,000 – 40,000
Hwang et al. [55]	2000	inline & staggered	Circular	2.5	2.5	2	both	6,000 – 40,000
Uzol and Camci [27,60]	2001	staggered	elliptical	2	2	1.5	endwall	10,000 – 47,000
Uzol and Camci [34]	2001	staggered	elliptical	2	2	1.5	-	10,000 – 47,000
Ligrani et al. [61]	2003	Review						
Won et al. [39]	2003	staggered	circular	2	2	1	endwall	10,000 – 20,000
Ames et al. [5]	2007	staggered	circular	2.5	2.5	2	both	3,000 – 30,000
Chyu et al. [56]	2009	inline & staggered	circular	2.5	2.5	2-4	endwall	10,000 – 30,000
Lawson et al. [57]	2011	staggered	circular	1.0 - 4	1.73 - 3.46	1	both	5,000 – 30,000
current study	2019	array	circular	2.5	2.5	2	endwall	10,000 - 30,000

Flow Field Analysis

Early work regarding flow visualization in a pin fin array goes back to Metzger and Haley [46] using the Schlieren method to understand the wall-shear stress at the endwall. Augmented wall-shear stress was observed in the region upstream of the pin and downstream due to the vortex shedding of the pin. Simoneau and VanFossen [24] used hot-wire probes in the wake of the pins to measure turbulent intensity profiles for a single row of pins, for two to six rows of pins, and in the wake of the fourth row for three different Reynolds numbers. Low turbulence intensities are reported for the first two rows. In pin fin rows thereafter, the turbulence intensity is much higher than for the first two rows. However, the turbulence levels that were observed for rows three to six are quite similar. Generally, one has to differentiate measurement techniques that are conducted in the flow volume such as hot-wire, LDV, and PIV and measurements that are obtained on the surface such as Schlieren method and oil visualization.

An example for the first approach is Uzul and Camci who used elliptical pins and circular pins as reference for heat transfer experiments [27,34,60] and conducted detailed PIV studies for a better understanding of the flow field in midplane of the pin wake – within a flow volume. The authors report delayed flow separation of elliptical pins compared to circular pins. Also, the turbulence levels in the wake of circular pins were higher, yielding 25-30% higher heat transfer on the endwall, however circular pins generate 100-200% more pressure drop. It was concluded that the heat transfer on the endwall is mainly driven by the flow structures within the wake. The elliptical pins, if not perpendicular to the flow, are similar to a teardrop shaped body. The aerodynamically advantageous shape delays the separation of the boundary layer, hence the wake is weaker compared to cylinders. Weaker flow separation causes for less pressure drop but no significant increase in turbulence, which maintains the increase in endwall heat transfer low. Uzol and Camci

studied the flow field in the wake of a two row pin fin array with circular and elliptical pins by PIV in the midplane parallel to both endwalls [27, 34, 60] reporting turbulent kinetic energies and mean flow fields. However, due to the measurements solely in the midplane in the wake of a pin, no contribution of the horseshoe vortex system on the endwall cooling was mentioned. The point is that heat transfer occurs in the wall-near region as turbulence transports away from the wall into the bulk flow. On the one hand, the overall heat transfer can be increased by generally increasing turbulence levels within the channel. The drawback is the approach leads to significant increases in pressure drop. As mentioned, the flow field is highly three-dimensional [28, 52, 53] in the region close to the wall. Conclusions from the midplane measurements cannot be necessarily related to the physics that occur close to the wall.

One of the highly three-dimensional flow patterns in a pin fin array is the horse shoe vortex system. The impinging flow on a pin fin creates a so called horse shoe vortex system close to the well. The vortex system causes high heat transfer on the endwall, wraps around the pin and increases heat transfer adjacent to the pin. The horse shoe vortex system was studied in great detail by Anderson and Lynch [62] investigating the horseshoe vortex and horseshoe vortex system buildup in a low aspect ratio (height equals pin diameter) staggered pin fin array [62]. Using time resolved stereo Particle Image Velocimetry (PIV), the team examined the various velocity components in the stagnation plane of pins in row 1, 3 and 5. It is reported that the shape and behavior of the HVS changes from the first row toward the more downstream rows. It is assumed that the acceleration due to the pin blockage imposes constraints on the location of the recirculation regions in spanwise resulting in a concentration towards the centerline with a more defined vortex core- an effect that was not observed in the unrestricted first row. When comparing the third and fifth row, none to small decrease was observed by Anderson and Lynch which they attribute to the fully developed nature of the flow. Nusselt num-

ber distributions by Won et al. [39] reported an increased in heat transfer at the endwall of a staggered pin fin array (upstream of the pin fins where the HVs are generated) and downstream between the wakes of the pins (where the HVs slowly decay and the shear layers separate, resulting in a reattachment of the flow [52, 53]). It was also observed that "remnants" exist due to the HVs from the row upstream. As previously reported by Goldstein and Karni, the effect of those remnants on heat transfer can be observed up to 3.5 cylinder diameters downstream [39, 52]. The authors' findings are in close agreement with data reported by Chyu and Natarajan with respect to the shear layer reattachment, about two pin diameter downstream of the pin, and a necklace vortex wraps around the leading edge of the pin up to one pin diameter upstream [53].

Although unrelated to heat transfer, Baker [63] looked into the horseshoe formation on a single wall bound cylinder with the help of smoke and oil flow visualization. Bělík [64] developed a correlation to predict the location of the separation line upstream of the pin. Later, Dargahi [65] investigated the HSV and wake shedding of a pin by using a hydrogen bubble technique for visualization and hot wire anemometry for velocity/turbulence measurements for a Reynolds Number range between 8,400 and 46,000. Dargahi observed quasi-periodic shedding of HSVs dependent of the Reynolds number. It was also observed that the number of vortices that are part of the horseshoe vortex systems (HVS) varies by number depending on the pin Reynolds number. By using an oblong shaped pin, it was managed to separate the HSV from the wake shedding and found that the wake shedding does barely influence the HSV shedding. Other research groups also have looked into the HVS at the junction between a flat plate and pin experimentally regarding the vortex structure [66–70] and turbulence measurements [27, 34, 60, 71, 72]. Eisenlohr and Eckelmann focused on the wake of a cylinder. A Kármán vortex street forms in the wake of the pin as a consequence of the period wake shedding of the pin. Adverse pressure gradients cause vortices to be shed from the pin. As they travel further

downstream, they rotate and spread out. The sequence of several vortices is called a Kármán vortex street. Researchers typically focus on two pins to observe how the Kármán vortices interact. If both sheddings are out of sync, it can occur that one vortex street pulls the vortices of the other towards it, resulting in a higher shedding frequency. Further, they report that the Strouhal number is different for wall-bound cylinders and free cylinders.

Motivated by observed flow induced vibrations in tube bundle heat exchangers, Umeda and Yang [73] conducted Laser Doppler Velocimetry (LDV) studies on an in-line and staggered array of cylinders at various diameter and pitches by analyzing the oscillation of von Kármán vortices. The authors point out a dependency between the spanwise and streamwise pitch of the pins with respect to flow oscillation. In case of pins arranged in isosceles triangles, the wake vortices are confined by the accelerated flow around the tubes. However, observations are defined with regards to the entire tube array, no row to row variations were observed.

Ostanek and Thole [74] also studied flow in the midplane at various pin spacings with time-resolved PIV. Although the author notes that heat transfer coefficients increase for reduced streamwise spacing, the observed turbulent kinetic energy decreases for decreasing streamwise spacing. This effect is assumed to be caused by three dimensional effects and recommended for further investigation [74] thus partially motivating this study. Work by Ames et al. was conducted on a staggered pin array which consists of 8 rows with 7.5 pins per row. The pins are half the height of the channel and spaced 2.5 diameters in spanwise and streamwise direction. The Reynolds numbers based on the pin diameter and maximum velocity were 3,000 (laminar boundary layer [75]), 10,000 and 30,000. Endwall heat transfer results were obtained from an infrared camera and are presented as contour plots with a clearly visible peak in heat transfer in the region of the horseshoe vortex buildup [33]. Static pressure measurements on the surface of the pins

and on the endwall were used to gain insight into the creation of the leading edge vortex; good agreement between literature and experiment in terms of location and strength of the vortex system was reported [75]. A hotwire probe was deployed to measure endwall boundary layers, time-averaged, and instantaneous velocities in proximity to the pin and in spanwise direction between two neighboring pins. A discrepancy in expectation and data occurred for the spanwise velocity fluctuations in magnitude and location, for which the author assumes the midplane data might be insufficient for explaining the physics in this case [5]; this potentially implies some three dimensional effects such as the contribution of the HVS on the turbulent fluctuations between the pins. Directly quoted from their work, the authors state that the "flow around the pin accelerates strongly and has positive W component. The source of this anomaly is unknown [...]" [33] indicating that the flow is yet, despite all the studies that have been conducted so far, not fully understood.

High-fidelity measurements resolving the horse shoe vortex system upstream of the pin and the development of the necklace vortex that wraps around the pin are more commonly found for single wall-mounted cylinders than for arrays [65, 69–71, 76]. These studies contribute to the understanding of the development of such vortex systems, however, the confining effect through neighboring pins is neglected. Furthermore, the flow encountering the single pin is very controlled and usually of low turbulence. In contrast, the flow field in a pin fin array located at one of the downstream rows is highly turbulent over wide range of turbulent scales including large scales such as remnants of vortex structures that directly impinge on the pin.

In summary, the review shows several efforts in understanding the flow structure of HSVs on a single wall bounded pin or vortex shedding on a single cylinder. For arrays of pins, the main interest is in the study of the flow field in the wake of the pin, not the wall effects due to the vortices created on the junction of wall and pin even though

its contribution on heat transfer has been described. An overview of relevant literature regarding flow field measurements is given in Table 2.2.

Table 2.2: Overview of applicable literature on pin fin array flow measurements

Authors	Year	Array Type	Feature Shape	$^{y}/_{D}$	$^{x}/_{D}$	$^{H}/_{D}$	Measurement Technique	Reynolds Number Range
Blevins [77]	1977	inline	circular	1.84	1.4 & 1.5	20	pressure probes	20,000 - 100,000
Metzger and Haley [46]	1982	inline	circular	2.5 & 1.5	2.5 & 1.5	2	Schlieren	5,000 - 50,000
Simoneau and VanFossen [24]	1984	inline & staggered	circular	2.67	2.67	3	Hot-wire	5,000 – 125,000
Dargahi [65]	1989	single	cylinder	NA	NA	NA	Hydrogen Bubble	6600 - 65,000
Eisenlohr and Eckelmann [68]	1990	two in parallel	cylinder	NA	NA	NA	smoke wire	50 - 150
Devenport and Simpson [71]	1990	single	NACA profile	NA	NA	NA	LDV & Schlieren	6700
Agui and Andreopoulos [66]	1992	single	circular	NA	NA	NA	Schlieren & pressure probe	10,000 - 220,000

Authors	Year	Array Type	Feature Shape	$^{y}/_{D}$	$^{x}/_{D}$	$^{H}/_{D}$	Measurement Technique	Reynolds Number Range
Chyu and Natarajan [53]	1996	single	cube & diamond	NA	NA	NA	Schlieren	5,000 – 25,000
Umeda and Yang [73]	1999	staggered	circular	various	various	various	LDV	800 - 20,000
Uzol and Camci [34]	2001	staggered	elliptical	2	2	1.5	PIV	10,000 – 47,000
Won et al. [39]	2003	staggered	circular	2	2	1	pressure probe & smoke	10,000 – 20,000
Ames et al. [5,33,75,78]	2007	staggered	circular	2.5	2.5	2	pressure probe & hot-wire	3,000 – 30,000
Sahin et al. [69]	2008	single	circular	NA	NA	4	PIV	1,500 – 6,150
Ostanek and Thole [74]	2012	staggered	circular	2	1.73 & 3.46	1	PIV	3,000 – 20,000
Kirkil and Constantinescu [70]	2015	single	circular	NA	NA	NA	PIV	16,000 – 500,000
Apsilidis et al. [72]	2015	single	circular	NA	NA	NA	PIV	29,000 – 123,000

Authors	Year	Array Type	Feature Shape	$^{y}/_{D}$	$^{x}/_{D}$	$^{H}/_{D}$	Measurement Technique	Reynolds Number Range
Anderson and Lynch [62]	2016	staggered	circular	2	1.73 & 3.46	1	PIV	10,000 – 50,000
Schanderl et al. [76]	2017	single	circular	NA	NA	NA	PIV	39,000
current study	2019	staggered	circular	2.5	2.5	2	PIV	10,000 - 30,000

Numerical Studies

Similar to the flow field analysis, high-fidelity LES or DNS on arrays are rare. However, numerically such as Large Eddy Simulation and Detached Eddy Simulation are found for single wall-bound cylinders and for arrays with a hybrid approach. At first, the relevant RANS literature shall be discussed. Ames and Dvorak [33] conducted steady RANS simulations in an array of staggered pin fins for 10,000 and 30,000 Reynolds number where the pin spacing was 2.5 in spanwise and streamwise direction. Ames and Dvorak also conducted heat transfer measurements using an infrared camera and conducted additional friction factor analysis. While comparing the numerical results from RNG, realizable and standard k-ω models with the experimentally obtained measurements, they found that array Nusselt number is similar for all three numerical models but substantially underpredicting the results from the experiment. An underprediction in friction factor was observed, too. Both observations are attributed to the wrong prediction of flow separation from the pin. As the separation point is wrong, the wake structure in the simulation does not agree with the experiment. Here lies the reason for the mismatch in pressure drop and heat transfer.

Delibra et al. [40, 42] conducted URANS and LES simulations at the same geometry as Ames et al. and used their data as validation. Delibra et al. demonstrated good agreement for the elliptical-relaxation eddy-viscosity model in terms of vortex shedding, but also report a mismatch in shedding magnitude for the first three rows compared to experiment and LES [40]. They further attribute the early separation of the shear layer due the insufficiency of RANS and URANS to resolve the small turbulence scales. The correct modeling of the scales shed by the cylinder in the first and second row is critical as they directly impinge on the third and fourth row and affect the boundary layer

growth on those particular pins. The agreements between endwall Nusselt number for 10,000 and 30,000 Reynolds number are reported to be within 20% and 10%, respectively.

In the next step, the group around Delibra [42] attempted an hybrid approach where RANS formulations were used to model the flow along the endwall and LES in the flow volume. The advantage of an hybrid model is that the mesh count can be significantly reduced compared to a pure LES, in particular at higher Reynolds numbers. The drawback is that turbulence close to the wall is modeled using conventional RANS formulations. This in turn reduces the spectrum of resolvable eddy scales as described earlier. They state that their mesh was too coarse for a proper LES at the higher Reynolds number, but good agreement for 10,000 Reynolds number case. Two major heat transfer transport schemes were identified. First, the near-wall heat transfer occurs predominantly due to small scale turbulence. Second, large eddies shed from the pins mix the warm small scales with the colder bulk fluid. It is obvious from this discussion that both, large and small scales, have to be correctly modeled to accurately predict turbulent transport of heat away from the wall and finally into the bulk flow.

Li et al. [79] compare the performance of six different turbulence models in a pin fin array similar to the one found in Ostanek [74]. The variety of turbulence models includes Reynolds stress model (RSM), linear eddy viscosity models such as k-ω and k-ϵ, and V2f. The performance of the models is gauged versus experimental data obtained through PIV. In agreement with Delibra et al. [40, 42], Li et al. locate the shortcomings of RANS in the lack of ability to resolve small scale turbulence and the isotropic assumption for turbulence[1]. Although overall endwall Nusselt number and pin Nusselt number agree with experimental data, it is found that the wrongful prediction of flow separation and shedding results in unphysical Nusselt number distributions on the endwall. Otto et al.

[1]This is a very crucial point. The theoretical background to the Boussinesq approximation and isotropic turbulence will be giving in the numerical simulations section in the methodology chapter.

made the samer observations regardings the local Nusselt number distribution on the endwall [43].

The high computational cost for LES and DNS prohibits its use for full arrays or higher Reynolds numbers. If no hybrid methods are used as for example by Delibra [42], the area of interest has to be significantly shrunk. Therefore, a variety of single cylinder LES and DNS simulations exists, each with a slightly different avenue. Escauriaza and Sotiropoulos [80] carried out a DES simulation of a single wall-bound cylinder with the focus on the understanding of the dynamics of the horseshoe vortex system at Reynolds numbers of 20,000 and 39,000. A strong dependence of the nature of the horseshoe vortex on Reynolds number is observed. At lower Reynolds numbers, the necklace vortex forming directly in the junction is shed at a higher frequency compared to the quasi-periodic shedding at higher Reynolds numbers. For higher Reynolds numbers, one dominant, large scale necklace vortex exists.

On the same token, Schanderl [81] and Manhart and Schanderl et al. [76] conducted a highly resolved LES on a single pin with the goal to understand the local wall shear stress. During their simulation, it was found that the simulation is highly susceptible by the incoming boundary conditions. Although the study was not related to heat transfer, a key observation made by the Schanderl et al. is that the instantaneous wall shear stress can be 40 times higher than the mean wall shear stress. This indicated that the wall heat transfer is highly time-dependent. However, it can be assumed that the time scale of the fluctuations is much smaller than the thermal response of an airfoil so that fluctuations in heat transfer do not pose a threat on the local cooling.

Table 2.3: Overview of applicable literature on numerical simulation on pin fins

Authors	Year	Array Type	Feature Shape	$^{y}/_{D}$	$^{x}/_{D}$	$^{H}/_{D}$	Numerical Technique	Reynolds Number Range
Rodi [41]	1997	single	cube	NA	NA	NA	RANS & LES	22,000 - 40,000
Fröhlich and Rodi [82]	2004	single	cylinder	NA	NA	2.5	LES	43,000
Ames et al. [33]	2007	staggered	circular	2.5	2.5	2	RANS	3,000 – 30,000
Delibra et al. [40]	2009	staggered	circular	2.5	2.5	2	URANS	10,000 – 30,000
Delibra et al. [42]	2010	staggered	circular	2.5	2.5	2	hybrid LES	10,000 – 30,000
Escauriaza & Sotiropoulos [80]	2011	single	circular	NA	NA	NA	DES	20,000 – 39,000
Kirkil and Constantinescu [70]	2015	single	circular	NA	NA	NA	LES	16,000 – 500,000
Li et al. [79]	2016	staggered	circular	2.16	2	1	RANS	20,000
Schanderl and Manhart [81]	2016	single	circular	NA	NA	NA	LES	39,000

Authors	Year	Array Type	Feature Shape	$^{y}/_{D}$	$^{x}/_{D}$	$^{H}/_{D}$	Numerical Technique	Reynolds Number Range
Schanderl et al. [76]	2017	single	circular	NA	NA	NA	LES	39,000
current study	2019	periodic section	circular	2.5	2.5	2	LES & RANS	10,000

Summary

The review of literature captured a variety of experimental setup, research goals, and partially contradicting results. In the first part, heat transfer and pressure drop research on various trailing edge geometries was introduced. Correlations for row and array averaged Nusselt number exist but meaningful research and spatially resolved Nusselt number distribution is sparse. The next section focused on several flow measurement techniques. It was found that the turbulence intensity increases downstream and increases pin heat transfer. The heat transfer on the wall is driven by local turbulent intensities but also two large scale vortical systems: horseshoe vortex system at the leading of the pin and a the von Kármán vortices in the wake of the pin. Several studies exist that focus on one or the other, but rarely in conjunction nor in the setting of an array as found in trailing edge cooling systems. The available literature on numerical methods reveals a lack accuracy when RANS-based models are used to predict turbulence or heat transfer within an array of pin fins. LES exist, but not with the sufficient mesh size to resolve small eddies and investigate their impact. It was stated that small eddies dominate the heat transfer in the wall-near region, but most measurements in describing the flow field were conducted in the mid-plane of the channel and not in the wall-near region.

CHAPTER 3: OBJECTIVE AND MOTIVIATION

Objective of the Present Study

Reflecting upon the concluding remarks in Chapter 1 and the review of literature, a gap in available knowledge was identified. The lack thereof limits the physics-based advancement of trailing edge cooling for improved turbine performance. The present study aims to address this gap by investigating the flow physics in the wall-near region and relate it to a highly resolved local Nusselt number distribution obtained through the transient thermochromic liquid crystal method. The local distribution of the Nusselt number on the endwall will be explained in detail with the findings from the PIV which was conducted in the same array. The first three rows are part of the developing flow regime and vary strongly amongst them. Difference in the flow field of the first and third row will be pointed out and will guide design engineers to optimize shapes and spanwise and streamwise spacing through the provided high-fidelity turbulence data.

RANS models are known to fail in the proper prediction of spatially resolved Nusselt number distributions on the wall. A periodic LES with a fully developed interface simulates the flow downstream of the first five rows in a pin fin array. Comparisons will be made with conventional RANS solutions based on the turbulent kinetic energy budget *why* and *where* RANS models fail.

Novelty

The novelty will be the investigation of the local flow field in the wall-near region rather than the investigation of turbulence statistics in the mid-plane of a staggered pin fin array. Furthermore, the fully developed interface boundary condition for numerical large eddy simulation of a fully developed flow through a pin fin array has not been uti-

lized. The periodic section allows a much higher mesh resolution than what is available in literature for array-based LES.

Rather than area averaged heat transfer, the use of the transient TLC methods enables the study of local heat transfer effects as the Nusselt number distribution is known over the entire surface of interested. The local knowledge of cooling distribution is crucially important to judge the performance of a certain cooling arrangements. Although overall heat transfer might be high, local uncooled spots could render the arrangement useless or hint where to add additional features to mitigate the negative effect on turbine life of locally undercooled spots.

The use of a high-definition camera with 1080 by 1920 pixels provide *unprecedented* insight into the local heat transfer in the developing region of a staggered pin fin array which in turn can be explained by unmatched *high-fidelity* turbulence statistics in the wall-near region obtained through stereoscopic PIV.

Intellectual Contribution and Research Impact

Although LES simulations provide high fidelity solutions and very dependable results for gas turbine engineers, they are not widely spread within the development phase for new, improved hot gas path components for gas turbines. The reasons are manifold. Most notable are the computational cost, the time, and resources required. The long computational time compared to RANS and URANS simulations prohibits the day-to-day use of LES simulations during the design phase. Otherwise, the time to market of new gas turbine generations would increase dramatically. Despite being less computationally expensive than LES thus suitable for quick design iterations, the result accuracy of common RANS simulations is often insufficient. This is in particular unacceptable for heat transfer design. Due to the nature of RANS simulations and the problem of turbulence closure,

many assumptions, as discussed in another chapter, are made. Partially due to those assumptions, flow physics are not correctly characterized, resulting in high error simulation results.

The present dissertation aims to address this issue by pinpointing the shortcomings of RANS models for pin fin cooling applications. Experimental data obtained through PIV and TLC are used in conjunction with LES to analyze the flow physics in a pin fin bank. Through the comparison of flow structures, velocity contours, turbulence statistics and additional flow quantities, the error source of RANS is qualitatively described.

The findings in this work will help gas turbine design engineers to tweak their turbulence models and give guidance towards the interpretation of the results. The knowledgeable reader may hesitate at this point since pin fins are a trailing edge geometry from the ages of casting. Admittedly, the advancements in additive manufacturing opens the design space for much more complex geometries without castability restrictions. The examples of successful implementations of additively manufactured components into aero and industrial turbines are plentiful. Noteworthy milestones are:

- A fully 3D printed and FAA[1] approved fuel injector for aero engines [83, 84],
- a fully printed and tested rotating airfoil including simple internal cooling passages manufactured by Siemens [85],
- an air-cooled shroud block with novel cooling geometries enabled through additive manufacturing presented by Siemens [86].

Regardless of these advancements, informed decision making has to be applied on how to optimize the novel shapes - in this case for the trailing edge region of the blade. Since

[1]Federal Aviation Administration. The regulatory institution for civil aviation in the United States of America.

pressure drop increase is an adversary to many designs, ways have to be found to significantly increase heat transfer without exceedingly increasing the aforementioned. The main goal during the phase just mentioned was to understand the relationship between geometric parameters, heat transfer augmentation, and increase in pressure drop. Ghosh et al. [87, 88] have taken this into consideration and applied a surrogate model based on Bayesian methods to optimize the shape of pin fins in pin fin arrays. Furthermore, with a relatively simple baseline case such as a pin fin array, Dynamic Mode Decomposition (DMD) can be applied to identify flow modes that contribute to heat transfer. With this information design engineers can now optimize shapes to promote these high heat transfer modes and suppress the undesired modes. For example, Elmore [89] has looked into this approach for rib turbulators for internal cooling.

In summary, two strong points were described of why the study of flow physics and the comparison between RANS and LES are crucial information for design engineers of internal cooling passages and contributing to better-performing geometries enabled through additive manufacturing.

CHAPTER 4: METHODOLOGY

The present chapter elaborates on the nature and application of the investigation techniques employed. The range of investigation techniques is twofold. On the one hand, experimental measurements: this includes the transient Thermochromic Liquid Crystal Technique for heat transfer and the Particle Image Velocimetry Technique for flow field analysis. On the other hand: numerical studies. This includes Large Eddy Simulation and RANS. The structure of the chapter is as follows. First, some key parameters for data reduction and fundamental correlations for normalization will be discussed. Next, the method of transient thermochromic liquid crystals (TLC) will be discussed. The fundamentals of the technique are elaborated followed by the comprehension of this technique for this study. This includes a discussion of the TLC processing code. The section following TLC discusses the PIV technique. Only the theoretical background for both methods will be discussed. Setup, functionality, and parameter specific to the experiment will be the subject of discussion in the upcoming chapters. The chapter ends with an examination of the theoretical background of computational fluid dynamics.

Key Parameter and Data Reduction

The thermal performance index (Equation 1.12) was already introduced at an earlier point. This is the key parameter that considers Nusselt number augmentation and friction factor augmentation to determine the performance of the present cooling arrangement with respect to the overall engine behavior. The friction factor augmentation is defined as the ratio of the actual friction factor f and a baseline friction factor f_0 derived from a correlation.

$$\frac{f}{f_0} \tag{4.1}$$

The Blasius correlation [90], is used as the baseline reference for the Darcy friction factor. The correlation is valid for Reynolds numbers smaller than 100,000 and turbulent flows in a pipe. By using the hydraulic diameter D_h, the correlation can be applied to non-circular channels as well.

$$f_0 = \frac{0.078}{Re_{D_h}^{0.25}} \tag{4.2}$$

The Nusselt number augmentation is defined in a similar fashion as the friction factor augmentation.

$$\frac{Nu}{Nu_0} \tag{4.3}$$

Here, the reference baseline case is the well-known correlation introduced by Dittus Boelter [18] for a fully developed turbulent flow in a circular pipe (Equation 4.4) where fully developed also includes thermally fully developed. The correlation is valid for Reynolds numbers greater than 10,000 and Prandtl numbers in the range of 0.6 to 160. The exponent to the Prandtl number n is 0.3 for a cooled fluid and 0.4 for a heated flow.

$$Nu_0 = 0.023 Re_{D_h}^{0.8} Pr^n \tag{4.4}$$

In order to make conclusions about the thermal performance, the test case-specific friction factor f and Nusselt number Nu are required. The overall friction factor is obtained by measuring the drop in static pressure throughout the test section. The test section is equipped with pressure taps upstream and downstream of the pins as well as centered between the pins. Measuring the pressure differential between the first and last row quantifies the pressure drop Δp. Armstrong and Winstanley [48] recommend in their review paper the use of a flow friction factor defined as

$$f = \frac{\Delta p}{2\rho(u_{max})^2 N} \tag{4.5}$$

where u_{max} is the computed velocity between the pins based on the continuity equation, ρ the density, and N the number of rows. Measuring the Nusselt number distribution over the surface is more challenging compared to the pressure drop measurement. A transient thermochromic liquid crystal technique was used for the Nusselt number measurement. The technique is introduced in the next section.

Not only the measurements are subject to normalization, critical geometric dimensions of the pin fin array are also presented in a non-dimensional manner to enable comparisons between different experimental setups. An example of a staggered pin fin array is shown in Figure 5.5. Most notable is the height-to-diameter ratio

$$\frac{H}{D} \tag{4.6}$$

between channel height H and pin diameter D. Generally, all geometric parameters are given as a ratio relative to the pin diameter D so that the definition for the streamwise spacing is

$$\frac{x}{D} \tag{4.7}$$

and for the spanwise spacing

$$\frac{z}{D}, \tag{4.8}$$

respectively. The streamwise spacing can be understood as the normalized distance between the center point of to pins in the flow direction in the length direction of the channel. Similarly, the spanwise spacing is the spacing perpendicular to the main flow direction, over the width of the channel. Again, the spacing is the distance between the center points of two pins. If a pin fin array is in-line, all pin center points form a grid with equal spacing in spanwise and streamwise direction. If a pin fin array is staggered, every other row is offset by half a pitch.

The wetted perimeter in the straight duct section leading up to the first row of pins and downstream of the last row of pins is defined as twice the sum of the width W and the height H of the channel

$$P_{wet} = 2(H + W) \tag{4.9}$$

and the cross sectional area A_c as the product of both

$$A_c = HW \tag{4.10}$$

The hydraulic diameter D_h is defined using Equations 4.9 and 4.10 as

$$D_h = \frac{4A_c}{P_{wet}} \tag{4.11}$$

The fluid bulk velocity is then calculated using the definition of mass flow rate. At a previous point, it was stated that the fluid properties in the unblocked area upstream and downstream of the pins are indexed with min. Taking this into account, the bulk velocity is then defined as

$$u_{min} = \frac{\dot{m}}{\rho A_{min}} \tag{4.12}$$

Consequently, the Reynolds number based on the hydraulic diameter becomes

$$Re_{D_h} = \frac{\rho u_{min} D_h}{\mu} = \frac{4\dot{m}}{\mu P_{wet}} \tag{4.13}$$

The effective flow area changes with the introduction of the pins which partially block the channel. The unblocked area A_{max} can be calculated by subtracting the projected footprints of the pins DH multiplied by the number of pins per row N_r.

$$A_{max} = A_{min} - (N_r DH) \tag{4.14}$$

All velocities and areas can be converted through the definition of the continuity equation in Equation 1.20. Further, the ratio between the unblocked and blocked area available for the flow is the blocking ratio BR. The higher the blockage ratio, the more area is occupied by the pins.

$$BR = 1 - \frac{A_{max}}{A_{min}} \tag{4.15}$$

Now, it turns out that many phenomena in pin fin arrays correlated with the local values rather than the free stream values. In consequence, the computed velocity between the pins u_{max} and Reynolds number based on pin diameter Re_D is of significance. From the combination of Equation 1.20 and Equation 4.12 follows

$$u_{max} = \frac{\dot{m}}{\rho A_{max}} \tag{4.16}$$

and finally

$$Re_{D_h} = \frac{\rho u_{min} D_h}{\mu} \tag{4.17}$$

Introduction to Thermochromic Liquid Crystals

The transient thermochromic liquid crystal technique was used for heat transfer data in this study. Further, TLC shall serve as an abbreviation for the quite clumsy and lengthy term transient thermochromic liquid crystal method. Thermochromic liquid crystals, also called thermochromatic liquid crystals, are crystals that change color based on temperature. The crystals are commonly sold as sheets or as a paint that can be sprayed onto various surfaces. Most paints are a composition of commonly three organic substances. The active temperature range with a color response is engineered by varying the mixing ratio between those substances and can vary between a few Kelvin for narrow-band TLC paint and more than 30 Kelvin for wide-band TLC paint. The paint is colorless

outside of the defined temperature range, yet is visible due to its milky opaqueness. That means that incoming white light passes through the crystal structure. Bragg diffraction occurs between those layers and only one dominant wavelength is reflected back. However, the spacing between the layers of the crystalline structure changes with temperature. As now the spacing between the layers in the crystal changes, the reflected wavelength changes, too. As the lower end of the temperature range is reached, the reflected wavelength is within the range of visible light. Here, the paint turns into a red-orange. As the temperature further increases, the paint's colors change through all spectral colors from red to green to blue. The color eventually becomes transparent again at the upper limit of the specified temperature range. The backside of the color is oftentimes covered with black backing paint. The paint absorbs any scatter except the reflected wavelength and thus increases the contrast of the color versus its surroundings. Further details on the composition and physics of color change can be found in [91] and [92]. The key take-away at this point is that this paint enables to establish a relationship between temperature and color. An example for the color change is shown in Figure 4.1. Heated air from a heat gun was blown onto the test surface to test the TLC paint. The local spot shows the impingement of the heated air on the surface over which it spreads out and encounters the pin.

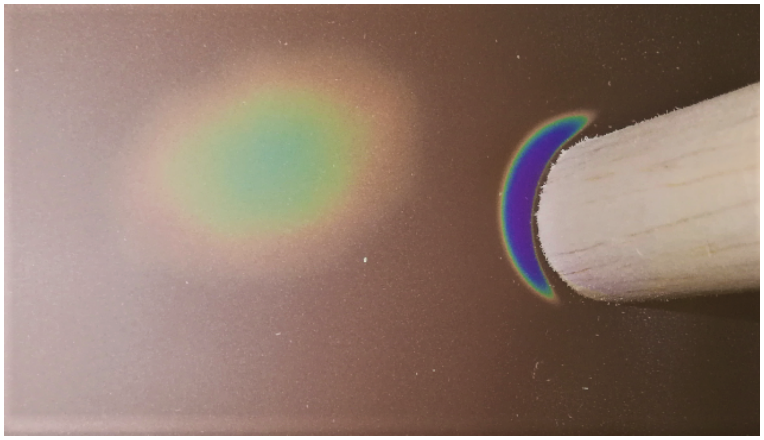

Figure 4.1: Applying heat with a heat gun to the TLC coated surface: the milky TLC changes colors at the leading edge of a pin based on the local temperature

If one now considers the challenge to determine the local heat transfer coefficient and recall Equation 1.13, a very powerful tool to obtain a local value for the wall temperature - the main challenge in determining a local heat transfer coefficient - is at hand. Nowadays, the approach on how to use TLC paint is twofold: steady-state and transient. Using thermochromic liquid crystals for heat transfer measurements was first introduced in 1981 by NASA [93]. Since then the various aspects of the method have been studied in great detail and many improvements in terms of accuracy and robustness have been made. Ireland and Jones [94] provide a good overview of the different approaches to the TLC technique and the modifications used in experiments all over the world.

In the case of the *steady-state* approach, heat is supplied through a heater attached to the target surface. Wide-band TLC paint is applied to the surface with a temperature range that covers the entire spectrum of expected temperature variation in the test. The target surface is cooled by forced convection. The temperature on the surface will vary according to the local heat transfer coefficient. As the heat supply is known from the heater, the local heat transfer coefficient can be determined based on difference between

the local wall temperature and bulk fluid temperature. However, the experimental setup has to be thoroughly calibrated prior to the tests. Ideally with the same camera and lighting conditions, the correlation between color and temperature has to be established. It is understood that any color in the color spectrum can be reproduced by only using red, green, and blue - RGB. The paint is heated to several different temperatures while the composition of the red, green, and blue component is saved. Later, the intensity of each RGB color component can be plotted versus temperature. Therefore, with a known intensity of all three colors, the temperature can be obtained. The downside of this method is that viewing angle, lighting, and others have an effect on the perceived color. As light does not always enter perpendicular through the camera lens on the camera sensor due to the three-dimensionality of the test section, the perceived color intensities do not always match the actual paint color. This reduces the accuracy of this method if no additional calibration is conducted with respect to viewing angle. Additional information on the calibration of TLC paint can be found in Abdullah et al. [95] and Kakade et al. [96] studied the effect of viewing angle in greater detail.

In the case of the *transient* approach, heat is not supplied to the target surface but to the airflow. Upon supplying heat to the air, the air temperature undergoes a change in temperature approximating a step function. The hot air now passes over the test area which is coated with narrow-band TLC paint with a temperature range of 1-3 K. Acrylic is selected due to it thermophysical properties, the ease of machining, and transparency a suitable material for the test surface. A temperature gradient exists between the target surface material temperature and the hot air. Over time, the material responds to the convective heating by soaking up heat on the surface which then conducts through the thickness of the acrylic slab. If the hot air temperature is larger than the temperature range of the TLC paint, the paint will eventually turn red, green, and blue once the corresponding temperatures to the colors are reached on the surface. Assuming the lumped

capacitance and purely one-dimensional conduction within the acrylic slab, the time from supplying heat to reaching a specific temperature on the painted surface corresponds directly to a unique local heat transfer coefficient. The method is more robust compared to steady-state TLC as only the arrival of the peak intensities for red, green, and blue are considered and not their intensity only. Therefore this method has a lower dependency on the viewing angle [97, 98]. The actual color is not relevant but rather the time between switching on the heat supply and reaching the temperature where either red, green, or blue reaches its peak intensity. Commonly the arrival of the green peak intensity is chosen. The intensity of green plotted against temperature shows the most discrete peak and the highest peak in magnitude [97, 98]. A discrete peak helps to accurately associate the peak intensity with a specific temperature. A strong peak in magnitude improves the accuracy of properly identifying the peak in the time series of color intensity versus time for each pixel.

The Transient Thermochromic Liquid Crystal Technique

The ultimate goal of the transient thermochromic liquid crystal method is to obtain a local heat transfer coefficient of a target surface by supplying heat to passing air instantaneously and measuring the time it takes for a pixel to reach the maximum green intensity. A camera is focused on the area of interest which is the region 2.5 pin diameter upstream of the first row, the entire length of the pin fin array and 2.5 pin diameter of the aforementioned. Two LEDs are connected to the heater system. The LEDs emit light as soon as the heater is switched on. This way the start of the experiment is easily identifiable in the video recording. The recorded video alongside the recorded temperature from the DAQ system is handed over to the TLC post-processing code. The detailed workflow of which is shown in Figure 4.2.

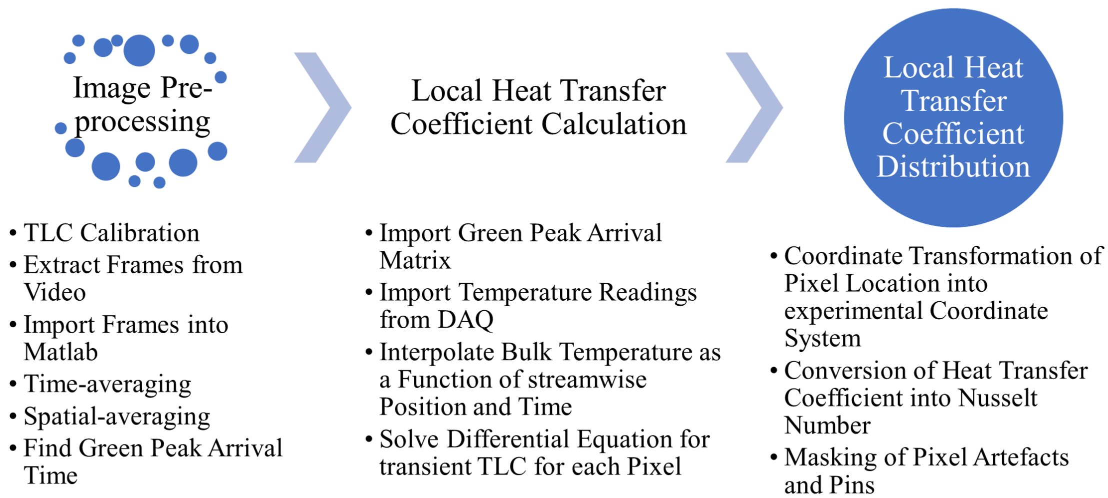

Figure 4.2: TLC work flow after recording the transient experiment

Before calculating the local heat transfer coefficient from the video recordings, several pre-processing steps have to be undertaken to extract the necessary input. A code composed of several MATLAB functions were developed to get the local heat transfer-/Nusselt Number distribution from the recorded video - which can be found in Appendix B. In the first step, each frame of the video has to be exported to be able to handle the recordings in Matlab. The file sizes of the videos ranged between 213 MB and 732 MB depending on the length of the recording. The total size of the exported images, the uncompressed TIFF format was chosen, ranges between 27.2 GB and 105.7 GB for the shortest and longest test, respectively. Memory became a computational bottleneck as it was required to import all images at once. It was decided to break down the raw images into several sections that are imported and processed independently to avoid memory issues. Additional memory is saved by cropping down the image to the actual area of interest. All images are loaded into a four-dimensional matrix array of the type x-coordinate, y-

coordinate, intensity values for red, green, and blue at each frame of the time series. The first frame, which shows the test section in the original state, is subtracted from all the following images. This background subtraction helps to increase the prominence of the green peak. The first frame can be readily identified by the red LED signal that appears as soon as the test starts. As discussed earlier, only the green peak information is used; the unrequired channels for red and blue are deleted to reduce computational time and memory requirements. The remaining green intensity value for each pixel at any given frame is averaged in terms of time and space. A three-point rolling average is chosen for the reduction of noise in the recording. The intensity values of a pixel pair i, j are averaged with the intensity value of the particular pixel before and after the target frame before a weighted average is used for spatial averaging. The weightings are shown in Table 4.1. The target pixel was weighted with 60% whereas the eight neighboring pixels contributed with 5% each. No special treatment for the edges was implemented so that the pixels along the edges of the image were lost. This was not a problem as the area of interest does not span the entire recordings. At this point, the data set is filtered and a time series of the green intensity exists for each pixel pair i, j. The nature of the transient TLC experiment requires the time until the surface temperature reaches the target temperature defined through the green peak temperature. Obtaining the time when the green peak is reached is the key output of the image pre-processing function.

Table 4.1: Filter matrix for weighted spatial averaging

5%	5%	5%
5%	60%	5%
5%	5%	5%

Therefore, the location of the green peak is then identified for every pixel in the test domain. The change of the green intensity over the course of the experiment for a

representative pixel pair is shown in Figure 4.3. The green peak can be clearly identified and is very distinct compared to the values of the remaining data series. However, upon closer inspection of the peak itself, it was found that the signal is noisy around the peak itself. The blue line in Figure 4.4 shows the raw signal as obtained through the code. The included peak finding function picks up every local maximum. It can be seen from the shape of the peak that the local maximum does not line up with the location of the bigger picture peak when considering a smoothed curve. For this reason, it was necessary to filter the data prior to identifying the peaks to obtain a more accurate time for the peak occurrence. The in Matlab implement Savitzky-Golay filtering function was used to smoothen the raw signal. The polynomial order and frame length for the Savitzky-Golay finite response filtering were 7 and 201, respectively. Although the filter results disagree in the magnitude of the fitted data, the location of the peak is preserved. The filtering resulted in much better accuracy in picking up the frame number of the green peak occurrence. All peaks were sorted by prominence and the most prominent peak was exported as green peak arrival frame number for that specific pixel pair i, j. Finally, the green peak arrival time is then calculated by dividing the frame number with the known frame rate of the video. The matrix containing the green peak arrival time for each pixel is ultimately saved as *.mat*-file which concludes the image pre-processing portion of the TLC post-processing code.

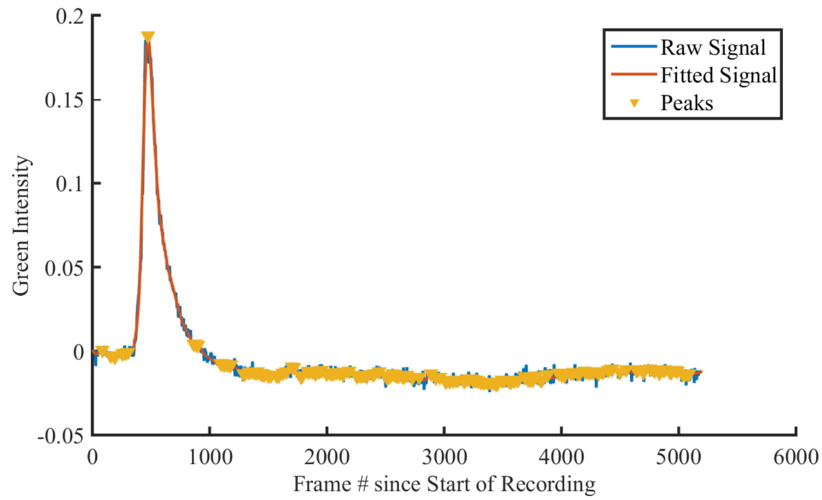

Figure 4.3: Green intensity value of one selected pixel over the entire test of the experiment for the raw and fitted signal

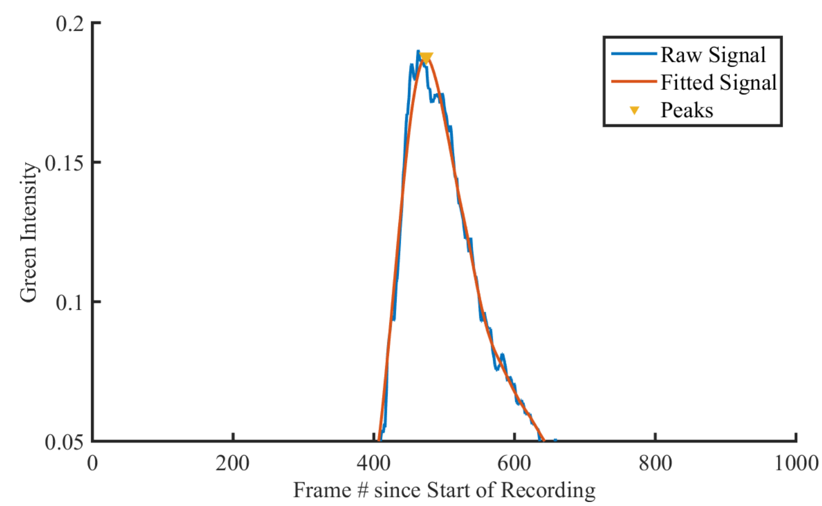

Figure 4.4: Zoom into the green intensity value of one selected pixel for the raw and fitted signal

The physical approach of the transient TLC method is the solution of the one-dimensional transient heat conduction in a semi-infinite solid. An analytical solution to that problem exists with a variation of temperature with respect to time and space. The solution to this particular problem can be found in any decent heat transfer textbook such as Incropera and DeWitt [18]. The maximum Fourier number (Equation 4.19) for the experiment has to be small enough so that this solution method can be applied. The maximum Fourier number is the Fourier number of the longest test which was 0.1, thus smaller than unity so that this assumption is valid for the suggested experimental setup. Since the conditions are satisfied, it can be assumed that the thermal penetration depth is much smaller than half of the material thickness.

$$Fo = \frac{\alpha t}{L^2} \tag{4.18}$$

with the thermal diffusivity α defined as the ratio of thermal conductivity k of the solid with the specific heat capacity c_p and density ρ. It is noteworthy that the availability of reliable thermophysical properties of acrylic is limited. The most common value for the thermal conductivity and thermal diffusivity of Arcylic is 0.19 and 1.10E-07, respectively. Dos Santos et al. [99] extensively report on the thermal properties on PMMA (the scientific name for acrylic) and find variations up to 9% based on the measurement technique.

$$\alpha = \frac{k}{\rho c_p} \tag{4.19}$$

The heat diffusion equation, also *Laplace's equation* with constant properties and no internal heat generation is written as

$$\frac{\partial^2 T}{\partial x^2} + \frac{\partial^2 T}{\partial y^2} + \frac{\partial^2 T}{\partial z^2} = \nabla^2 T = \frac{1}{\alpha}\frac{\partial T}{\partial t} \tag{4.20}$$

with the necessary assumption of only one-dimensional conduction in wall-normal direction y, Equation 4.20 reduces to

$$\frac{\partial^2 T}{\partial y^2} = \frac{1}{\alpha}\frac{\partial T}{\partial t} \tag{4.21}$$

Two boundary conditions and one initial condition is required to solve Equation 4.21. The initial condition is that the temperature at time 0 is equal to the initial Temperature everywhere.

$$T(y, 0) = T_i \tag{4.22}$$

The two boundary conditions are the convective boundary condition at the surface

$$-k\frac{\partial T}{\partial t}\bigg|_{y=0} = h(T(0,t) - T_\infty) \tag{4.23}$$

and that the acrylic slab has the initial temperature far away from the convection surface, respectively. It should be noted at this point that $T(0, t)$ in Equation 4.23 is nothing else but the wall temperature that changes over time.

$$T(y \to \infty, t) = T_i \tag{4.24}$$

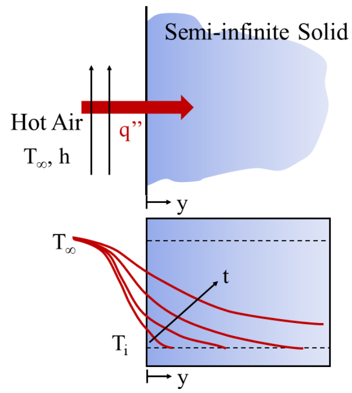

Figure 4.5: Visualization of the solution for the semi-infinite solid with convective boundary condition at $y = 0$

A closed form, analytical solution for the one-dimensional heat conduction problem Equation 4.21 and the convective boundary condition Equation 4.24 exists and is reported in [18] based on the solutions developed by Carslaw and Jaeger [100] and Schneider [101] as

$$\frac{T(y,t) - T_i}{T_\infty - T_i} = erfc\left(\frac{y}{2\sqrt{\alpha t}}\right) - \left[exp\left(\frac{hy}{k} + \frac{h^2 \alpha t}{k^2}\right)\right]\left[erfc\left(\frac{y}{2\sqrt{\alpha t}} + \frac{h\sqrt{\alpha t}}{k}\right)\right] \tag{4.25}$$

The complementary error function $erfc()$ is a short form for $1 - erf()$. The temperature response of the solid with time also known as the solution for Equation 4.25 is shown in Figure 4.5. As time increases, the heat penetrates deeper into the slab and rises temperature for larger y. The surface temperature also increases further until it eventually reaches to free stream temperature. The TLC method only requires information on the surface. The temperature distribution within the solid is not required. Therefore, Equation 4.25 is to be evaluated at the location $y = 0$ and simplifies to

$$\frac{T(0,t) - T_i}{T_\infty - T_i} = 1 - \left[exp\left(\frac{h^2 \alpha t}{k^2}\right)\right]\left[erfc\left(\frac{h\sqrt{\alpha t}}{k}\right)\right] \tag{4.26}$$

Further let

$$\beta = \frac{h\sqrt{\alpha t}}{k} \tag{4.27}$$

so that finally

$$\frac{T(0,t) - T_i}{T_\infty - T_i} = 1 - exp\left(\beta^2\right) erfc\left(\beta\right) \tag{4.28}$$

It can be seen from Equation 4.25 and 4.27 that the temperature ratio on the left-hand side of the equation is a function of heat transfer coefficient and time only. The evaluated temperature ratio can range between 0 and 1. Zero when the wall temperature is the same as the initial temperature throughout the entire experiment, for example, if no heat is supplied, and 1 if the wall temperature is equal to the bulk temperature. The right-hand side of the equation can be tabulated with the known properties for thermal diffusivity and thermal conductivity by varying t and h. Each combination of t and h is assigned a temperature ratio on the left-hand side. The heat transfer coefficient can now be found in the tabulated values since the time t is known as the green peak arrival time and the temperature ratio on the left-hand side is known from the experiment. This lookup approach for the local heat transfer coefficient is much faster than iteratively solving the differential equation for each pixel.

The experimentalist using the transient TLC method, however, encounters another challenge. The solution introduced above requires a constant free stream temperature T_∞ during the entire length of the experiment. That, in turn, requires that the temperature change of the fluid follows an ideal step function as soon as the fluid is heated. A clever design of the heater with a large wetted area to transfer heat to the flowing fluid can approximate a step function but never achieve an ideal step function. Figure 4.6 shows the temperature development obtained through measurement at a location upstream of the first row of pins. About 15 seconds pass until the hot air reaches 90% of its final temperature. An additional three minutes pass until 99% of the temperature step is achieved.

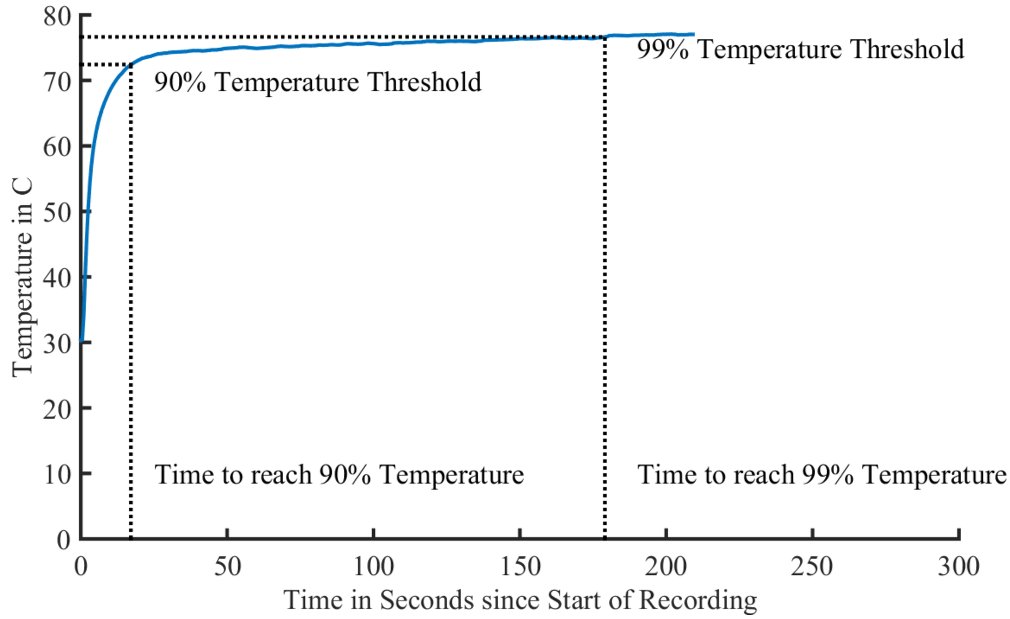

Figure 4.6: Bulk temperature development at location between pin row one and two over time

In consequence, the bulk temperature of the free stream has to be treated as a function of time itself. The use of Duhamel's theorem [102] allows the calculation of time-dependent boundary conditions by using the superposition principle. Details on the derivation of the Duhamel's theorem and the application to many linear problems can be found in the aforementioned reference. In general terms, the Duhamel theorem is a discretization with respect to time of heat diffusion equation (Equation 4.21) with the step-wise application of the time-dependent convective boundary condition (Equation 4.23). As always, the finer the time steps and therefore the temperature steps, the more accurate the approximation of Duhamel's theorem becomes. The application of Duhamel's theorem for local heat transfer measurement experiments is discussed by Metzger and Larson [103]. The authors discuss the derivation of the discretized version (Equation 4.29) from the analyt-

ical solution in Equation 4.28 and the resubstitution of β.

$$T_{GreenPeak} - T_i = \sum_{j=1}^{\infty} \left[1 - exp\left(\frac{h^2\alpha(t-\tau_j)}{k^2}\right) erfc\left(\frac{h\sqrt{\alpha(t-\tau_j)}}{k}\right)\right] \left[\Delta T_{m(j,j-1)}\right] \quad (4.29)$$

It is necessary to discuss the interpretation of bulk temperature before concluding the mathematical derivation of the transient TLC method. The hot air loses thermal energy as it passes through the channel. The heat is absorbed by the surface between the heater and the last row of pins. The heat *loss* is necessary in the area of the actual TLC measurement itself, however not desirable for any other surfaces in contact with the flow. The bulk temperature of the free stream decreases as a result of this heat *loss*. Therefore, it is required to monitor the bulk temperature throughout the channel and the knowledge of the local bulk temperature at all times everywhere. The calculation of the correct temperature that drives heat transfer is subject to many studies. Von Woltersdorf et al. [104] discuss a new data reduction approach for the identification of the proper temperature determination. It is stated that particularly in long channels the use of the inlet temperature yields erroneous results and it is proposed to use a method for the bulk temperature calculation instead that accounts for history of the local wall temperature. The temperature lost to the wall over time, related to the local heat transfer coefficient, ultimately determines the local bulk temperature. For this method, however, heat transfer coefficients on all walls are required. The method by Woltersdorf et al. is very similar to the approach described by Chyu et al. [30] who also compares five common methods for the bulk temperature calculation, mostly based on solving the local energy balance on all walls. Unfortunately, neither of those methods can be applied in the current study for two reasons. Reason one being that the TLC measurements are only conducted at one wall. One may claim that due to symmetry, the opposing wall has a very similar heat transfer, but that does not solve the lack of heat transfer data on the side walls. The second reason is that the pin

fins itself, albeit made from a material of very low thermal conductivity - thus assumed to be almost adiabatic, also contribute to heat transfer. Both reasons prohibit the use of the approaches suggested by Chyu et al. and Woltersdorf et al. As a result thereof, the local bulk temperature distribution is obtained through linear interpolation what is deemed a valid approach as the area of interest is only a short section of the wind tunnel. TCs are inserted into the flow to measure the local bulk temperature upstream, downstream, and in between the pins. At each measurement location in streamwise direction, three TCs are distributed over the width of the channel to pick up any temperature variations in spanwise direction caused by the pin wakes and other flow structures. Although a more detailed discussion on those temperature readings and the validity of this approach follows in the heat transfer validation section, it can be said at this point that a linear interpolation approach between the TCs upstream and downstream of the pin fin array is supported by the TCs within the pin fin array. Furthermore, the lateral variation of the thermocouple readings is negligible as well; boosting the confidence in the interpolation method.

The theoretical foundation is now laid out. The principle of the transient TLC method was described; mathematical formulations for the conversion of TLC color play and the local heat transfer coefficient are derived. Moving forward, the implementation of this knowledge into the Matlab code will be discussed. All codes are attached in the appendix and can be used for non-profit, non-commercial research and whilst properly referencing this source.

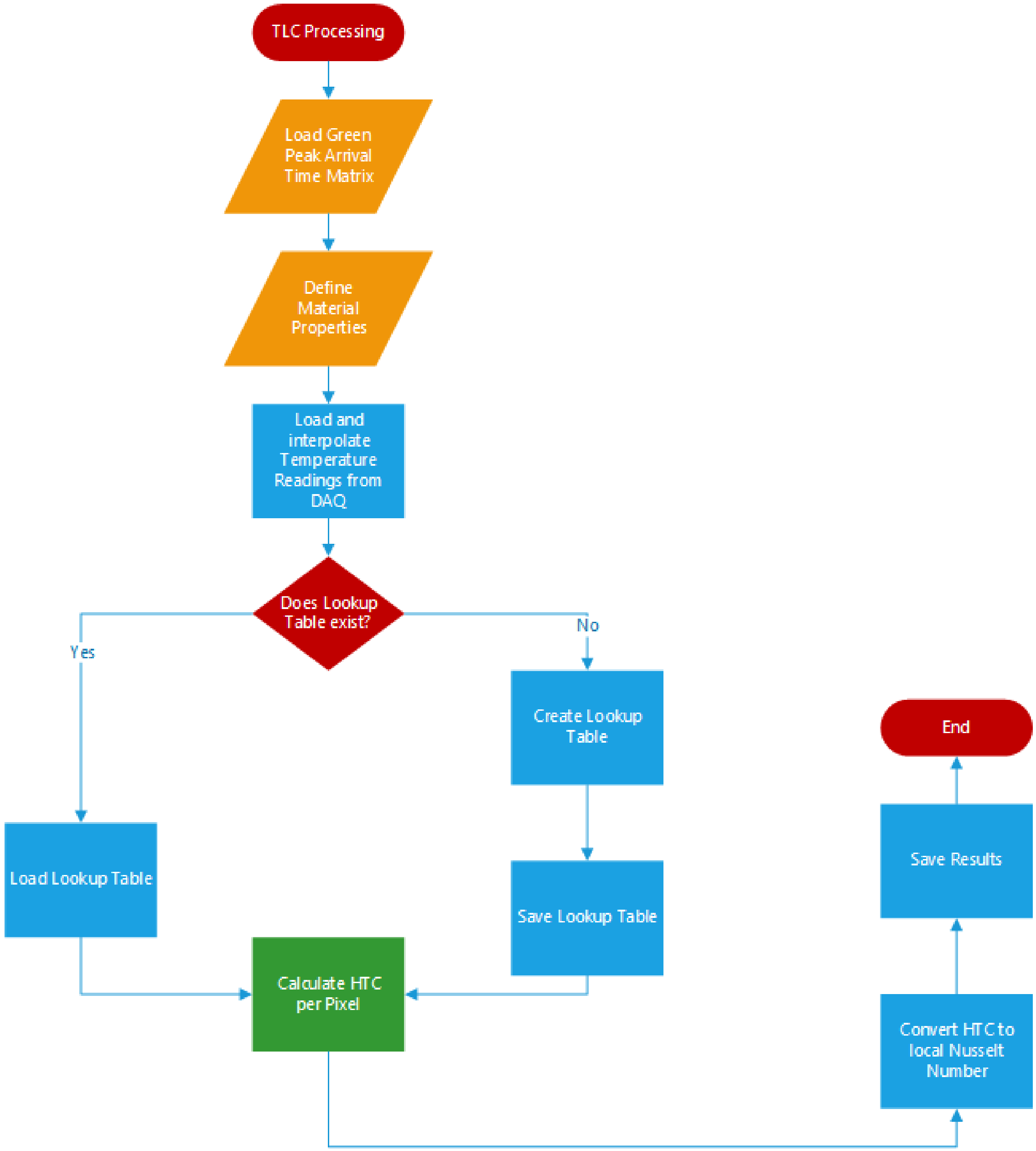

Figure 4.7: Overview of structure of TLC post-processing code

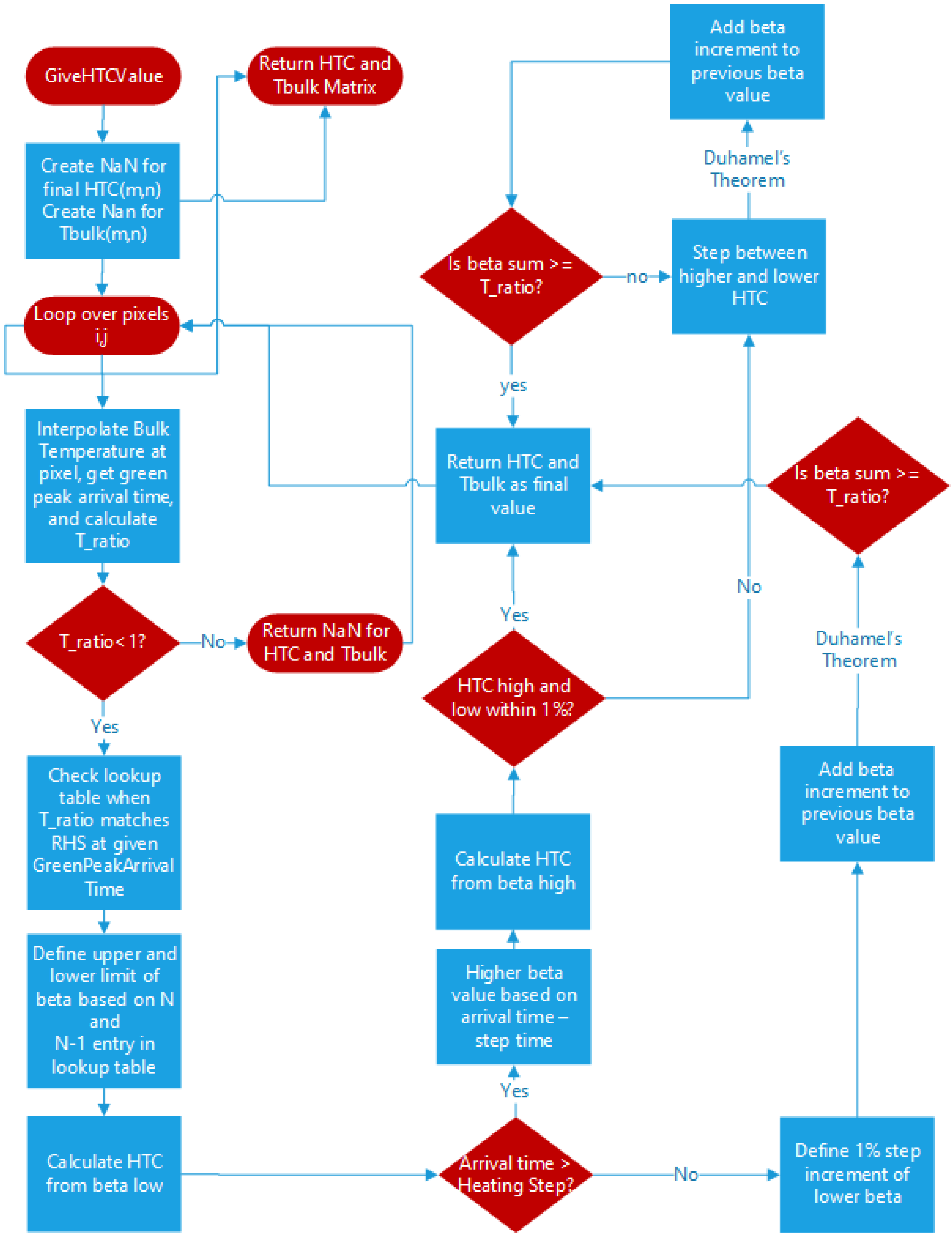

Figure 4.8: Detailed structure of heat transfer coefficient calculation code

The flow chart in Figure 4.8 shows the general flow of information and major processing step of the overall TLC post-processing routine. At the heart of the program is the actual heat transfer coefficient calculation, shown in the green box, which will be discussed in detail. The TLC post-processing requires input from three different data sources. The first being the green peak arrival time as the saved output from the image processing. The second being the exact temperature $T_{GreenPeak}$ when the green intensity value is maximum. This value is obtained through the initial TLC calibration. Third and lastly, the bulk temperature readings in the spatial and temporal form are required. The *.csv* file containing the thermocouple data is automatically imported into the software. Prior to this step, the user is required to remove all data leading up to the activation of the heating process. This is necessary so that the temperature readings are aligned with the image series. This step ensures that the green peak arrival times can be directly paired with the recorded time series of the TCs. Only the three sheathed TCs upstream and three sheathed TCs downstream of the flow are used for linear interpolation. First, the readings of all three TCs in one row are averaged at a know location $^{x}/_{D}$. Now, the corresponding temperature for each pixel is calculated. Here, the assumption is made that the temperature varies only in streamwise direction and not in spanwise direction perpendicular to the flow. Through this assumption, each pixel location is assigned one temperature at one particular time where the time step is given by the acquisition rate of the data acquisition system. The algorithm loops over all times and interpolates the temperature between the upstream and downstream locations of the pins so that $T_{\infty}(x,t)$ is known for every location x at every time step $t = \tau_i$. The initial temperature can be readily calculated by setting $t = 0$ and evaluating the first time of data. The readings of the TCs at this point should be within the precision uncertainty of each other. Since the peak finding algorithm can return a green peak arrival time between two frames and potentially between two temperature measurements, it is also required to interpolate temperature in time. The

two nearest neighbors (in terms of time) to the green peak arrival time are used for linear interpolation which returns the bulk temperature for every pixel pair i, j at the time of maximum green intensity. Now, the temperature ratio on the left-hand side of Equation 4.28 can henceforth be readily calculated for every location.

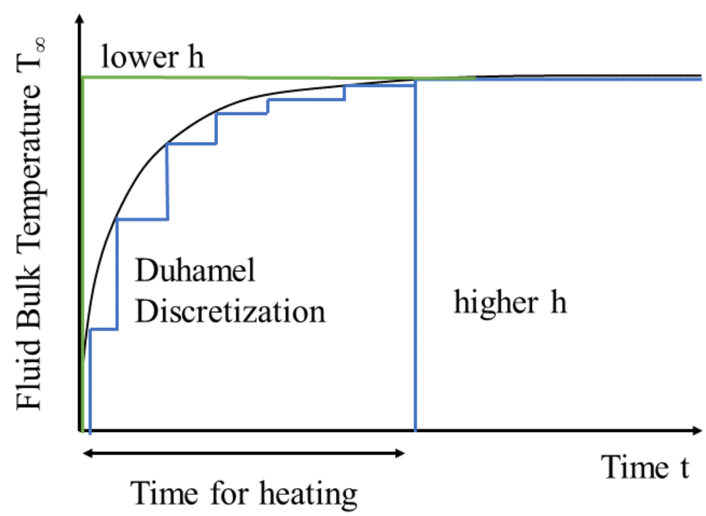

Figure 4.9: Treatment of non-ideal step function

It was mentioned in the mathematical derivation of the analytical solution that it is advantageous to create a lookup table for the right-hand side of Equation 4.28 which is solely dependent on β which itself is a function of the heat transfer coefficient h and time t. The lookup table is created by looping through increasing values of h and t between 0 and 300 in 0.1 intervals and between 0s and 1000s in 0.1s intervals, respectively. The lookup table is structured in a way that for every pair of h and t one β value and one evaluated right-hand side value is stored. The dependency of β on time is removed since the time of evaluation is the known time of the green peak arrival. The algorithm now loops through all β values at a given time to probe whether the known temperature ratio on the left-hand side is smaller than the evaluated right-hand side for a specific beta. As soon as

the condition is met, the matching local heat transfer coefficient is set as the upper limit (the green step in Figure 4.9) of the possible heat transfer coefficient range. The previous value of beta is converted to the local heat transfer coefficient by subtracting the time step to reach 99% of the final temperature from the green peak arrival time as shown in Figure 4.6 and Figure 4.9 *if* the green peak arrival time occurs *after* reaching 99% of the temperature jump. The upper and lower limit of the possible range are known. The step of the step function is assumed to be ideal for the green behavior. As there is no warm-up phase, the heat transfer coefficient will be smaller to slightly smaller than the actual heat transfer value. The blue shape assumes that the ideal step function of the heat supply occurs delayed by the time it takes to reach 99% of the final temperature. As the time is shorter to reach the same heating effect, the corresponding heat transfer coefficient must be larger to slightly larger than the actual value. The actual heat transfer coefficient is within the established ranged between green and blue. If the upper and lower limits are within 1% of each other than the upper limit is chosen as the final value for h. There is no need to apply Duhamel's theorem as stepping through the increase of temperature would not increase the accuracy of the heat transfer coefficient.

If the 1% condition is not met, the summation of the τ_i time steps begins and Duhamel's theorem is applied in this case. The maximum number of possible steps is defined by the difference between the upper and lower end of the possible heat transfer range and the step size which is set to be 1% of the difference of both. A new β, hence a new right-hand side value, is calculated for every single time step and added up. A final β is found as soon as the summation of the right-hand side values is larger than the temperature ratio on the left-hand side. The final value can be obtained by plugging in $\Delta timestep * number of timesteps$ for t and solving for h. The local value of h for one pixel pair i, j is finally found.

If the condition is not met where the green peak arrival time is later than the heating and the green color occurs *before* 99% of the temperature are reached, a special treatment of the upper heat transfer limit has to be introduced. Actually, an upper heat transfer limit does not exist, hence no discrete range of possible heat transfer coefficients is available. The only way to determine the final heat transfer coefficient is a summation based on Duhamel's theorem. The lower band heat transfer coefficient is set as a starting point. The step size is defined as 1% of this value. A new β value is calculated for each step and added to the sum of the previous βs. If the result of the right-hand side of Equation 4.28 for β at the end of the summation is still smaller than the temperature ratio, h is increased by one step and the β summation starts over. The break-out conditions is defined in the same fashion as in the previous case. The final heat transfer coefficient is found and stored as soon as the right-hand side of the equation with the current $beta$ sum is larger than or equal to the temperature ratio.

The final step of the endeavor is reached. The local heat transfer coefficient for every pixel in the area of interest has been obtained through the time it takes each pixel to reach a certain temperature characterized through the green peak. The bulk fluid temperature at this pixel for this specific instance in time is known so that with Duhamel's superposition approach a β is found that in turn gives the final heat transfer result. The following steps are mainly of a cosmetic nature. The pins in the original images have a very different color than the black backing paint of the color. This allows to automatically create a mask to crop out the data underneath the pins[1]. Furthermore, the heat transfer matrix is converted into a local Nusselt number distribution employing the definition in

[1]The pins were made from Balsa wood which has a light brown color. Since all colors are a unique combination of red, green, and blue, the algorithm also falsely calculated a heat transfer coefficient for the pins. The noise in the green intensity of the solid brown color over time was picked up as peaks and was treated as green peak arrival times as any other pixel. The human eye and brain are much better picking up logical peaks compared to a computer.

Nusselt number in Equation 1.14 and the local film temperature for the thermal conductivity as the ratio of the bulk temperature at the green peak arrival time and the green peak temperature is obtained from the correlation. The center point locations of three pins are used as a reference to transform the coordinate system from pixel location i, j to experimental coordinates ${}^{x}/_{D}, {}^{z}/_{D}$ of the actual experiment. The coordinate-transformed Nusselt number distribution is saved and is easily accessible for further data analysis.

Calibration of Thermochromic Liquid Crystals

Although a calibration was provided by the manufacturer of the TLC paint, it was deemed necessary to independently obtain the relationship between color intensities and temperature as the manufacturer temperature is $\pm 1K$. Besides the insufficient accuracy, TLC paint may age and change its properties based on other environmental conditions. The original thermal profile for the paint is listed in 5.5. A separate calibration rig was built for this purpose. One of the design requirements was compactness. It is recommended to calibrate the TLC paint in the same light and video conditions as the experiment. The compactness of the calibration unit allows easy transport and alignment in the experimental area. The setup is shown in Figure 4.10. Heat is supplied through a heater on the right of the acrylic box that is connected to a copper block. The copper block itself is bolted to a copper slab. The copper block minimizes possible non-uniformities coming from the heater due to its large Biot number and ensures a minimal temperature variation over the width of the copper slap. A temperature gradient forms along the length of the copper piece. The length of the copper slab was chosen to be 12 inches so that a temperatures in the range of 54 to 60 deg C can be displayed plus additional two inches to mount the heater. Calibrated TCs are cemented into the backside of the copper plate to accurately measure the temperature distribution within it. Two calibrated TCs were cemented together in one hole for increased accuracy and redundancy. The holes with the TCs are

three inches apart from each other measured from the center points. The spacing of the TCs is 0.5 inches in the center of the test section since the green color peak is expected in this region. Furthermore, an acrylic enclosure with tight margins was built around the copper block to shield it from forced convection due to ambient conditions and minimize internal natural convection due to the temperature gradient. The only desired heat transfer mode is conduction.

Figure 4.10: TLC calibration: Heat is supplied from the right-hand side and travels towards the left through the copper slab

A video over three minutes was taken of the front side of the copper. Notches at the edges of the copper piece were machined as reference. The notches can be seen in the video and help to identify the location of the TCs in the recordings. A resolution of 32.6 pixel per mm was calculated based on the spacing of the notches. The paint color close to the heater is blue as expected (Figure 4.10) and changes to green and red eventually based on the local temperature. A specific temperature can be assigned to every pixel along the length of the copper through the knowledge of the thermocouple readings. As every pixel has a specific color - hence a unique combination of red, green, and blue - color and temperature can be correlated against each other. The intensity values of all three RGB components are plotted against temperature and a temperature can be assigned to all three color peaks (Figure 4.11).

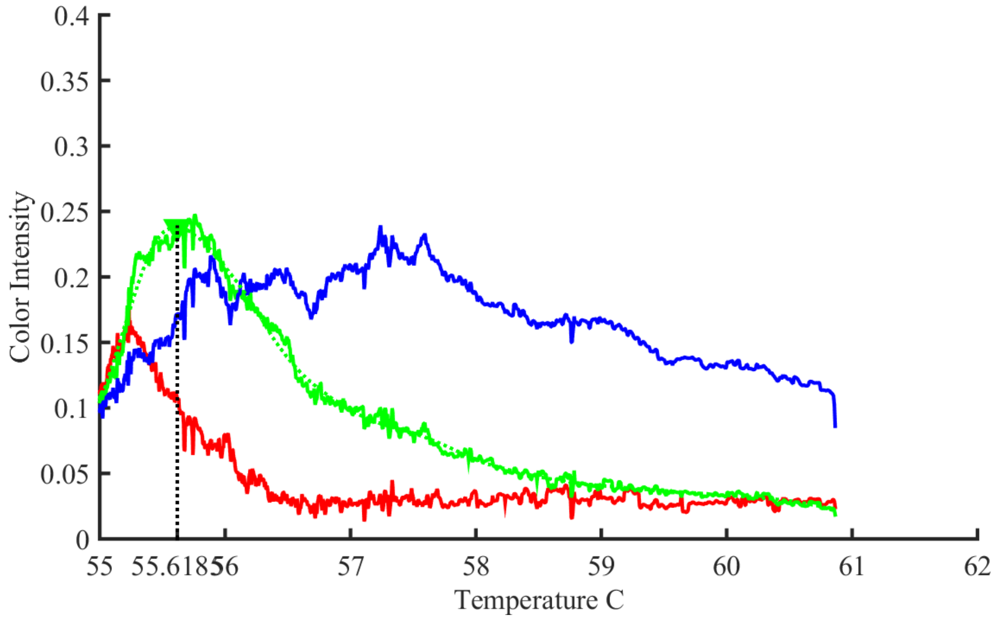

Figure 4.11: Intensity distribution of red, green, and blue based on temperature

The temperature corresponding with the green color peak is a direct input parameter to the transient thermochromic liquid crystal technique which is explained in the previous section. The calibration test was repeated three times. The individual green peak temperatures are listed in Table 4.2. All calibration readings are within 0.2 K. The mean from all three calibration experiments is 55.74 C.

Table 4.2: Green peak tempertature obtained through calibration

Test Number	1	2	3	μ	σ
Temperature in C	55.71	55.61	55.81	55.74	0.047

Particle Image Velocimetry

Particle image velocimetry is a non-interfering, instantaneous, planar fluid measurement technique where the fluid is seeded with particles that follow the flow as accurately as possible, used to obtain the instantaneous velocity field in an interrogation region. A pulsed laser beam is emitted and spread into a laser sheet through a series of optical lenses. As the tracer seed particles pass through the laser plane, they reflect the emitted laser pulse. The reflection is picked up by an sCMOS camera. The basic setup and functionality of a PIV setup are shown as a cartoon in Figure 4.12.

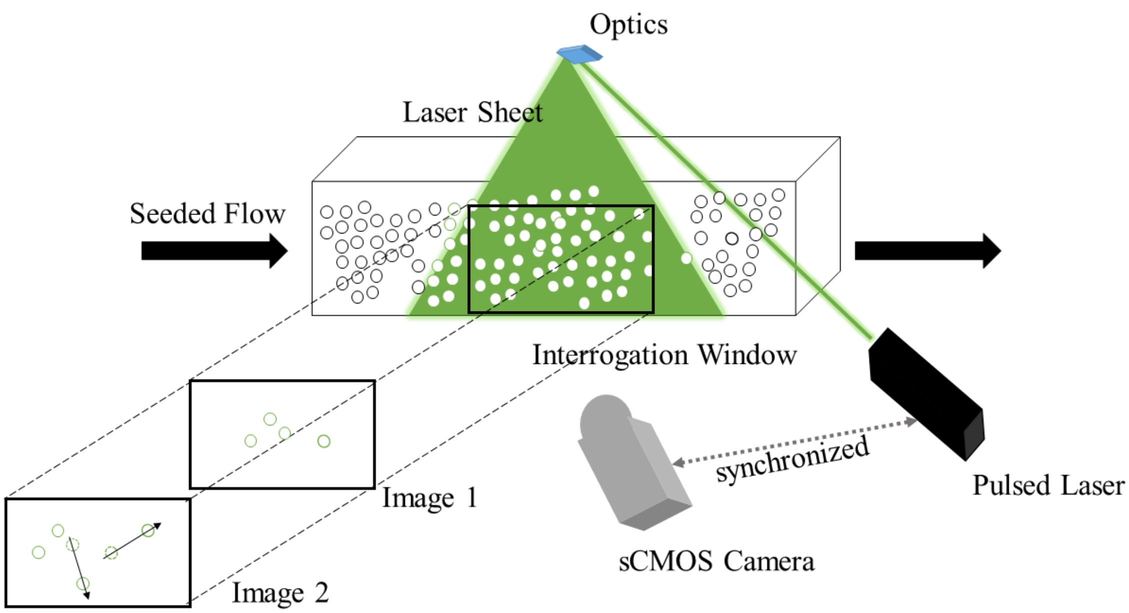

Figure 4.12: A cartoon depicting the basic PIV principle

Two laser pulses are emitted back to back with a short time in between, usually in the order of a few micro-seconds. The relative location of the particle will change between both taken images as the particles follow the flow. The time between both image pairs is to be adjusted so that the particles travel enough between both images. Rule of thumb is a

displacement of approximately four pixels between both laser pulses. The displacement of the particles is calculated by comparing both images via cross-correlation. The area of interest is broken down into several smaller sub-images. Involving the cross-correlation, the displacement vector for each sub-images is calculated. The instantaneous velocity is then calculated with the displacement vector and the time between both images. This process is repeated for several hundred to a few thousand images pairs to obtain statistical convergence of the turbulence statistics which can also be calculated from the displacement of the particles. If the reader feels inclined to delve more into more details, [105–108] can be recommended for further study.

Numerical Techniques

This section discusses Computational Fluid Dynamics (CFD), which is a powerful tool to compute a multitude of fluid dynamic problems. The solution approach is not analytical but rather a numerical approximation of the real solution. However, CFD is also a powerful tool to fool upper management with colorful images and results. The bottom line for CFD is the same as for many other computational tools: garbage in, garbage out. The user of such software has to be very aware about boundary conditions, his or her assumptions to simplify the physical problem, and the general limitations of CFD. The less physical assumptions are made the more accurate becomes the solution, but this is considerably offset by much higher computational time. Modeling of turbulence is the most critical aspect when it comes to the quality of a CFD solution. Several approaches exist to realize turbulence modeling, each with its own advantages and drawbacks. The basic turbulence modeling approaches will be discussed alongside with a more holistic discussion of turbulence itself.

The basic work flow of a CFD simulation consists of five key elements as listed below:

1. Geometric modeling of the problem,
2. meshing,
3. physical modeling of the problem,
4. iterative solution of the problem,
5. post-processing and analysis.

Usually a test geometry is imported into the CFD solver or is built within it. In the case of a pin fin array, the geometrical shape of the test section is imported. However, CFD does not solve for the solid but for the fluid domain. So that the required geometric input is the negative of the test section. The fluid volume has to be modeled with the pin fins removed from it. There are cases where the solid is modeled as well as the fluid region. For example in the case of conjugated heat transfer where the change in the solid affects the solution in the fluid as well. This fluid domain is then discretized in the meshing step. The fluid volume is divided into many cells that make up the mesh. Instead of solving the basic governing equations (mass, momentum, energy, etc.) for the entire domain at once, they are solved for each tiny mesh cell. The way how the mesh cells are used to reconstruct the original geometry can be either structured or unstructured. The structured approach usually improves convergence rate and results in slightly smaller mesh counts due to the high space efficiency. The generation of unstructed meshes is more automated and can be use for complex geometries. Unstructured mesh cells have the shapes of tetrahedrons or pyramids which have 4 or 5 vertices and faces, respectively. Polyhedrons have more vertices, edges, and faces and are the most common cell type for three-dimensional unstructured meshes. As they have usually a higher face count than

tetrahedrons and pyramids, they required more computational power but reward with higher accuracy.

Boundary conditions have to be applied to all sides of the fluid domain. Examples for boundary conditions are wall, symmetry, periodic interface, velocity inlet, constant heat flux or constant temperature surface and many more. The proper specification of the boundary conditions is crucial for obtaining a meaningful solution (*garbage in, garbage out*). If the simulation is of transient nature, additional initial conditions have to be specified.

The solution is obtained through iteratively solving the governing equations in integral form over each cell of the computational grid. The transport of governed quantities is approximated over the cell surfaces. The flow through the surfaces and integrated values of the cell control volume are connected through Gauss's theorem. An algebraic systems is built from all discretized volume cells and then solved. Once the residuals of the solution are below a certain threshold, the solutions is considered converged and many information about the nature of the final flow field, such as local vorticity, local heat transfer, and velocity profiles can be exported.

The goal of newer CFD applications is not the flow field itself but the optimization of geometric input in order to achieve certain criteria [87, 88] Here, a feedback loop is introduced to the CFD work flow. Based on the result of the simulation, a change in geometry is introduced, remeshed, and solved again. If the result is closer to the specified target, the algorithm keeps moving in this direction; otherwise pivots.

Solutions to CFD Problems

The continuity equation as first essential governing equation for fluids was introduced in previously as Equation 1.20 as velocity ratio. Here, the continuity equation is

reintroduced in differential form (Equation 4.30). It follows for an incompressible flow without sources and sinks:

$$\frac{\partial \rho}{\partial t} + \frac{\partial u_i}{\partial x_i} = 0 \tag{4.30}$$

With the same conditions of incompressible flow without momentum sinks or sources and the absence of body forces, the governing equation for momentum, the famous Navier-Stokes Equation is

$$\frac{\partial u_i}{\partial t} + u_j \frac{\partial u_i}{\partial x_j} + \frac{1}{\rho}\frac{\partial p}{\partial x_i} = \nu \frac{\partial^2 u_i}{\partial x_j^2} \tag{4.31}$$

where ν is the kinematic viscosity also known as momentum diffusivity. In the same manner, the simplified governing equation for energy (Equation 4.32) is defined as follows:

$$\frac{\partial T}{\partial t} + u_j \frac{\partial T}{\partial x_j} = \alpha \frac{\partial^2 T}{\partial x_j^2} \tag{4.32}$$

According to the Einstein notation, $i = 1, 2, 3$, corresponds to the velocity components u, v, w and coordinate directions x, y, z, respectively. The set of Equation 4.30, Equation 4.31 evaluated in three coordinate directions, and Equation 4.32 provides five independent equations for the five unknown quantities pressure, temperature, and three velocity components. With this set, a (Newtonian) fluid can be described at any point in time and space. While inspecting in particular the Navier-Stokes equation and the energy equation, it can be seen that both equations are non-linear partial differential equations for which no analytical solution is known. One possible way to solve those equations is to discretize the fluid domain and obtain a solution to the equations numerically. First, the equations are integrated over the volume of a mesh cell so that the Navier-Stokes equation becomes

$$\iiint_V \left[\frac{\partial u_i}{\partial t} + u_j \frac{\partial u_i}{\partial x_j} + \frac{1}{\rho}\frac{\partial p}{\partial x_i}\right] dV = \iiint_V \left[\nu \frac{\partial^2 u_i}{\partial x_j^2}\right] dV \tag{4.33}$$

if no body forces are presented. In the next step, the time dependent term is assumed to be constant within the cell and can be pulled out from the volume integral (Equation 4.34).

$$\frac{\partial u_i}{\partial t} V + \iiint_V \left[u_j \frac{\partial u_i}{\partial x_j} + \frac{1}{\rho} \frac{\partial p}{\partial x_i} \right] dV = \iiint_V \left[\nu \frac{\partial^2 u_i}{\partial x_j^2} \right] dV \tag{4.34}$$

As previously stated, the Gauss theorem relates a flow or flux through a surface with the change of the integrated quantity within the mesh cell. Applying Gauss's theorem to Equation 4.34 yields with the surface normal n_i and the cell surface A:

$$\frac{\partial u_i}{\partial t} V + \iint_A \left[u_i u_j n_j + \frac{p}{\rho} n_i \right] dA = \iint_A \left[\nu \frac{\partial u_i}{\partial x_j} n_j \right] dA \tag{4.35}$$

The discretization of the Navier-Stokes equation shown in Equation 4.35 can be solved for a given cell if the flows through the surface are know. This is the so called finite volume method. The consideration of all mesh cells altogether creates an algebraic system that can be solved for the entire fluid domain.

The purest approach in solving Equation 4.35, since no assumptions are made, is the Direct Numerical Simulation (DNS) approach. There is a very big challenge though: The resolution of the mesh has to be extremely fine. Fine enough to resolved the smallest turbulent length scales, the Kolmogarov scales l_K. This might be feasible for a very small test domain at low Reynolds numbers, however, as the Reynolds number increases, the Kolmogarov scales become smaller and smaller which in turn increases the mesh count by the power of three [19]. The contribution of smaller scale eddies cannot be neglected without introducing errors into the solution of the Navier-Stokes equation.

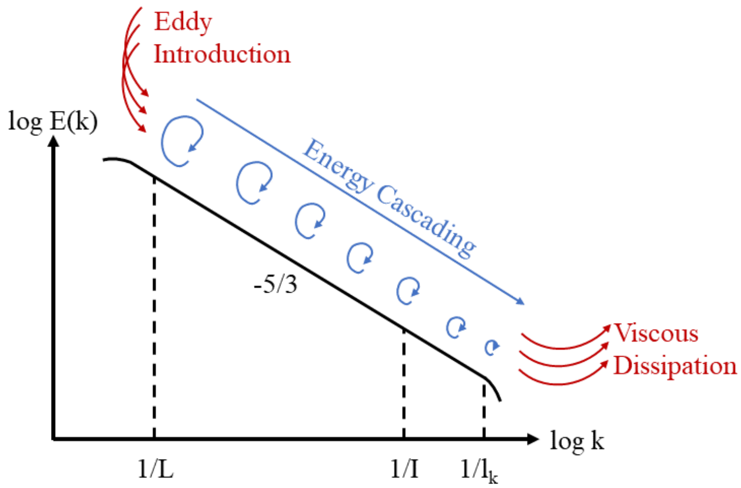

Figure 4.13: Energy cascade from large scale eddies to Kolmogarov scale eddies

The Kolmogarov scales are at the lower end of the energy cascade as shown in Figure 4.13. Eddies are introduced into the flow for example through the transient vortex shedding of cylinder in cross flow. The eddies travel further and dissipate energy through viscosity consequently the eddy shrinks. The wavenumber k is the inverse of the eddy scale. With increasing wavenumber, the kinetic energy decreases. Large eddies contain the most kinetic energy. Once the point of the smallest sustainable eddy size is surpassed, the eddy dissipates into the flow by friction. All remaining kinetic energy of the eddy is converted to thermal energy. Integrating the eddy kinetic energy over all possible eddy wave length returns the expression as defined in Equation 4.36. The integral of $E(k)$ is also referred to as energy spectrum.

$$\frac{1}{2}(\overline{u_i u_i}) = \int_0^\infty E(k)dk \tag{4.36}$$

The turbulent dissipation rate (Equation 4.37 is derived from Equation 4.36.

$$\epsilon = 2\nu \int_0^\infty k^2 E(k) dk \tag{4.37}$$

Further, it is observed that the dissipation rate of kinetic energy is linear (in a log-log representation) in the interial subrange between large scale eddies and the Kolmogarov scales. The energy of an eddy with the wavenumber k can be expressed based on the Kolmogarov hypotheses as shown in the equation below [19]. An intensive amount of studies have verified the exponent of the wavenumer to be $k = -5/3$ and the constant to be $C = 1.5$ [19,20].

$$E(k) = C\epsilon^{2/3} k^{-5/3} \tag{4.38}$$

A similar expression exists for the spectrum of pressure fluctuations π. Without further derivation, they could be found for example in George et al. [109], the pressure spectrum becomes

$$\pi(k) = C\rho^2 \epsilon^{4/3} k^{-7/3} \tag{4.39}$$

Another significance revealed by the study of the energy cascade is that most energy is contained within the largest eddies. The kinetic energy decreases when the eddy wavenumber increases. Here is root of the Large Eddy Simulation (LES). LES resolve larger eddy scales and model smaller eddy scales. Modeling smaller scales is a simplification from the DNS approach. However, Pope [19] notes that about 99% of the computational effort of DNS is to calculate the scales that are barely energy-containing.

Reynolds Averaged Navier-Stokes Equation (RANS)

On the other end of the numerical spectrum are Reynolds-averaged Navier-Stokes methods, short RANS. This method, as the name gives away, tries to solve the Reynolds-

averaged Navier Stokes equations (RANS equations) as defined in Equation 4.31 with the Reynolds stress tensor introduced in Equation 1.18. The majority of the terms in this Navier-Stokes equation is related to the time averaged properties. Only the Reynolds stress tensor contains information about the fluctuating components in the flow field. The stresses along the diagonal of the tensor are normal stresses, the mixed terms are shear stresses. Due to the symmetry of the Reynolds stress tensor, six variables are independent and unknown. However, in the derivation of the DNS approach, it was stated that the governing equation provide only closure for five independent variables: three velocity components, temperature, and pressure. No additional equations exist to solve for the six components of the Reynolds stress tensor. Consequently, the problem is underdefined and unclosed. The famous problem of *turbulence closure* [19].

Additional assumptions have to be made to obtain closure since no governing principles are available. But first, the turbulent kinetic energy k shall be introduced (Equation 4.40.

$$k = \frac{1}{2}\overline{u'iu'_i} = \frac{1}{2}(\overline{u'u'} + \overline{v'v'} + \overline{w'w'}) \tag{4.40}$$

The turbulent kinetic energy k is the sum the normal stresses along the diagonal of the stress tensor. The turbulent kinetic energy per unit mass is used to link the normal stresses with the shear stresses via the Boussinesq hypothesis (Equation 4.41).

$$\tau_{ij} = \mu_t \left(\frac{\partial \overline{u_i}}{\partial x_j} + \frac{\partial \overline{u_j}}{\partial x_i}\right) - \frac{2}{3}\rho k \delta_{ij} \tag{4.41}$$

The Boussinesq approximation links mean flow properties to the turbulent fluctuations through the concept of eddy viscosity with *one* proportionality constant: turbulent eddy viscosity μ_t. Turbulent eddy viscosity is a proportionality constant that describes the internal momentum transfer from the fluid to the eddies - key point of Boussinesq's hypoth-

esis. The eddy viscosity is assumed to be the same for all shear stresses also referred to as isotropic assumption. This assumption, however, only holds true for simple flows. The more complex to flow becomes where more velocity gradients are present, the approximation becomes less and less applicable for the particular flow field. Yet, the Boussinesq hypothesis is a cornerstone of many turbulence models.

The simplest two-equation model to describe turbulence is the $k - \epsilon$ model which is commonly used in CFD calculations and is attributed to Jones and Launder [110] and in furtherance heavily improved by Launder and Sharma [111]. The two turbulence quantities for which the transport equations are solved are turbulent kinetic energy k and turbulent dissipation μ_t. The formulation for the turbulent eddy viscosity can be derived through the analysis of the turbulent diffusion and dissipation so that the turbulent eddy viscosity becomes

$$\mu_t = C_\mu \frac{k^2}{\epsilon} \tag{4.42}$$

where C_μ is a constant, k the turbulent kinetic energy, and ϵ the turbulent dissipation as introduced in Equation 4.37. It is important to point out that Equation 4.37 shows a clear dependency of the turbulent dissipation on the eddy wavenumber (eddy length scale). Yet, the definition of the turbulent viscosity only takes into account a constant value, independent of the actual eddy length scale. Another downside is the constant value C_μ [19]. It turns out that different constants are need for the homogeneous turbulent region and the viscous region close to the wall.

The other widely used two-equation model $k - \omega$ aims to provide a solution for that. This model was originally introduced by Wilcox [112]. The use of turbulent kinetic energy is again one of the transport quantities for turbulence. The other quantity in the

two-equation model is the turbulence frequency defined as

$$\omega = \frac{\epsilon}{k} \tag{4.43}$$

The advantage of this model over the $k - \epsilon$ model is the performance in the wall-near viscous region of the flow which makes it a good choice for boundary layer flows. The downside is, however, the performance within the homogeneous turbulence region. Therefore, a blending function between both models so that the $k - \epsilon$ is primarily used in the free stream region and $k - \omega$ in the wall-near region.

The performance of both turbulence models rely heavily on the choice of constants. Although tweaking of the model constants, for example through the availability of good experimental data - sometimes even DNS results - can result in better predictions of turbulence for a certain region of interest, other regions experience a worsening of the prediction. This was for example observed by Otto et al. [43] for the flow in a pin fin array. Tweaking the model constants improved the pin heat transfer predictions as the separation for the shear layer is predicted more accurately, but the at the same time the turbulent transport away from endwall caused less accurate heat transfer coefficients in this region. The flow separation around the pin and the endwall are boundary layer driven problems. The model coefficients can be tweaked for one or the other case, but not for both. Not to mention the high anistropy in the flow for which both models are not suited.

The Reynolds Stress model (RSM) performs much better when a highly anisotropic flow is present. This is due to the fact that RSM is not based on the eddy viscosity hypothesis but models the turbulent transport and dissipation for all six tensor components independently. The novelty of this concept is that the pressure term is also decomposed into a mean and fluctuating component. Further, the transport of Reynolds stresses is understood as a redistribution of energy directly related to the pressure strain tensor [19,20].

Due to the modeling of the pressure strain tensor, Reynolds stress models are second order models compared to first order RANS models. The downside of the model is that six additional equations for the six additional Reynolds stress have to be solved which results in increased computational time.

Large Eddy Simulation (LES)

A Large Eddy Simulation is basically a Direct Numerical Simulation with a filter function. All (larger) eddies above the filter function are directly calculated; smaller eddies below the filter function are modeled. This approach allows to increase the cell size of the mesh thus significantly lowering the computational time compared to DNS. A good LES calculates at least 80% of the turbulent kinetic energy. If the mesh is refined more and more, the LES eventually approaches DNS as no remaining scales have to be modeled.

As mentioned, at the heart of LES is a filter functions which separates the large eddies from the small eddies. Consequently, LES lastly discussed borrows methods from either side of the approaches available to solve the transport equations with the governing equations. The filter function is applied to the continuity equation (Equation 4.30) for an incompressible flow so that:

$$\frac{\partial \overline{u_i}}{\partial x_i} = 0 \tag{4.44}$$

In the same fashion, the filter function is applied to the Navier-Stokes equation (Equation 1.17) so that:

$$\frac{\partial \overline{u_i}}{\partial t} + \frac{\partial}{\partial x_j}(\overline{u_i u_j}) = -\frac{1}{\rho}\frac{\partial \overline{p}}{\partial x_i} + \nu \frac{\partial}{\partial x_i}\left(\frac{\partial \overline{u_i}}{\partial x_j} + \frac{\partial \overline{u_j}}{\partial x_i}\right) \tag{4.45}$$

The filter is applied to the pressure field $\overline{p}$ as well as the velocity. The problem is that the advection term $\overline{u_i u_j}$ is non-linear and cannot be calculated from the filtered flow field, hence it has to be modeled. The filter of the product is not known. However, the product

of the filtered velocities can be obtained. According to Leonard [113], the term can be split up into the product of the filtered velocities and a remaining residual stress tensor τ_{ij}^r as shown in Equation 4.46.

$$\overline{u_i u_j} = \overline{u_i}\,\overline{u_j} + \tau_{ij}^r \tag{4.46}$$

The inclusion of the residual stress term (Equation 4.46) into the filtered Navier-Stokes equation (Equation 4.45) yields

$$\frac{\partial \overline{u_i}}{\partial t} + \frac{\partial}{\partial x_j}(\overline{u_i}\,\overline{u_j}) = -\frac{1}{\rho}\frac{\partial \overline{p}}{\partial x_i} + \nu \frac{\partial}{\partial x_i}\left(\frac{\partial \overline{u_i}}{\partial x_j} + \frac{\partial \overline{u_j}}{\partial x_i}\right) - \frac{\partial}{\tau_{ij}^r}\partial x_j \tag{4.47}$$

At this point, the only unclosed term is the residual stress tensor. The interaction amongst large scales, the interaction between large scales and filtered small scales, and the interaction amongst filtered small scales themselves have to be accounted for in the residual stress tensor to provide closure. The Smagorinsky model [114] and the Germano dynamic model [115], which is a modification of the aforementioned Smagorinsky model, are the two mostly utilized models for the resolution of the residual stress tensor. The Smagorinsky sub-grid model assumes that the production and dissipation of turbulence is isotropic for small scales. Smagorinsky's model is based on the linear eddy viscosity model, as previously discussed in context of the Boussinesq approximation, modified with a variable turbulent eddy viscosity μ_t that is assumed to be function of the Smagorinsky lengthscale l_s, similar to the Prandtl mixing length. The proportional relationship between Smagorinsky lengthscale and eddy viscosity is shown in Equation 4.48

$$\mu_t \sim l_s^2 = C_s \Delta_{LES} \tag{4.48}$$

and the Smagorinsky lengthscale can be expressed by the LES filter width Δ and the Smagorinsky coefficient C_s. This provides closure to the turbulence problem for Large Eddy Simulation.

Another important aspect of LES is the wall treatment. The eddy scales become naturally smaller towards the wall. The computational grid has to be significantly refined to also capture 80% of the energy contained within the eddies which counteracts the goal to reduce computational time compared to DNS. The wall treatment is achieved through a exponential damping function that is applied to the Smagorinsky lengthscale as defined in Equation 4.48 to artificially reduce the Smagorinsky lengthscales to lengthscales associated with viscous dissipation. Additional details on the damping function are written in Pope [19].

CHAPTER 5: EXPERIMENTAL SETUP

The wind tunnel testing took place in the facilities of the University of Central Florida in Orlando where also all components were machined. A wind tunnel, under suction, was operated in an open loop setup. A 250 hp Siemens blower was used to in combination with a bleed valve to achieve the desired mass flow rates which were measured initially by one calibrated Preso 2 inch venturi where either fluid temperature was measured for correct density calculations. In addition to the venturi meter, a pitot static probe was installed into the sidewall for the test section to an additional velocity measurement. It was found that the pressure drop of the flexible tube and venturi exceeded the blowers capabilites. Therefore, as good agreement between flow rate measurements from calibrated venturi and pitot static probe was observed, the venturi was removed to restrict the flow less.

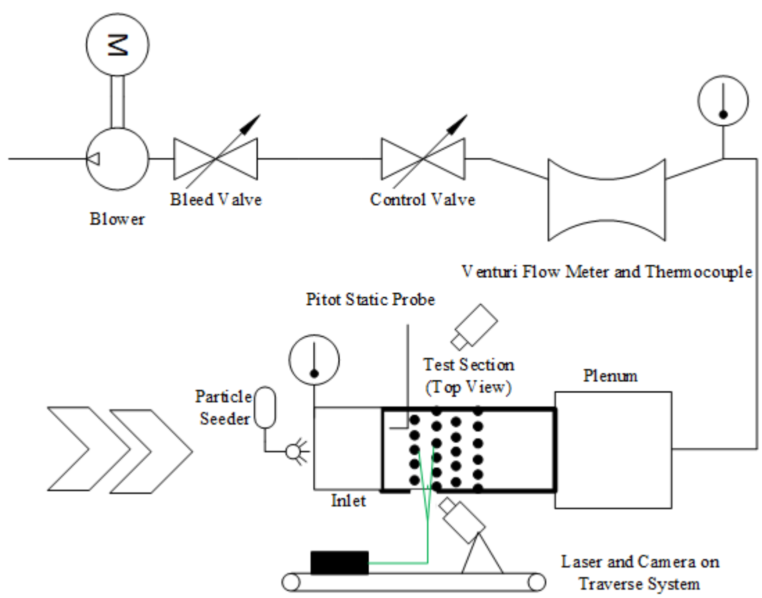

Figure 5.1: Experimental PIV setup as schematic including flow path, measurement locations and PIV setup

Due to the generated heat by the motor and fan in combination with the Florida heat, tests were conducted at dusk and dawn to minimize temperature variations during tests. The test layout is schematically shown in Figure 5.1. In this specific case, the diagram depicts the setup for the PIV measurements. With slight modifications, the setup could be easily converted for heat transfer measurements.

Regular flow leakage tests were conducted to ensure a valid assumption of conservation of mass between the test section inlet and venturis. The flow enters through a one-dimensional foam contraction with an area ratio of 5:1 shaped for smooth inlet conditions before entering the test section. The modular test section is constructed of 25.4 mm (1 inch) optical grade acrylic for optimal visual access from all sides. The inner dimensions of the test section are 50.8 mm (2 inch) in height and 317.5 mm (12.5 inch) in width resulting in a hydraulic diameter of 87.59 mm. As common in the field of pin fin geometries, all lengths are normalized by the pin diameter D. This results in the non-dimensionalized lengths ${}^{x}/_{D}$ in flow direction, ${}^{y}/_{D}$ in wall-normal direction, and ${}^{z}/_{D}$ in spanwise direction as shown in Figure 5.5. The midpoint of the projected circle formed by the center pin of the first row with the bottom endwall is set as origin. Accordingly, the midpoint of the pin of the first row is at ${}^{x}/_{D} = 0$, ${}^{y}/_{D} = 1$ and ${}^{z}/_{D} = 0$.

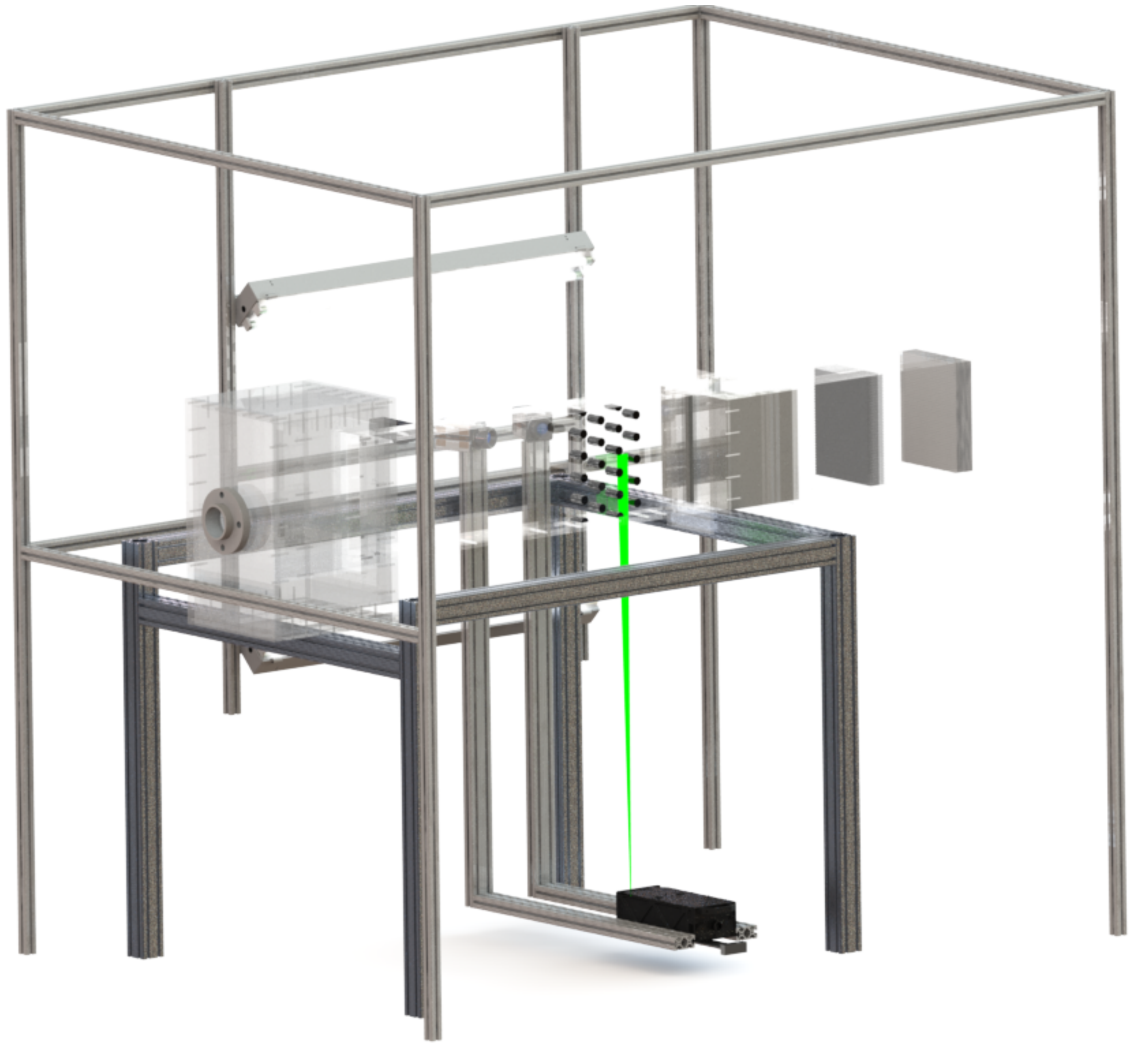

Figure 5.2: Overall rig layout including mounting structure, laser and camera setup for PIV, and heater system for heat transfer testing

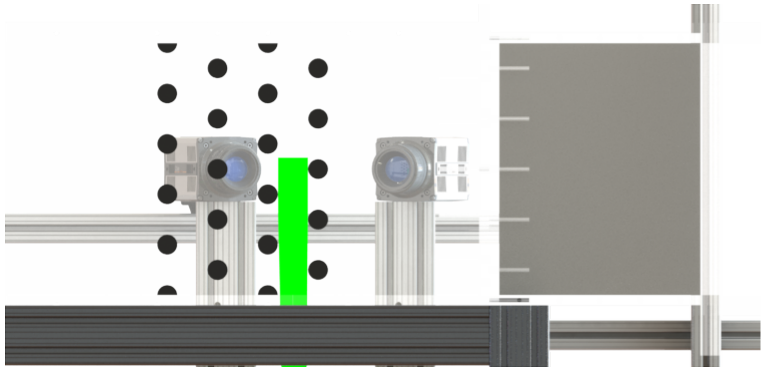

Figure 5.3: CAD model of the experiment including contraction and a four row staggered pin fin array from normal perspective

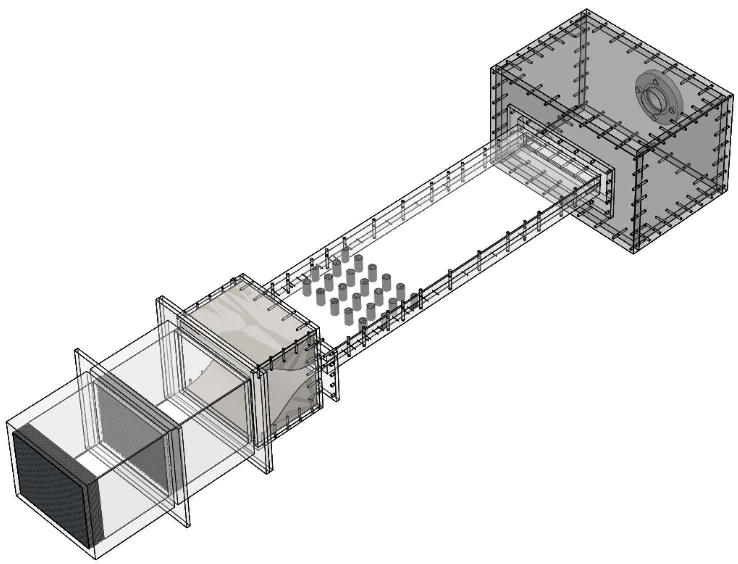

Figure 5.4: CAD model of the experiment including contraction and a four row staggered pin fin array from isometric perspective

For fast turnaround and easy change of geometric features, the top place of the test section is removable. Finally, a large volume plenum connects the test section and ducting to the blower. In the presented study, the tested geometric features are circular acrylic pin fins in a staggered array of four rows with a focus on the developing region of the flow. With a channel height of 50.8 mm and a pin diameter of 25.4 mm (1 inch), the height to diameter ratio ${}^{H}/_{D}$ results in 2. Each of the rows consists of five pins for constant blockage. Row one and three have five full pins, row two and four have four full pins and two half pins that are glued to the side walls. The pins are machined from an acrylic rod that was roughly cut to 2.2 inch length with a band saw. The final cut was achieved by constraining the pin into a jig on the CNC and achieve the desired height of 2 inches and two planar surfaces. At the same time, a pilot hole was drilled into the pin. In the next machining step, the pilot hole was drilled deeper into the pin and threaded. The pin spacing in spanwise ${}^{z}/_{D}$ and streamwise direction ${}^{x}/_{D}$ is held constant at 2.5 pin diameters. The pin fin array is symmetric about its centerline. The center points of the first row are located eight pin diameters from the inlet. The CNC was used to drill holes into the acrylic top plate. M8 bolts were used to connect the pins and the acrylic top plate. Washers with gaskets are used to act as a seal and prevent leakage at the location of the bolts. Although the pins also could have been glued to the surface, bolting promises higher repeatability of the correct location of the pins. This is in particular relevant as the acrylic pins had to be replaced by wooden pins for heat transfer experiments. However, since no bolt could be fitted into half pins, they were glued to the sidewalls in order to maintain constant blockage throughout the channel. The velocity within the channel increases due to the additional blockage of the pins. The free stream velocity is referred to as minimum velocity, u_{min}, calculated based on the mass flow rate and channel open area. In the region of the smallest area between two pins, in this case in spanwise direction, the velocity increases and is referred to as maximum channel velocity, u_{max}. The detailed flow

path is shown in Figure 5.2, the test section from normal perspective in Figure 5.3, and in an isometric view in Figure 5.4.

The test section iteself is shown in Figure 5.5 including the geometric definition of spanwise and streamwise spacing along side other dimensions that fully describe the tested geometry. The geometric key parameters are kept intentionally the same or similar to the test setup by Ames et al. in [5,32,33,75]. Pressure taps are installed on the sidewall and located between the rows as well as half a pitch before and after the first and last row, respectively. A Scanivalve was used for static pressure measurements in order to calculate the pressure drop and friction factor throughout the channel.

As mentioned, the mass flow rate was measured with a pitot static probe close to the inlet. As common in pin fin literature, the Reynolds number can be defined based on the hydraulic diameter, D_h, of the open channel and free stream velocity, u_{min}, as channel Reynolds number, Re_{D_h}, or based on the pin diameter, D, and maximum velocity, u_{max}, as local Reynolds number, Re_D:

$$Re_{D_h} = \frac{\rho u_{min} D_h}{\mu} \tag{5.1}$$

$$Re_D = \frac{\rho u_{max} D}{\mu} \tag{5.2}$$

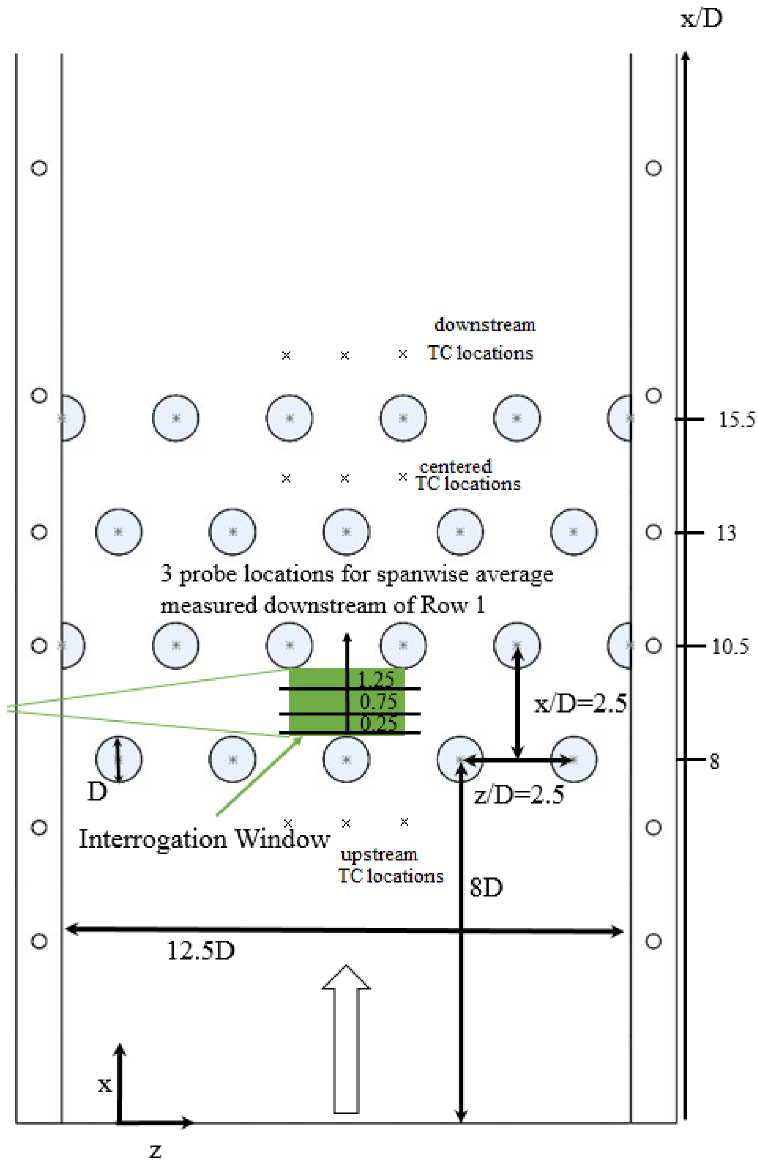

Figure 5.5: Test section design including basic dimensions and the location of the laser sheet in downstream of the center pin in row 1 and 2 as well as the location of data probes downstream. Flow direction is along the x axis.

Both representations can be easily converted based on the velocity ratio and the ratio between the hydraulic diameter and pin diameter. The Reynolds number definition based on hydraulic diameter is particularly important as an input parameter for the Dittus Boelter and Blasius correlation as introduced in Equation 4.4 and 4.2, respectively. However, since the local heat transfer is highly dependent on the local velocity and the critical scale pin diameter, the Nusselt number results will be presented based on the pin diameter based Reynolds number definition.

Table 5.1: Experimental Test Matrix

Reynolds Number Re_D	10,000	30,000
PIV	Row 1 & 3	Row 1 & 3
Heat Transfer	Row 1-4	Row 1-4

When designing the experiment, special care was taken to ensure that the setup is multifunctional with only minor changes required. The required changes are described in the following two sections. The scope of the experimental work is summarized in the test matrix as found in Table 5.1. The range of local Reynolds number Re_D is 10,000 and 30,000, respectively. The Reynolds number range was chosen as common Reynolds numbers within literature and within the range and capabilities of the test facilities. PIV data was taken in the wake of Row 1 and 3. The entire array of pins from upstream row 1 and downstream of row 4 is the basis for heat transfer measurements. A summary of all geometric key parameters can be found in Table 5.2. The area highlighted in green is the interrogation window in which PIV data in different heights above the wall was obtained. Although not shown, the interrogation area was also in the wake of the center pin of row three. The three black lines found in this area designate the location of three line probes along which the data was processed in spanwise direction. The location of those probes at 25%, 75%, and 125% of the pin spacing downstream of the junction of pin and endwall

were chosen based on the different characteristics of the flow physics in the wake of the pin. This corresponds to ${}^{x}/_{D}$ positions of 0.75, 1.25, and 1.75, respectively.

Table 5.2: Geometric Key Parameters

Parameter	Symbol	Value
Pin Diameter	D	1 inch
Channel Height	H	2 inch
Height to Diameter Ratio	${}^{H}/_{D}$	2
Channel Width		12.5 D
Inlet Length		8 D
Spanwise Spacing	${}^{z}/_{D}$	2.5
Streamwise Spacing	${}^{x}/_{D}$	2.5
Reynolds Number Range	Re_D	10,000 - 30,000

PIV Setup

For the purpose of capturing the wake of the pins and the structure of the HVS, a stereoscopic particle image velocimetry (PIV) system and *LaVision*® software for post-processing of the image pairs was used. The laser sheet was generated by an EverGreen laser from *Quantel*®. The laser is a 15Hz double-pulse Nd:YAG system at 532 nm wavelength and 200 mJ. The emitted laser beam was focused with a single spherical lens and a cylindrical lens was used to spread the laser beam into a laser sheet. The laser sheet was aligned with a system of mirrors. Ultimately, the 2 mm thick laser sheet was shot through the 25.4 mm acrylic sheet sidewall parallel to the endwall thus the main flow direction. The area of interest was at a distance of approximately 0.75 m to 1 m from the point of emittance. The locations of the measurements are ten planes each at two different streamwise locations within the channel. Location number one is between the trailing edge of pin row one and the leading edge of pins row two, and location number two is between row three and four, respectively. The ten locations varying in height are at 5% increments

between 5% and 50% of the channel height as shown in Figures 5.1 and 5.5. The plane at 5% ($^y/_D = 0.1$) is 0.1 inches away from the wall and 50% corresponds to the midplane of the flow ($^y/_D = 1$). The center pin, as well as the two neighboring pins for row one and three, were painted flat black as well as the two centered pins in row two and four to avoid reflections and minimize background disturbance. Cameras and laser, as well as optics, were mounted on a traverse system and carefully calibrated together (Figure 5.6).

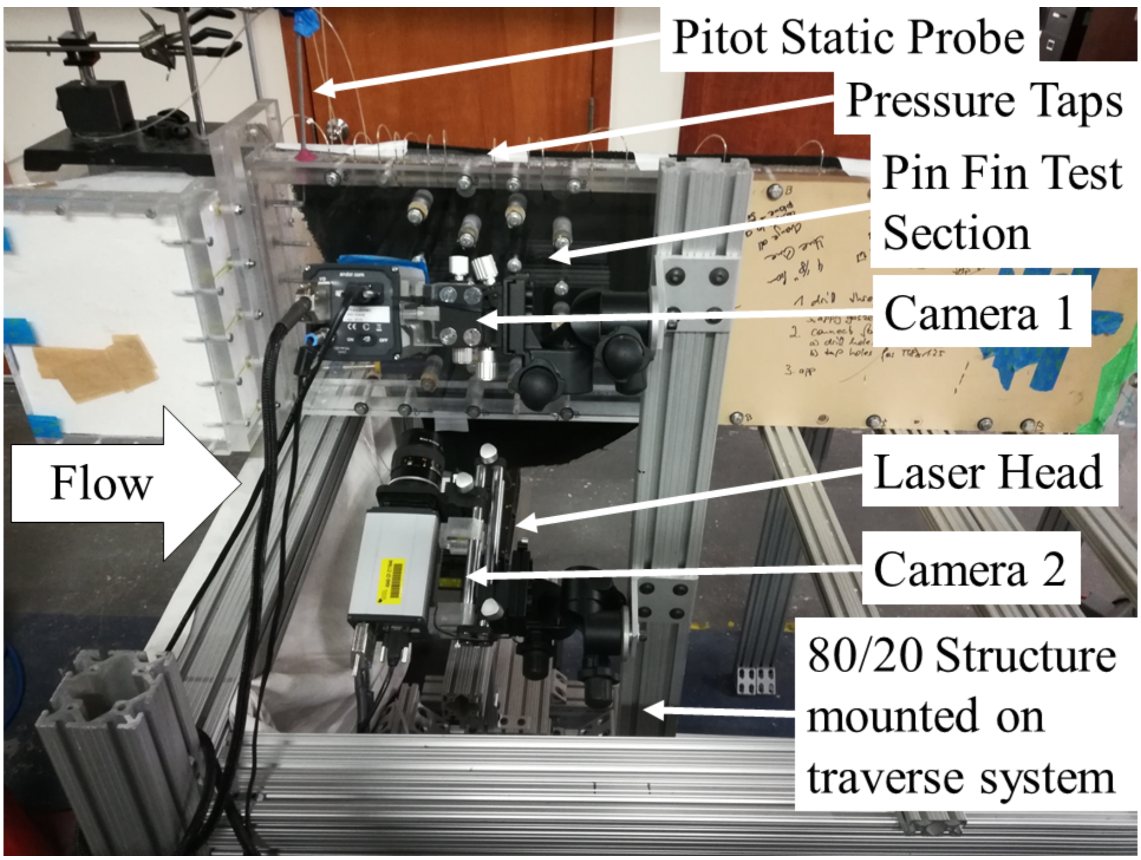

Figure 5.6: PIV Setup

The traverse system was driven by a stepper motor that was controlled by an Arduino Uno microcontroller to accurately move the setup to the ten measurement planes. The microcontroller was connected to a PC via a USB connection. A step motor controller

together with a DC power supply was used to move the traverse system. The finest resolution of movement (16 substeps per step) and lowest acceleration settings were used to achieve the highest accuracy and reduce the chance of skipped steps. The step motor control setup is depicted in Figure 5.8. The Aduino code consists of two major routines that were developed in-house. Both can be found in the appendix of this dissertation. Routine #1 was used to continuously move the laser sheet to any location. This was especially used during calibration. A *LaVision*® calibration grid was taped against the backwall of the test section. The laser sheet was moved with the continuous routine to slightly gaze the calibration plate. Since the thickness of the calibration grid is known (Figure 5.7), an origin was defined. The distance of all ten test locations was calculated based on the origin and implemented into the other routine.

Figure 5.7: Calibration Grid for Stereoscopic-PIV

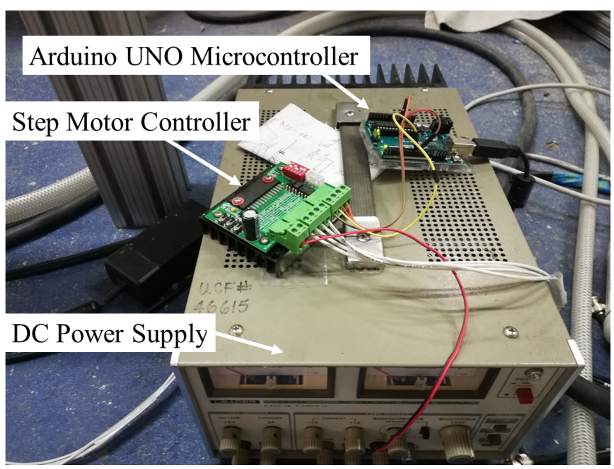

Figure 5.8: Arduino Motor Control Setup

Routine #2 was used to move the setup to the proper channel height location $^y/_D$. In addition to the calibration, the laser sheet was traversed to either endwall (top and bottom wall). This was done to ensure that the traverse system is aligned with the test section and that all measurement planes are parallel to each other. All steps of the calibration procedure were repeated for the center pin of row one and row three PIV measurements. The center pin was chosen particularly to avoid sidewall effects since this pin is neighboring with two additional pins on either side. Two Andor Zyla 5.5 megapixel CCMOS cameras (2560x2160 pixels) with 55 mm lenses and Scheimpflug adapter were focused on the area of interest from one side of the test section under a view angles of approximately -24° and 30° relative to the wall-normal vector, respectively.

Both cameras and laser were controlled via a time box. The time delta between two pulses was varied between 10 and 30 micro-seconds based on sample images optimized towards pixel displacement. For each test location, 1500 image pairs were taken and post-processed in *DaVis*® from *LaVision GmbH*® including the polynomial image dewarping based on calibration. The resolution of the camera sensor and the size of the interrogation window yielded gave a spatial resolution of approximately 33 pixel per mm.

Background subtraction was performed within the software prior to the cross-correlation algorithm to remove background noise and improve the quality of the result prior to the cross-correlation algorithm. Eight multipasses were used for stereoscopic PIV post-processing with two passes at 48x48 pixels with 50% overlap and 6 final passes at 24x24 pixels with 75% overlap. Atomized Di-Ethyl-Hexyl Sebecat (DEHS) was injected approximately 40 cm upstream of the contraction to ensure a good spreading of the particles in width and height. The target density of particles per interrogation region was approximately 10 with a mean particle size of 1 micro-meter.

Table 5.3: PIV Key Parameters

Parameter	Symbol	Value
Location of Interrogation Window 1	${}^{x}/_{D}$	0.5 - 2 (between row one and two)
Location of Interrogation Window 2	${}^{x}/_{D}$	5.5 - 7 (between row three and four)
Wall-normal Locations	${}^{y}/_{D}$	0.01 to 1
Number of wall-normal Locations		10
Number of Cameras		2
Camera Type		Andor Zyla 5.5 megapixel CCMOS
Camera Angles		-24° and 30°
Number of Image Pairs		1500
Particle Size		1 micro-meter
Particle Density		10 particles per interrogation region
Laser Sheet Thickness		2 mm

Heat Transfer Setup

As previously stated, the experiment was built in such a fashion to accommodate PIV testing and heat transfer testing simply by adding and removing certain components. The PIV test setup could be converted easily into a heat transfer measurement setup by removing the laser, camera setup, and particle seeder and replace it with the equipment required for the transient TLC measurement technique. This measurement technique requires video equipment to record videos of the color change of the paint, a data acquisition unit for reading TCs and a heater to supply heat to the flow. Independent of the actual rig, a frame structure had to be erected around the test section. All sides of the box were covered with white blackout curtains. The advantage of this cloth is that it prohibits light from entering the box and ensures evenly bright lighting everywhere within the box which was emitted from two light fixtures with two fluorescent light tubes each. The light fixtures were attached to the side of the frame structure to illuminate the test section. The angle incidence was approximately +/- 45 ° to avoid glare and reflections on the test section. A Canon VIXIA HF G10 Full HD Camcorder with HD CMOS sen-

sor and live HDMI output, and ten times optical zoom was used for recording the video signal. The resolution of video recordings is 1920x1080 pixels at 30 progressive frames per second. The camera is attached to the same frame structures as described before and about 0.6 meters away from the area of interest. The camera was placed behind the light fixtures so that no shadow seen on the acrylic surface. It was found later that the light itself is partially reflected by the shiny acrylic surface so that a light shadow of the experiment mounting structure and camera was seen. As those shadows are stationary and did not change through the experiment, they were eliminated from the images during post-processing through a background subtraction. Furthermore, the true color values on the surface are not of importance (only the change in green intensity over time). The setup for heat transfer experiments is shown in Figure 5.9. The heated flow enters through the right side of the channel, is straighned by the honeycomb before it enters the contraction and the actual test section. The lighting and camera fixture including the white blackout curtain can be seen in the background.

The internal camera software uses compression when saving the video onto the internal memory. In order to get the highest possible, uncompressed image quality, it was decided to use an HDMI signal grabber. The HDMI output from the camera provides a live stream that was stored on the fly with the HDMI signal grabber onto a flash drive as an *mp4* movie file. At the same time, the device allowed the pass-through of the video signal so that live video signals could be displayed on a monitor. This became a very powerful tool in the debugging phase of the experiment and allowed constant monitoring of the color change of the TLC paint as the experiment progressed.

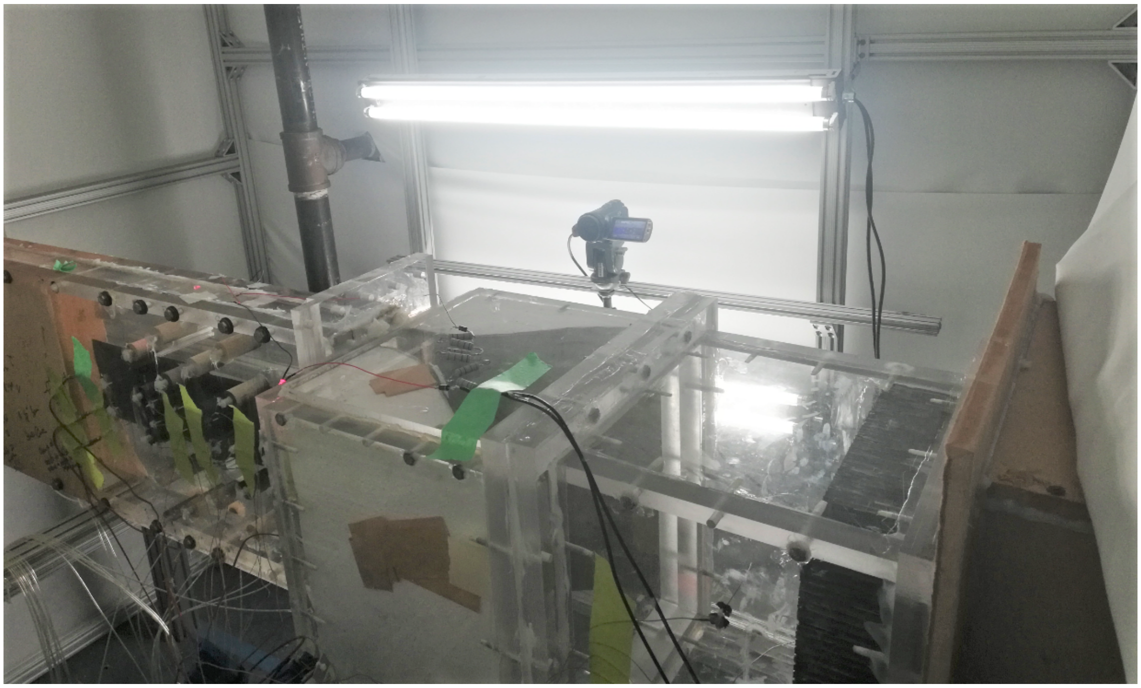

Figure 5.9: Setup for heat transfer experiments

Another modification compared to the PIV setup was the addition of heater box and honeycomb upstream of the contraction. In addition to these changes, the acrylic pins are replaced by basal wood pins to achieve endwall heat transfer only heat transfer as basal wood with a much lower thermal conductivity compared acrylic can be assumed adiabatic and non-participating in terms of convective heat transfer. All encountered thermal conductivity in this experiment are listed in Table 5.4. The thermal conductivity for Balsa wood is highly dependent on the orientation of the wood fibers. The value reported corresponds to conduction perpendicular to the fibers as occurring in this experiment. The thermal conductivity is a function of temperature. The value reported below is in the anticipation of 70-80 deg C air temperature during tests. The thermal conductivity is calculated for the film temperature T_{film} at each pixel. A correlation between thermal conductivity and temperature is known. Obtaining the proper properties for acrylic is not

straightforward. The theoretical value can be found in [116], yet the properties may vary depending on the manufacturing process and purity of the material.

Table 5.4: Comparison of thermal conductivities found in this experiment

Thermal Conductivity of Acrylic $[W/m.K]$	Thermal Conductivity of Balsa Wood $[W/m.K]$	Thermal Conductivity of Air $[W/m.K]$
0.1966	0.0339	0.026

A special jig to accurately glue the pins was 3D printed. The jig ensured that all pins have the proper spanwise and streamwise spacing and do not move while the glue dried. The the remnant half pins from the PIV test were not removed and could be used as reference for the inserted jig. The alignment process of the pins is shown in Figure 5.10.

Figure 5.10: Pin alignment using a 3D-printed jig

The flow path for heat transfer experiments is sketched in Figure 5.12. Most notable is the modified inlet section made out of a heater and an acrylic duct before entering the contraction. Details of this added section can be seen in Figure 5.11. First,

a commercially available HKR4-20A, a 20kW conventional three phase air-conditioning heating unit from *Goodman*®, for heating the incoming air. During preliminary testing, it was found that the very discrete coils of the heater caused thermal streaks and a highly uneven temperature profile entering the test section.

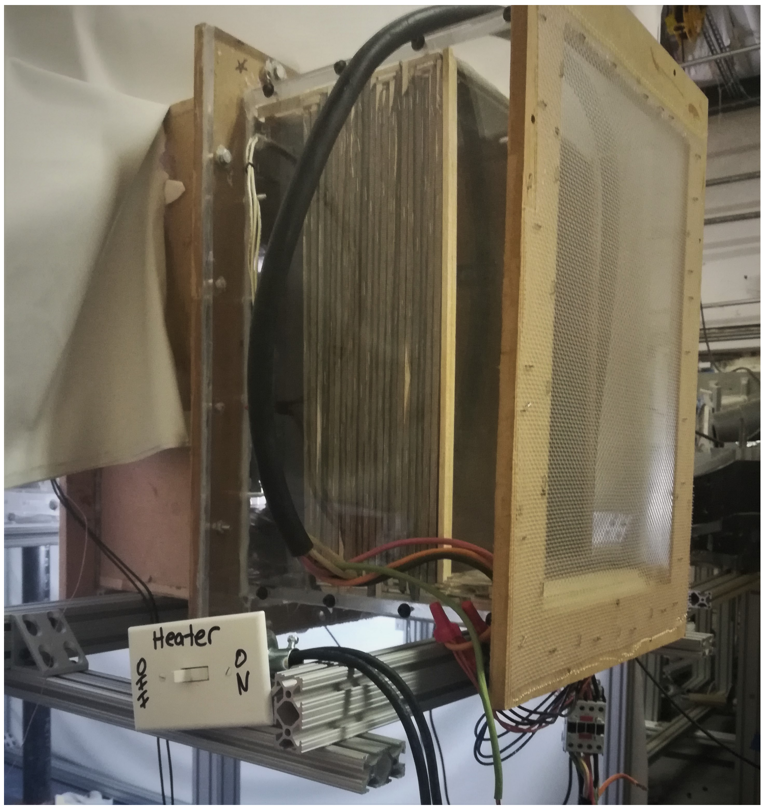

Figure 5.11: Heater box with stainless steel mesh screens

For this reason, it was chosen to build a heater in-house. Three sheets of 500 micron stainless steel mesh with mesh size of 500 were connected together and separated by a plastic mesh to avoid contact, thus short cutting. Each sheet was folded nine times so that the incoming air was heated by 21 mesh layers in total. A wooden frame was built around the outside of the mesh to keep all layers in place and under tension. Wrinkles in the mesh can create local hot spots that may burn out the mesh locally. Since less area

available is for the current, the heat production in the remaining mesh increases; consequently the mesh temperature rises as well which can lead to further damage. For the same reason, it was ensured to optimized the the contact between mesh and power supply. The ends of the mesh sheets were sandwich between to copper pieces and bolted together. Additionally, electric grease was applied at the electric junction between stainless steel mesh and copper. This ensures that an equal amount of current with supplied over the width of the mesh screen. Figure 5.11 shows the heat box and the enclosure. Air enters from the right and is heated through the many mesh passes. A easily accessible switch is used to shut off the power supply from the heater. The three phase power was supplied on the cold side of the heater where each of the three mesh sheets was connected to one of the three phases. All meshes were connected to a common ground at the hot side of the heater. One mesh path had to be removed as it burned out during one of the higher flow rates tests. However, the remaining heater mesh was sufficient to supply the necessary power to heat the air to the desired temperature.

The heating unit can be controlled via a relay and 220 Volt AC. The switch of the heater was connected with two LEDs that were placed in the field of view of the camera. The LEDs lightened up at the same time as the heater was turned on and give an optical reference in the video of the start of the experiment. The heat release of the heating unit is controlled via a three phase variac from *STACO Energy Products Co.*® in order to freely adjust the voltage between 0 and 460V. The heating unit is enclosed in a box made from MDF. This section is flanged to a 16 inches long acrylic duct that directly connects with the inlet plenum. The acrylic box itself holds a honeycomb mesh for flow straightening. Besides holding the honeycomb, another purpose of the acrylic duct is to provide optical access to the flow exiting the honeycomb. This is important to evaluate the quality of mixing of the flow to ensure a high temperature uniformity to avoid thermal streaking which would reduce the quality of the TLC measurements.

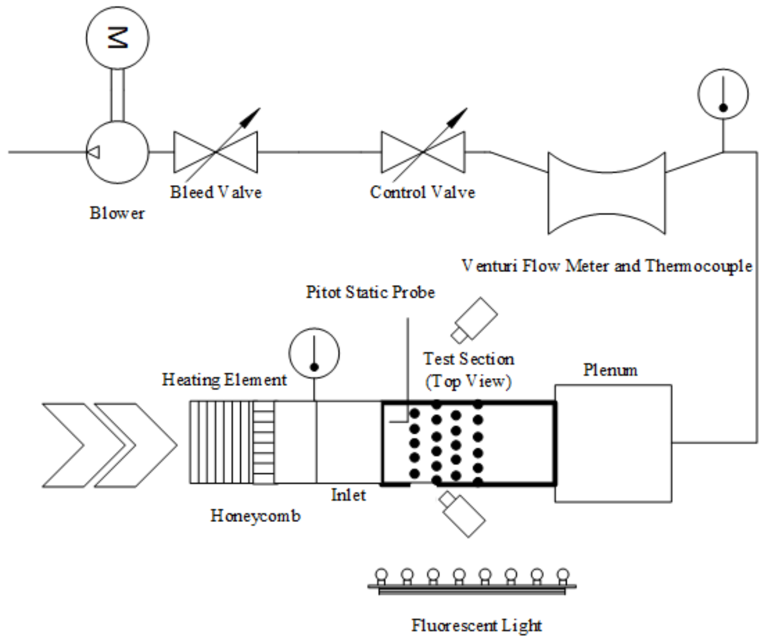

Figure 5.12: Flow Path Diagram for the Heat Transfer Experiment

As the heat source for the transient TLC measurements is established at this point, the remaining components for the measurement technique according to the outlined methodology in the previous chapter have to be implemented as well. This includes TLC paint, lighting, and camera setup. The TLC paint of choice is a sprayable coating from *LCR Hallcrest LLC*®. Two types of TLC paints are commonly differentiated: wide-band TLC paint and narrow-band TLC paint. Wide-band TLCs have a color range from red to green to blue which spreads over a range of 20-30K. For narrow-band TLCs however, the color peaks for red and blue are within a few Kelvin. In this particular case, all three color peaks are found within 0.8K. Table 5.5 shows the peak temperatures based on the information based on the manufacturer. The TLC paint was sprayed onto the acrylic of the endwall using an air-pressurized spray gun. Using the same equipment, a black backing paint was applied onto the TLC paint to provide a larger contrast of the paint colors against

the background to provide a clearer image. This time using the wooden balsa pins, the test section was reassembled and connected to the heater unit. A metal frame made from *80/20*® was used to enclose the experimental setup including camera setup and lighting. The white fabric was used to block out the lighting from the outside and minimize internal reflections and maximize light efficiency. The only opening in the enclosure was connected to flow inlet so that cold stationary air from outside the enclosure could be sucked through the various components of the flow path.

Table 5.5: TLC Paint Thermal Profile with a tolerance of $\pm 1K$

Red Start	Green Start	Blue Start
54.5°C	54.8°C	55.3°C

The measurement of the surface temperature is only one part of the heat transfer experiment. The method also requires knowledge of the bulk flow temperature within the test section itself. Twenty additional TCs were used for this purpose. All TCs were of type T. Two TCs are installed upstream of the heater to monitor the ambient temperature conditions. Additional three TCs are located downstream of the honeycomb upstream of the contraction. The remaining 15 TCs were located within the test section: Three TCs 1.25 diameter upstream of row 1, and three each centered between the rows, as well as three 1.25 diameter downstream of the last row. The three TCs at one streamwise location were also spread in spanwise direction. The detailed location of all TCs is depicted in Figure 5.5. The six TCs upstream of the array and downstream of array were sheathed, calibrated TCs. Sheathed TCs are reinforced with a thin metal tube around the wires so that they bent less. This was chosen to avoid bending of the TCs due to the flow velocity.

The data acquisition system consisted of a *FLUKE* 2688A data logging system and two *FLUKE* 2680 precision analog input modules to continuously read the TCs. A

medium fast acquisition rate was chosen as a compromise between accuracy and time. The heating process is highly transient and therefore requires a good resolution in terms of time to capture the quick increase in temperature. The DAQ systems reads 40 channels at medium speed. Since 20 channels were used, the data points are half a second apart. The detailed temperature behavior within the channel will be discussed in the results section.

Conducting the experiment at the desired Reynolds numbers of 10,000 and 30,000 was not straightforward. An iterative process was needed to obtain the proper flow rates in the heated experiments. Fluid temperature and velocity changed immediately as soon as heat was supplied to the flow. However, the target was to match 10,000 and 30,000 Reynolds number at the heated flow rather than cold flow. Therefore, the gate valve had to be set to an estimated higher flow rate so that the Reynolds numbers will match after heat is supplied. Due to the transient nature of the experiment and the assumption that the wall temperature are at initial conditions during the test, the flow rate could not be adjusted after the experiment was started. Once the flow rate matches for the heated flow, the fluid temperature dropped as now the same amount of heat was supplied to a larger mass flow rate which in turn required an increase in heat power. Several iterations of trial and error were required to match the Reynolds numbers closely.

CHAPTER 6: NUMERICAL SETUP

In order to compliment the results obtained in the PIV and TLC experiments, but also to further understand shortcomings in the numerical models, a comprehensive set up numerical testing was performed on the entire test domain. The scope of the numerical simulations included both Reynolds numbers 10,000 and 30,000 for Reynolds Averaged Navier-Stokes (RANS) simulations; both steady and unsteady. Furthermore, the RANS models were varied for both Reynolds number cases. Additionally, a Large Eddy Simulation (LES) was performed on a periodic section of the pin fin array. The meshing and simulations were performed using the commercially available software *Simcenter Star-CCM+®* by *Siemens PLM®*.

Reynolds Avaraged Navier-Stokes Equation

As already mentioned, the numerical setup for RANS and LES simulation is different. The study aimed at obtaining additional information about heat transfer and vortex structures within the capabilities of tweaked RANS turbulence models. Therefore, the experimental test domain including parts of the inlet and test section was modeled for the RANS simulation. This, however, exceeds the computational capacities in the case of a Large Eddy Simulation. For this reason, it was decided to use a periodic section instead of the larger domain and shift the focus more towards fundamental flow physics. The fluid domain is shown in Figure 6.3. The domain itself is reduced to a slice of its physical representation containing one center pin and two half pins in the staggered layout. The slice is assumed to be the center-line of the experimental setup, two periods away from the sidewalls on either side. No modifications were made with regard to the height of the channel so that top and endwall are included in the fluid domain. Since boundary layer

thickness is an important factor in the formation, build-up, and strength of the horseshoe vortex system (HVS), it was decided to include the upstream region of the pin fin array as well as the contraction. The flow enters through the left and exits through the right. The scope of simulations within the RANS category includes the Reynolds numbers 10,000 and 30,000 as well as a variation of turbulence models per Reynolds number case. Mesh and boundary conditions were carefully chosen to closely mimic the actual physical testing in order to provide a high degree of comparability between experiment and simulation. Since the Mach number of the flow for both Reynolds numbers is significantly smaller than 0.3 and the temperature rise of the fluid compared to ambient conditions is small, the fluid was modeled as an ideal gas and the flow equations were solved based on a segregated flow solver with segregated fluid temperature. A monitor plane was introduced upstream of the heat section to report out density, viscosity, and mass flow rate in order to track the Reynolds number within the channel.

Boundary Conditions

Based on the fluid section in Figure 6.3, six key regions can be identified for each of which a unique set of boundary conditions is defined:

- Flow inlet: Velocity inlet with specified velocity profile to match the appropriate Reynolds number and specified ambient temperature and pressure as found in the test facilities during the PIV testing
- Flow exit: Pressure outlet
- Periodic interfaces on the left and right side of the fluid portion excluding the surface of the half pin fins

- Endwalls on top and bottom: No-slip wall boundary condition with uniform heat flux of 1000 ${}^{W}/_{m}^{2}$
- Pin surfaces: No-slip wall boundary condition with uniform heat flux of 1000 ${}^{W}/_{m}^{2}$
- Contraction: No-slip wall boundary condition without heat flux

Applying periodic boundary conditions on the side is common practice in pin fin array simulations as found in impactful papers by Delibra et al. [40, 42] and others [43]. As this section is adequately distant from the sidewalls in the actual physical representation, the research community believes that sidewall effects change the center slice physics. Originally, the simulation comprised of the test section and the inlet contraction. This setup is shown in Figure 6.1.

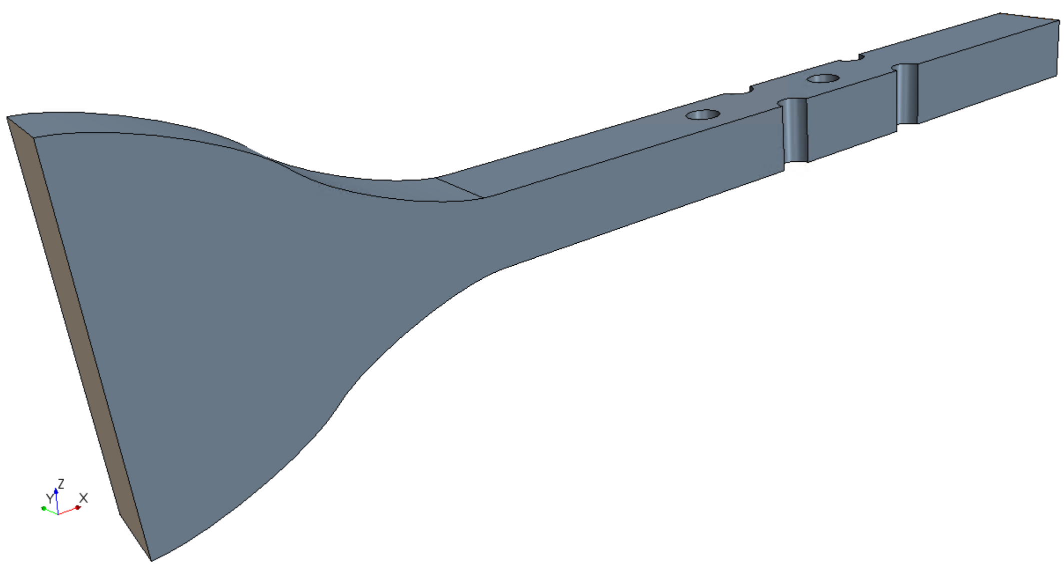

Figure 6.1: Original Geometry prior to removing the Inlet Section

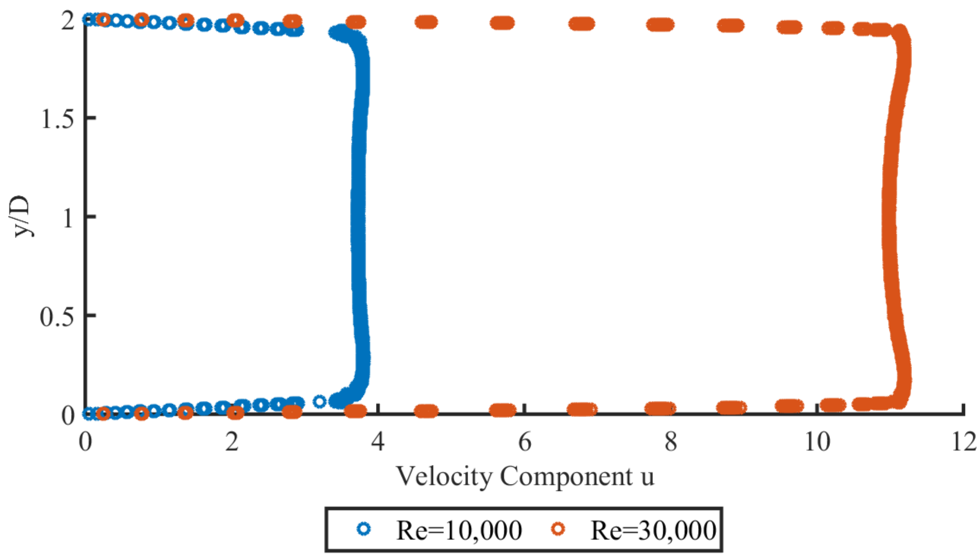

Figure 6.2: Profiles for streamwise Velocity Component exiting the Contraction used as Inlet Boundary Condition

In order to reduce the mesh count, it was decided to remove the inlet section from the model. However, prior to this, the inlet boundary condition at the contraction was set as a mass flow inlet with the proper mass flow rate to match the desired Reynolds number. All three velocity components were measured at the exit of the contraction. The velocity profiles for the streamwise velocity component for Reynolds numbers of 10,000 and 30,000 are shown in Figure 6.2. Both profiles show the expected top hat shape as expected and show moderate boundary layer growth within the contraction. This information was then used to specify the velocity at the inlet of the test section for velocity inlet. This way, the incoming boundary layer thickness from the contraction is accurately captured within the model whilst reducing the computational time. This method was applied to both Reynolds number cases. The modified geometry including the used boundary conditions is shown in Figure 6.3.

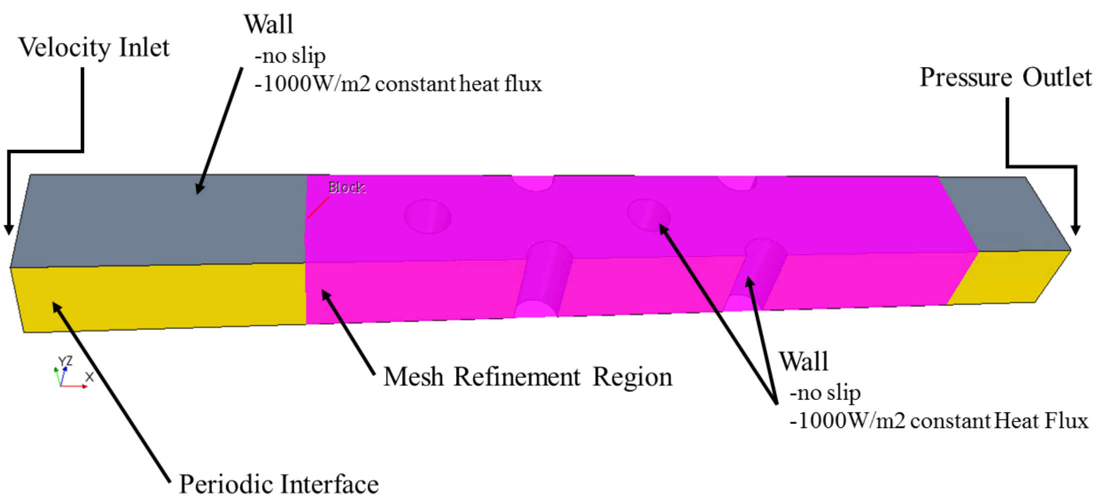

Figure 6.3: Modified Geometry including Definition of Boundary Conditions

Mesh

Originally it was attempted to use a trimmer mesher consisting of mostly hexahedral cells. However, it was found that highly skewed cells not very well lining up with the boundary layer prisms were complicating the convergence due to the transition from the circular shape of the pin to the predominantly rectangular design of the channel. For this reason, it was decided to move forward with a polyhedral mesh. Prism layer cells of particular thickness are arranged around the top and bottom wall of the fluid domain as well as around the pin to capture and model the boundary layers. The prism cell mesher within the used commercial solver tends to retract the thickness of the prism layers to zero when approaching corners as they are found between the endwalls and the pins. On the parts-based level, a modified meshing algorithm is available that enhances and provides a conformal prism layer mesh in these regions. The advancing layer mesher is a combi-

nation of prismatic meshers and polyhedral meshers. First, the surfaces are wrapped in several prism layers and the remaining voids are filled with polyhedral cells. Since this works specifically focuses on the effect of the vortices created in this junction, specific care was taken to adequately model this junction. The resulting prism mesh on endwall and pin, the treatment of the junction, and the blending into the core mesh is shown in Figure 6.4.

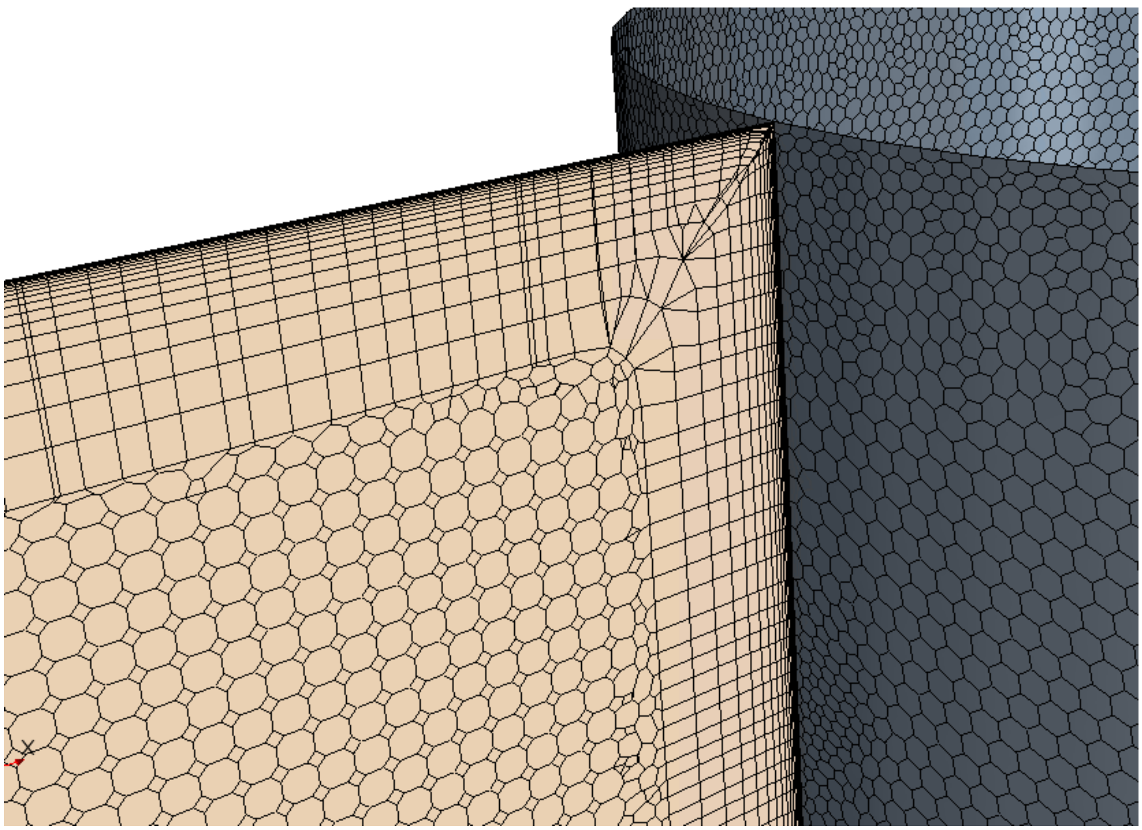

Figure 6.4: Corner Treatment and Prism Mesh

As the flow enters the fluid domain, the turbulence levels and velocity gradients are relatively small compared to the flow in the area that contains the pins. This allows to mesh to be coarser and thus save computational time and cost. The region of a finer mesh starts 2.5 pin diameter upstream of the first pin centered in the flow. As the last row

of pins shed a wake, the refined area ends 5 pin diameter downstream of the last rows of pins before the coarser region starts again. Both, surface size and base size of the cells were varied to smoothly transition between regions. The transition in surface size and core mesh size is shown in Figure 6.5. The mesh in the area around the pins is four times denser compared to the inlet and exit section of the fluid domain. The target surface size was 1 mm in the coarse region and 0.25 mm in the refined region. The minimum surface size was set to 0.2 mm.

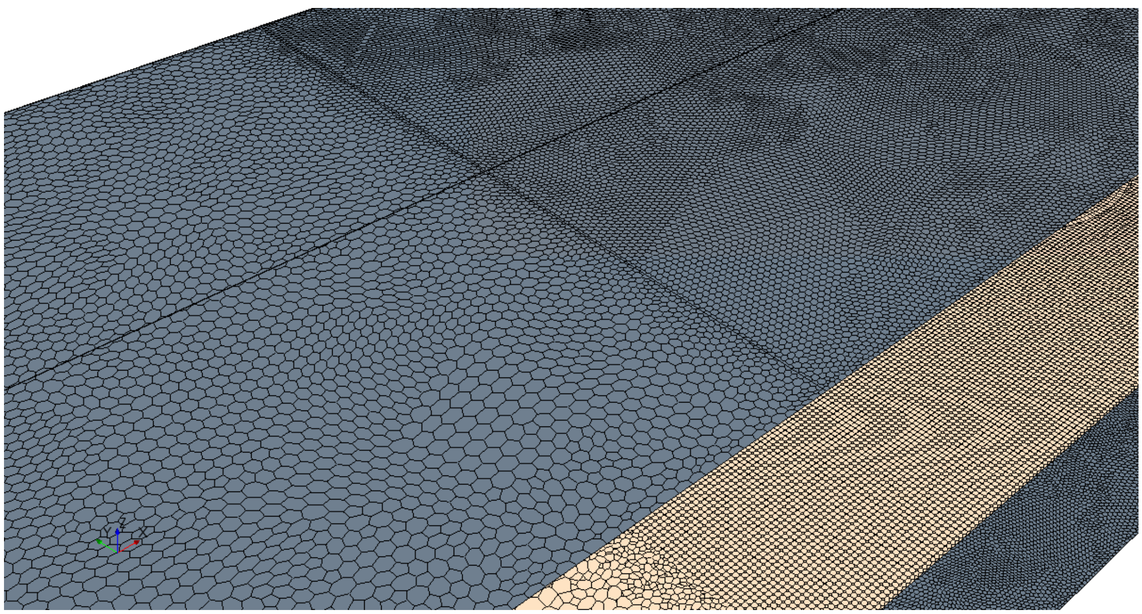

Figure 6.5: Visualization of Mesh Refinement Area in terms of Surface Size and Base Size

When specifying the prism layers for the boundary layer cells, two parameter are of crucial for a correct prediction of the flow field and heat transfer. First, the overall height of the combined prisms has to be large enough to capture the steep velocity gradient close to the wall. Second, the thickness of the first prim layer close to the wall has to be small enough to capture the viscous sublayer so that no assumptions on the wall function are required. The total thickness of the expected boundary layer thickness was

approximated using the Blasius correlation for turbulent boundary layers as introduced earlier as Equation 4.2. A requirement for proper heat transfer results in numerical simulations is a non-dimensional wall thickness y+ of 1. This determines the thickness of the first cell. It was decided to grow 18 prism layers where each layer is 30% thicker than the previous layer. The prism layer parameters were kept the same on the endwall and pin to create a conformal mesh in the junction. The final thickness of the prisms is 2.4 mm. Accordingly, the thickness of the first cell is in the order of 0.0065 mm. Such small value was required to achieve y+ values of smaller than 1 everywhere. The impinging effect of the flow in the stagnation region of the pin required a much smaller first cell size than expected by common flat plate estimations. With all these values, the requirement for heat transfer analysis was satisfied everywhere at the wall. The final y+ distribution is shown in Figure 6.6. The figure shows that the most crucial area in terms of managing the Y+ value is the leading edge of the pin where the air impinges on the pin surface. In terms of endwall, the most critical area is the outline and imprint of the horseshoe vortex that wraps around the pin.

Grid Convergence Study

It is widely recognized within the scientific community that there is a strong correlation between the result of the numerical simulation and the count and size of the mesh cells. At one point, the accuracy of the solution does not increase with a higher mesh count. From this point on, it is not beneficial to further reduce the cell size and thus increase the cell count. In acknowledgment of this fact, a grid convergence study was conducted to find the smallest required mesh count for an accurate result without wasting computational time and sacrificing accuracy.

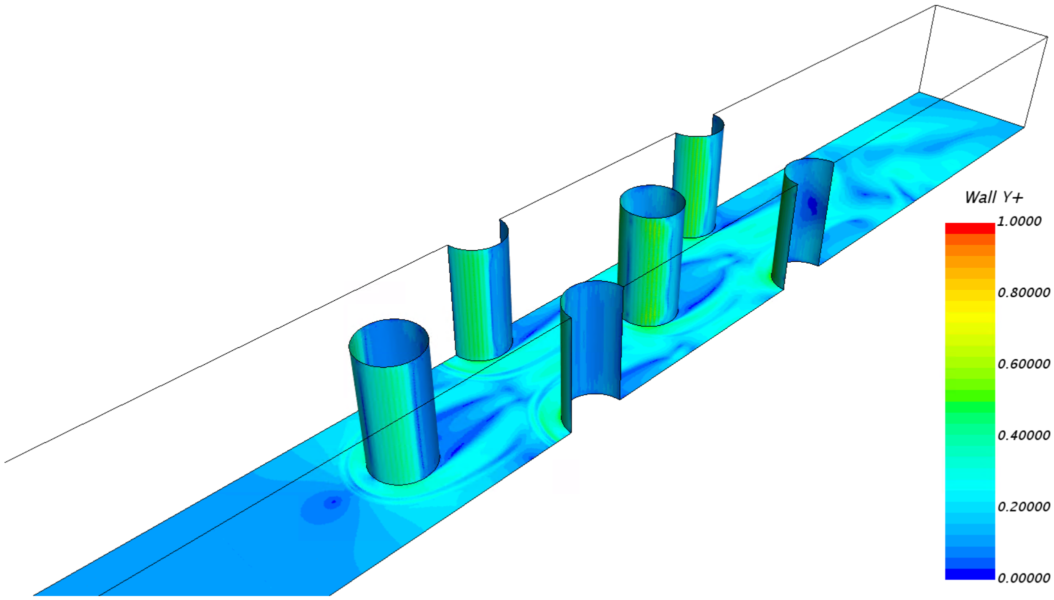

Figure 6.6: Final wall Y+ distribution for a Reynolds number of 30,000

The grid convergence study was conducted on the test case with Reynolds number of 30,000 and the k ω SST turbulence model. Hereby, the base cell size was varied from 2.54 mm down to 1.75 mm which corresponds to a mesh count of 13, 19, 28, and 35 Million, respectively. As the base cell size was reduced, the cell size in the mesh refinement region automatically changed proportionally as well as the surface size. Since the prism layer total height and thickness of the first layer was defined in absolute values, the height and stretching of the prism cells did not change, only the surface size, resulting in a better resolution in the wall region of endwall and pins. For this reason, the y+ value on the wall was invariable compared to the most coarse mesh. As mentioned previously, it was ensured that the y+ value was smaller than 1 everywhere in order to allow meaningful conclusions on heat transfer.

The initial characteristics for grid convergence were friction factor, area-averaged Nusselt number on either endwall and the area-averaged Nusselt number on all pins. The

results are tabulated in Table 6.1. After it was ensured that the simulation has converged, the simulation was continued for an additional 1000 iteration over which the solution was averaged. This is required as some of the residuals fluctuate as the pin fin case is an unsteady problem due to wake shedding. Unless otherwise noted, all presented results are obtained through iteration averaging.

Table 6.1: Grid Convergence Study Results

Mesh Count in Million	Friction Factor	Endwall Nusselt Number	Row 1 Pin Nusselt Number	Row 2 Pin Nusselt Number
13	0.1271	71.2	93.9	115.6
19	0.129	67.9	93.4	115.9
28	0.1289	68.3	93.1	116.1
35	0.1289	67.61	93	115.9

It was found that this approach was not suitable to determine the convergence of the grid as the average values were within a few percents of each other. Therefore, the conclusion of gird convergence was made based on the local Nusselt number on six line probes located downstream of the center pin of row one and row three. The location of the line probes is identical to ones highlighted in the test section in Figure 5.5 as they are key locations for the data analysis.

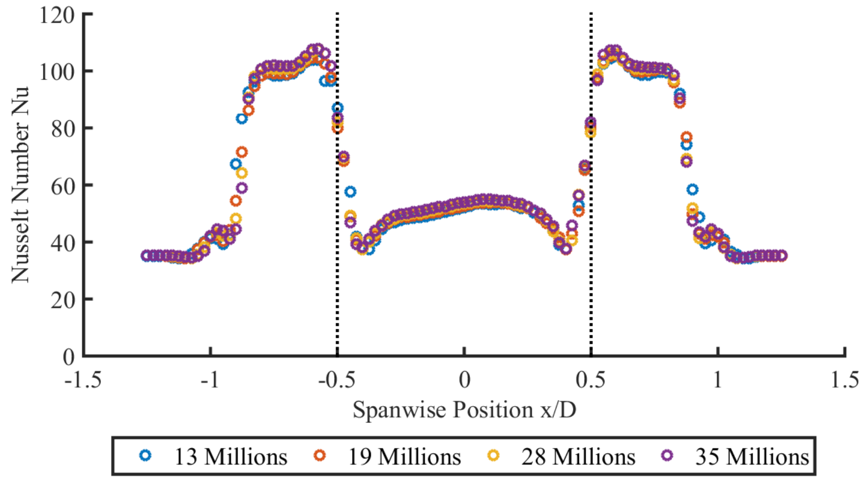

Figure 6.7: Comparison of spanwise Nusselt Number distribution for various Meshes 0.2 Pin Diameter downstream of Row 1

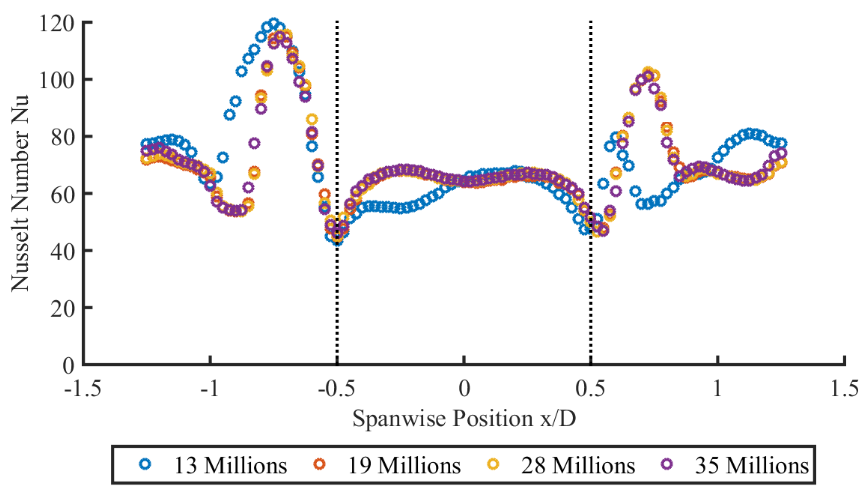

Figure 6.8: Comparison of spanwise Nusselt Number distribution for various Meshes 0.2 Pin Diameter downstream of Row 3

It is apparent from the mesh convergence study that the Nusselt number trend of all meshes is very similar, yet differences can be spotted. For the results behind the center pin of the first row, shown in Figure 6.7, the 13 Million and 19 Million cell meshes, shown in blue and orange respectively, do not pick up the magnitude of increased heat transfer in the region of $^{z}/_{D}$ to -0.5 and 0.5 to 1. Since the pin is one diameter wide, these particular regions are directly neighboring the pin. The dotted lines show the pin location relative to the data. As the two coarser mesh variants underpredict, the two finer meshes are spot on. The underperformance of the most coarse mesh is even more obvious in the third row as shown in Figure 6.8. In this more turbulent region, the magnitude and trend are not correctly picked up by the 13 Million cell mesh. Even though it was decided to average over more and more iterations - which is expected to produce a more symmetric Nusselt number distribution relative to the location - the non-symmetric behavior persisted. The differences between 19 Million, 28 Million, and 35 Million cells are marginal. Based on those findings, the coarsest and the finest mesh with 35 Million cells can be ruled out as unnecessarily refined. Although the 19 Million cell mesh only deviates slightly from the finer 28 Million cells mesh in terms of solution quality, the decision was made in favor of the 28 Million cells mesh as the scope of work also includes RSM simulations whose convergence is known to be heavily reliant on the mesh quality.

Turbulence Modeling

The choice of ideal turbulence model was a result of a large number of numerical experiments, as the flow over a cylinder-bank problem is one yet to be fully solved with RANS models in many industries (turbomachinery, nuclear, etc.). A general challenge herein was correctly predicting the change of the turbulent scales and dissipation in the flow with subsequent rows. As shedding and wake propagation from one row interact with the subsequent row, the challenge of correctly predicting the separation points

on downstream pins is inherently difficult. Turbulent length scales locally calculated in RANS models have a first-order impact on when separation is predicted, which is entirely influential on the resulting heat transfer. Additionally, the wakes are inherently unsteady and characterized by recirculation and high streamline curvature; a known failure for RANS models. RSM is superior to RANS models in capturing the anisotropic behavior of the turbulence in the flow, as it directly calculates the Reynolds stresses in their respective transport equations and does not introduce the assumption of isotropy via the Boussinesq approximation. An elliptic blending model variant as discussed by Manceau and Hanjalić [117] is used for the pressure-strain term, which offers a superior inhomogeneous near-wall formulation and was shown to improve the accuracy in the heat transfer predictions. Throughout the series of numerical experiments, it was found that the Daly-Harlow [118] modification for the diffusion of Reynolds stresses improved the heat transfer prediction capability and was therefore used in the final model formulation. Lastly, the turbulent dissipation rate tabulated on a per-row basis by Ames [32] was useful to assess how well the turbulence models herein were predicting the decay rate with respect to downstream position. As such, the Cε2 coefficient, which scales the destruction term for ε, was only slightly varied from Manceau's [117] value of 1.83 to 1.86. This showed more appropriate decay rates of the turbulence which better represented the behavior in Ames [32] and this study.

The conventional RANS models used in this study were the standard k-ω model and the LAG EBKE model. The correct separation of the boundary layer from the pin seems to be one determining parameter for the quality of the simulation. It was suspected that the boundary layer in the first pin might be laminar and requires special treatment. For this reason, a laminar model and a transitional model were chosen in addition to the previously mentioned turbulence models. The transitional $\gamma - Re_\theta$ is a modification of the k-ω SST model that tries to account for the change of flow regime between laminar and

turbulent flow. A detailed list which turbulence models were used for which Reynolds number case are shown in Table 6.2.

Table 6.2: List of turbulence models used

$Re = 10,000$	$Re = 30,000$
k-ω	k-ω
LAG EBKE	LAG EBKE
RSM	RSM
laminar	
$\gamma - Re_\theta$	

The problem of vortex shedding from a cylinder is an inherently unsteady process. Although steady RANS simulations are a valid approach for this problem, the under-relaxation factors for velocity, pressure, and turbulence had to be lowered to obtain a mean solution and dampen the effect of oscillating residuals. This significantly accelerated the convergence of the simulation, yet the residuals were still slightly oscillating. All flow mean properties were averaged over at least 1000 iterations to compensate for the oscillation.

Large Eddy Simulation

The computational requirements for a LES exceed the one's for a RANS simulation by far. More equations have to be solved per volume element to account for the additional six Reynolds stresses. In addition, the mesh sizes has to be fine enough the resolve about 80% of the turbulent kinetic energy; whereas the remaining energy contained in smaller eddies will be accounted for by the sub-grid models. For these reasons, it unfeasible to conduct a LES simulation at an fluid volume as introduced at in the previous section. Two ways exist to cut down the computational requirements: On the one hand, the Reynolds number can be decreased. A smaller Reynolds number does not require a high mesh

count. On the other hand, the computational domain can be shrunk. It was decided to proceed with the second option. The geometry was reduced in a such a way that utmost advantage was taken of any available symmetry within the pin fin array. This includes an reduction of the fluid volume to two pitches in streamwise direction and on pitch in spanwise direction as shown in Figure 6.9. The reduced volume contains half a pitch upstream of a full pin, two half pins, as well as half a pitch downstream of the half pins.

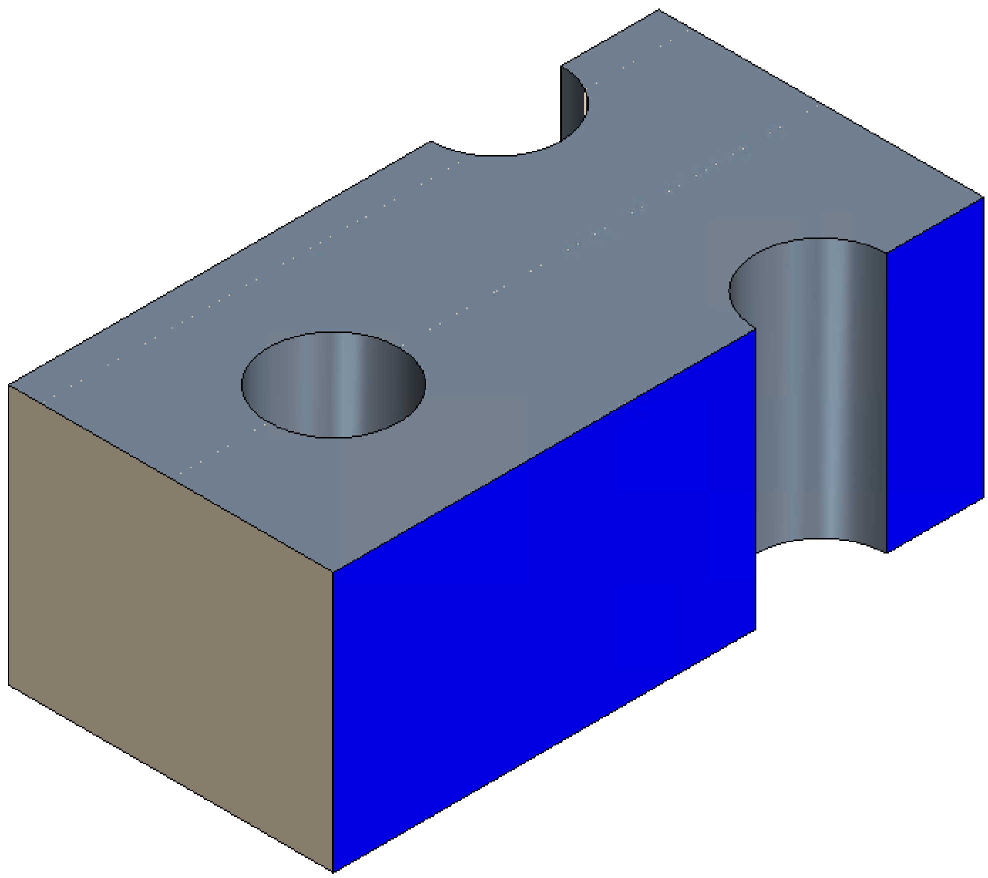

Figure 6.9: Reduced fluid domain suitable for Large Eddy Simulation

Even though the volume was reduced significantly, several additional assumptions and restrictions had to be made. The first one is that only one LES was done at a

Reynolds number of 10,000. The second is, that in contrast to the previous RANS simulations, not the developing flow is in focus but rather the fully developed flow in a pin fin array as commonly found after the fifth row.

On of the objectives in this study is to compare the performance of RANS models. Selected RANS turbulence models were also used on the fully developed LES fluid domain to allow direct comparison between both approaches. The choice includes the Reynolds stress model (RSM), a laminar model, the $\gamma - Re_\theta$ transitional model and the LAG EBKE model. The mesh and boundary conditions were the same for all RANS, RSM, and LES.

Boundary Conditions

The periodic sidewalls (blue surfaces in Figure 6.9) and constant heat flux pin and endwall surface (gray surfaces in Figure 6.9) are identical to those in the whole domain study. The only difference in the boundary conditions between the full domain compared to this shorten domain is the treatment of the *inlet* boundary conditions; the brown inlet section and the hidden exit section on the backside of the periodic section in Figure 6.9. Here, the inlet boundary condition is not to be understood in the literal sense of the word. The technical description of the boundary condition at the inlet and exit of the fluid domain is referred to as fully developed interface. This means nothing else but that the flow exiting the fluid domain is directly fed back into the inlet of the domain. Therefore no developing effects of the flow can be observed. The setup can be understood as an infinitely long cascade of segments connected together. The approach of an fully developed interface is thoroughly described by Ahmed [119] for a fully developed flow through a square channel with rib turbulators.

Mesh

An LES does not need a grid convergence study in contrast to RANS. The criterion for a good LES mesh is the sufficient resolution of the energy spectrum that contains at least 80% of the turbulent kinetic energy. Further refinement of the mesh would yield a DNS. The smaller the mesh, the more eddies can be resolved. A trimmer mesh approach was chosen. A trimmer mesh consists of mostly hexahedrons that combined make up the volume. The hexahedrons blend into the prism layers that are located around the pins. Prism layers are also added on the endwalls. Table 6.3 gives a brief overview over the structure of the mesh. The wake regions of the full and the two half pins experience a mesh refinement at 30% of the base size. The total mesh count was 9.2 Million.

Table 6.3: Mesh parameter for Large Eddy Simulation

Base size	Number of prism layers	Mesh refinement
2 mm	10	in pin wake region

Specific mesh details regarding the pin prism layer treatment and the overall mesh structure are shown in Figure 6.10. The mesh refinement areas can be clearly identified in the wake region of the pin as well as the ten prism layers that wrap around the pin. The breakout section visualizes the near wall treatment and the blending of the prism cells into the hexahedrons mesh.

As the wall y+ citerion was used to judged the quality of the prism layer right next to the wall, so it is used at this point again. Figure 4.44 shows the (instanteneous) wall y+ distribution on the endwall and pin surfaces. A wall y+ smaller than unity is maintained everywhere within the fluid domain indicating a valid mesh in this regard.

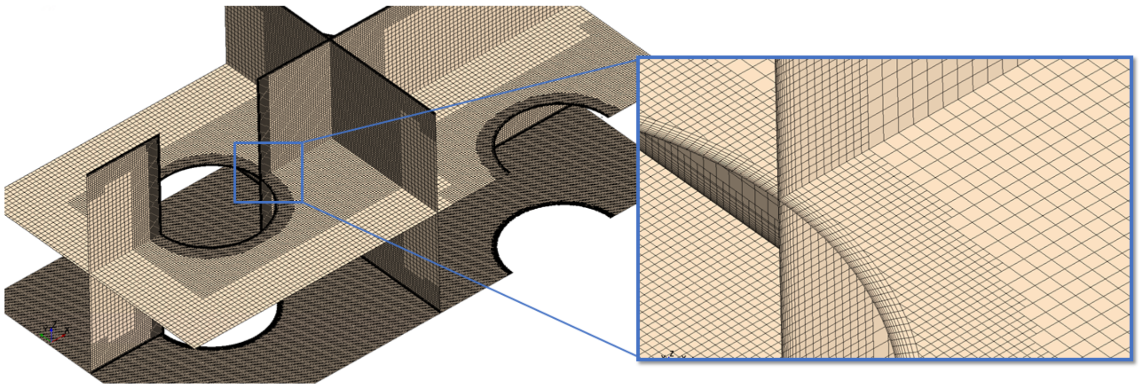

Figure 6.10: Mesh for LES including mesh refinement areas

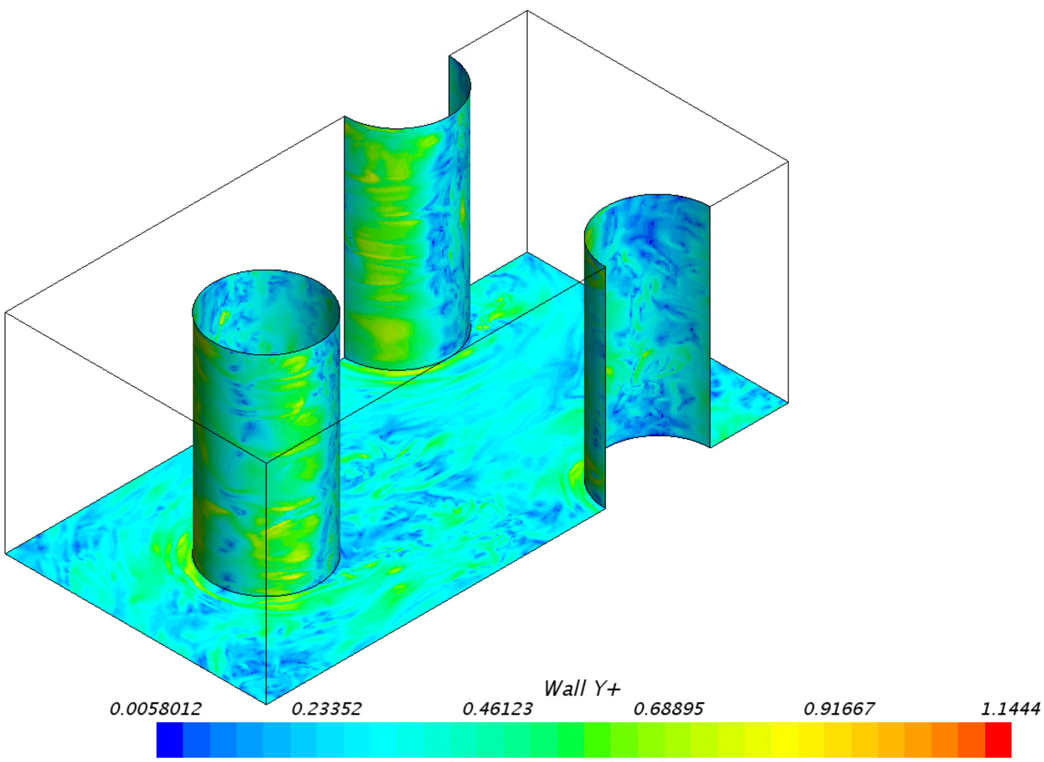

Figure 6.11: Instanteneous wall y+ distribution on the endwall and pin surface

CHAPTER 7: UNCERTAINTY

A proper and thorough uncertainty analysis and discussion of potential error sources is essential for the proper understanding and interpretation of that data and increases soundness of the experimentally obtained results. Part of this uncertainty analysis are two types of error: systematic error and random error. The systematic error, also called statistical bias, comes from the measurement device itself and its proper use and handling. Examples for systematic error could be a wrong calibration of the measurement device, a wrong zeroing of the measurement instrument, or a drift of measurement over time. The random error is due to inherent randomness of the experiment. Even if the experiment is repeat with the same conditions, the results will be slightly different. Random errors tend to be normally distributed around a mean. Repetitive testing will reduce the random error and increases confidence in the measurement. Here, a confidence interval of 95% was chosen. Another contributor to the random error is the accuracy of the used measurement device. For most standard equipment, the uncertainty of a measurement instrument is provided by the manufacturer of the equipment.

The uncertainty analysis is based on methods described by Kline and McClintock for single-sample experiemtns [120], Moffat [121] for error propagation, and the Test Uncertainy Standard PTC 19.1 - 2018 by the American Society of Mechanical Engineers (ASME) [122]. The aforementioned method is a partial differential method that propagates the error contribution of each independent measurand towards the total uncertainty of the engineering property. Let X_i be the mean of a measurable property with an uncertainty δX_I so that

$$X_i = X_i(measurement) \pm \delta X_i \tag{7.1}$$

at a 95% confidence interval. This property could be air temperature for example which can be easily measured with a thermocouple reader. However, it can be seen that the determination of the uncertainty in Nusselt number is not readily available as know device exists to directly measure Nusselt number. In fact, Nusselt is a quantity derived from a measured quantities: heat transfer coefficient, pin diameter, and thermal conductivity of air. The uncertainty in the diameter of the pin is related to the accuracy of the caliper. The thermal conductivity of air is a function of the air temperature. The error in the reading of the air temperature directly affects the accuracy of the Nusselt number. The heat transfer coefficient is even more so dependent on other measurable quantities such as air temperature, time, and surface temperature if we assume the heat transfer coefficient measurement was conducted by using the transient TLC method. This brief example clearly shows the dependency of the final property on many other measurements which in turn contribute to the total uncertainty. The consideration of each uncertainty for the total uncertainty is referred to as *[*error propagation]. In the terminology of uncertainty, the air temperature would be a measurable property X_i and Nusselt number a result R of some kind of data processing. As the Nusselt number is a function of temperature X_1 (amongst many others independent measurements $X_2..X_N$), the dependency can be written in a more generalized way that

$$R = R(X_1, X_2, ...X_N) \tag{7.2}$$

where the error of each measurement δX_i contributes to the total error of the result R. Equation 7.3 shows the partial differential contribution of that error to result error with respect to that measurement. The partial derivative can be understood as the sensitivity

of the result relative to the particular measurement.

$$\delta R_{X_i} = \frac{\partial R}{\partial X_i} \delta X_i \tag{7.3}$$

As explained in the Nusselt number example, a result is rarely dependent only on measurement. All contributing independent measurements are combined using the root-sum-square method (RSM) as shown in Equation 7.4. Accoring to Moffat [121], the error obtained through this method and finally calculated by 7.4 accounts for systematic and random error.

$$\delta R = \sqrt{\sum_{i=1}^{N} \left(\frac{\partial R}{\partial X_i} \delta X_i \right)} = \sqrt{\left(\frac{\partial R}{\partial X_1} \delta X_1 \right)^2 + \left(\frac{\partial R}{\partial X_2} \delta X_2 \right)^2 + ... + \left(\frac{\partial R}{\partial X_N} \delta X_N \right)^2} \tag{7.4}$$

Table 7.1: Experimental uncertainty in Reynolds number and friction factor

Reynolds Number	10,000	30,000
Reynolds number uncertainty	3.9%	1.1%
Friction factor uncertainty	8.3%	7.2%

Since the experimental work contains to fundamentally different approaches, this chapter is divided into a dedicated discussion of the PIV uncertainties and TLC uncertainties; only the determination of flow Reynolds number was the same in both setups. Separate measurements to determine the pressure drop within the array were conducted mainly for validation purpose. During the friction factor tests, no seed particles were introduced nor was the flow heated. The total uncertainty for Reynolds number and friction factor are reported in Table 7.1 and the corresponding uncertainty trees are shown in Figure 7.1 and Figure 7.2, respectively. The main error contribution to the Reynolds number was the correct measurement of the dynamic pressure used to calculate the bulk flow

velocity. In terms of friction factor, the measurement of the row-resolved static pressure contributed the most to the total error. In both cases, the highest uncertainty was observed for the smaller Reynolds number where the static pressure differential and dynamic head was the smallest.

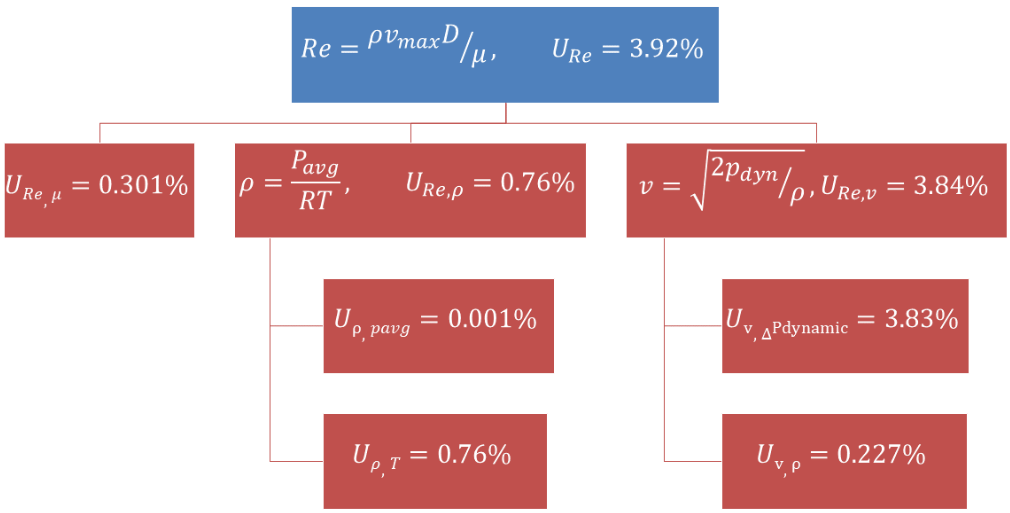

Figure 7.1: Reynolds number uncertainty for Reynolds number of 10,000

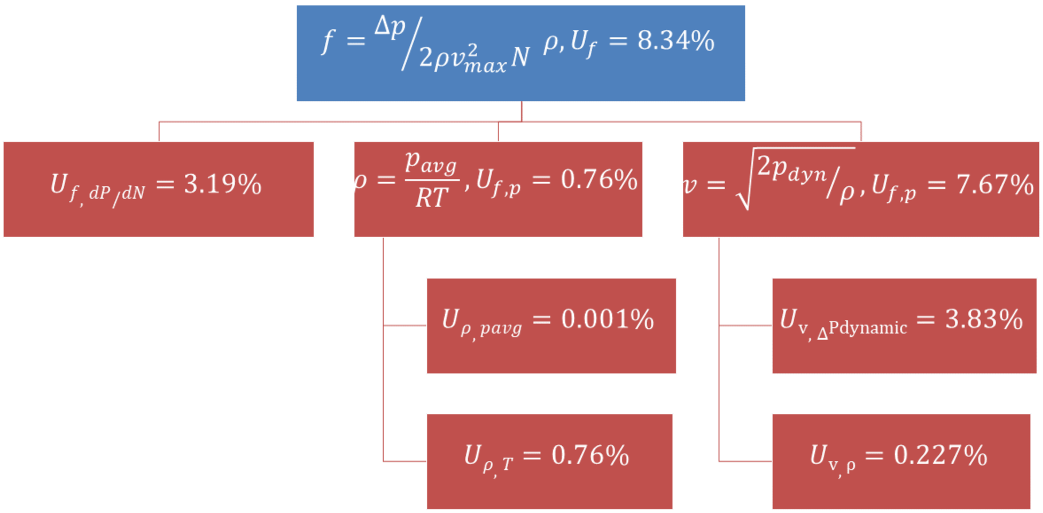

Figure 7.2: Friction factor uncertainty for Reynolds number of 10,000

PIV Uncertainty

Uncertainties in the PIV data are calculated within DaVis software, using Wieneke's Correlation Statistics method [123, 124]. These instantaneous uncertainties, are then appropriately propagated in order to estimate the statistical uncertainties on the mean quantities. The uncertainty field can be derived for the velocity magnitude and the three velocity components, respectively. The local uncertainty is then normalized by the maximum channel velocity to indicate the percentage error relative to the velocity. Maximum uncertainties in any velocity component in the wall-far regions, are below 4% of the maximum channel velocity u_{max} as used in the Reynolds number definition. The local uncertainty for both Reynolds numbers and both measurement locations downstream of row one and three are shown in Figure 7.3. The error is reported for the mid-plane section and at location 5% from the wall in the wake of the first row. The uncertainty follows the main flow

structures. In region of higher turbulence, shear layer for 10,000 Reynolds number and von Kármán vortices at 30,000 Reynolds number, the uncertainty is higher than for the bulk flow. This is due to the fluctuation of the Reynolds stresses and wake shedding so that less instantaneous image pairs are available for each state of the flow during vortex shedding and recirculation. Yet, the uncertainties in velocity magnitude are similar to what is found in comparable studies [17, 43, 125].

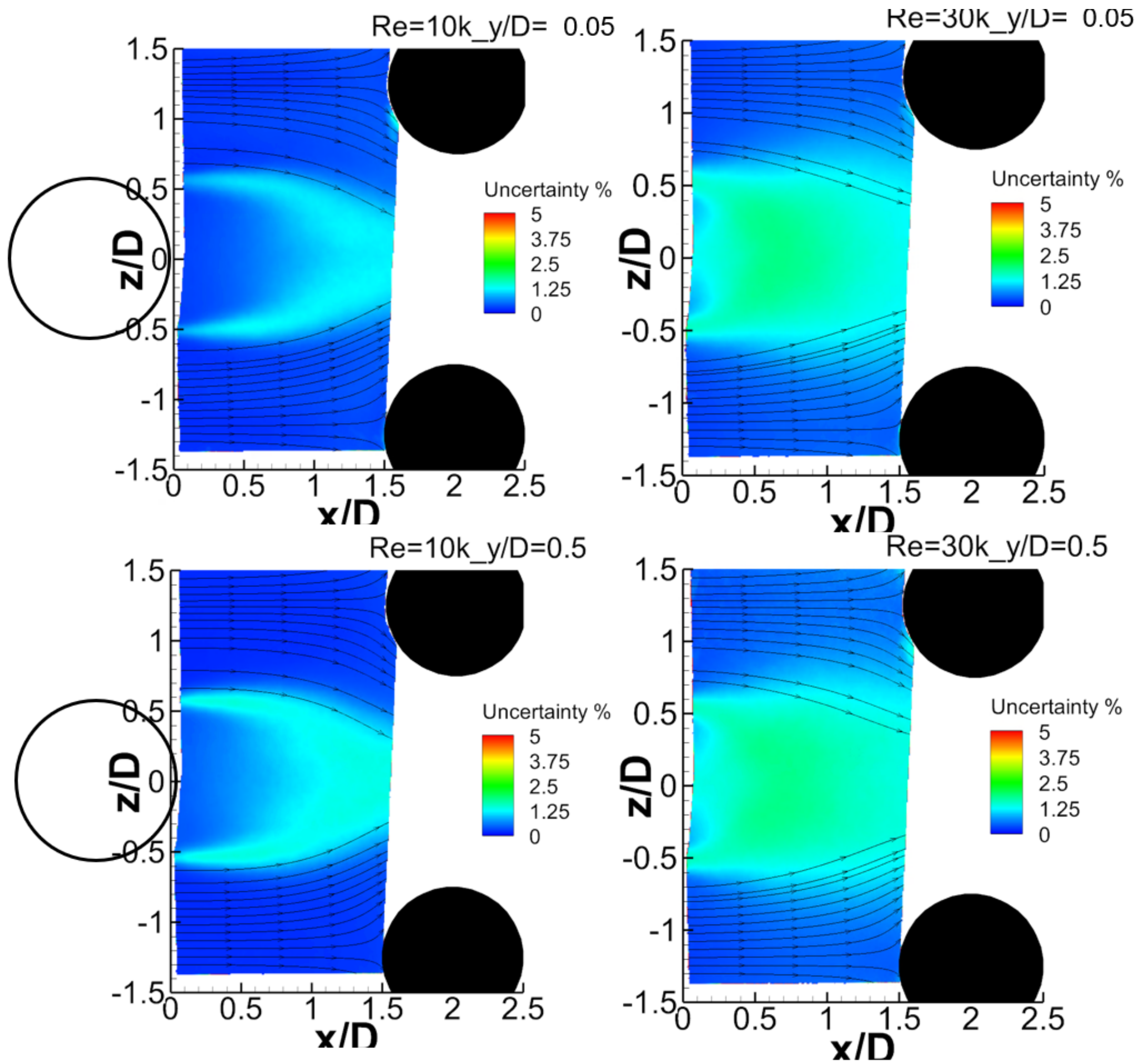

Figure 7.3: Uncertainty in velocity magnitude for Reynolds numbers of 10,000 and 30,000 in mid-plane and wall-near region in the wake of row one

TLC Uncertainty

The uncertainty estimation for the Nusselt number obtained through the transient TLC method is based on the same theoretical foundations as found in the earlier discussion. The complexity of the measurement technique and the data post-processing requires a more detailed analysis of the error sources and at the same time introduces additional potential error sources. The entire uncertainty tree for the uncertainty in array averaged Nusselt number is shown in Figure 7.4 for a Reynolds number of 10,000.

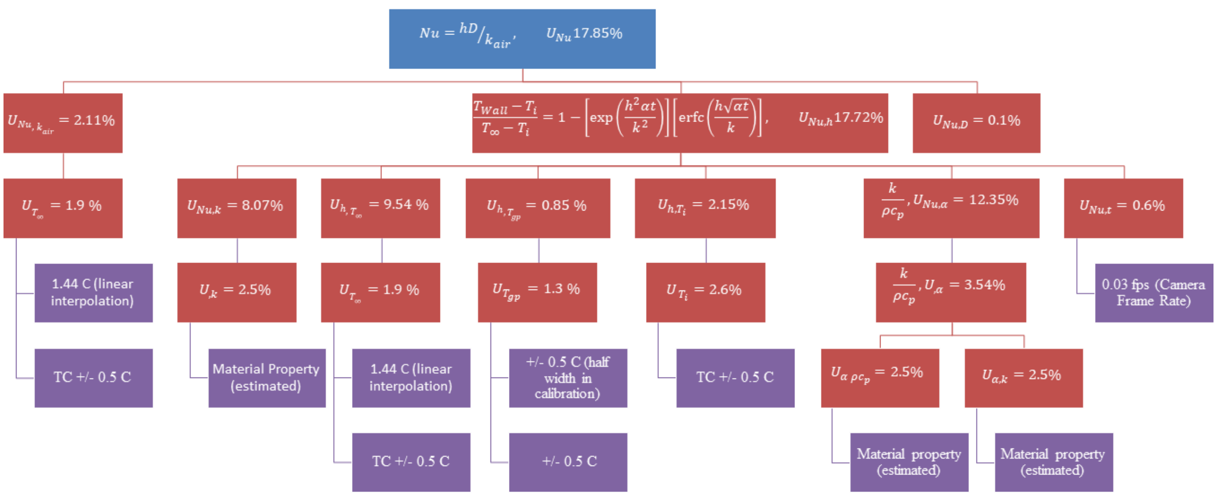

Figure 7.4: Uncertainty in Nusselt number for Reynolds numbers of 10,000 and 30,000

The total uncertainty in Nusselt number is 17.85% and 14.97% for 10,000 and 30,000, respectively. It is apparent that the main error contribution comes from the solution of the 1D conduction equation. Here, the biggest contributors the to the total uncertainty are the measurements of bulk temperature and the knowledge of the material properties of the acrylic.

It can be assumed that the total uncertainty as stated above is too ambitious. It was found that the thermal conductivity and thermal diffusivity of acrylic are main contributors to the total error. It is very challenging, however, to obtain proper material values as they are not provided by the manufacturer. The entire estimation is considered ambitious as the property variation of 2.5% for either value is a the lower end of the range. An increase in the material property uncertainty would significantly increase the total experimental uncertainty. Therefore, it is recommend at this point to conduct a thorough study of the thermal conductivity and diffusivity to obtain correct material properties.

Additionally, it was found that uncertainty in green peak temperature contributes 6% for a larger Reynolds number whereas the contribution at a Reynolds number of 10,000 is less than 1%.

Local TLC Uncertainty

One of the key statements made in the derivation of the TLC code was that the conduction into and through the substrate of the test section must be one-dimensional. This is necessary to obtain a closed form analytical solution for diffusion equation (Equation 4.28). Heat is expected to penetrate into the acrylic due to forced convection and increases the surface temperature with time. The heat further propagates through the solid indicated by the red line as shown in Figure 7.5. The region under the pin (black) is not subject to convective heat transfer hence the surface temperature under the pin does not change and remain at initial conditions. A temperature difference exists between the acrylic surrounding the pin and directly underneath it which causes lateral conduction perpendicular to the main conduction direction within the solid. This causes slower change in surface Temperature in the region around the pin. Since the time to reach a certain surface temperature is a direct input required for the local heat transfer coefficient,

the actual heat transfer coefficient is underpredicted in this region. This, however, is a systematic error that cannot be further quantified. Nonetheless, methods exists to partially mitigate this effect on the heat transfer data. The conduction equation close to the pin could be solved by using a finite volume approach with a given heat transfer coefficient. For each radial position away from the pin, the time can be determined until the fluid temperature is achieved. The resulting relationship provides a new lookup table for β with respect to the distance from the pin.

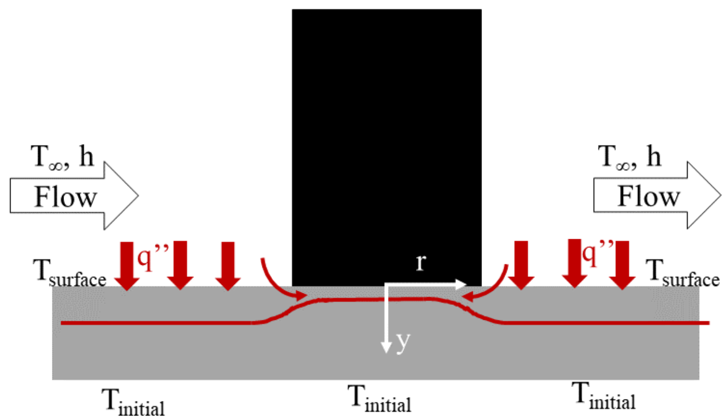

Figure 7.5: Heat Leakage under the Pin due to multi-dimensional Conduction

Yet, five data sets are available for a Reynolds number of 10,000 and 7 data sets are available for a Reynolds number of 30,000. This allows to local further into the local error distribution of the data. First, a mean μ of the data X with N data points can be calculated for every pixel using Equation 7.5.

$$\mu = \frac{1}{N}\sum_{i=1}^{N} X_i \tag{7.5}$$

Second, the standard deviation can be calculated using the newly defined mean.

$$\sigma = \sqrt{\frac{1}{N}\sum_{i=1}^{N} |X_i - \mu|^2} \tag{7.6}$$

Both calculations can be easily applied to the matrix containing the local Nusselt number distribution. Figure 7.6 and 7.7 show the spatially resolved standard deviation for the tested pin fin array. The white circular cutouts are the locations of the pins. The flow enters through the left. Additional zones between the first row of pins up stream of the second row. This region has relatively small heat transfer which results in a long heating up time for this particular area. The experiments were stopped before the green peak was reached. This sacrifice had to be made, especially in context with the heat leakage discussion before. The difference is that there is no artificial heat sink underneath the pin, but that there is a steep temperature gradient within the acrylic. With increasing experimental time, heat leaks lateral from the high heat transfer region into the low heat transfer region which reduces the accuracy of the local measurement in this area. Therefore, it was decided to omit this region which is not of significant interest anyways.

The standard variation for the 10,000 Reynolds number cases ranges between values smaller than one upstream up the first row of pins and up to 15 directly upstream of the fourth row. The majority experiences a standard variation around 5 to 8. The values found for the standard deviation for a Reynolds number of 30,000 are higher and mainly range between 8 and 15. The data set varies the least directly downstream of the pin within the wake whereas the largest deviations are observed in the regions directly adjacent to the pin and the flow encompassing the wake region.

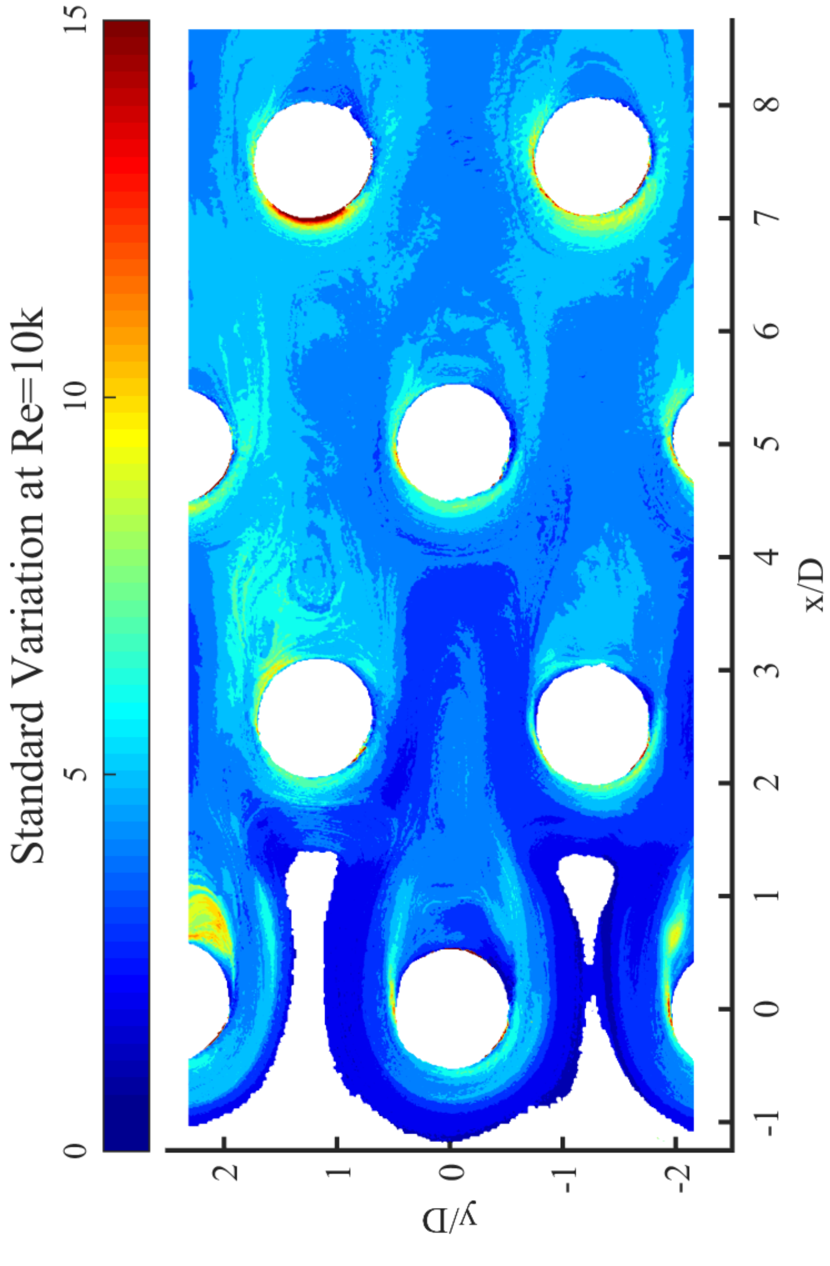

Figure 7.6: Distribution of standard deviation for $Re = 10,000$

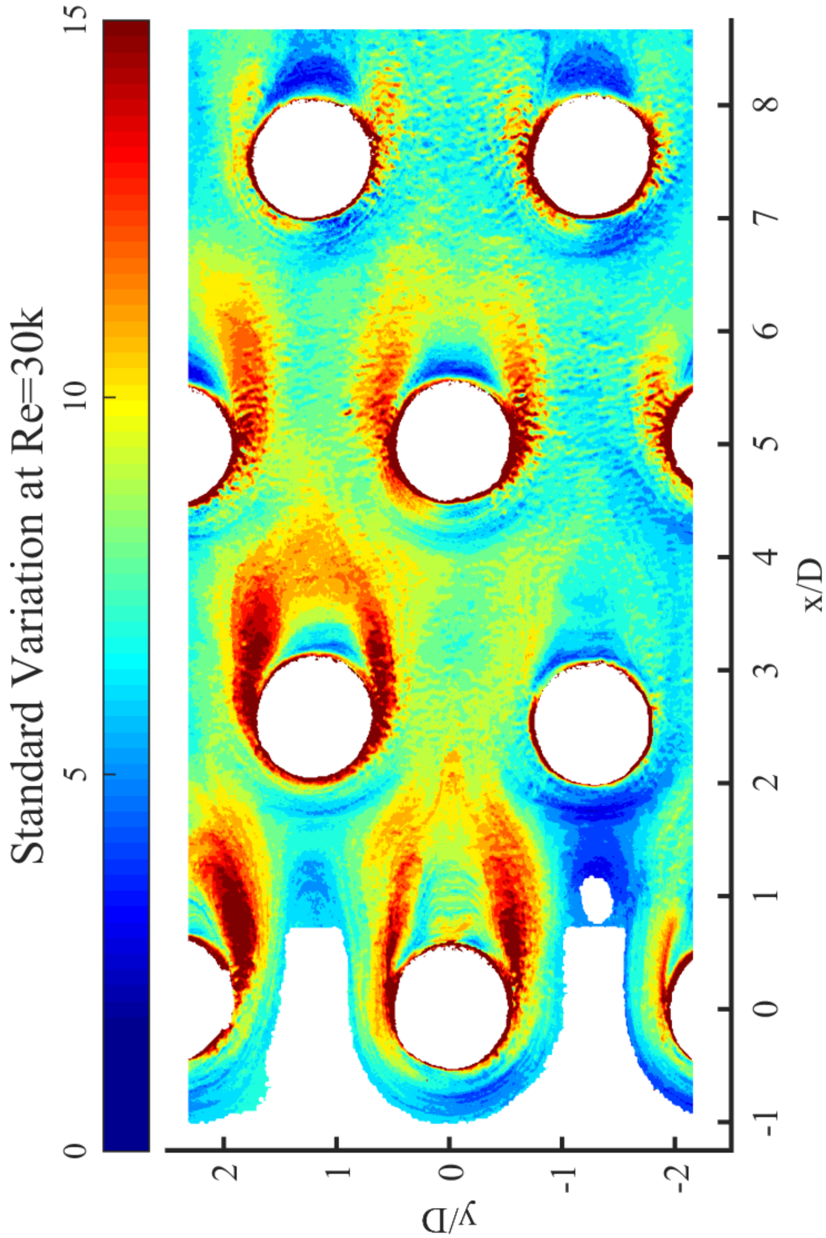

Figure 7.7: Distribution of standard deviation for $Re = 30,000$

It can be challenging to derive meaningful conclusions from the local standard deviation which is heavily dependent on the mean and the amount of available data sets. For this reason, the coefficient of variation is introduced as the ratio of standard deviation and mean. The ratio is expressed in percent.

$$\frac{\sigma}{\mu} \tag{7.7}$$

The coefficient of variation expresses the variability of the data relative to its mean value. Although the standard deviation is the same for two arbitrary points, the dispersion of the data has to be seen in context with the mean value itself. Figure 7.8 and 7.9 shows the distribution of the coefficient of variance. It can be seen that the robustness of the data for $Re = 30,000$ is higher than for $Re = 10,000$. This can be attributed to the smaller amount of data sets for the lower flow rate which were 5 compared to 7 at a higher flow rate. Generally, the variance in the available data is larger for the first two rows. Also, the regions of strong vortex structures, as it will be discussed in the results section, show increased variance of the data. The formation of the horseshoe vortex system upstream of the pin and the wake vortices are strongly dependent on the inlet boundary conditions. Slight variations there result in different vortex shapes thus different heat removal from the endwall. Further downstream, row three and four, the flow is less structured and has a higher overall turbulence. The local variance decreases with less discrete vortex structures and more general turbulence.

The local standard deviation relative to the mean is about 6 to 10 % in the region of the wake of the first row and upstream of the second row for both Reynolds numbers. The coefficient drops to levels around 5 to 6% downstream of row 3 and 4 for higher of both Reynolds numbers and to levels of 6 to 7% for the lower Reynolds number

The local distribution of error is a helpful tool to evaluate the method and allow proper judgment of the local distribution of Nusselt number. However, it is also useful from an engineering perspective to analyze the experimental error in terms of area-averaged quantities. Table 7.2 lists the Nusselt number mean values obtained for all tests. The area which was used is exactly the area after filtering. The obtained area averaged mean Nusselt numbers are 67.79 and 145.71 for 10,000 and 30,000 Reynolds number, respectively. In the case of the lower flow rates, the points range between 61.27 and 72.61 which results in a calculated standard deviation of 4.21. For the larger flow rates, the test results spread between 132.91 and 159.35 which results in a standard deviation of 10.21.

Table 7.2: Nusselt number distribution and simple statistics obtained through experiment

Test Number	1	2	3	4	5	6	7	μ	σ
$Re = 10,000$	70.03	61.27	67.62	67.41	72.61			67.79	4.21
$Re = 30,000$	137.28	139.65	159.35	156.2	149.14	132.92	138.34	145.71	10.21

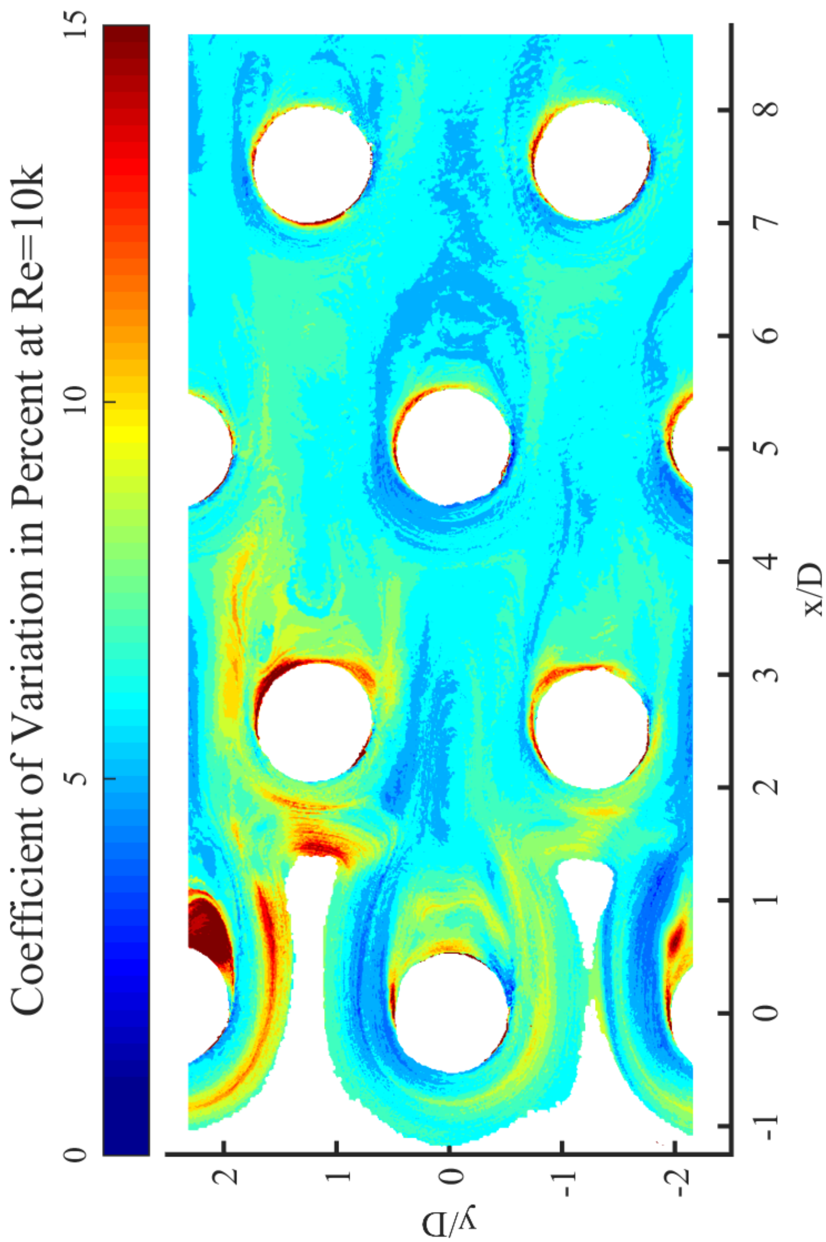

Figure 7.8: Coefficient of variation for $Re = 10,000$

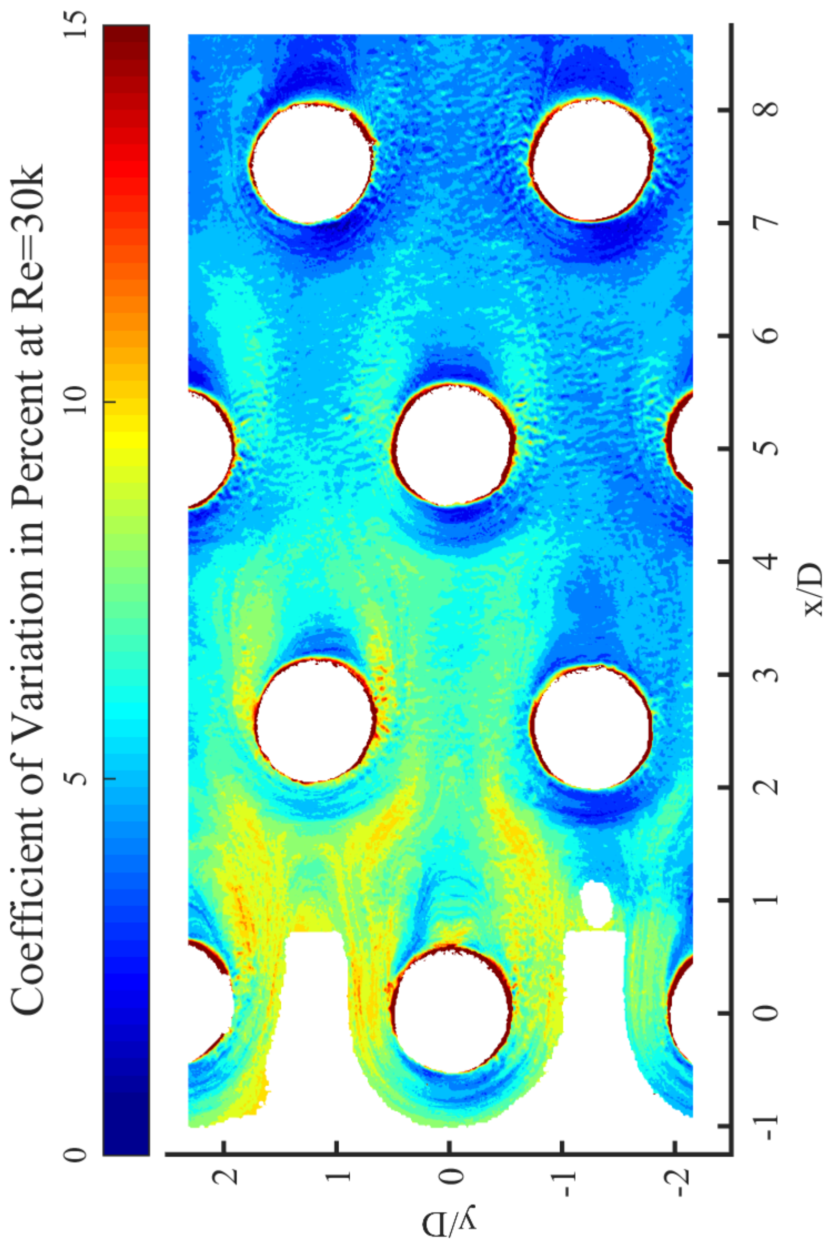

Figure 7.9: Coefficient of variation for $Re = 30,000$

CHAPTER 8: RESULTS AND DISCUSSION

The results and discussion chapter is structured into two main section. The first one is the analysis of the experimental data obtained trough PIV and TLC. The second main section is the analysis of the LES.

Validation of Experimental Apparatus

Pressure measurements and PIV velocity measurements were conducted in the described setup which consisted of four rows of staggered pin fins. The pressure drop measurements - taken on the side wall of the test section - are used to validate the experimental setup and are often presented as friction factor. The static pressure drop was measured 2.5 pin diameter upstream of the first row and 2.5 pin diameter downstream of the last row of pins. The delta in static pressure is then normalized with the density, maximum velocity, and the number of rows. This relationship was introduced in Equation 4.5.

Jacob [126] and Metzger et al. [47] reported friction factor correlations which are plotted as reference. As the experimental setup is very similar to Ames et al. [5, 32, 33, 75], an agreement between both experimental setups and CFD serves as validation of the present study with respect to the core functionality of the experimental apparatus. The experimentally measured friction factors are within range, yet smaller than what was expected based on the correlations and what was observed by Ames for a Reynolds number of 10,000 but matches well for 30,000. The reason is in the applicability of the correlations and the setup used by Ames in and in this study. Ames tested on a pin fin array with eight rows, whereas this study only consists of four rows. In the derivation

of Metzger et al. [47] it is stated that the correlation is only valid for arrays with are sufficiently long so that the flow reaches fully development.

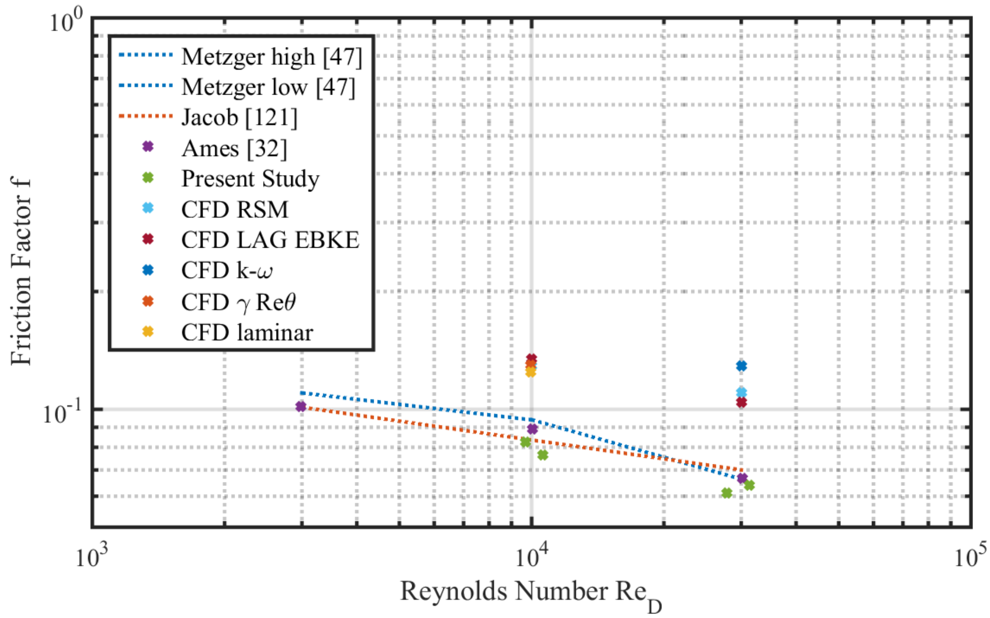

Figure 8.1: Experimental, numerical, and reference friction factors

As the flow encounters the first rows, dominant vortex structures exist and the general level of turbulence is inhomogeneous. However, the pressure recovery on the backside of the pin changes. Pin further downstream expierence higher drag compared to the pin in the first row. This phenomenon is discussed by Zdravkovich [127]. Therefore it can be assumed that the friction factor is not constant throughout the pin fin array. As this study focuses only on the first rows within the array, the viscous dissipation due to high turbulence levels is lower compared to the cases discussed by Ames [32], in particular for the lower Reynolds number of 10,000, so that a lower friction factor compared to available literature is justifiable as this pin fin array consists of only four row compared to eight or

more rows so that the contribution of different pressure drop in the developing region is stronger than for longer channels.

Interesting is that all numerical simulation, for either Reynolds number, overpredict pressure drop significantly. This is opposing to what was found by Ames et al. [33] who observed an underprediction in friction factor for their simulations. They attribute it to an overprediction in pressure recovery as simulations give a later flow separation downstream than observed in experiments. This discrepancy will be subject to the further discussion of the mismatch between RANS and experiment.

In summary, it can be stated that the channel friction factor matches for higher Reynolds numbers but is slightly lower than what is commonly reported in literature. The reasons for this is shorter pin fin array and the length of the channel affects the pressure drop. Nonetheless, the validity of the experimental setup can be attested.

Validation of TLC Method

The heat transfer section mainly consists of the analysis of the obtained heat transfer measurements obtained through transient liquid crystals; the procedure was outlined extensively at an earlier point. Although pin fin and endwall heat transfer are often reported for these kind of trailing edge channels, this study focuses on the endwall heat transfer alone. As pointed out during the review of literature, the endwall heat transfer is highly dependent on local vortex structures. The obtained TLC results will be interpreted in conjunction with the flow field analysis in the PIV section. But first, the validity of the experimental method shall be established.

Before the spatially resolved Nusselt number distribution is compared to the baseline case established by Ames et al. [5], a few more general statements regarding lessons learned and observations during the TLC experiment are presented.

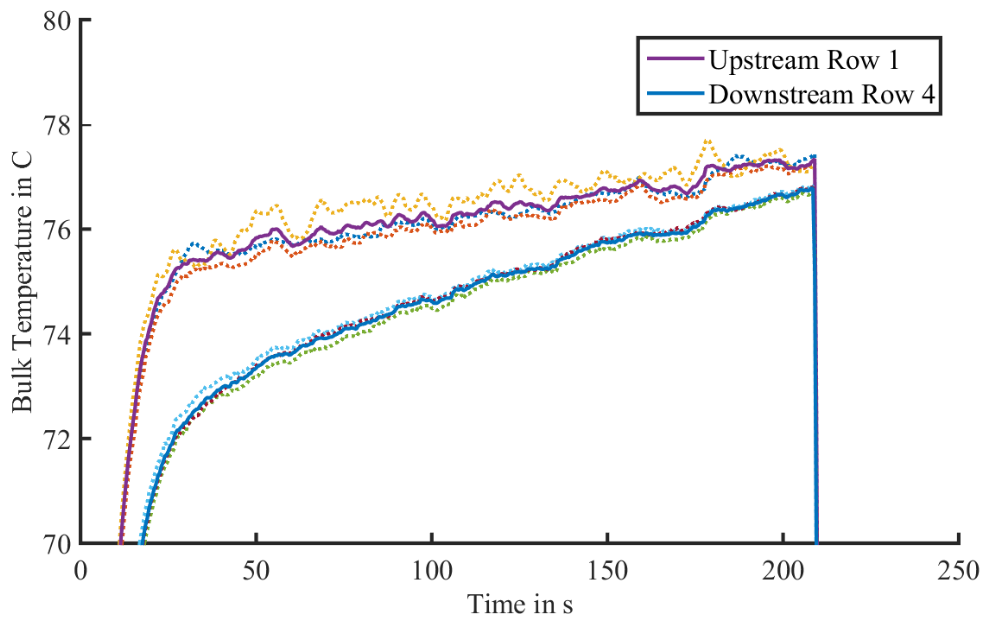

Figure 8.2: Temperature reading over time upstream and downstream of the pin array for a Reynolds number of 30,000

The temperature can vary in spanwise direction of the with of the channel. Therefore, all three TCs at one streamwise location were averaged to account for local bulk temperature variation. Such variations could be introduced through entrailed hot air within the vortices or wakes. All TCs were located in the midplane of the channel. The readings of three TCs upstream and three TCs downstream of the test array is shown in Figure 8.2. In general, decrease in temperature over the length of the pin fin array is observed. The dotted lines are the readings of the three TCs and the solid lines is the location average.

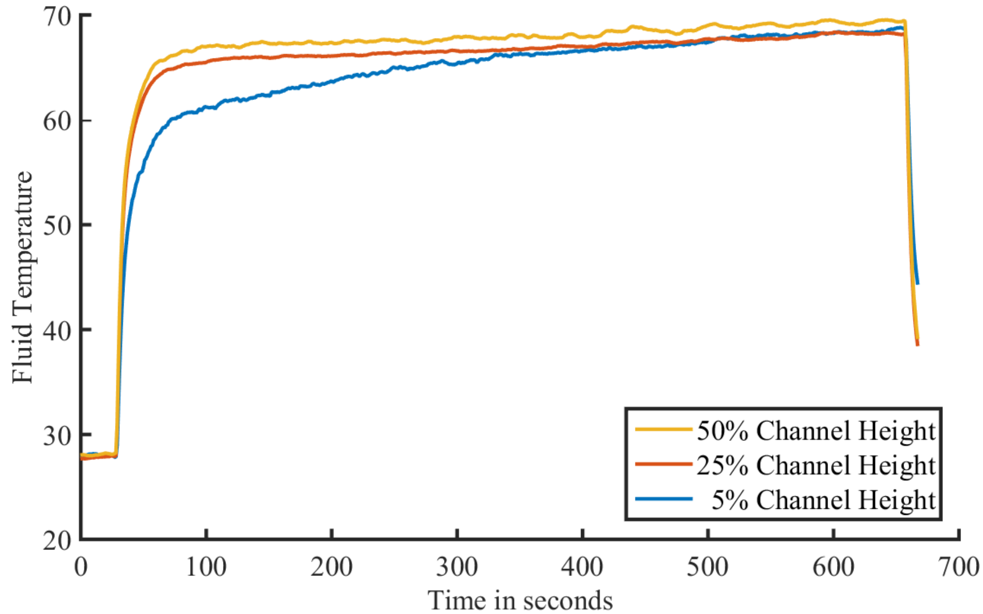

Figure 8.3: Temperature variation during experiment depending on wall distance for a Reynolds number of 10,000

It can be seen that the temperature fluctuations at the inlet are higher than downstream of the array. Also, the bulk temperature decreases through the channel. This is due to the heat absorption of the acrylic. The difference decreases as the solid becomes more and more saturated and the rate of heat storage decreases. Yet, the temperature does not reach steady conditions during the experiment and keeps increasing as long as heat is supplied. The region upstream to the pin fin array acts as a heat sink as well. The temperature as a function of channel height upstream of the first row is shown in Figure 8.3. It can be seen that there is a different in the bulk temperature. The fluid closer to the wall is colder as it looses heat to the wall. As the wall becomes warmer, it looses less heat relatively and approaches the temperature in the middle of the channel.

The definition of Reynolds number for the heated test cases is not straight forward and needs further clarification. As the bulk fluid temperature changes, its density and ve-

locity changes - both parameters used to calculate the pin-based Reynolds number. The effect of this temperature change is shown in Figure 8.4. The inlet and exit temperature increase with time, in turn, the Reynolds number drops by almost 20%. After a short time though, the Reynolds number at the inlet steadies out as the temperature barely changes anymore. This steady Reynolds number will be taken as reference for the further discussion. Nonetheless, in consequence of this observation, it has to be stated that the early flow rate through the test section is up to 20% higher than intended. This can cause an exaggeration of heat transfer and adds to the uncertainty of the experiment. The only way to mitigate that is a different experimental setup where the hot flow is already established and gets diverted into the test section. Through this method, the temperature step length is minimized.

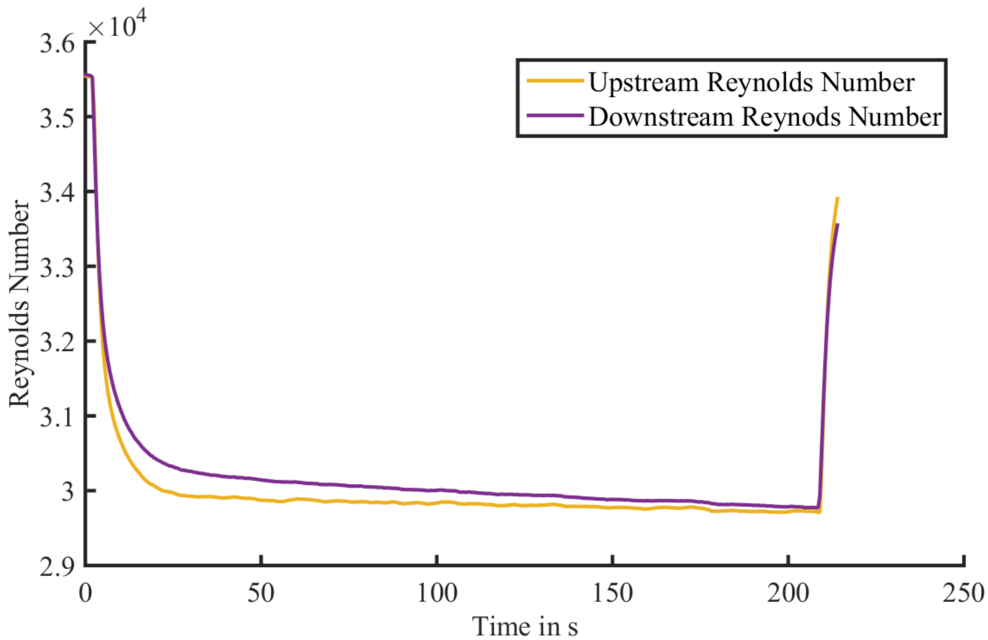

Figure 8.4: Temperature variation during experiment depending on wall distance for a Reynolds number of 30,000

Validation of Nusselt Number Results

As the reference data by Ames et al. [5] served as a baseline reference case for the general validation of the experimental setup, their endwall Nusselt number distribution will be used to determine the validity of the TLC method which was used in this study. The array-averaged Nusselt number for this test and for the Ames reference case are shown in Table 8.1. It can be seen the Nusselt numbers in this study are higher than what was previously reported by Ames et al. [5]. The array average for a Reynolds number of 10,000 is 25% higher than what is reported as reference and the average for 30,000 is 30% higher. This is still without range of the experimental uncertainty which was established at an earlier stage. At this point, however, it shall be noted at this point that the array averaged Nusselt number from 1.25 diameter upstream of row one up to 1.25 diameter downstream of row 4 has the masked section as the local Nusselt number at these regions were out of the capabilities of the TLC method as they were too small. This area contributes to the overall heat transfer with relatively low local Nussel numbers. Through the omittance of those, the array average Nusselt number is large than it theoretically is.

Table 8.1: Array-averaged Nusselt number in comparison with literature

Case	Present Study	Ames et al. [5]
$Re = 10,000$	67.79 ± 8.42	54.1
$Re = 30,000$	145.71 ± 20.21	111.5

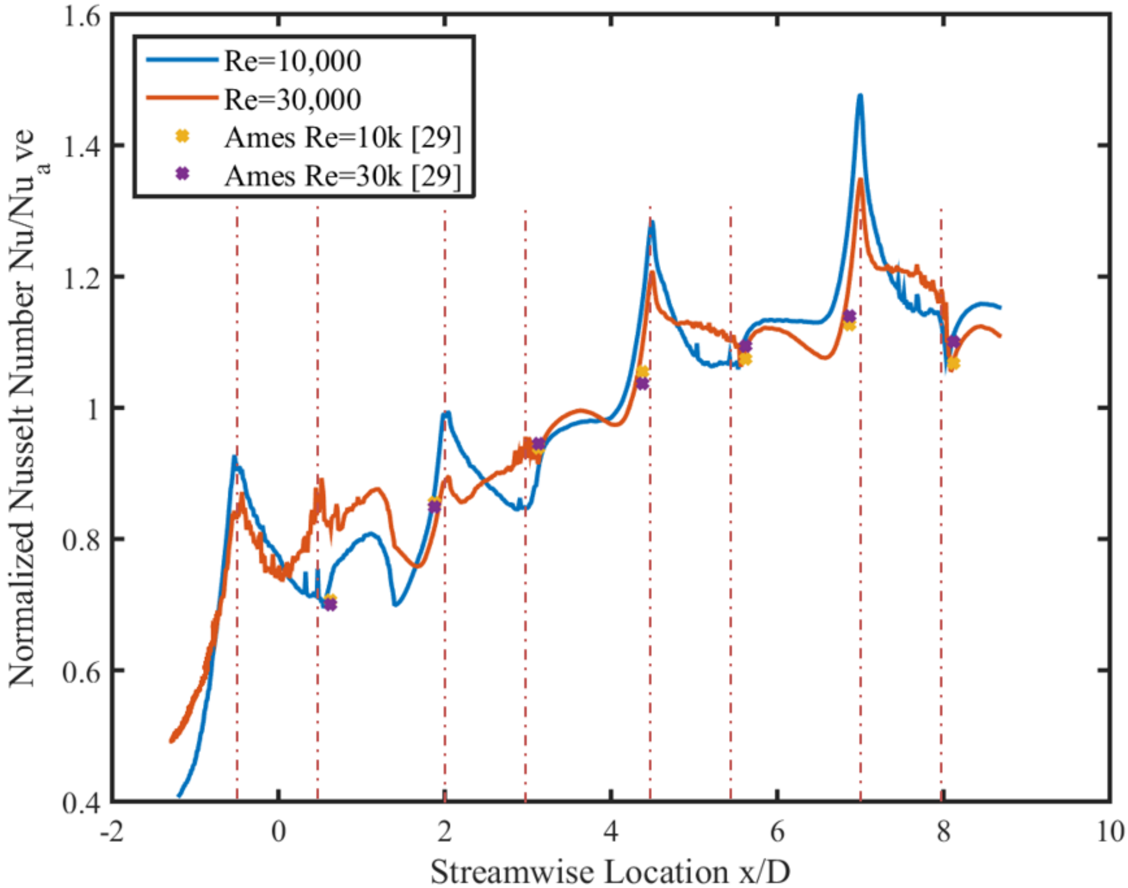

Figure 8.5: Spanwise Nusselt number augmentation

As the overall array Nusselt number appears to be insufficient to validate the TLC method, the spanwise averages shall be investigated. The spanwise average is the average Nusselt number over the span at a given streamwise location. The spanswise average is normalized with its respective array average. The current study and the baseline case show good agreement and follow the expected physics of heat transfer. It is apparent from Figure 8.5 that the data points for 10,000 Reynolds number and 30,000 Reynolds number reported by Ames et al. [5] line up at six out of seven locations. The only discrepancy that is observed is the Nusselt number augmentation in the wake of the first row

where the heat transfer augmentation is 15% higher than the reference case and the lower Reynolds number experimental case.

The detailed spatial distribution of heat transfer augmentation results normalized by the average Nusselt number reported by Ames (instead of the array average obtained in this study) can be found in the Appendix in Figures A.1 and A.2 for comparison.

In conclusion, it can be stated that there is a disagreement between experimental data and baseline case by 25-30%. However, the spanwise-averaged Nusselt number augmentation lines up fairly accurate between the current study and available data in literature. Therefore, it can be concluded that statements about the magnitude might be pushing the limits of the experimental uncertainty, yet, the local distribution of the Nusselt number augmentation can be treated as valid and reflects the behaviors found in reliable literature.

The Nature of Endwall Heat Transfer in Staggered Pin Fin Arrays

The beauty of the TLC method compared to for example copper block experiments is the local Nusselt number distribution as output. Studying the local Nusselt number distribution over then endwall of a pin fin array reveals valuable information about the cooling performance with respect to the pin location. Through the aforementioned method, the local Nusselt number distribution was obtained for two Reynolds numbers of 10,000 and 30,000. It is common to express the local data as a ratio of local Nusselt number and the array averaged Nusselt number. The resulting quantity is referred to as Nusselt number augmentation. The local heat transfer in areas with an augmentation smaller than one is below the array average and vice versa.

It was stated during the experimental validation with respect to Figure 8.5 which shows the spanwise Nusselt number distribution along the channel, that the observed

trends match the expectations fueled by physics. Upstream of the first row of pins, the pin position is indicated by the red dashed line, the heat transfer increases from very low values (basically Nusselt number of a flow through a rectangular smooth channel) to a local maximum directly upstream of the pin. This is the effect of the horseshoe vortex that forms at the leading edge of the pin. The horseshoe vortex wraps around the pin and looses its intensity, therefore the spanwise heat transfer distribution decreases in the region of the first row pin. Heat transfer reaches a local maximum one pin diameter downstream from the rear edge of the pin. Here, the von Kármán collide that are shed from either side of the pin and cause a highly turbulent mixing zone with high heat transfer. Further downstream, the heat transfer enhancement decreases again as the mixing zone is confined by the bulk flow that accelerates already as it encounters the the blockage of the second pin fin row. The encountered local minimum and maximum in heat transfer in the wake of the pin is also borne in the data by Ames et al. [5] and Chyu et al. [29].

This region is immediately followed by the second row of pins. Here, a high heat transfer zone is found again at the leading edge of the pin due to the forming horseshoe vortex system. The heat transfer augmentation due to this vortex system is higher for a 10,000 Reynolds number. That indicates a stronger relative vortex system. However, this vortex system decays at a faster rate for the lower flow rate seen by the drop of Nusselt number adjacent two the pin. Further downstream, the wake in the second row is much larger for 10,000 Reynolds number so that the spanwise average encounters a minimum. This is not seen for the higher flow rate where the Nusselt number augmentation increases slightly but steadily downstream of the second pin. The question is why both trends show different behaviors. It is expected that the analysis of the wake physics will shed light on this observation and provide further understanding of this local endwall heat transfer.

Downstream of pin two and upstream of pin three, the Nusselt number distributions follow the trend outlined for the first two rows but at a much higher level. The heat transfer augmentation of the horseshoe vortex upstream of row three is comparable to the effect found in row three, however, the augmentation for row four spikes. The heat transfer adjacent to the pin at a lower Reynolds number shows less of a minimum downstream of row three which indicates a shorter wake region. The maximum Nusselt numbers in the entire array are found directly upstream of row four followed by a steep drop in the region between the pins of row four. The wake length of row four is even shorter compared to the previous rows, in particular for the lower flow rate. A drop in Nusselt number can be observed in the wake region directly adjacent to the backside of the pin. The von Kármán vortices collide about half a pin diameter downstream and cause a local peak in heat transfer. At this point, the flow becomes more and more developed before it eventually reaches fully development around row five to six which manifests in repeating trends found in the spanwise Nusselt number distribution. However, these rows were not subject in the present study and no spatially resolved Nusselt number trends are available after one pin diameter downstream of row four.

Obviously, besides averaged values, the entire space of the test domain is associated with a corresponding Nusselt number augmentation value. The augmentation is shown in Figure 8.7 for $Re = 10,000$ and Figure 8.8 for $Re = 30,000$, respectively. The images are rotated to take maximum advantage of the paper aspect ratio. The images were taken in full HD with a resolution of 1080x1920, exceeding the image quality and details of all previous studies. Again, a filter mask - as discussed at a previous point - was applied to the data, blocking regions of low heat transfer upstream of the first row. It can also be seen that the region of low heat transfer penetrates almost up to the second pin. The incoming flow is very structured and only locally affected by the first row pin. An increased area of high heat transfer is seen directly upstream of the pin. This is attributed

to the horseshoe vortex system that forms upstream of the pin and removes heat locally. The horseshoe vortex wraps around the pin and also removes heat directly adjacent to the pin as seen for both Reynolds numbers. A low heat transfer region is found directly in the wake downstream of the pin. Here, the flow velocity is generally very low thus small wall shear stress to remove heat from the endwall. It can be seen that the wake region is more dominant for a lower Reynolds number than for a higher Reynolds number. KVs are shed periodically from the pin resulting in a vortex street. These vortices increase the local heat transfer downstream of the wake. The vortices are stronger for a higher Reynolds number seen as the spreading of the higher heat transfer region at the streamwise location of approximately 1.

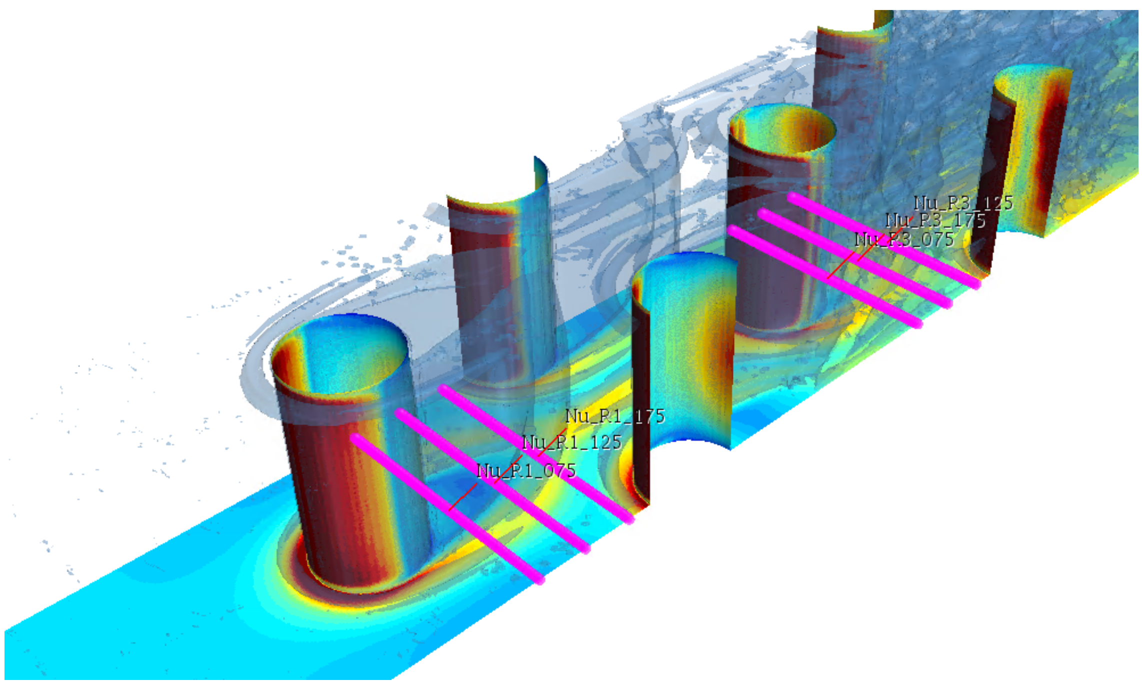

Figure 8.6: Local Nusselt number augmentation and vortical structures in a pin fin array obtained through CFD including probe locations highlighted in purple

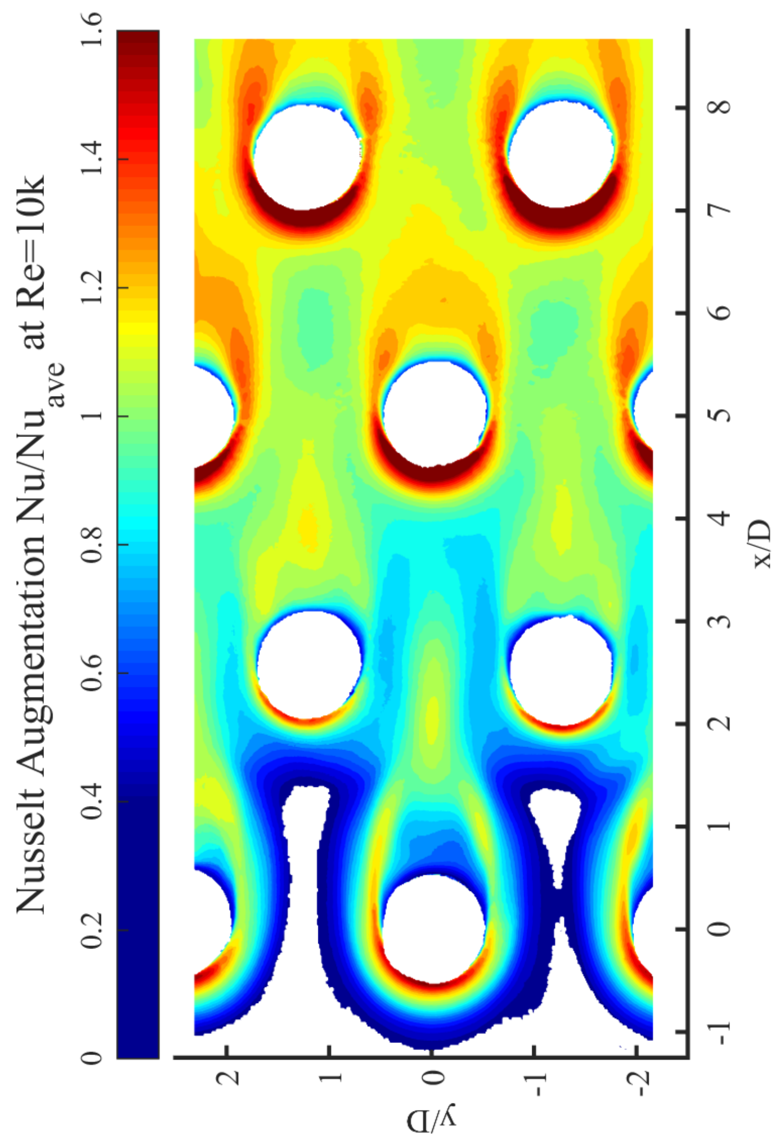

Figure 8.7: Local Nusselt number augmentation normalized with array Nusselt number average of $Nu_{ave} = 67.79$ at $Re = 10,000$

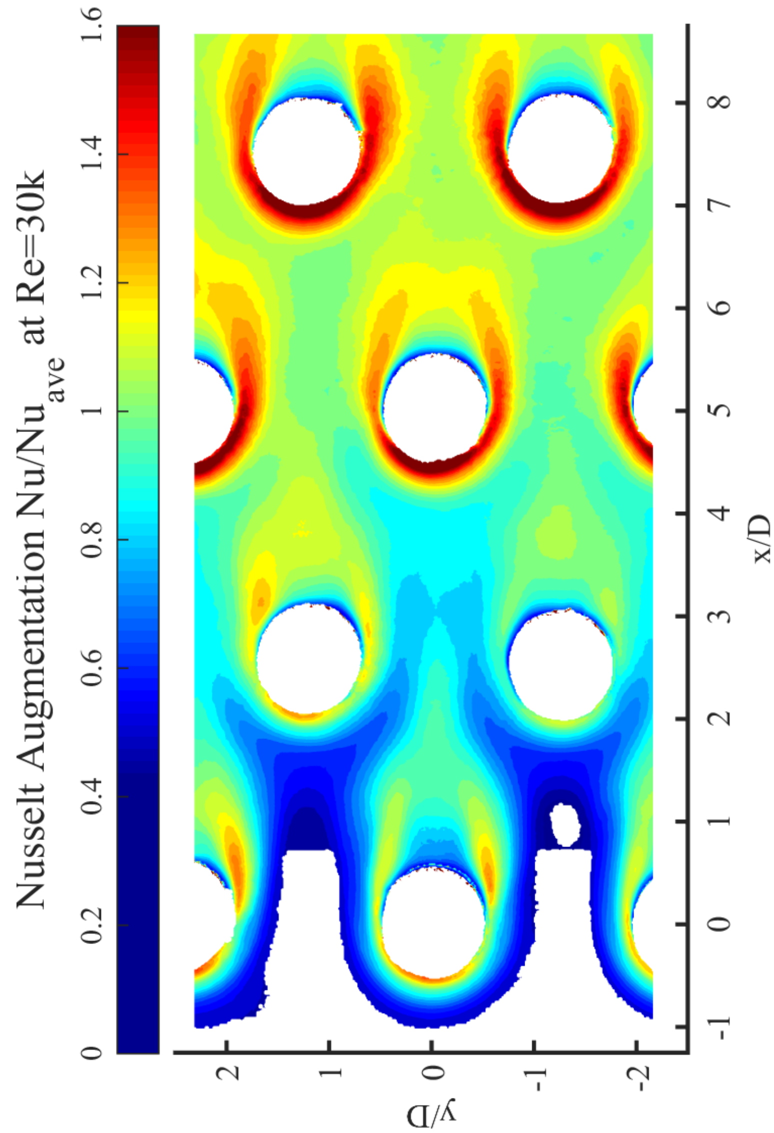

Figure 8.8: Local Nusselt number augmentation normalized with array Nusselt number of $Nu_{ave} = 145.71$ at $Re = 30,000$

The leading edge of the second row is a streamwise location of 2. The fluid encounters the pin and is deflected due to the blockage. The fluid experiences a local acceleration since the effect flow area is reduced. This effect *squeezes* the KV together and prevent them from further traveling downstream. The wake of the pins in the second row is significantly shorter than the pin in the first row which means that the low heat transfer region is smaller. Generally, the endwall heat transfer is higher than in the first row due to increased of overall turbulence levels.

The horseshoe vortex system that forms at the junction of the pin and the endwall in the third and fourth row becomes more dominant, in magnitude as well as size. A larger region upstream of the pin itself is cooled better. In the case of the lower Reynolds number, the region adjacent to the pin that is cooled is more discrete and narrower than the higher Reynolds number. As the channel turbulence levels further increase, the endwall cooling on the leading edge of the pin becomes stronger as well as the region next to it. The *legs* of the vortex system now spread wider and propagate further down stream. It is not shown here but extensively reported in literature [18, 44, 47] that the flow now becomes fully developed and and the endwall heat transfer pattern becomes periodic.

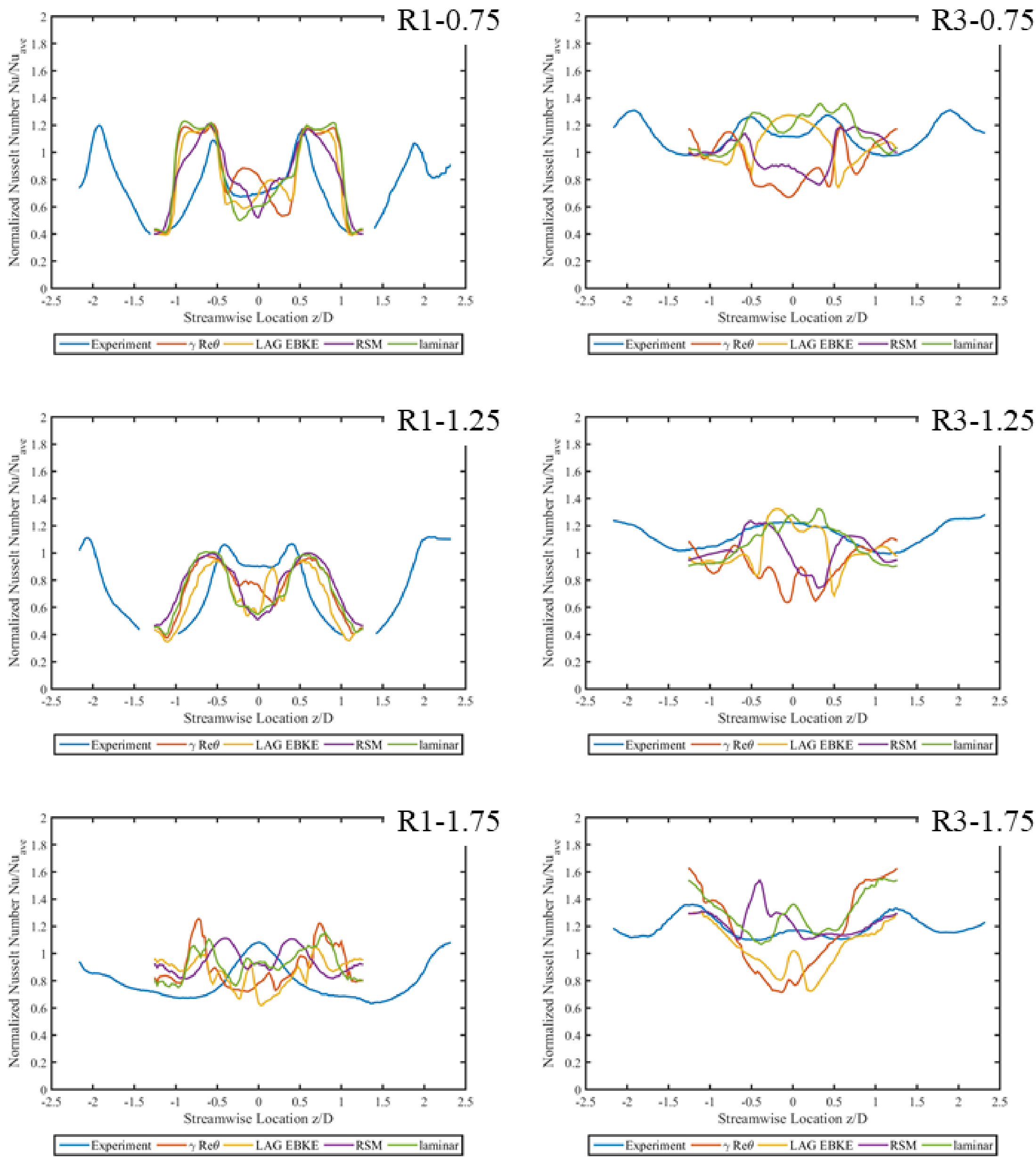

Figure 8.9: Spanwise Nusselt number augmentation at various streamwise locations normalized with array Nusselt number of $Nu_{ave} = 67.79$ at $Re = 10,000$

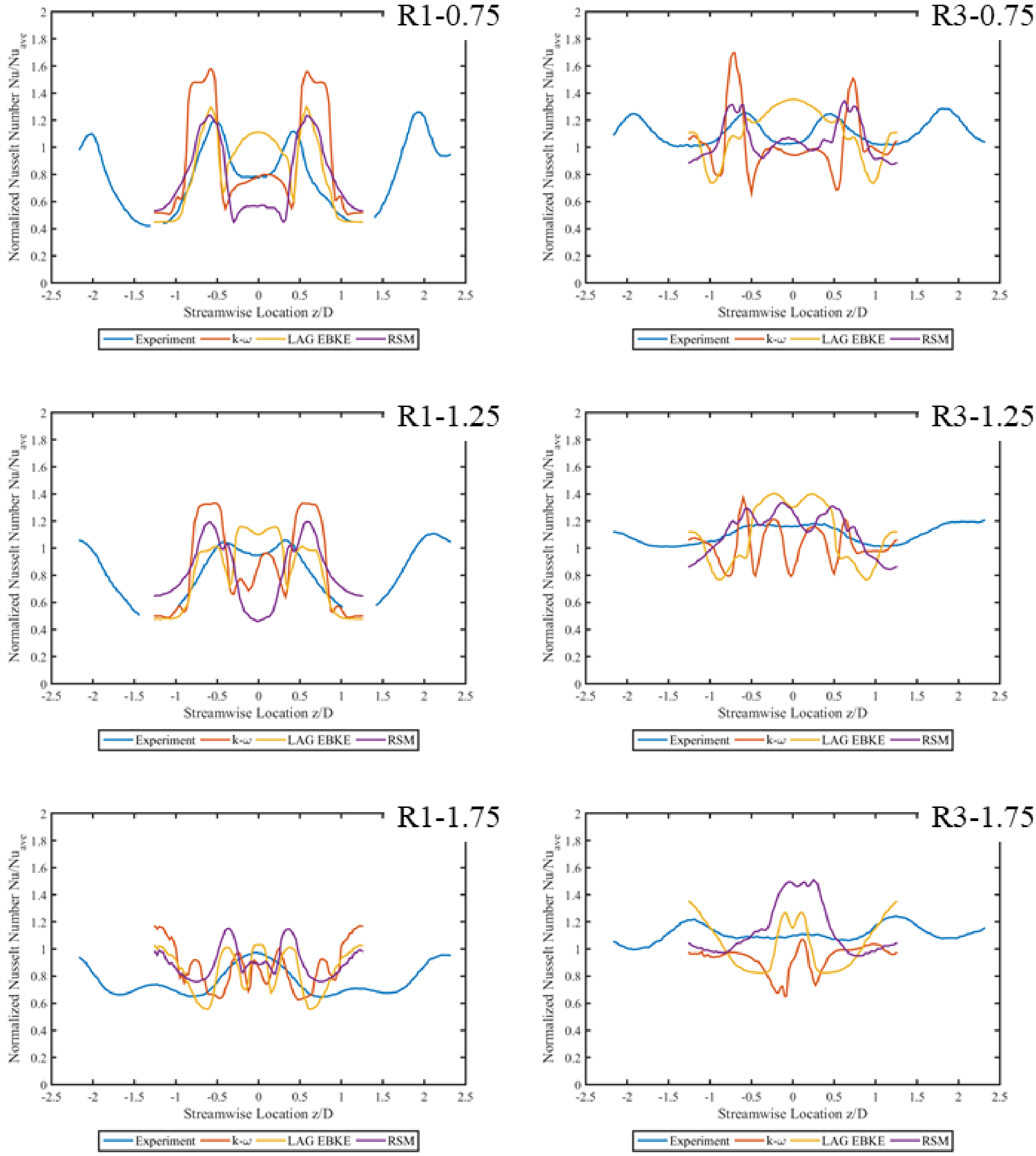

Figure 8.10: Spanwise Nusselt number augmentation at various streamwise locations normalized with array Nusselt number of $Nu_{ave} = 145.71$ at $Re = 30,000$

The trend outlined by analyzing the local Nussel number augmentation is visible in the spanwise Nusselt number augmentation plot in Figure 8.5. As a reminder, the location of the pins are at streamwise positions of 0, 2.5, 5, and 7.5 and stretch half a diameter before and after these locations. The heat transfer rises steeply from the low heat transfer region upstream of the first row of pins. As the flow encounters, the heat transfer spikes due to the horseshoe vortex and the spanwise average drops towards the wake region. Here it is noteworthy that the drop is stronger for the lower Reynolds number. This is consistent for all rows. The leading edge spike is larger, but the drop in the wake is stronger. The 30,000 Reynolds number case shows a more balanced behavior compared to the lower flow rate case. As described earlier, the heat transfer augmentation increases as the flow moves further down the channel.

Additional interesting facts are borne in Figures 8.9 and 8.10 which show the probing of Nusselt number augmentation on the endwall at distinct streamwise locations over the span of the channel as outlined in the experimental setup. For a better understanding, the probing locations relative to the pins are shown in Figure 8.6. Location 1 is 0.75 diameter downstream of the center of the row 1 pin, Location 2 is 1.25 diameter downstream, and Location 3 1.75 diameter. Locations 4 through 6 have the same downstream distance, but from row 3. The pin is located at an spanwise location of 0 and stretches half a diameter to either side.

The blue line in all plots is the experimentally obtained Nusselt number augmentation. In case of $Re = 10,000$ all numerical models overpredict heat transfer directly downstream of row one. In addition, the lateral spreading of the augmented heat transfer region is also overpredicted whereas the heat transfer is underpredicted in the wake of the pin. Further downstream, directly between row one and two, the numerical prediction matches the heat transfer magnitude, but the affected area is spread even further, a trend not born in the experimental results. The experiment shows heat transfer close

to unity directly in the wake, but CFD predicts a low heat transfer region in the wake. The heat transfer profile upstream of the second row also overpredicts the effect of the horseshoe vortex legs left and right of the pin and underpredicts the heat transfer in the wake.

The spanwise behavior of the Nusselt number downstream of the third row shows differences between the turbulence models. Interestingly, the laminar flow model produces the best results in terms of Nusselt number augmentation. The other models show a much more fluctuating distribution over the width of the channel compared to the relatively smooth experimental data.

The observed trends for the 10,000 Reynolds number persist for the higher Reynolds number of 30,000. Directly downstream of row one, all three investigated models fail to predict magnitude and lateral spreading of the highly cooled area and predict a unreasonably low heat transfer in the direct wake region. The same is found for the spanwise Nusselt number distribution at the next two locations between row one and three. The simulated shaped of endwall heat transfer shows many more distinct features and fluctuations than what is observed in experiment. Likewise the behavior between row three and four. The numerical predictions show much higher fluctuations - which can be attributed to specific flow patterns - then what was observed in the experiment.

The contour plots for the local Nusselt numbers obtained through CFD and experiment are shown in Figures 8.11 and 8.12 where each case is averaged by its own respective array Nusselt number. The differences are striking even after the discussion of spanwise probed locations.

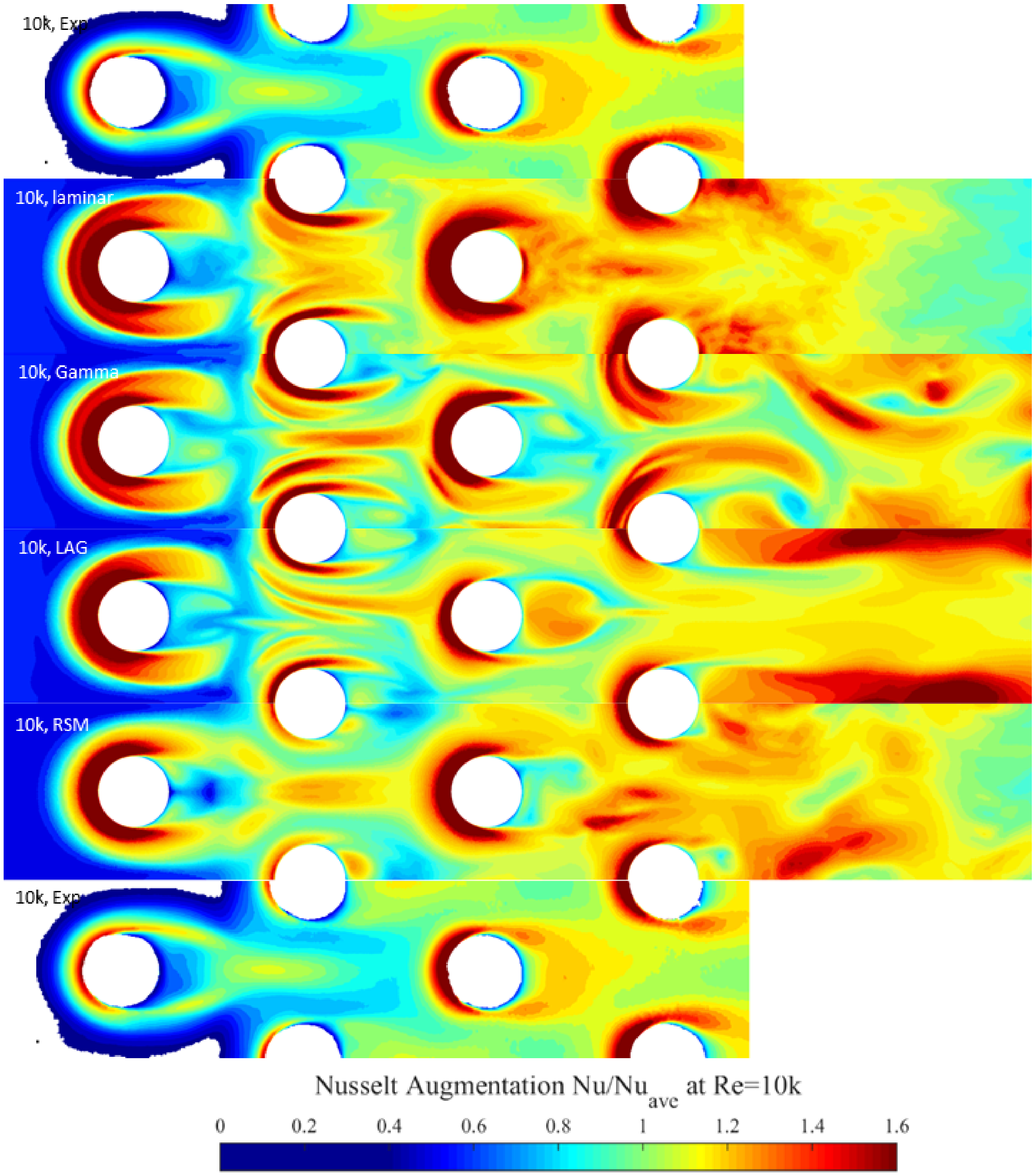

Figure 8.11: Overview of experimentally and numerically obtained endwall Nusselt number normalized with the respective array Nusselt number averages at $Re = 10,000$

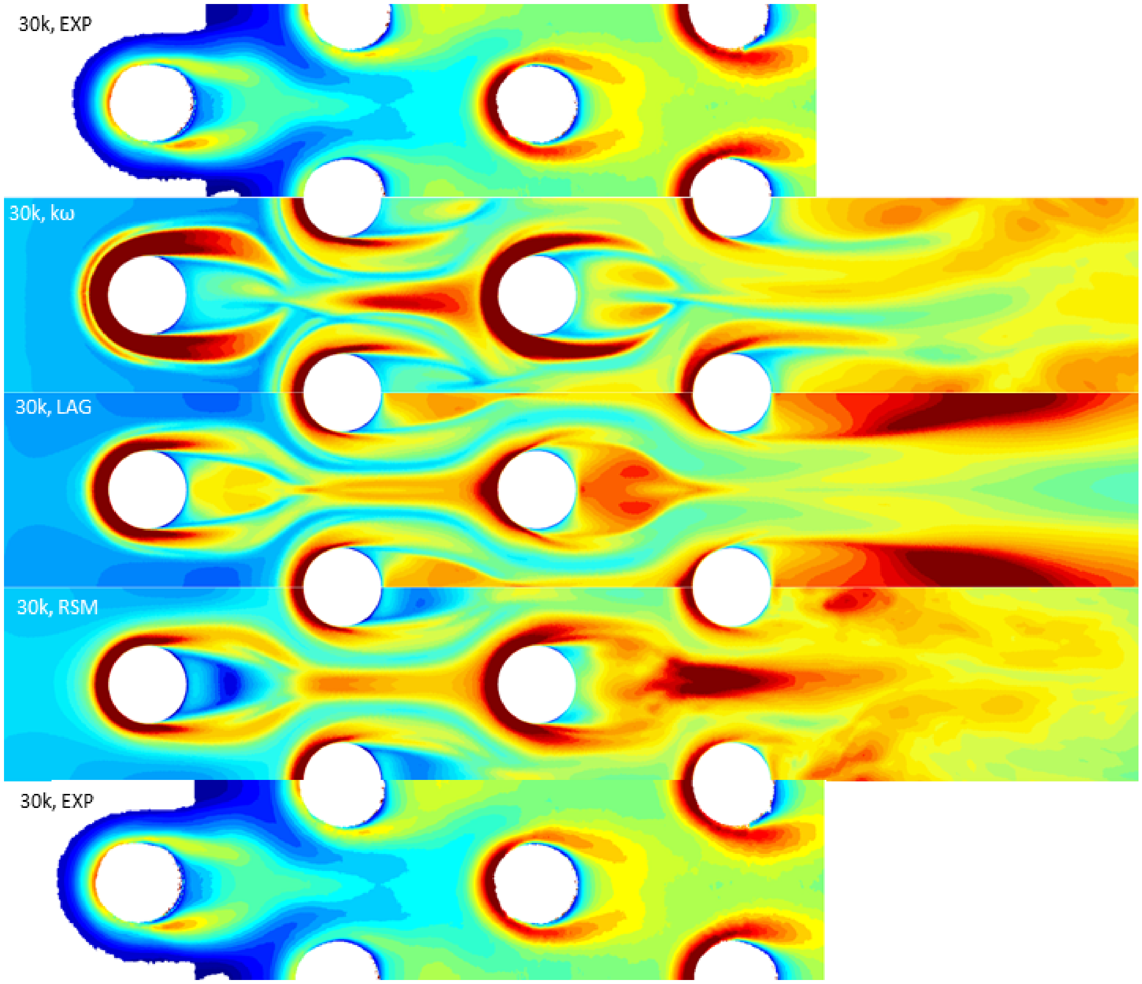

Figure 8.12: Overview of experimentally and numerically obtained endwall Nusselt number normalized with the respective array Nusselt number averages at $Re = 30,000$

First of all, all turbulence models show strongly different results for either Reynolds number case. For a Reynolds number of 10,000, all simulations have an exaggerated horseshoe vortex cooling zone upstream of the pin in the first row. Not only the Nusselt number magnitude exceeds the experimental data, the entire footprint of the vortex system is significantly larger than what was found experimentally. This error propagates downstream as the HSV wraps around the pin. Due to the artificial strength of the system, the vortices do not dissipate as quickly as in the experimental environment. The strong vortices narrow the channel that is available for the fluid as it approaches the second row of pins. Consequently, the fluid approaches with a higher velocity as expected. This will be shown in the next chapter by comparing the numerical results with the velocity contours obtained through PIV.

The wrong flow field structures passing through row one and two as well as the wrong turbulent structures cause again an exaggeration of magnitude and size of the high heat transfer region in row three. This, in turn, causes again the legs of the horseshoe vortex system to extend further downstream. Also, the wake length in all numerical cases is elongated.

Table 8.2: Detailed comparison of CFD results with literature

Case	Nu_{ave}	Nu Pin 1	Nu Pin 2	Nu Pin 3	Nu Pin 4	f
			$Re = 10,000$			
Ames et al. [5]	43.4	51	64	79	83	0.89
laminar	30.5	48.74	52.2	57.17	55.53	0.1244
$\gamma - Re\theta$	31.59	54.84	56.3	58.21	55.3	0.1298
RSM	33.5	57.3	57.8	61.93	60.25	0.129
LAG EBKE	32.99	54.83	60.3	65.51	62.4	0.1343
			$Re = 30,000$			
Ames et al. [5]	88.7	104	132	163	171	0.067
k-ω	67.9	93.1	103.6	116.1	107.7	0.129
RSM	77.8	101.2	110.1	137.54	127	0.11
LAG EBKE	81	108.65	120.76	152	159.34	0.1044

In summary, it is established that there is strong discrepancy in the predictions of Nusselt number augmentation on the endwall observed in experiment and CFD. However, not statements have been made about the general performance of the CFD models with respect to average engineering quantities such as averaged pin Nusselt number, averaged endwall Nusselt number, and friction factor. The exact values are listed in Table 8.2. The key take-away is that the pressure drop is overpredicted by every single configuration - up two a factor of two. All array averaged Nusselt numbers are underpredicted. The performance in estimating heat transfer on pins is twofold: All models capture the heat transfer correctly within 10% for a Reynolds number of 10,000 and within 5% for a Reynolds number of 30,000. However, the performance for the subsequent rows is inferior where all models underpredict pin Nusselt numbers. The models fail to pick up the pin heat transfer in particular in rows 2 and 3. Here, the heat transfer is highly impacted by the flow structure caused by the first row.

At this point the question has to be asked why are the behaviors of heat transfer so different. It seems that the flow structures found in *real world* are very different than what

RANS models predict. Therefore, the flow field will be analyzed and direct comparisons made between RANS and PIV results.

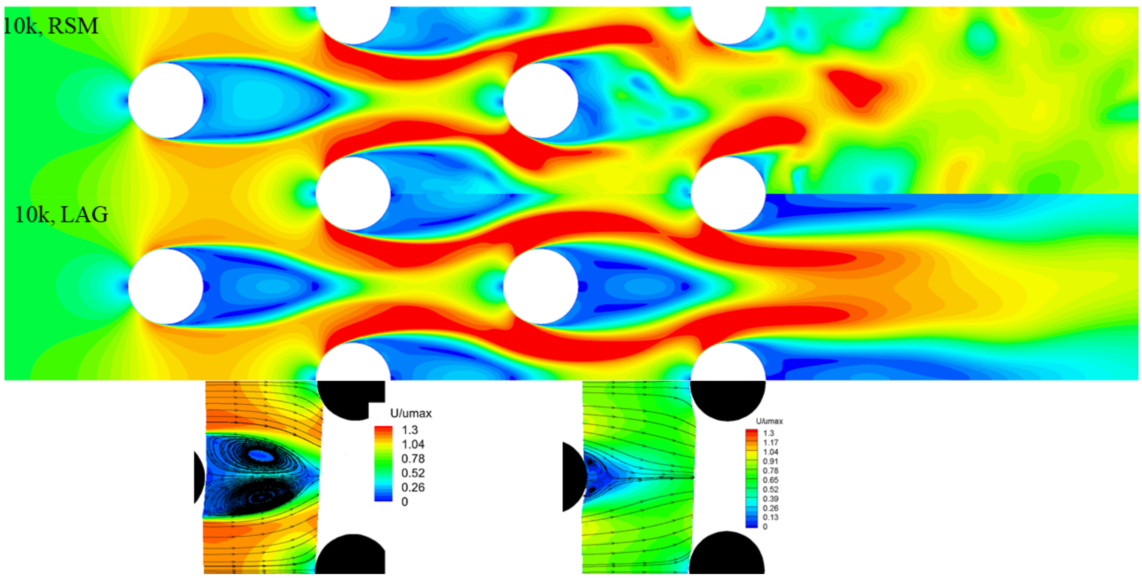

Figure 8.13: Normalized velocity magnitudes for 10,000 Reynolds number

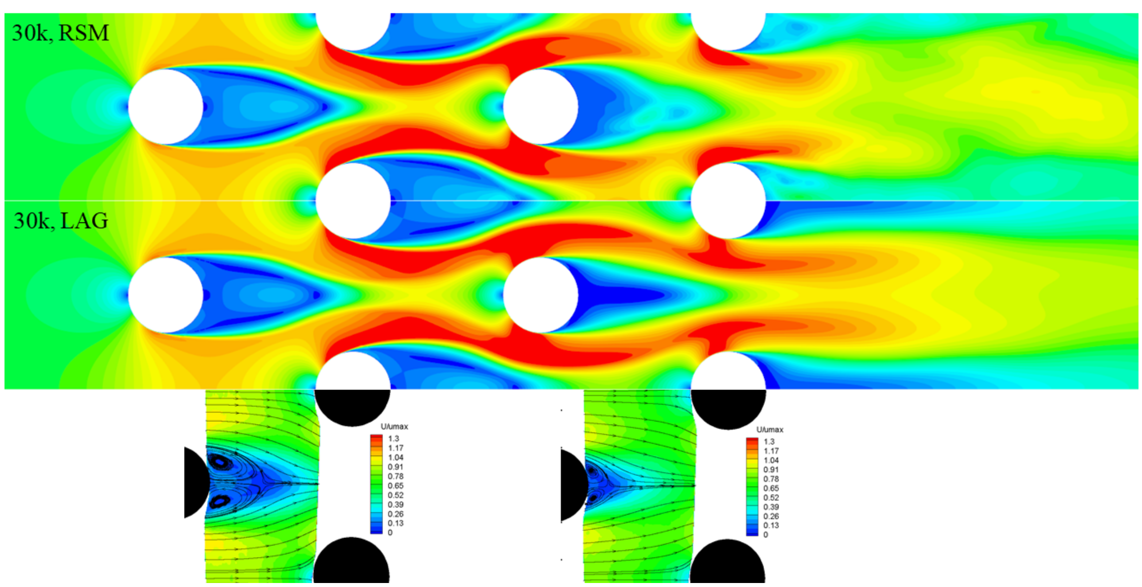

Figure 8.14: Normalized velocity magnitudes for 30,000 Reynolds number

Flow Field Analysis

The advantage of stereo PIV as used in this study is that all three velocity components and all Reynolds stress tensor components are available for an interrogation window. That allows the analysis of the velocity components, but also an investigation of turbulence within the channel.

Velocity Contours

The time averaged mean velocity field was calculated with the PIV data and normalized with the maximum velocity due to the pin blockage for the respective Reynolds number. Therefore, the mean velocity maps are presented in the form u/u_{max}; normalized by their respective maximum channel velocity. All normalized and time-averaged velocity contour plots with streamlines from PIV and CFD are presented in Figures 8.13 and 8.14 in the midplane of the channel. The streamlines and velocity contours show a different behavior for both Reynolds number cases. For a higher Reynolds number, the wake of pin in row one is smaller. Furthermore, the velocity field itself appears to be more homogeneous with less streamline curvature at higher flow velocities. This indicates a higher degree of lateral flow due to the blockage of the downstream row of pin fins. However, this is not captured within the CFD. The flow field of the LAG model at Re=30,000 shows shares more similarities with the fluid behavior at lower flow rates. An overly strong blockage due to stronger separation on the second row of pins artificially reduces the flow area which results in a more jetting like behavior of the flow with a concentration of axial momentum along the centerline behind the pin. This is also the reason for the streak of higher heat transfer as seen downstream of the pin between upstream and in between of the second row of pins in the staggered setup.

The discrepancy between numerical simulation is even more striking for the higher flow rate. The third row pin exhibits a very long wake region which again artificially reduces the available area for the fluid which causes a high velocity at the smallest cross-section between wake and pin. This is not at all supported by the PIV data. The wake itself is quite short and the flow velocity is at the order of 75% of the maximum velocity u_{max} over the entire channel width.

The corresponding spanwise velocity profiles over the width of the channel at the six well-known probing locations are shown in Figures A.5 and A.6 for 10,000 and 30,000, respectively. Here, the axial velocity component u is shown. The velocity profiles for the velocity components v, w can be found in the appendix. The velocity profiles emphasize what was stated based on the study of the contour plots: The axial velocity in the experiment is distributed more evenly over the width of the channel downstream of row one and even more so in the wake of row three. Since the wake length is apparently overpredicted, two jet like streams are found at half a pin diameter above and below the pin and a low velocity region in the wake.

It appears that the understanding of the wake length in the first and third row is crucial to the understanding of the flow field found in the staggered pin fin array. With an erroneous prediction of the flow around the first row, wrong velocity magnitudes are transported downstream through the pin fin array. With a wrong velocity (therefore also a wrong pin Reynolds number), it is easy to imagine that the subsequent rows will be mispredicted as well. For this reason, a more detailed analysis on the wake closure length is the logical next step.

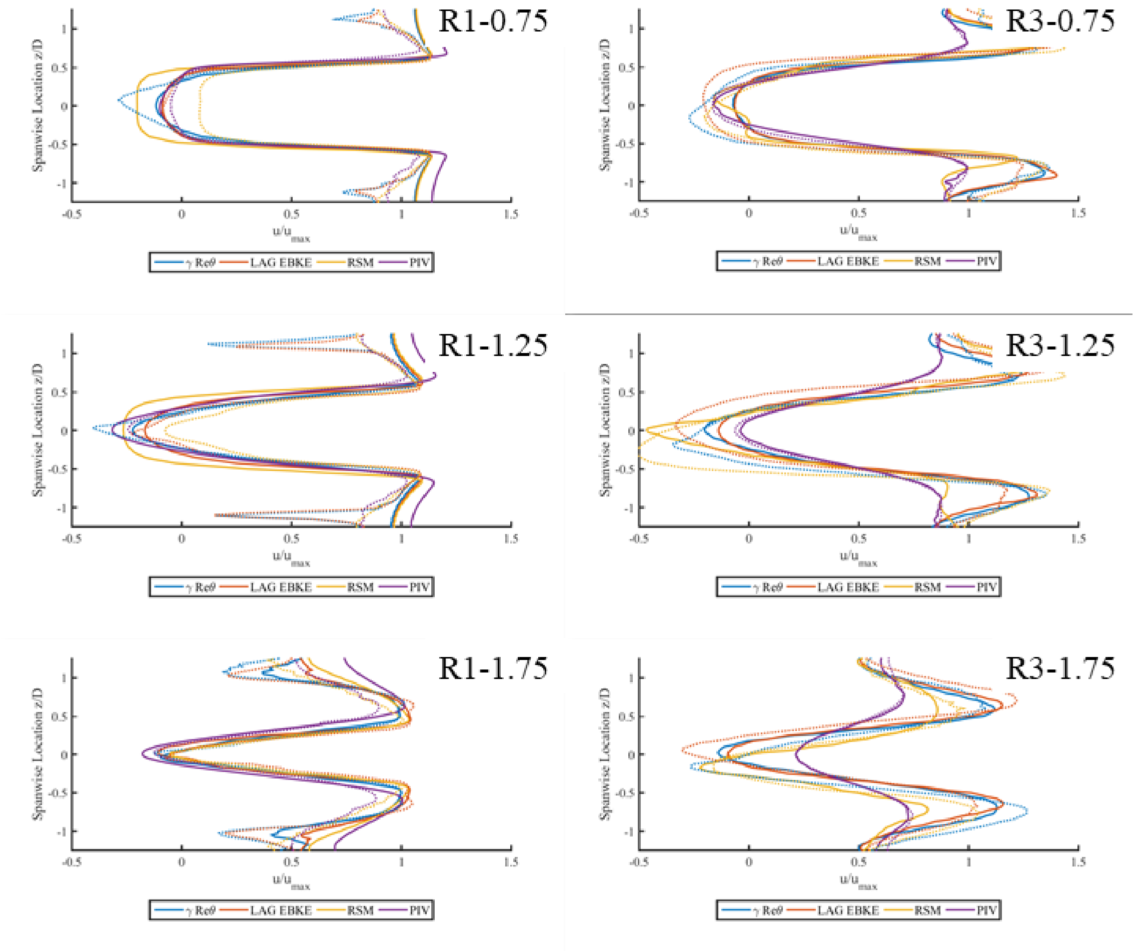

Figure 8.15: Normalized spanwise velocity profiles of component u at $Re = 10,000$

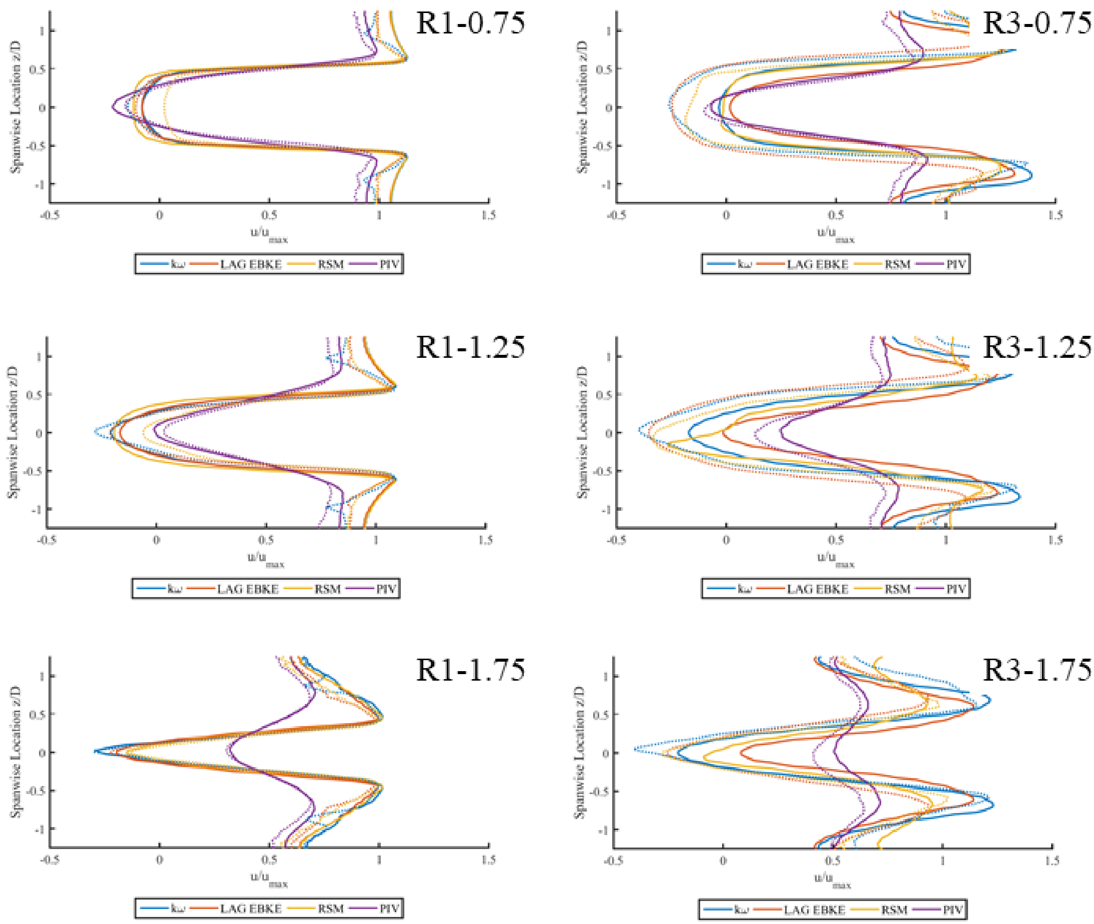

Figure 8.16: Normalized spanwise velocity profiles of component u at $Re = 30,000$

Wake Closure Length

As previously mentioned, strong deviations are found in the length of the wake through the analysis of the velocity contours. Deeper understanding of the wake closure length is revealed through the study of the streamlines. The experimentally found wake closure length for $Re = 30,000$ is significantly shorter than its pendant at 10,000 and from CFD. The wake closure length is a critical length scale when describing flow phenomena in pin fin arrays. The wake closure length can also be referred to as the length of the recirculation region and can be identified as the junction area of the time-averaged streamlines downstream of the pin. It was found that the wake closure length is not a function of the wall-normal distance. In other words, the wake length is the same in the wall-near region and the channel mid-plane.

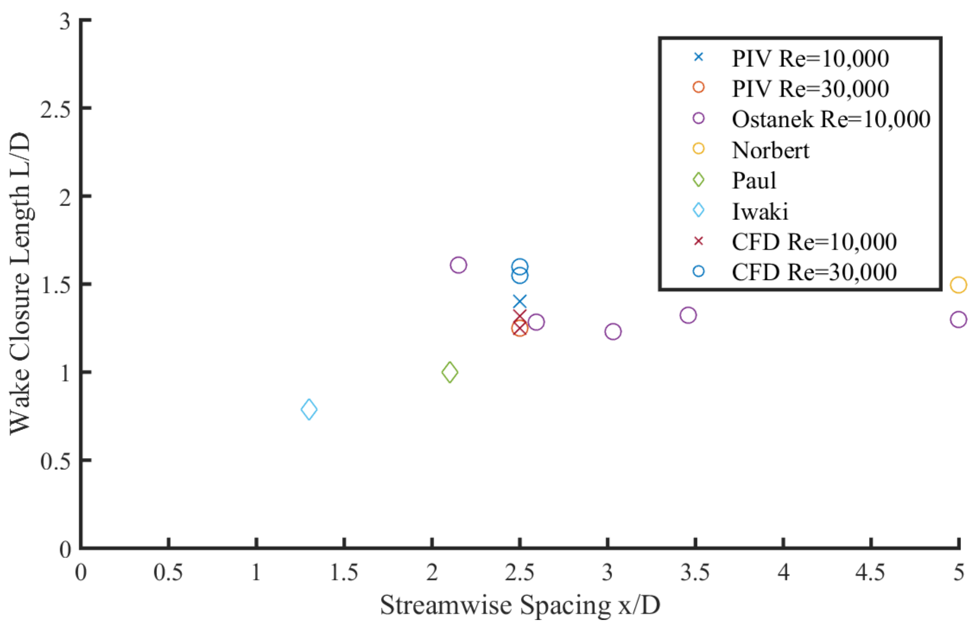

Figure 8.17: Wake closure length of row one

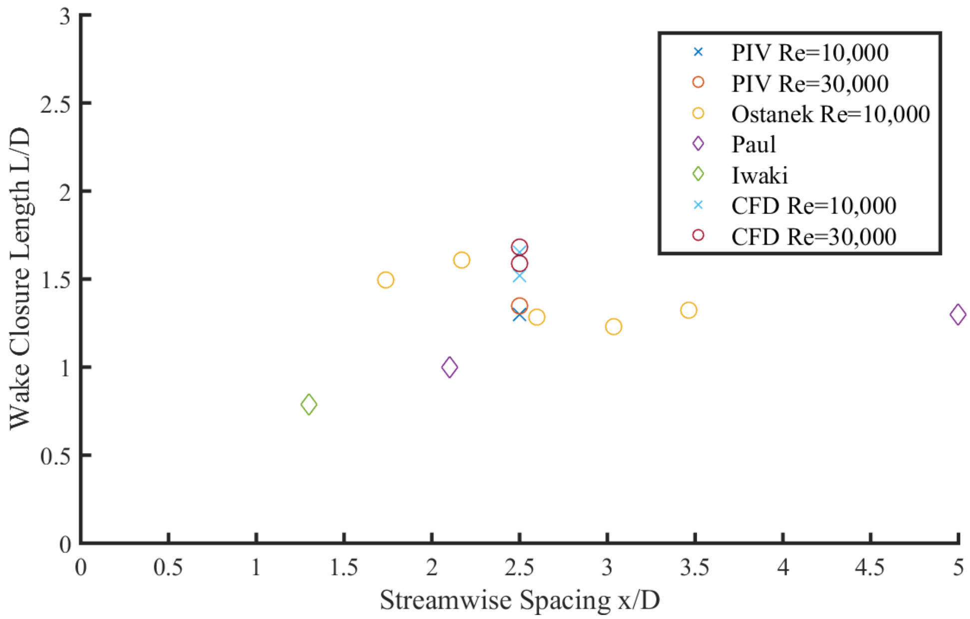

Figure 8.18: Wake closure length of row three

PIV data and CFD data is compared with data reported for staggered pin fin arrays by Ostanek [74], Paul et al. [128], Iwaki et al. [129], and Norbert [130] for a single cylinder. The wake closure length L from the current study, numerical and PIV results, and the reference data is shown in Figure 8.17 for the wake of row one and Figure 8.18 for the wake of row three, respectively. The wake closure length is then normalized by the pin diameter. For 10,000, all three data sets are in very good agreement. A deviation for 30,000 can be observe. The length of the wake according to CFD is similar to a single cylinder setup; however, the experimental results indicate a shorter wake. When taking the velocity contour plots into consideration, it is apparent that the flow deflected due to the stagnation region in front of the pins in the subsequent row downstream acts as a confinement on the wake which causes a shorter length compared to a single cylinder in crossflow. With increasing Reynolds number, more momentum and mass flow are

deflected by the downstream row. Moreover, increased turbulent mixing, which increases with Reynolds Number, also causes a shortening of the recirculation region as the shear layers become more and more unstable where the von Kármán vortices become stronger and stronger and diffuse less quickly.

The agreement between literature and the current experiment is also given for the wake of the third row. Considering the proper streamwise spacing of the pin, the current wake length is on point what is reported - manifesting the confidence in the given experimental setup. Yet, the trend for the numerical simulations is similar to what was observed in the wake of the first pin. The predicted wake is much longer than what is found in the current study and what was reported by Ostanek [74].

Turbulent Kinetic Energy

In order to support the claim that the deviation in the length of the recirculation region is due to turbulent mixing, it is required to study in detail the spanwise distribution of Turbulent Kinetic Energy (TKE). Six locations are selected for an in-depth analysis of the TKE and Reynolds stresses. The locations are the probing locations at 0.75, 1.25 and 1.75 pin diameters downstream of the center of the pin and wall-normal heights of y/D of 0.05 and 0.5, respectively. In furtherance of comparison between different Reynolds Numbers, TKE is normalized by the square of u_{max}. Contour plot results are reported in Figures 8.19 and 8.20 for Reynolds numbers of 10,000 and 30,000, respectively. The turbulent kinetic energy can be calculated with the knowledge of the three values along the tensor diagonal. The turbulent kinetic energy gives a good idea about the overall turbulence levels a given point.

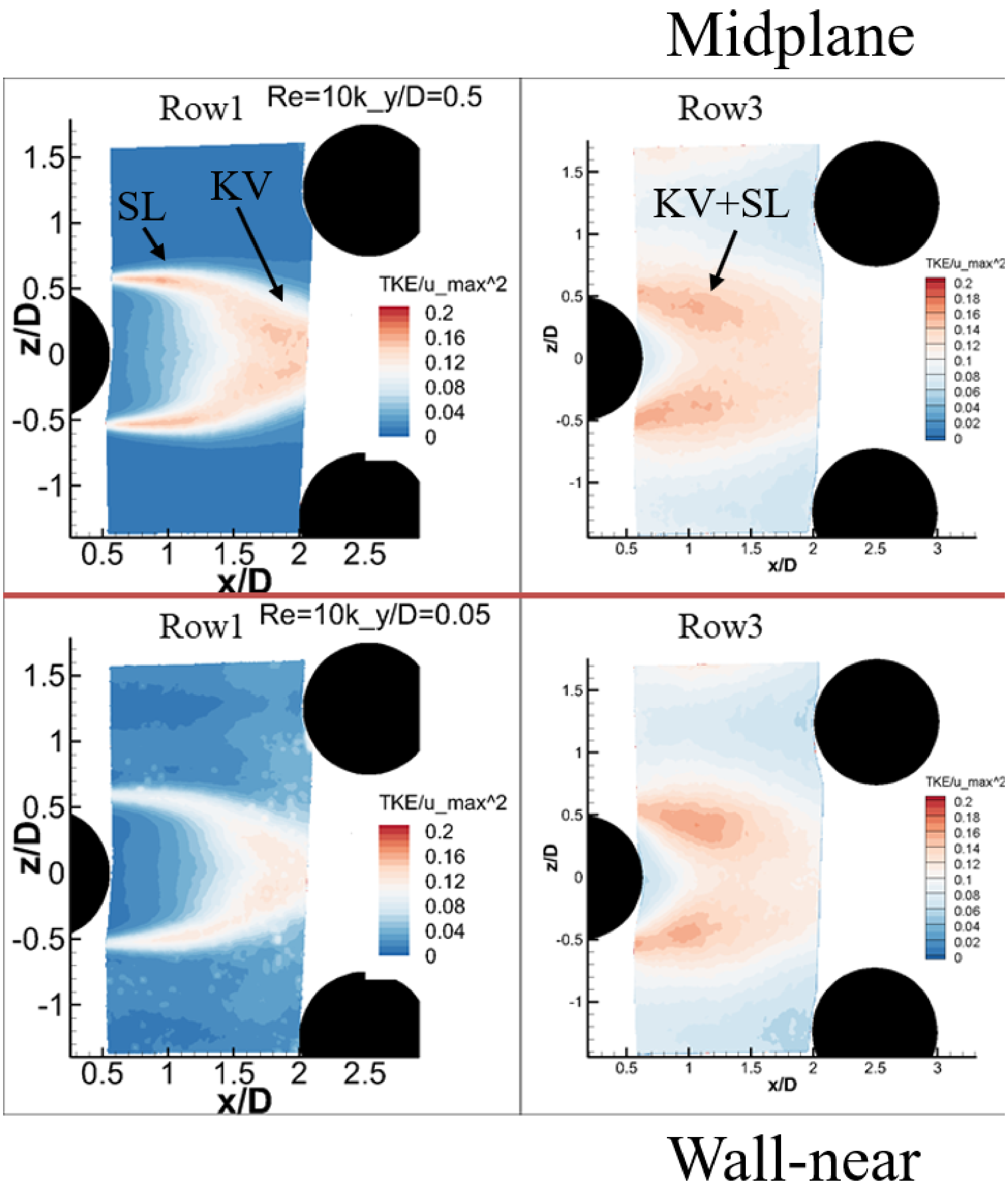

Figure 8.19: Normalized TKE distribution in the wake of row one and three obtained through PIV in the mid-plane of the channel and at 5% channel height at $Re = 10,000$

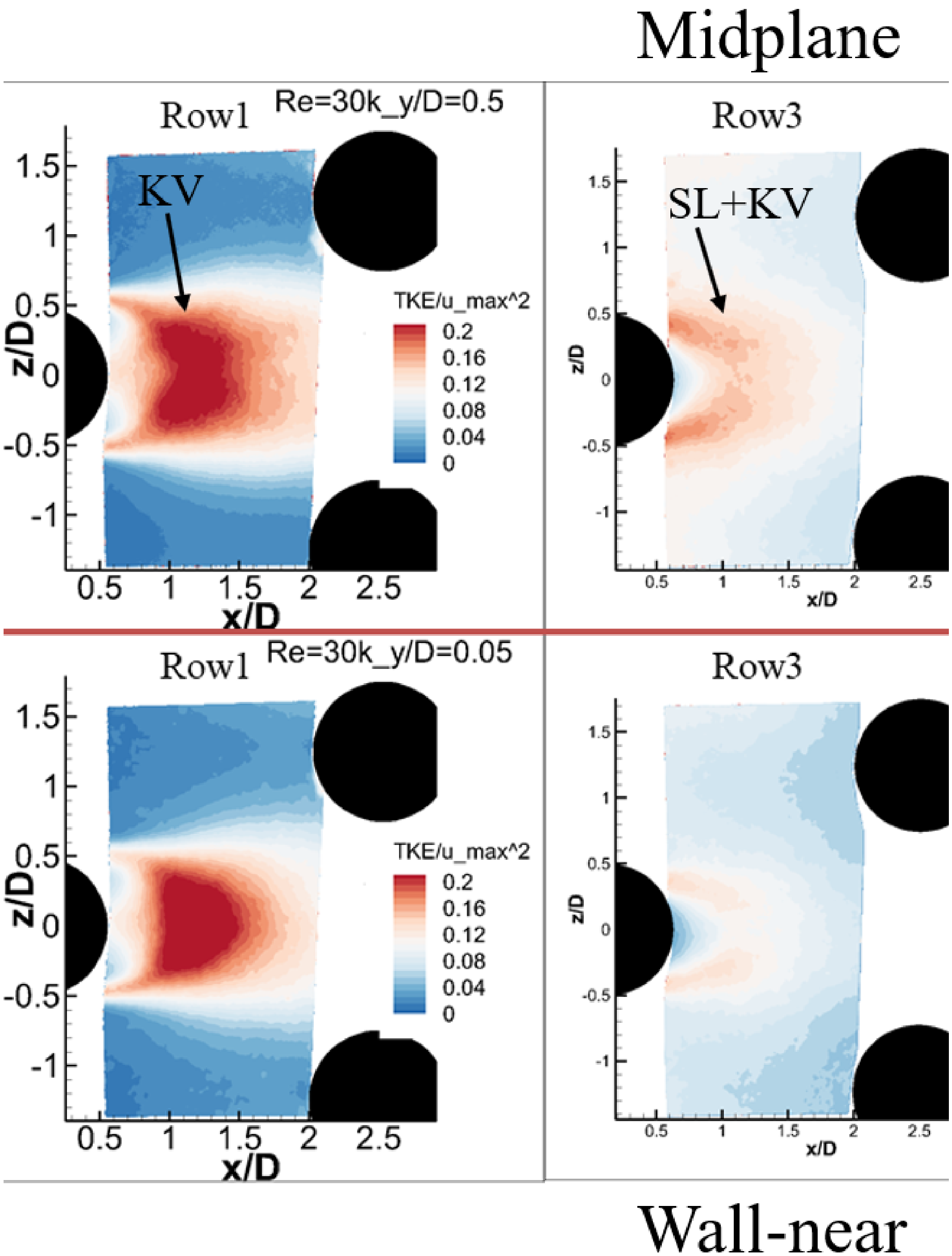

Figure 8.20: Normalized TKE distribution in the wake of row one and three obtained through PIV in the mid-plane of the channel and at 5% channel height at $Re = 30,000$

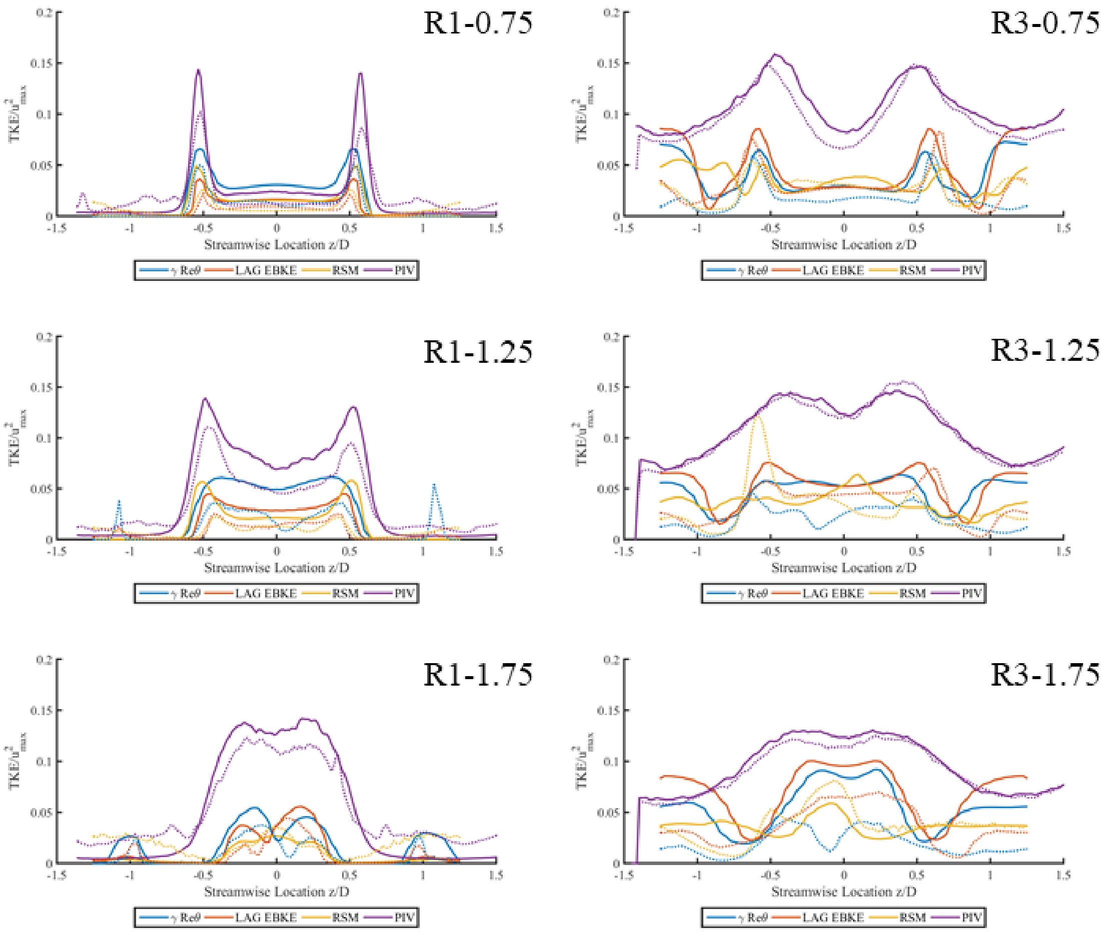

Figure 8.21: Spanwise turbulent kinetic energy distribution at $Re = 10,000$

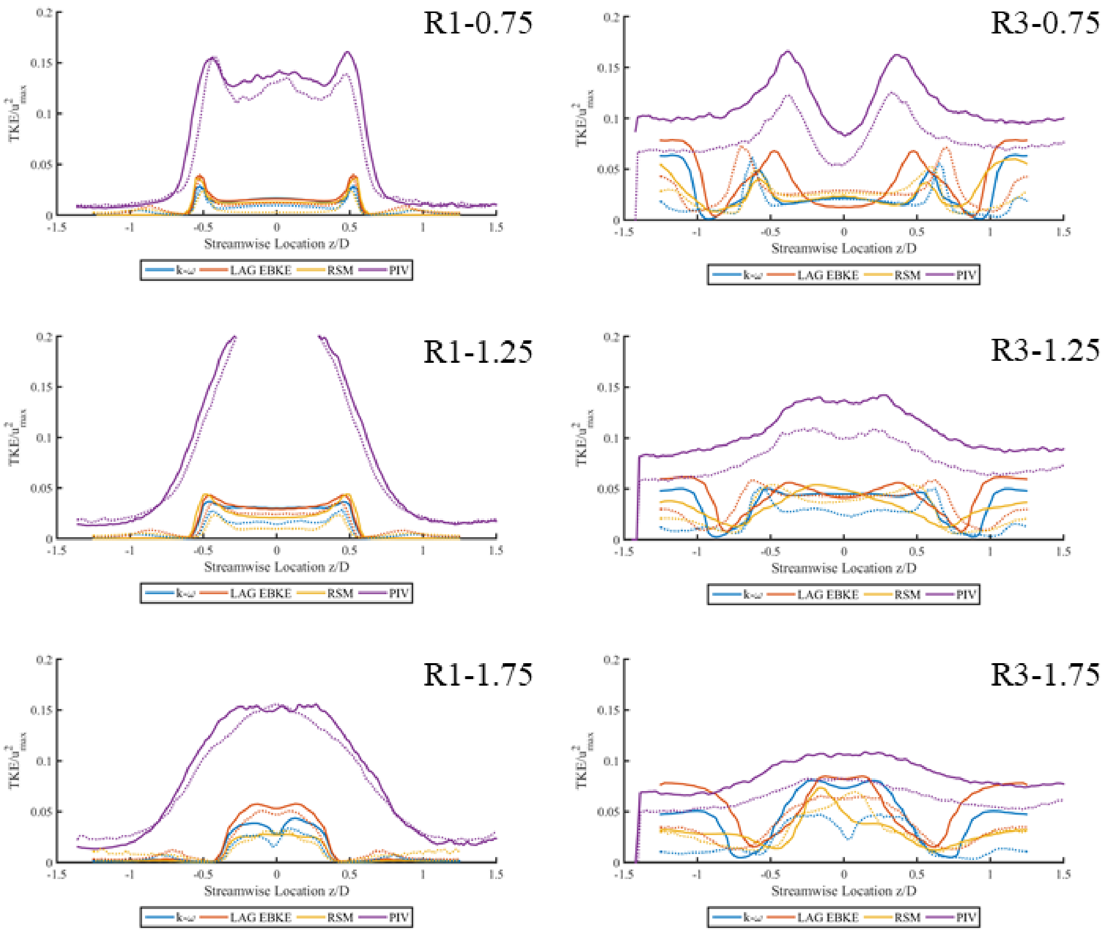

Figure 8.22: Spanwise turbulent kinetic energy distribution at $Re = 30,000$

The distribution of TKE over the width of the channel is shown in Figures 8.21 and 8.22 at both Reynolds numbers. The turbulent kinetic energy itself is normalized with the square of the maximum channel velocity.

The three plots of the left-hand side are found in the wake of row one, the three plots on the right-hand side were extracted from the wake of row three. The purple line corresponds to the PIV data where the solid line is extracted in the middle of the channel and the dotted line is the TKE extracted at a non-dimensional height of 5%, 0.1 inches away form the wall.

Although the experimental results in shape and magnitude of the augmented reason are in good agreement with Ostanek's PIV data for a similar configuration ($H/D = 1$, $z/D = 2.5$) [74], CFD findings are significantly underpredicting the shape and value of local TKE. Two main flow structures can be identified in the wake region: periodic von Kármán vortices (KV) and shear layer eddies (SL) which are in nature random.

First, KV are periodically shed from the pin in crossflow and are carried downstream. The increased turbulence in the region between a half pin diameter downstream of row one up the row two is contributed to the KV. As the wake closes, the vortices expand from both sides towards the imaginary centerline behind the pin which causes the highest turbulence levels along this center line. Secondly, SL are forming right downstream of the pin and can be seen in form of augmented TKE between $x/D = 0$ to 0.5 where the intensity is generally stronger in the midplane compared to the near-wall region. This behavior is barely captured by CFD and similar to the finding of Li et al [79]. In order to provide further understanding for the differences, it is necessary to break down the composition of the TKE into Reynolds stress to pinpoint the shortcoming of the numerical modeling. This will be investigated in the next chapter. Generally, at this point it can be noted already that the shear layer eddies as well as the von Kármán vortices are not

accurately captured by CFD thus underpredicting local turbulence levels and turbulent mixing downstream.

Two centerline symmetric peaks indicate a highly turbulent region right at the outer edges of the pin (Figures 8.21 and 8.22, frames in row 1) caused by the separating flow around the pin. In case of $Re = 30,000$, the wake region itself is more turbulent compared to the 10,000 case. The larger velocity difference between bulk fluid and wake causes a stronger recirculation within the wake region which ultimately impinges on the trailing edge of the pin. Furthermore, the turbulent shear layer is wider at a higher Reynolds Number and diffuses quicker. Contrarily, for lower flow rates, the SL eddies propagate further downstream and shield the wake region from cross flow which explains the longer wake (Figures 8.17 and 8.17) and the reduced heat transfer close to the pin as observed in Figures 8.7 and 8.8. In addition to that, a variation of the height of the pin can be observed at lower flow velocities. The peaks in TKE become less distinct towards the wall. Generally, the turbulence levels closer to the wall are smaller in case of Re=10,000 but not for 30,000. As the flow travels downstream, mixing in lateral direction occurs and the spanwise distribution of TKE becomes more even, yet, the shielding-like behavior of the shear layer diminishes the lateral transport compared to higher flow rates. This can be seen in row two of Figure 8.21. This is only valid for the first row though. The aforementioned KV become the dominant vortex structure in case of $Re = 30,000$. As the KV from either side of the pin start interacting about 0.75 diameters behind the pin along the centerline, the turbulence peaks and reaches it maximum. Further downstream, the shear layer and KV diffuse more and more as seen in row three in Figures 8.21 and 8.22. The turbulent region eventually spreads in lateral direction as the velocities at this point as well as the velocity fluctuations are more evenly for $Re = 30,000$ compared to $Re = 10,000$ as the wake closes further upstream and a longer mixing length is available. Due to the diffusion of the formerly strong shear layer in case of $Re = 10,000$, it cannot

effectively protect the wake region from the momentum of the deflected bulk flow. For this reason, the turbulent region is compressed to about half the width of the pin diameter as the flow has a dominant component of x-momentum compared to lateral cross flow. This is in close agreement with the findings of Ames et al. [33] who also describes the importance of lateral velocities and velocity fluctuations on. The authors observed a larger than expected lateral velocity w of unknown source during the acceleration around the pin. At this point, it shall referred to the previous discussion related to Figures 8.11 and 8.12 in terms of heat transfer deviations and Figures A.5 and A.6 in terms of velocity contours. The source of lateral momentum was seen in the experimental velocity contour plot, however not being picked up in either turbulence model.

In terms of comparison between numerical and experimental results, it is to mention that the magnitude of TKE is always underpredicted by a factor of three for $Re = 30,000$. As mentioned earlier, the utilized CFD model fails to the shear layer vortices. With this initial discrepancy, the error propagates downstream and does not match wake and mixing zone. It can be concluded that the proper simulation of the shear layer and shear layer instabilities is the bottleneck and main error source. For generally lower inlet turbulence and lower Reynolds Numbers, this effect is less severe as the incoming slow flow undisturbed and flow instabilities are minimal which, however, increase with increasing flow velocities. Due to this reason, the flow is more unstable and the instabilities drive the collapse of the shear layers from the pin to shedding vortices. However, with higher Reynolds Numbers, another complexity is added to the problem: The subcritical regime for a flow past a confined cylinder is defined as the local Reynolds Number range between 350 and 20,000. In this region, the boundary layer on the cylinder is laminar before separation. The shear layers between wake and bulk flow become unstable, collapses and forms the shedding vortices. With increasing Reynolds Number, the small-scale vortices increase in strength with a decrease in vortex shedding frequency. In this

flow regime, the Strouhal Number is usually in the order of 0.2 [33]. As commonly known and recognized, the transitional flow from laminar to turbulent boundary layers is still a challenge within the development of RANS turbulence models. Here is the reason why a transitional turbulence model and a purely laminar model were chosen. Nevertheless, it is noteworthy to emphasize at this point, that even though the flow characteristics are not accurately reproduced, the relevant engineering quantities such as pressure drop, pin Nusselt Number and endwall Nusselt Number are reasonably correct.

Horseshoe Vortex System

Unfortunately, the initially planned investigation of the contribution of the horseshoe vortex system (HSV) on the overall flow field is propagating into the wake region cannot be described by the evidence from TKE plots or velocity maps. Possibly the TKE of the HSV is much smaller than the other observed modes or they are found outside the investigated area (e.g. within the 10% of the channel height). Traversing the laser sheet closer to the wall caused disturbing reflections. A bigger pin could mitigate that challenge since Dargahi [65] reported that the diameter of the main vortex in the HSV is independent of the Reynolds Number, but a function of the pin diameter. For the smallest Reynolds number, the vortex is still visible in the plane between third and fourth row. However, for the larger Reynolds Numbers, the vortex is not identifiable. Either the area of interest is insufficient to resolve the vortex or due to the accelerated flow in this region, the vortex is quenched and pushed back towards the wake region.

Reynolds Stresses

The flow is highly anisotropic and TKE only gives the contribution of the three principal components combined, it is relevant to investigate the contribution of each term

of the Reynolds Stress Tensor separately. The contour plots for the three Reynolds Normal Stresses and three Shear Stresses are shown in Figure 8.23. As all previous data shown before, stresses are again normalized by the square of u_{max}. In the visualization of the longitudinal Reynolds normal stress $\overline{uu}$ the structure of the SL can be clearly seen as well as their bending towards the symmetry line and in their diffusion into the bulk flow. As expected, the contribution of the wall normal stress $\overline{vv}$ is almost insignificant in the midplane as the main flow happens in the x-z-plane such as the wake field including recirculation and impingement on the backside of the pin as depicted in lateral normal stress distribution $\overline{ww}$. Even more interesting are the findings from the shear stress components. KV can be readily identified based on the components $\overline{uv}$ and $\overline{uw}$. A closer examination of $\overline{uv}$, a term related to a momentum flux in the wall-normal direction y, is not zero which means that the shed vortices have a rotational component to it while propagating downstream or that the phase of the KV is varying with the height of the cylinder resulting in a non-zero $\overline{uv}$ component. The flow structure slowly diffuses as it interacts with the curved streamlines which experience flow acceleration to the blockage of row two. The same diffusional behavior can be observed by analyzing the <uw> component of the stress tensor. The turbulent transport inside the wake region can be observed as well as the contribution of the KV vortices rotating and traveling towards the centerline. The $\overline{uw}$ component is the most dominant shear stress component and is approximately 5 times larger in magnitude than the other two shear stresses. The tensor components vary strongly over the investigated area; however, three zones can be identified: wake zone, wake closure zone including KV shedding, and area of eddy diffusion and high mixing upstream of the next row.

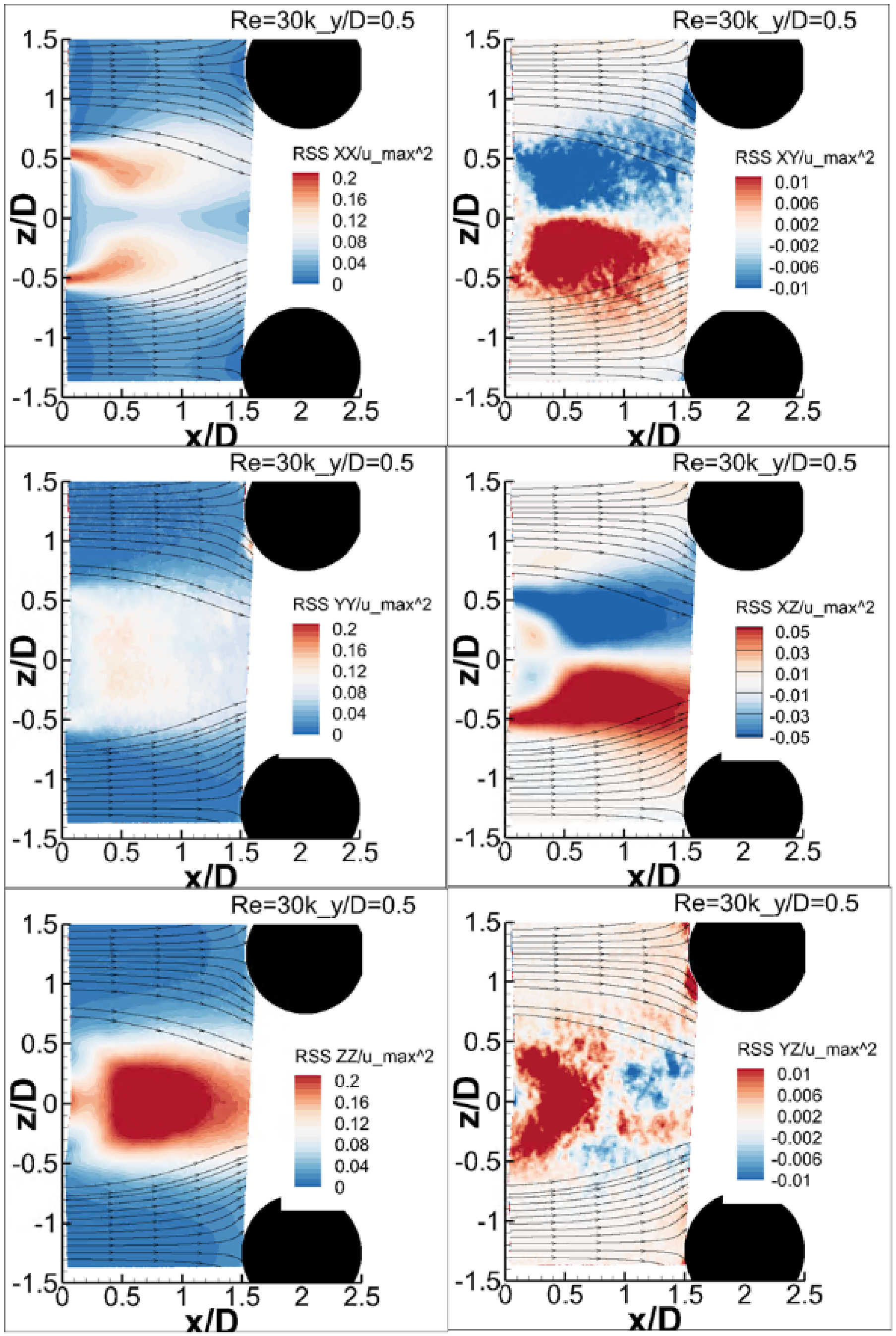

Figure 8.23: Normalized Reynolds stresses at $Re = 30,000$ in the mid-plane of the channel downstream of row one

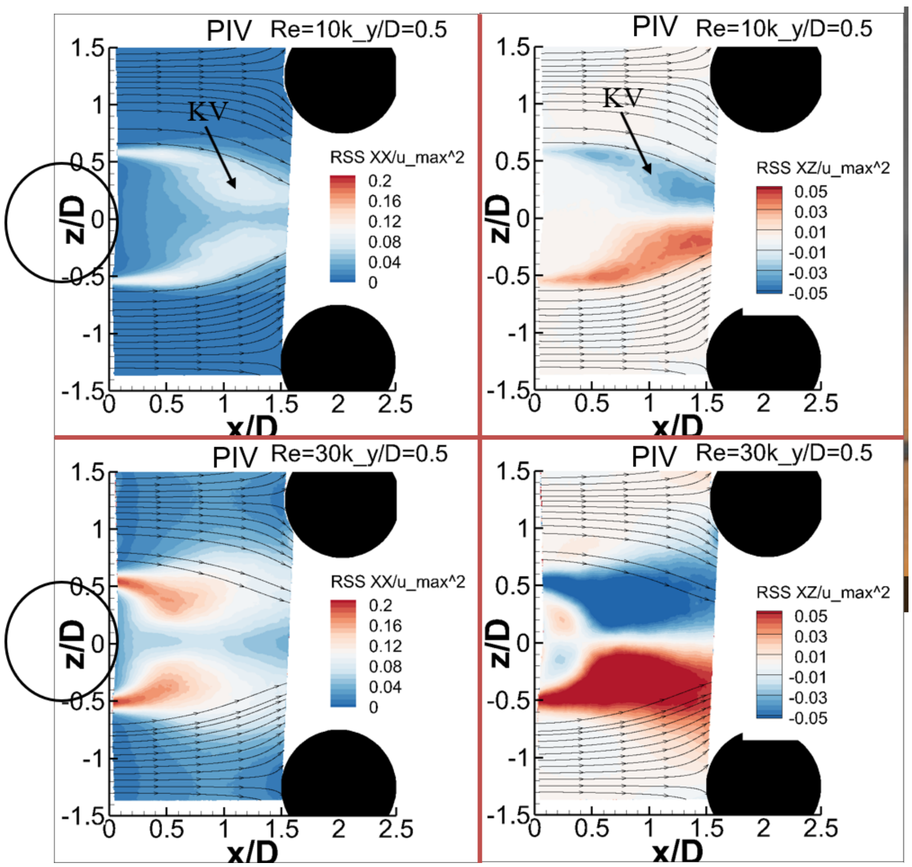

Figure 8.24: Normalized Reynolds stresses at $Re = 10,000$ and $Re = 30,000$ in the mid-plane of the channel downstream of row one

Figure 8.24 directly compares the different wake structures for both tested Reynolds numbers. The top right frame shows the KV vortex for 10,000 Reynolds number wrapping around the wake of the pin and as both sides meet on the center-line of the pin. The bottom right frame shows the same mixed Reynolds stress $\overline{uw}$ but for the higher Reynolds number. The very short recirculation zone is visible directly adjacent to the trailing edge of the pin. Two very strong turbulent fields point outwards from the wake towards the downstream pins. This are the KVs. Here, they are shedding left and right and are not as confined as in the lower Reynolds number case. Due to their unsteadiness, they move up and down wiping over a large surface area downstream. This explains the higher heat transfer in that region. Furthermore, the KVs extend further downstream and eventually impinge onto the second row pin as they are not confined towards the center line behind the pin of row one. This swiping motion helps to distribute momentum of the fluid so that the velocity distribution becomes more even as found in the velocity contour plots. This swiping motion might be the source of the unknown lateral velocity w.

Local Anisotropy

The study of the distribution of the Reynolds stress tensor components also reveals high anisotropy of the turbulence. Certain components seem to be stronger than the others. This is problematic with respect to assumption made for the eddy viscosity models that are the foundation of the RANS models. An elegant way to visualize local anisotropy is the an Invariant maps as shown in Figure 8.25. The anisotropy tensor $\mathbf{A} = a_{ij}$ can be computed by the Equation given in 8.1 where k is the turbulent kinetic energy. [131]. The anisotropy tensor is the normalized Reynolds stress tensor by twice the turbulent kinetic energy minus the isotropic assumption. Corresponding eigenvalues $\lambda_1, \lambda_2, \lambda_3$ can be cal-

culated for the tensor.

$$\mathbf{A} = a_{ij} = \frac{\overline{u_i' u_j'}}{2k} - \frac{\delta_{ij}}{3} \tag{8.1}$$

The second and third principal component II and III of the turbulence anisotropy is calculated based on the three eigenvalues and are:

$$II = a_{ij}a_{ji}/2 = \lambda_1^2 + \lambda_1\lambda_2 + \lambda_2^2 \tag{8.2}$$

$$III = a_{ij}a_{jn}a_{ni}/3 = -\lambda_1\lambda_2(\lambda_1 + \lambda_2) \tag{8.3}$$

The domain of the Lumley triangle can be scaled using the equations below (Equations 8.4, 8.5). The resulting diagram is referred to as *Invariant map*. The advantage is a higher resolution in the isotropic region compared to the unscaled Lumley triangle.

$$\eta^2 = II/3 \tag{8.4}$$

$$\xi^3 = III/2 \tag{8.5}$$

The visualization in form of the Lumley triangle and invariant map was originally introduced by Lumley and Newman.

To aid the understanding, isotropic turbulence can be imagined as a perfect sphere. All points in x, y, z have the same distance to the center of the sphere. If the sphere is now pulled along one axis, meaning one component becomes dominant, the sphere changes shape into a cigar. In the same fashion, two dominant tensor components would correspond to squeezing the sphere into a pancake. Now, depending on the position in the invariant map, either one or two components are dominant. Data points were extracted

along the probing locations in the wake of the first row pin. Further downstream, the flow is dominated by one tensor direction: most likely due to the high fluctuations in streamwise directions. However, directly in the wake the flow is highly anisotropic and exhibits a transition from isotropic turbulence within the bulk flow to high anisotropy in the shear layer and wake.

The statement made earlier is still valid: the flow field is highly turbulent and anisotropic. Not ideal situations for common RANS models. The vortex structures forming around the first pin are highly dependent on the incoming boundary conditions, such as turbulence intensity, turbulent length scale, and any kind of other disturbances. For this reason, a Large Eddy Simulation will be conducted and described in the next section. A periodic approach with a fully developed interface was chosen to mitigate the challenges outline before.

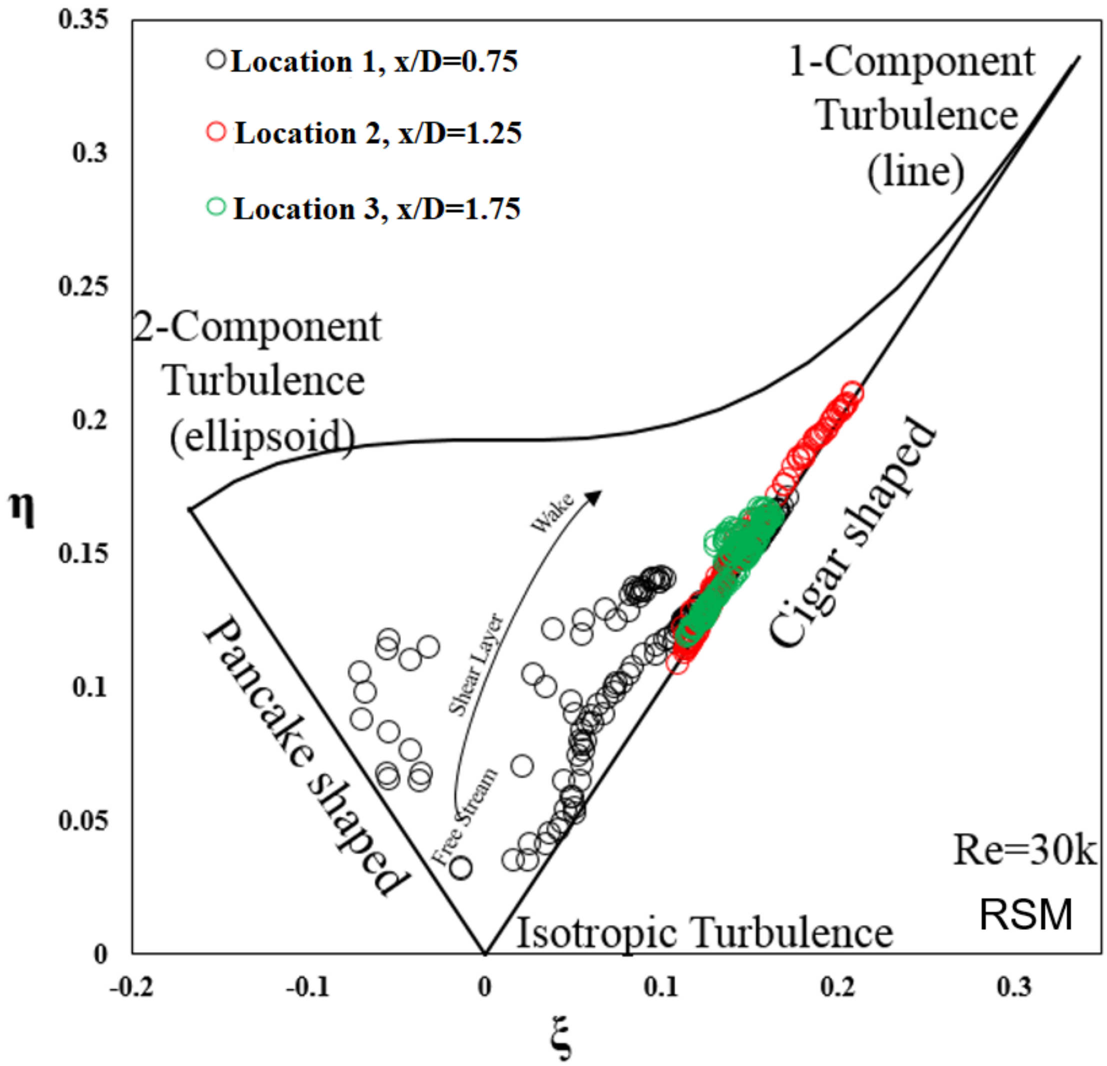

Figure 8.25: Invariant map: Local anisotropy in the wake of row one at $Re = 30,000$ based on the stresses in the RSM model

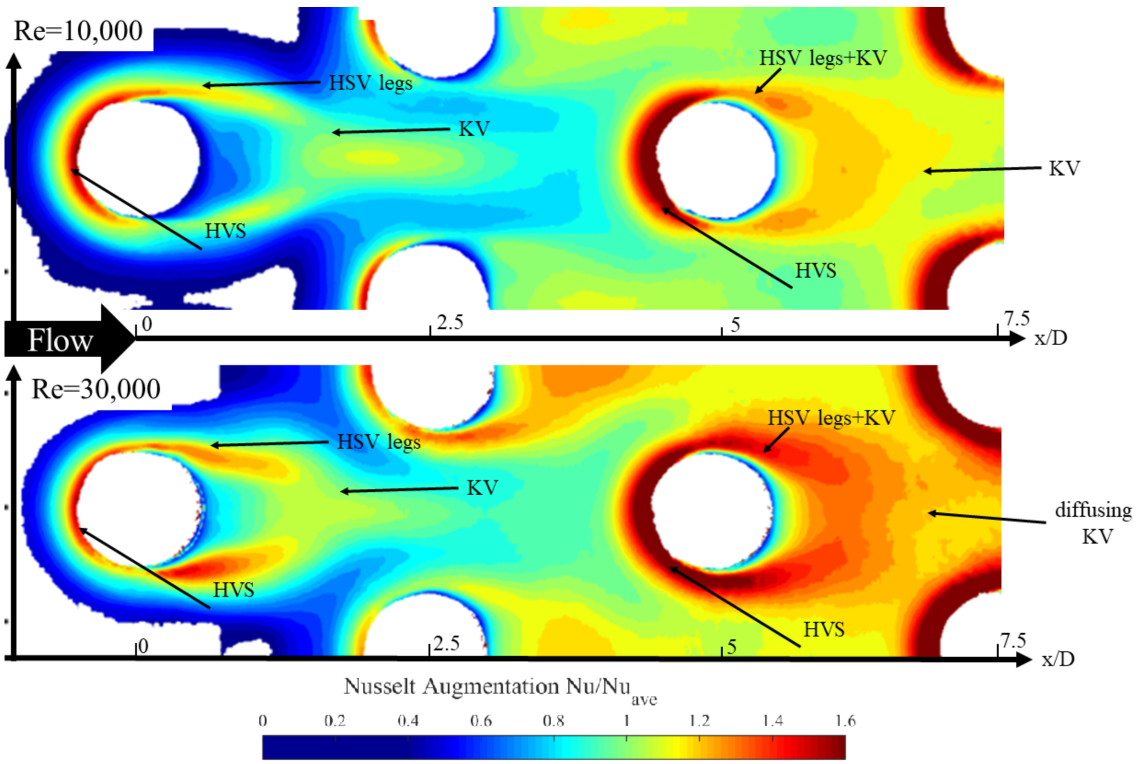

Figure 8.26: The effect of vortical structures on endwall heat transfer in a staggered pin fin array for in comparison for Reynolds numbers of 10,000 and 30,000

The effect of vortical structures on endwall heat transfer was qualitatively touched upon in the first sections for the results and discussion while interpreting the endwall Nusselt number distribution. This analysis was followed by a discussion of the flow field, turbulent kinetic energy, occurring vortex structures, and turbulence statistics. The missing link is to actively tie the endwall heat transfer distribution to the vortical structures found in such staggered pin fin array. A cropped section for the Nusselt number results obtained through transient TLC for Reynolds numbers of 10,000 and 30,000 is shown in Figure 8.26. The cropped section highlights the endwall heat transfer in pin row one and

three. At the first glance, both normalized Nusselt number distributions appear similar. The devil is in the details.

The most obvious difference is the length of the wake in the first row for both Reynolds numbers. This was discussed in detail in the previous sections. As the wake is longer for lower flow rates, the KVs stretch further downstream where they meet at the center-line behind the pin after they were confined by the bulk fluid passing by. The KVs at the higher flow rate are much shorter and do not show much of the confinement effect. Due to their stronger shedding, a wider area in the wake is cooled and the low heat transfer zone directly downstream of the pin in the wake is therefore smaller.

The differences become more apparent at the third pin. The horseshoe vortex system is larger for the higher Reynolds number. It was found and reported in several studies that overall increased turbulence levels promote the horseshoe vortex buildup and generate larger structures [62]. Furthermore, the legs of the HSV become shorter but wider and are not clearly distinguishable from the KVs that are developing. The area over which the transient KVs are shed also is wider, yet shorter than for the first row pin. This is in agreement with the discussion of the turbulent kinetic energy and the rapid lateral dissipation of the turbulent momentum flux. This trend is even more so observed for the higher flow rate. At a Reynolds number of 30,000, the core of the KVs are clearly visible up to one pin diameter downstream. However, the strong shedding and fluctuations cause the vortices to impinge onto the pin of the fourth row under an angle of approximately 45 degrees. Consequently, the area between row three and four experiences are strong cooling due to the KVs wiping over the endwall in the wake and wider spread high heat transfer upstream as the KVs diffuse as they travel downstream.

It was found that the main turbulence in the mid-plane of the channel is caused by the shear layers eddies that form at the interface between the recirculating fluid in the wake of the pin and the faster bulk fluid velocity. This is not necessarily the case in

the endwall region. Here, the horseshoe vortex system and its legs that wrap around the pin are the dominant driving force of heat transfer. Further downstream, the KVs are the main mode of heat removal from the pin finned endwall. However, the formation of the KVs is strongly dependent on the shear layer behavior as it was described in the section on the distribution of turbulent kinetic energy.

Importance of the right Choice of Numerical Models

As aforementioned, the endwall heat transfer is strongly driving by larger turbulence scales that cause wall-shear stress and transport hot fluid from the endwall into the bulk flow. Small eddy scales on the endwall itself transport the hot fluid upwards into a region where the larger scales can pick up the warmer sections. Furthermore, it was found that the flow field and the nature of turbulence is highly anisotropic and therefore conventional RANS models are not the ideal choice for properly modeling these kind of flows.

This means, in turn, that more advanced numerical methods have to be applied to correctly understand the transient nature of the vortical structures and the proper interaction of the smaller scale and larger scale turbulence. A Large Eddy Simulation was employed for this purpose. The numerical setup was already described previously. To identify why LES is expected to outperfom RANS, typical RANS simulations where also added to the simulation of the fully developed pin fin flow to allow easy benchmarking.

Quantification of Simulation Quality

Besides friction factor, pin fin and endwall heat transfer, a more general and a quick check for validity of a large eddy simulation or similar is to compare the Fast-Fourier-Transform (FFT) of the turbulent fluctuation with the ideal energy spectrum. If the input

is velocity and the slope of the energy spectrum is not $-5/3$ than something must be fundamentally wrong with the simulation. Often it is easier to perform this analysis with the pressure signal as it tends to be less noisier. Here, the slope should be around $-7/3$. Several probing locations where introduced into the fluid domain. Mainly at locations with high turbulent kinetic energy. However, additional probes where added in the wake of the pin and in wall-near regions as well as it is one objective of the study to investigate the wall-near behavior and its effect on heat transfer. The power spectral densities are for velocity and pressure are shown in Figures 8.27 and 8.28, respectively. The corresponding slopes are added as well. Good agreement is seen so that it can be assumed that the LES is converged and sufficiently resolves the energy spectrum. Another parameter for validation is the Strouhal number Sr. The Strouhal number is directly related to the shedding frequency, the most dominant frequency found in the fluid domain. It might be tricky due to the log-log scale to identify the most dominant frequency. Therefore, Figure 8.29 shows the frequency spectrum in a single log plot. The shedding frequency can be identified as $f = 31.51Hz$ which results in a Strouhal number of $Sr = 0.123$. It should be mentioned thought, that it was aimed to achieve a pin diameter based Reynolds number of 10,000, however, the actual Reynolds number came out to be 10,391. The Strouhal number is smaller than what is commonly found in literature. Nonetheless, the spread in literature is significant and the Strouhal number is within the range. An overview of literature values compared to this study is given in Table 8.3.

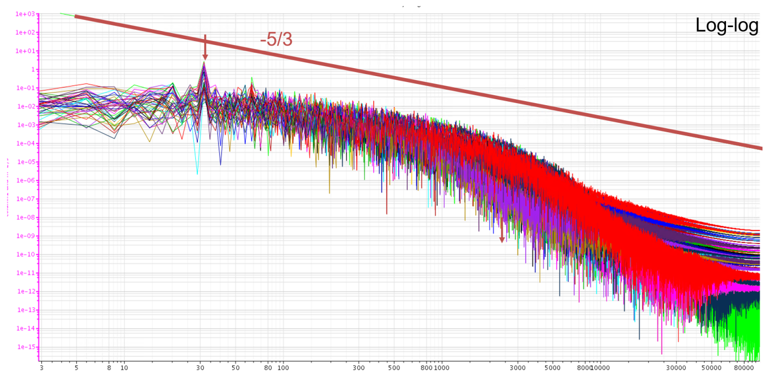

Figure 8.27: Velocity power spectral density of LES monitor points in log-log

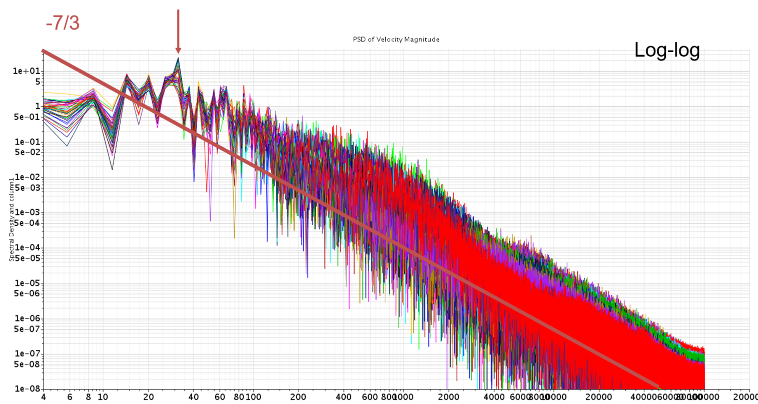

Figure 8.28: Pressure power spectral density of LES monitor points in log-log

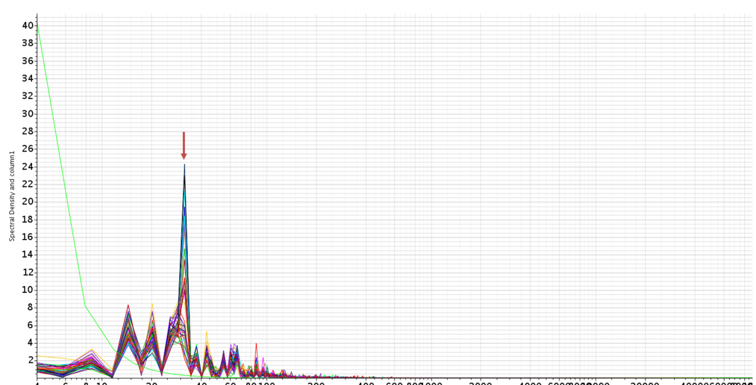

Figure 8.29: Pressure power spectral density of LES monitor points in single log

Table 8.3: Overview of Strouhal numbers found in literature and current LES

Re	Sr	Author	Comment
10,391	0.123	current study	fully developed
20,000	0.2	Ostanek [74]	first row
3,000	0.4	Ostanek [74]	first row
10,000	0.158	Tran [125]	fully developed, same geometry

The current LES does not match exactly the results in literature, however, the simulation can be assumed to be valid.

The Difference between RANS and LES

With the validity of the simulation established, the heat transfer and friction factor results can be compared to experimental data and other RANS models. The comparison is shown in Table 8.4. As previously stated, the actual Reynolds number was about 4% higher. The friction factor of the LES is within 6.7% of the reference case. The pin and endwall heat transfer is within 3.3% and 2%, respectively. Larger variations are observed for the RANS models. The friction factor assessment is accurate, however, the results for pin and endwall heat transfer deviate strongly whereas the endwall Nusselt number shows a better agreement than the pin heat transfer. This can be attributed to the strong shedding effect of the wake and KVs which are not properly picked up in the RANS formulations.

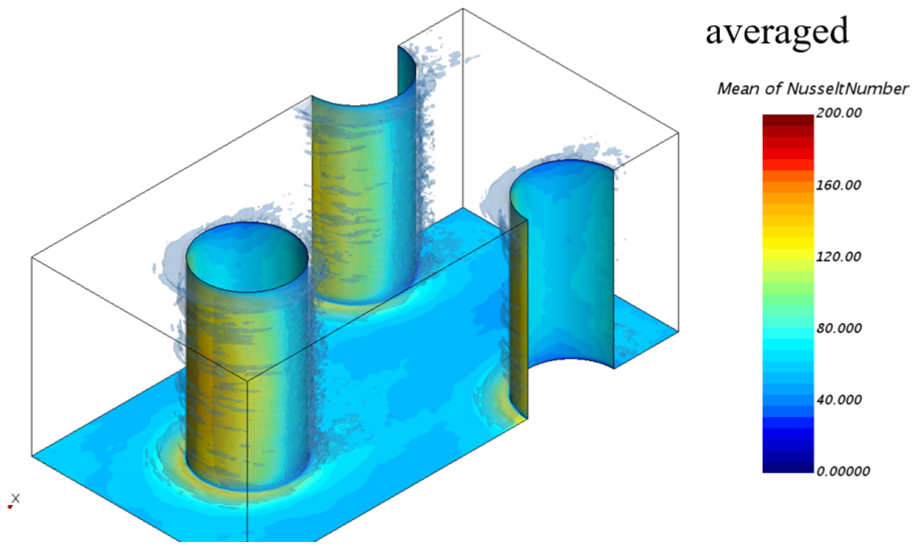

Figure 8.30: Mean of Nusselt number on pin fin and endwall

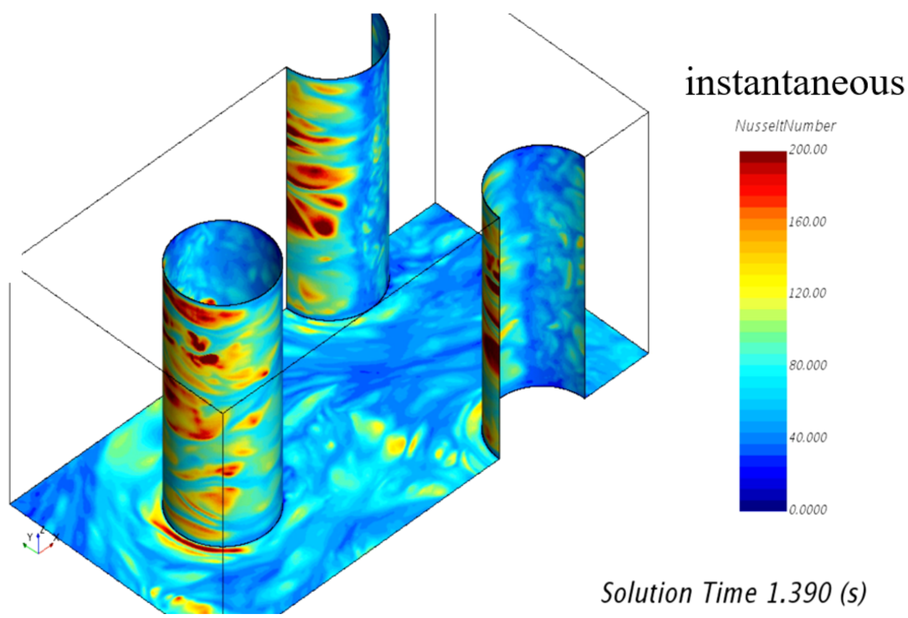

Figure 8.31: Instantaneous distribution of Nusselt number on pin fin and endwall

Table 8.4: Overview of Strouhal numbers found in literature and current LES

Re	Model	Friction factor	Pin Nusselt number	Endwall Nusselt number
10,391	LES	0.083	83.35	59.1
10,286	$\gamma Re\theta$	0.09	76.67	41.1
10,372	RSM	0.093	97.51	52.2
10,370	LAG	0.093	105.2	53.9
10,370	laminar	0.086	88.7	49.3
10,00	Ames [5]	0.089	80.65	57.9

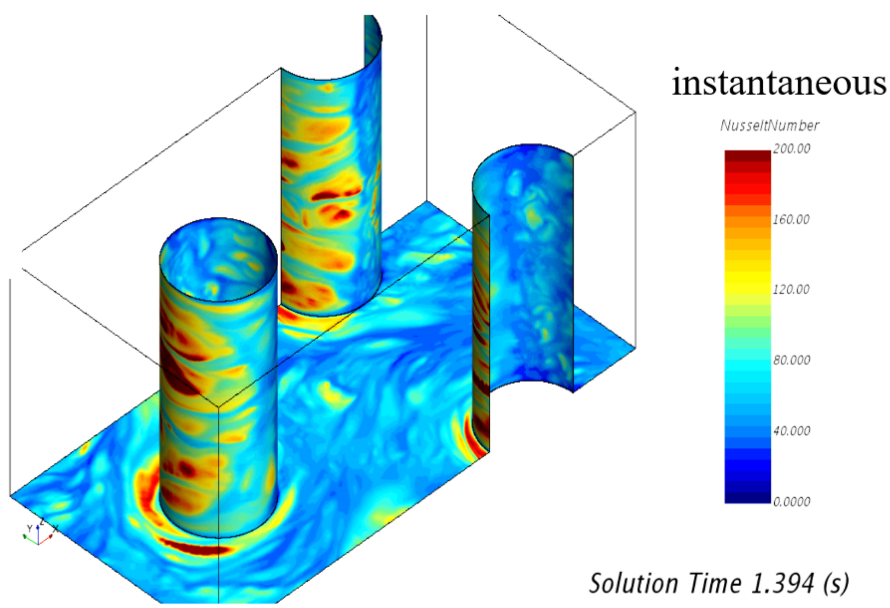

Figure 8.32: Instantaneous distribution of Nusselt number on pin fin and endwall at another instant in time

Figures 8.30 and 8.31 show the time-average and instantaneous distribution of the Nusselt number on the pin surface and endwall. The findings are very interesting. The instantaneous Nusselt numbers are significantly larger than the time-averaged values but occur only in very discrete regions. Surprisingly, the local heat transfer bubbles also occur on the pin surface. That indicates that the wake shedding is not only transient but also alternates over the height of the pin so that bubble-like vortices are shed and impinge on the pin surface. The horseshoe vortex is clearly visible at the junction between pin and endwall in the instantaneous snapshot (Figure 8.31). At another instant in time, the structure of the horseshoe vortex has changed as shown in Figure 8.32. The magnitude of the vortex has increased and it splits up to travel downward on either side of the pin.

Also, the shedding is a highly dynamic process as shown in three instantaneous snapshots in Figure 8.33. The wake points in frame one diagonally towards the downstream pin. The impingement on this pin causes the flow field to alter and flip so that the wake slowly turns down into the opposing direction. At this point, the shedded wake still travels downstream and hits the downstream pin with an delay. The impingement effect alter the flow field and the velocity and disconnects the wake from the pin. The eddy keeps rotating and diffuses as it travels downstream.

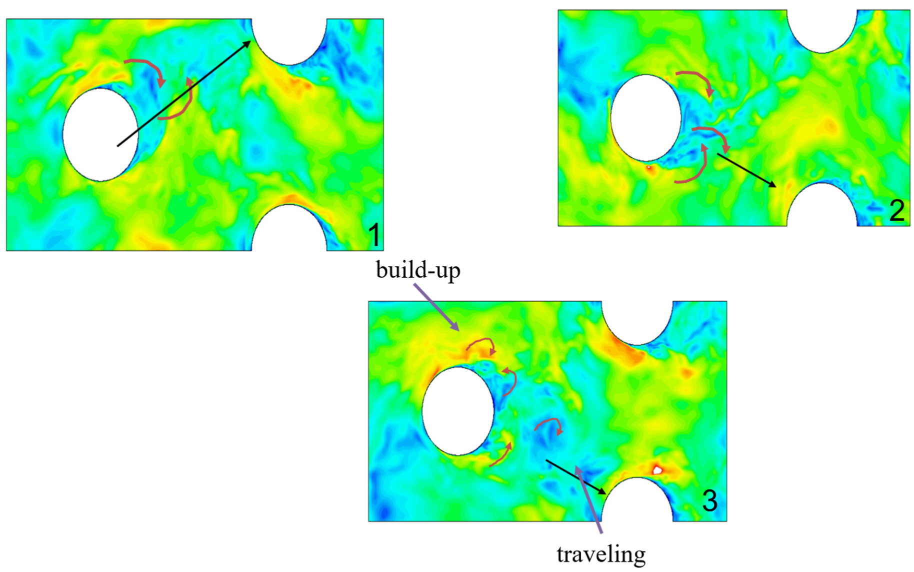

Figure 8.33: Instantaneous velocities showing the transient wake shedding effect

CHAPTER 9: CONCLUSION AND FUTURE WORK

The presented study aimed to investigate the vortex buildup, interaction of vortex structures and wake in a low aspect ratio pin fin array as commonly found in modern gas turbines for power generation and aviation. The nature of the flow characteristics is closely related to the heat transfer behavior of pins and endwall. The study was supplemented with two numerical simulations. Stereoscopic PIV was used in ten planes downstream of the first and third row at different channel heights to obtain detailed understanding of the turbulence characteristics. In summary it was found that the wake closure length decreases with increasing Reynolds Numbers as mixing occurs and the shear layer, which could act as a protective barrier between free stream and wake region, dissipates quicker. Details were shown by plotting the turbulent kinetic energy as well as each component of the Reynold stress tensor. Significant lateral velocities and velocity fluctuations were found which cause the flow field particularly close to the pin to be highly anisotropic. The wall-near horseshoe vortex system could not be identified within the provided data so that no conclusions between the interactions of the HSV with KV can be reported. A larger pin or close wall PIV measurements could advance the understanding in this area. The results from the transient thermochromic liquid crystal technique yielded the local distribution of heat transfer over the endwall upstream of row one up to downstream of row four. The observed array averaged Nusselt numbers were greater compared to what is reported in literature, however, the trends of normalized Nusselt number match exactly the expected results. Generally, the results obtained through TLC are highly convincing and exhibit a high degree of symmetry.

One of the reasons for overpredicting heat transfer might be a systematic error in the experimental setup. A thorough uncertainty and error analysis was conducted. A high sensitivity of the array Nusselt number on the material properties such as thermal

conductivity and thermal diffusivity of the base material was observed. The total error in array Nusselt number for the tested Reynolds numbers of 10,000 and 30,000 was 17.85% and 13.97%, respectively. However, some assumptions, in particular those for the accuracy of the material properties might be too optimistic what would eventually yield a higher uncertainty.

Despite the uncertainty, clear connections between the local distribution of the Nusselt number on the endwall and the observed vortical structures and turbulence patterns from PIV were made. A strong effect of the horseshoe vortex system upstream of the pin row one and three is responsible for high heat transfer upstream of the pin. Further downstream and with increasing flow rate, the vortex structure growth and removes more heat relatively. Although the legs of the horseshoe vortex wrap around the pin and also remove heat adjacent to the pin, the effect become less and less with a decreasing wake size. The von Kármán vortices shed in the wake of the cylinder become the main mode of heat removal from the endwall. Close to the pin, on Kármán vortices mix with the horseshoe vortex legs. With increasing flow rates, the wake becomes more and more unstable. In consequence, the KVs are not travel centered behind the pin but rather shed outside of the pin in a flip-flopping motion. The KVs impinge on the downstream pin row under an angle of approximately 45 degrees and alternate the flow field that the pin encounters. Here, the flow does not impinge centered on the pin but under the aforementioned angle. This causes to vortices shed from the downstream pin to travel into the opposite direction. The transient shedding increases overall turbulence levels due to high mixing of the wake region with the bulk flow and cause a rapid diffusion of dominant vortex structures as the travel downstream. This introduces a lateral momentum flux component and velocity which causes a highly homogeneous velocity distribution over the width of the channel. This trend was not at all picked up by the RANS simulations that were conducted as a supplement to the experimental work.

The numerical simulations were capable of predicting reasonably engineering quantities such as heat transfer and pressure drop, however failed to correctly model the flow physics as the strong contribution of shear layer eddies and shear layer diffusion was not captured. The shear layer breakdown occurs further downstream than predicted in CFD. The shielding behavior of the shear layers prevent lateral flow which causes an underprediction of heat transfer in the wake. Slight variations were found between the mid-plane and the wall-near region in terms of turbulence statistics and turbulent kinetic energy, indicating that the study of the mid-plane region is sufficient. However, it is strongly advised to repeat the study with time-resolved PIV. This might reveal different large-scale turbulent structures.

Further research could to be directed into the effect of fillets on the flow structures which dominated the endwall heat transfer. Due to fabrication limitations of investment casting, ideal shaped pins cannot be produced and are not desired from a lifing perspective. A PIV analysis with the methodology described in this paper can shed light onto the underlying physics and the impact on the occurring vortex structures thus heat transfer.

It is suggested to refine the transient thermochromic liquid crystal technique by using several paints with different green peak temperatures. This would allow to also measure the local heat transfer coefficient in the regions with small heat transfer. With shorter experimental times, the effect of lateral conduction becomes less important and increases the accuracy of the entire method. In addition, the accuracy of the local Nusselt number on the endwall close to the pin could be increased by utilizing the 1D conduction correction as outlined in the uncertainty chapter. As heat also conducts underneath the pin in a at least two-dimensional fashion, this correction would account for that error.

In conclusion, it can be said that the objectives of the studies were achieved with both experimental approaches, namely PIV and TLC, and significant differences in experimental data and CFD were observed. Comparing the vortical structures for either

approach helped to identify the shortcomings of the RANS results. Therefore, this dissertation is directly applicable to the gas turbine design engineers concerned with trialing edge cooling.

APPENDIX A: ADDITIONAL TEST RESULTS

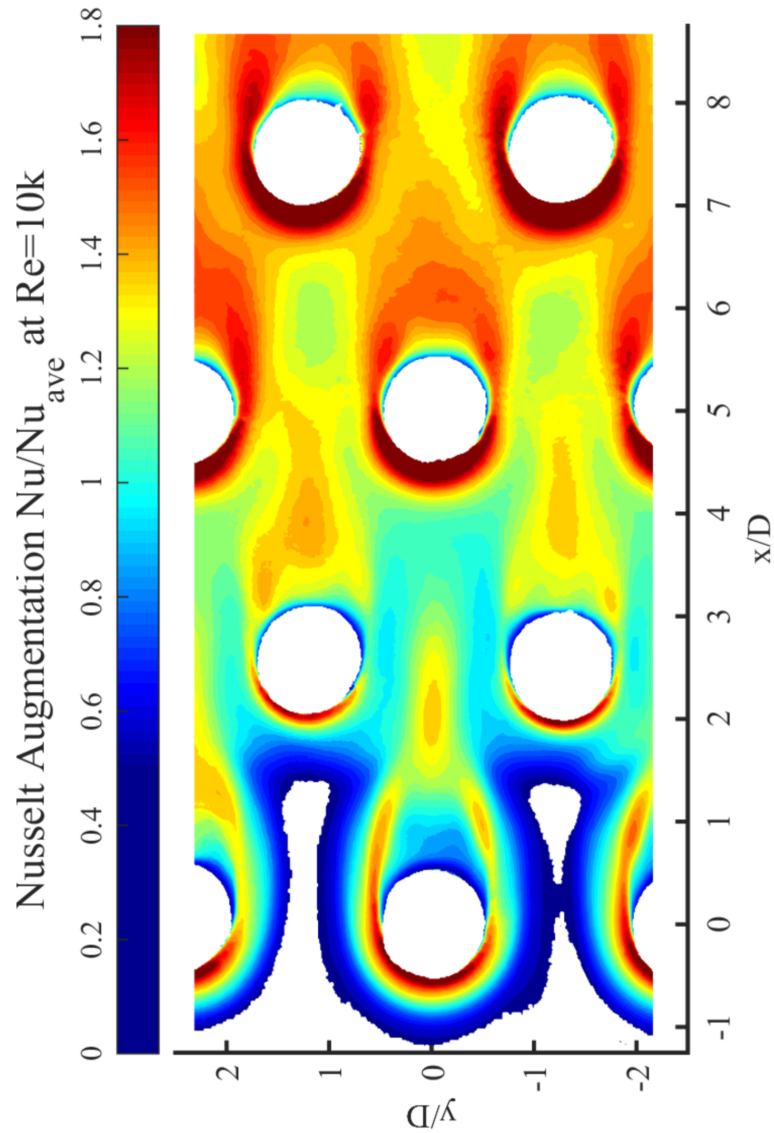

Figure A.1: Local Nusselt number augmentation normalized with array Nusselt number average reported by [5] at $Re = 10,000$

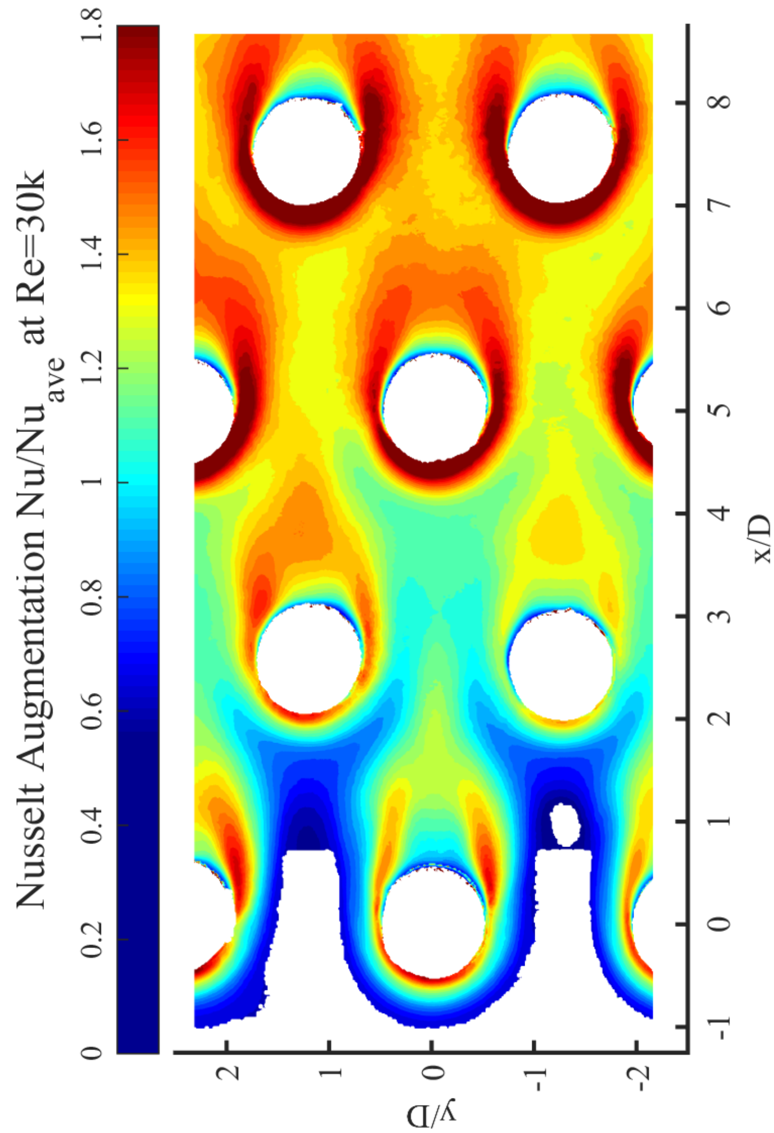

Figure A.2: Local Nusselt number augmentation normalized with array Nusselt number average reported by [5] at $Re = 30,000$

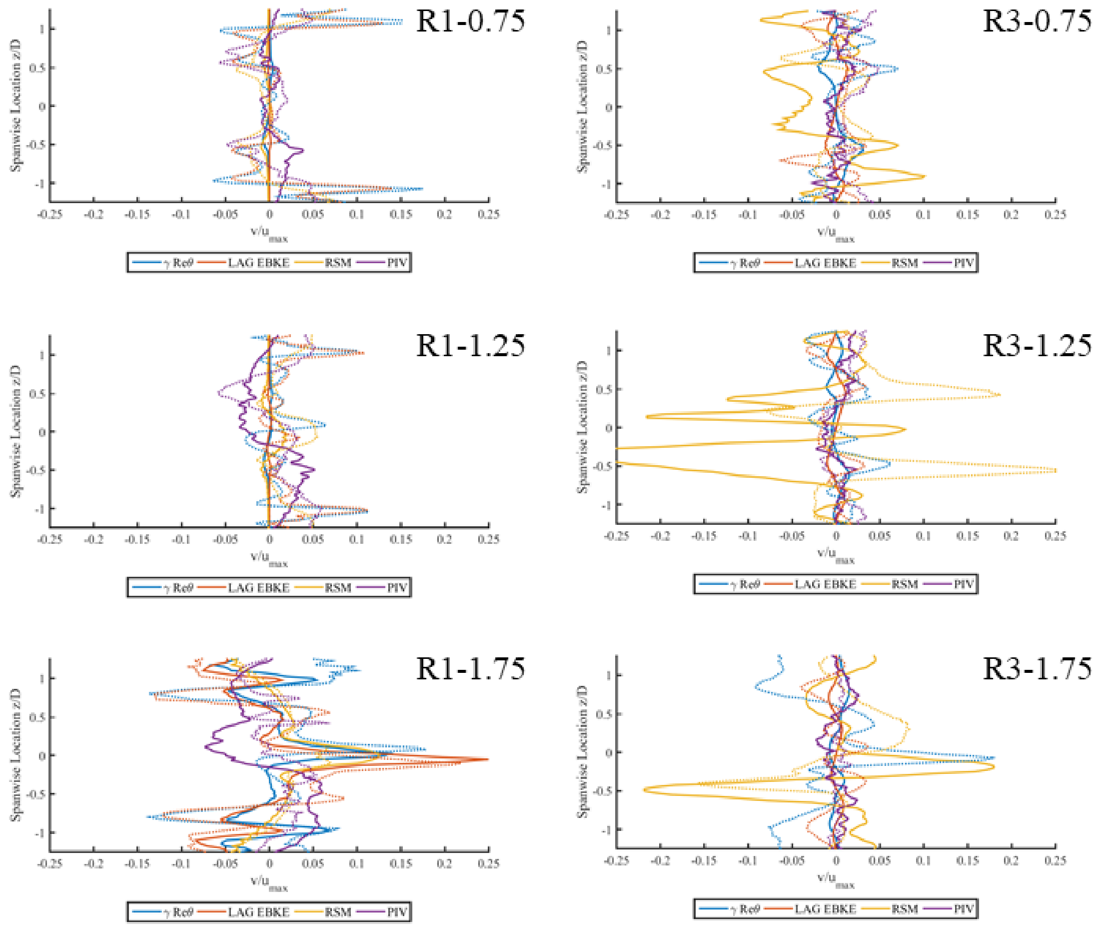

Figure A.3: Normalized spanwise velocity profiles of component v at $Re = 10,000$

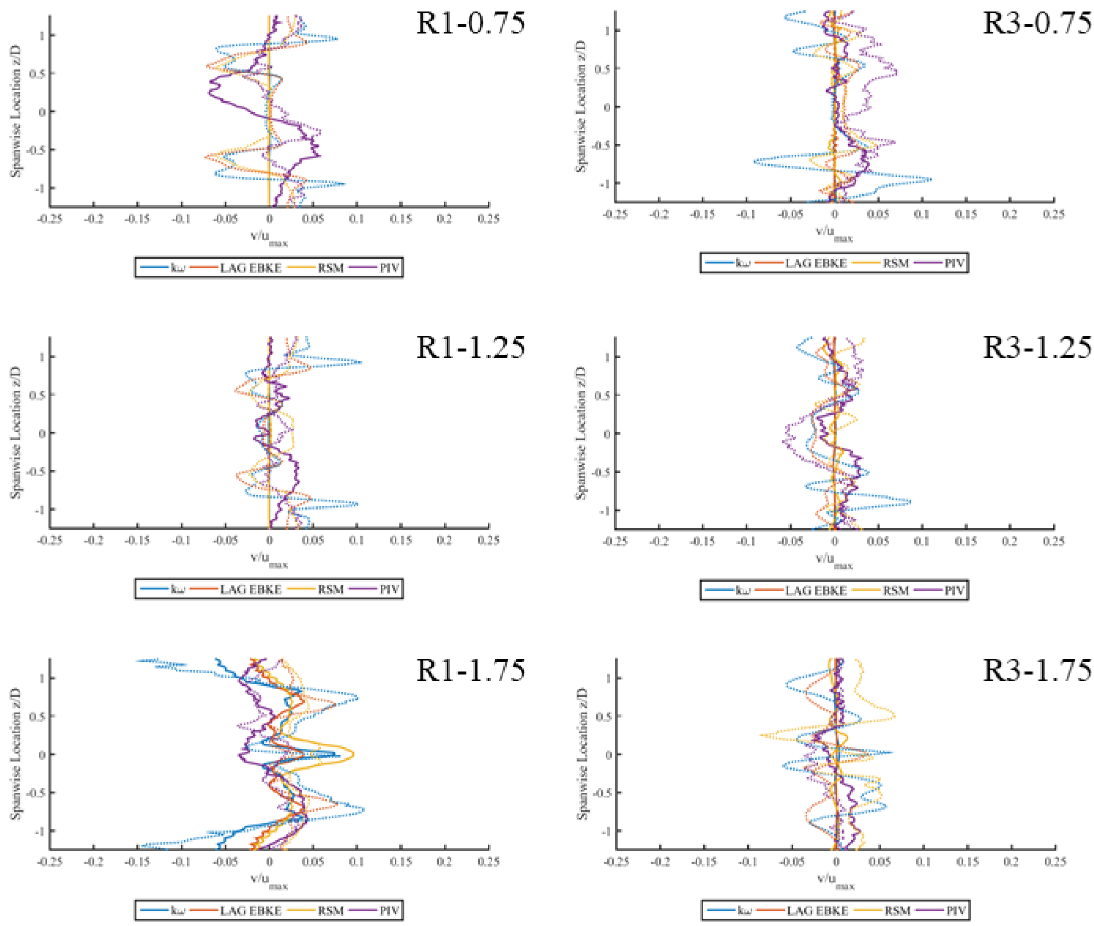

Figure A.4: Normalized spanwise velocity profiles of component v at $Re = 30,000$

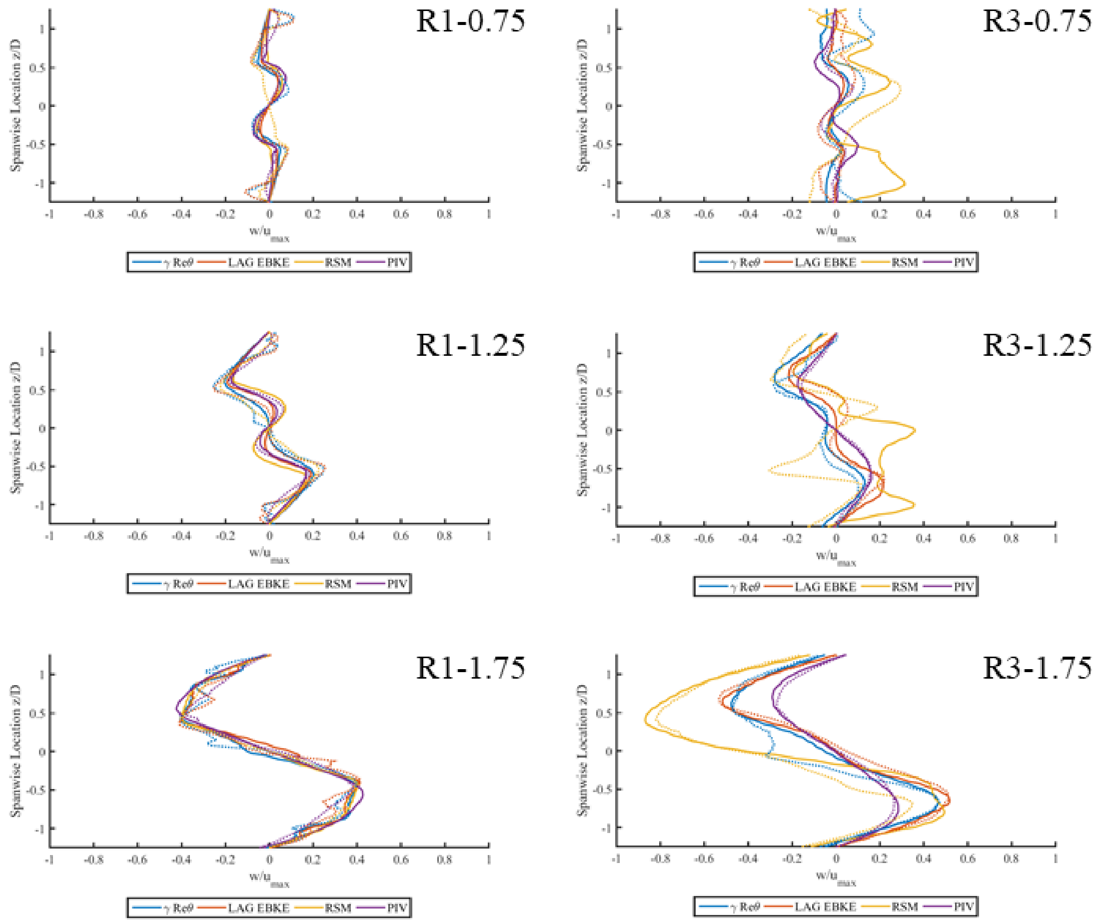

Figure A.5: Normalized spanwise velocity profiles of component w at $Re = 10,000$

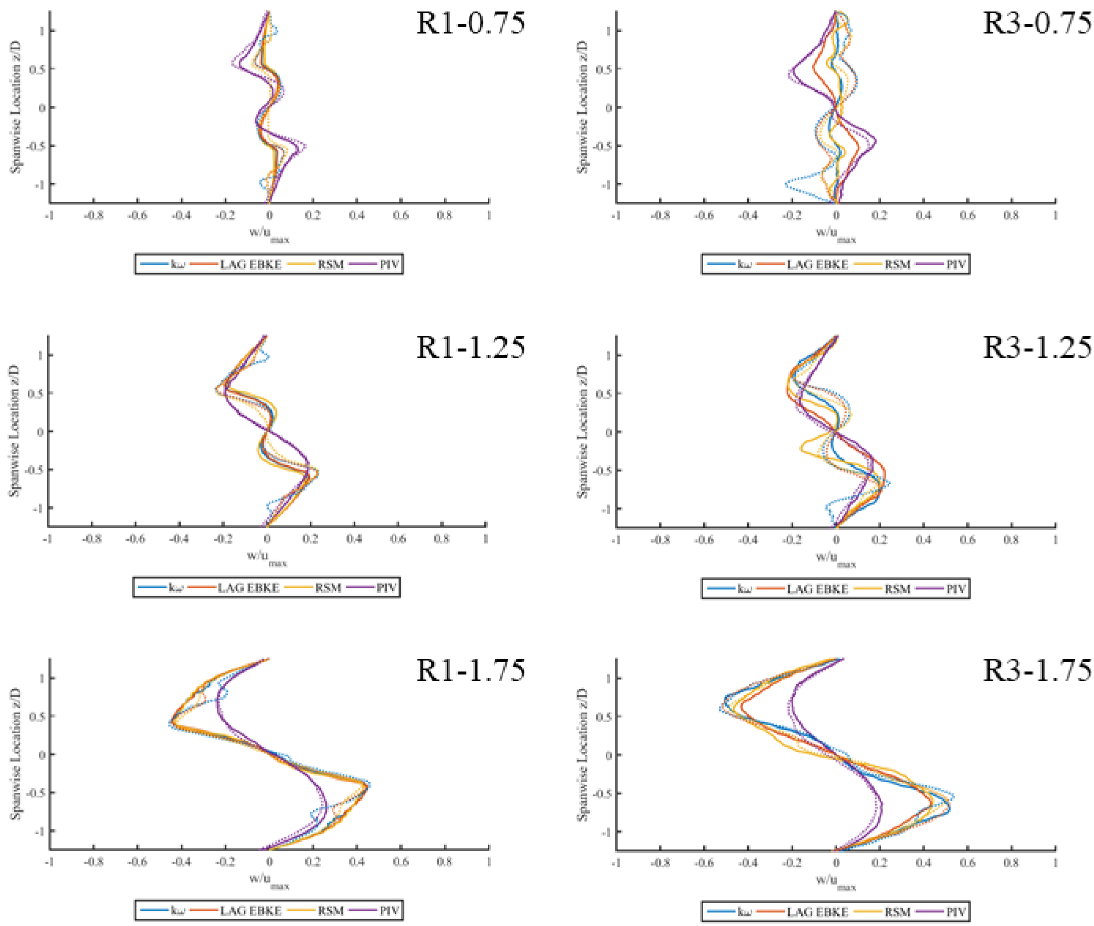

Figure A.6: Normalized spanwise velocity profiles of component w at $Re = 30,000$

APPENDIX B: MATLAB CODES

The TLC post-processing required several codes written in Matlab. All codes are listed in this appendix including the user-defined functions and pre and post-processing codes.

Listing B.1: TLCPreProcessing.m

```
% %%%%%     Post Processing TLC  %%%%%%%%%%%%%%%%%% %
% %         Marcel Otto, Gaurav Gupta, Jay Kapat  % %
% %  Sole Purpose of LAB and Experimental USAGE   % %
% %  Code is not to be comercialized              % %
% %%%%%%%%%%%%%%%%%%%%%%%%%%%%%%%%%%%%%%%%%%%%%%%%%% %

%main code
tic
clc;
clear all;
%%%%%%%%%%%%%%%USER VARIABLE%%%%%%%%%%%%%%%%%%%%%%%
Videoname='2019-9-26-test5_10k.mp4'; %Video name including file
   extension
fps=29.98; %29.98 specify frames per second of recording
first = 39; %first image with data reading, let's not mess with
   it and consider the acutal time when converting time-step to
   seconds
%green_threshold=100/255; %comes from calibration, for now
   defined as 86% of max intensity
%Please define the area of interest of the test. The imported
   images will
```

```
%be cropped to this size. The top left corner has the standard
   coord 0,0

%Left_Top_Corner_Height=509; %for actual TLC: 380
%Left_Top_Corner_Width=1038; %for actual TLC: 1
%Right_Bottom_Corner_Height=711; %, %for actual TLC: 847,   338
   for examply color circle import
%Right_Bottom_Corner_Width=1242;  % %for actual TLC: 1920,   640
   for example

Left_Top_Corner_Height=380; %for actual TLC: 380
Left_Top_Corner_Width=1; %for actual TLC: 1
Right_Bottom_Corner_Height=847; %, %for actual TLC: 847,   338
   for examply color circle import
Right_Bottom_Corner_Width=1920;  % %for actual TLC: 1920,   640
   for example
%%%%%%%%%%%END USER VARIABLE%%%%%%%%%%%%%%%%%%%%%%

%%%%%%%%%%%Initialization%%%%%%%%%%%%%%%%%%%%%%
dummy_frame_for_export=200;

%since the image is too big to be handled at once, the code will
   sweep
%through four cases separately and then stitch all the data
   togehter
```

```
Case1=[Left_Top_Corner_Height, Right_Bottom_Corner_Height,
   Left_Top_Corner_Width, Left_Top_Corner_Width+301];
Case2=[Left_Top_Corner_Height, Right_Bottom_Corner_Height,
   Left_Top_Corner_Width+299, Left_Top_Corner_Width+601];
Case3=[Left_Top_Corner_Height, Right_Bottom_Corner_Height,
   Left_Top_Corner_Width+599, Left_Top_Corner_Width+901];
Case4=[Left_Top_Corner_Height, Right_Bottom_Corner_Height,
   Left_Top_Corner_Width+899, Left_Top_Corner_Width+1201];
Case5=[Left_Top_Corner_Height, Right_Bottom_Corner_Height,
   Left_Top_Corner_Width+1199, Left_Top_Corner_Width+1501];
Case6=[Left_Top_Corner_Height, Right_Bottom_Corner_Height,
   Left_Top_Corner_Width+1499, Left_Top_Corner_Width+1801];
Case7=[Left_Top_Corner_Height, Right_Bottom_Corner_Height,
   Left_Top_Corner_Width+1799, Right_Bottom_Corner_Width];
%%%%%%%%%%%END Initialization%%%%%%%%%%%%%%%%%%%%%%

% %%%%%%%%%%%%%%%%%%%%%%%%%%%%%%%%%%%%%%%%%%%%%%%%% %
%0st : Play video to set first frame
% %%%%%%%%%%%%%%%%%%%%%%%%%%%%%%%%%%%%%%%%%%%%%%%%% %
%PlayVideo(Videoname);

% %%%%%%%%%%%%%%%%%%%%%%%%%%%%%%%%%%%%%%%%%%%%%%%%% %
%1st : Extract frames from video
% %%%%%%%%%%%%%%%%%%%%%%%%%%%%%%%%%%%%%%%%%%%%%%%%% %

```

```
disp('Start extracting Images from Video');
disp('Status: Running');
%ExtractFramesFromVideo(Videoname); %only on pause that images are not imported over and over
Videoname_no_extension=Videoname(1:end-4);
FolderName=sprintf(['Frames_', Videoname_no_extension]);

%Output some info text about progress
disp('Finished extracting Images from Video');
disp(' ');

%Check via user input if start frame is properly defined and if frames
%after test are deleted
%disp('Now it is time to delete the exported frames where the LED is turned off');
%t = timer('StartDelay',10,...
 %   'TimerFcn',@(~,~)delete(findall(groot,'WindowStyle','modal')));
%start(t)
%answer = questdlg('Would you like to open the folder to inspect the exported frames? Note the number of the start frame of the test, delete all frames after the test.',       'Show Frames');
```

```
% Handle response if clicked yes, 2 minute timer starts to inspect folder
% and figure out first frame number and delete frames after test
%if answer==1
%    winopen(FolderName);
%    t = timer('StartDelay',120,...
%    'TimerFcn',@(~,~)delete(findall(groot,'WindowStyle','modal')));
%    start(t)
%    promt = 'Please enter the starting frame number for import. You have 120 seconds to decide or otherwise all frames will be imported automatically.';
%    first=input(promt);

% Handle response if clicked no, 2 minute timer starts input first frame
% number and delete frames after test, if no input is made, all franes in folder will be imported
%elseif answer==2
%    t = timer('StartDelay',120,...
%    'TimerFcn',@(~,~)delete(findall(groot,'WindowStyle','modal')));
%    start(t)
```

```
%    promt = 'Please enter the starting frame number for import. You have 120 seconds to decide or otherwise all frames will be imported automatically.';
    % Handle response and set first value to user input. If no input
    % occurs, all frames from image 1 on will be imported
%    first=input(promt);
%end;

% %%%%%%%%%%%%%%%%%%%%%%%%%%%%%%%%%%%%%%%%%%%%%%%%%% %
%2nd : Read frames into one Array
% %%%%%%%%%%%%%%%%%%%%%%%%%%%%%%%%%%%%%%%%%%%%%%%%%% %
%for Case 1%

%Output some info text about progress
disp('Start importing Images to Matlab, Case1');
disp('Status: Running');

%calling user funtion to import frames into matlab. All frames are stored
%in Image_Collection_Numbered which has the structure (i location, j
%location, RGB layers, frame_number); The import is limited to the area of
%interest as defined in the USER VARIABLE Section
```

```
[Image_Collection_Numbered, pixel_i, pixel_j] = ImageReading(
    first, FolderName, Case1(1), Case1(3), Case1(2), Case1(4));
whos Image_Collection_Numbered
Only_Green=Image_Collection_Numbered(:,:,2,:);
whos Only_Green
clear Image_Collection_Numbered;
%Output some info text about progress
disp('Finished importing Images to Matlab');
disp(' ');
%imshow(Image_Collection_Numbered(:,:,:,dummy_frame_for_export));
%imwrite(Image_Collection_Numbered(:,:,:,dummy_frame_for_export)
    ,'Image_as_read.png');

% %%%%%%%%%%%%%%%%%%%%%%%%%%%%%%%%%%%%%%%%%%%%%%%%% %
%3rd : Image Post Processing and Averaging
% %%%%%%%%%%%%%%%%%%%%%%%%%%%%%%%%%%%%%%%%%%%%%%%%% %

%Output some info text about progress
tic
disp('Start time-averaging images');
disp('Status: Running');

%calling user funtion to time-average frames with a centered
    moving mean of
%3 data points
```

```
Images_Time_Averaged=ImageTimeAverage(Only_Green);
clear Only_Green;

%Output some info text about progress
disp('Finished time-averaging images in');
toc
disp(' ');
%imshow(Images_Time_Averaged(:,:,:,dummy_frame_for_export));
%imwrite(Images_Time_Averaged(:,:,:,dummy_frame_for_export),'Image_time_averaged.png');


disp('Start xy-averaging images');
disp('Status: Running');

%calling user funtion to XY-average frames with a weighted filter. The
%center pixel counts for 60%, all eight sourrunding pixels count 5% each.
XYt_averaged_Images=XYRollingAverage(Images_Time_Averaged, pixel_i, pixel_j);
% try
%     export=squeeze(XYt_averaged_Images(400,200,1,:));
%     save('squeeze.mat', 'export', '-v7');
% catch
```

```
%     disp('Something wrong here, skipping');
% end

clear Images_Time_Averaged;

%Output some info text about progress
disp('Finished xy-averaging images in');
disp(' ');
%imshow(XYt_averaged_Images(:,:,:,dummy_frame_for_export));
%imwrite(XYt_averaged_Images(:,:,:,dummy_frame_for_export),'
    Image_xyt_averaged.png');


% %%%%%%%%%%%%%%%%%%%%%%%%%%%%%%%%%%%%%%%%%%%%%%%%%%% %
%5th : Green Peak Arrival Time Calculator
% %%%%%%%%%%%%%%%%%%%%%%%%%%%%%%%%%%%%%%%%%%%%%%%%%% %
tic
disp('Start calculating green peak arrival time');
disp('Status: Running');
%GreenPeakArrivalTime_threshold_method=
    GreenPeakArrivalTimeCalculator(XYt_averaged_Images, pixel_i,
    pixel_j,green_threshold, fps);

%value in timehistory and then checks if larger than threshold
    and saves
```

```
%value and time, otherwise rejected
%[GreenPeakArrivalTime_max_value_method, max_green_value]=
   GreenPeakArrivalTimeCalculator2(XYt_averaged_Images, pixel_i,
   pixel_j,green_threshold, fps);


GreenpeakArrivalTime1=peakfinding(XYt_averaged_Images, pixel_i,
   pixel_j);
disp('Finished calculating green peak arrival time');
toc
disp(' ');

clear pixel_i;
clear pixel_j;
clear XYt_averaged_Images;
disp('Case 1 finished, continuing with remaining cases');
% %%%%%%%%%%%%%%%%%%%%%%%%%%%%%%%%%%%%%%%%%%%%%%%%% %
%6th : repeat code for remaining cases
% %%%%%%%%%%%%%%%%%%%%%%%%%%%%%%%%%%%%%%%%%%%%%%%%% %
%%%%%%%%%%%%%
%%CASE 2%%%%%%%

[Image_Collection_Numbered, pixel_i, pixel_j] = ImageReading(
   first, FolderName, Case2(1), Case2(3), Case2(2), Case2(4));
Only_Green=Image_Collection_Numbered(:,:,2,:);
```

```
clear Image_Collection_Numbered;

Images_Time_Averaged=ImageTimeAverage(Only_Green);
clear Only_Green;

XYt_averaged_Images=XYRollingAverage(Images_Time_Averaged,
   pixel_i, pixel_j);
clear Images_Time_Averaged;
GreenpeakArrivalTime2=peakfinding(XYt_averaged_Images, pixel_i,
   pixel_j);

clear pixel_i;
clear pixel_j;
clear XYt_averaged_Images;
disp('Case 2 finished, continuing with remaining cases');

%%CASE 3%%%%%%%
[Image_Collection_Numbered, pixel_i, pixel_j] = ImageReading(
   first, FolderName, Case3(1), Case3(3), Case3(2), Case3(4));
Only_Green=Image_Collection_Numbered(:,:,2,:);
clear Image_Collection_Numbered;

Images_Time_Averaged=ImageTimeAverage(Only_Green);
clear Only_Green;

```

```
XYt_averaged_Images=XYRollingAverage(Images_Time_Averaged,
   pixel_i, pixel_j);
clear Images_Time_Averaged;
GreenpeakArrivalTime3=peakfinding(XYt_averaged_Images, pixel_i,
   pixel_j);

clear pixel_i;
clear pixel_j;
clear XYt_averaged_Images;
disp('Case 3 finished, continuing with remaining cases');

%%CASE 4%%%%%%
[Image_Collection_Numbered, pixel_i, pixel_j] = ImageReading(
   first, FolderName, Case4(1), Case4(3), Case4(2), Case4(4));
Only_Green=Image_Collection_Numbered(:,:,2,:);
clear Image_Collection_Numbered;

Images_Time_Averaged=ImageTimeAverage(Only_Green);
clear Only_Green;

XYt_averaged_Images=XYRollingAverage(Images_Time_Averaged,
   pixel_i, pixel_j);
clear Images_Time_Averaged;
GreenpeakArrivalTime4=peakfinding(XYt_averaged_Images, pixel_i,
   pixel_j);
```

```
clear pixel_i;
clear pixel_j;
clear XYt_averaged_Images;
disp('Case 4 finished, continuing with remaining cases');

%%CASE 5%%%%%%%
[Image_Collection_Numbered, pixel_i, pixel_j] = ImageReading(
   first, FolderName, Case5(1), Case5(3), Case5(2), Case5(4));
Only_Green=Image_Collection_Numbered(:,:,2,:);
clear Image_Collection_Numbered;

Images_Time_Averaged=ImageTimeAverage(Only_Green);
clear Only_Green;

XYt_averaged_Images=XYRollingAverage(Images_Time_Averaged,
   pixel_i, pixel_j);
clear Images_Time_Averaged;
GreenpeakArrivalTime5=peakfinding(XYt_averaged_Images, pixel_i,
   pixel_j);

clear pixel_i;
clear pixel_j;
clear XYt_averaged_Images;
disp('Case 5 finished, continuing with remaining cases');
```

```

%%CASE 6%%%%%%
[Image_Collection_Numbered, pixel_i, pixel_j] = ImageReading(
   first, FolderName, Case6(1), Case6(3), Case6(2), Case6(4));
Only_Green=Image_Collection_Numbered(:,:,2,:);
clear Image_Collection_Numbered;

Images_Time_Averaged=ImageTimeAverage(Only_Green);
clear Only_Green;

XYt_averaged_Images=XYRollingAverage(Images_Time_Averaged,
   pixel_i, pixel_j);
clear Images_Time_Averaged;
GreenpeakArrivalTime6=peakfinding(XYt_averaged_Images, pixel_i,
   pixel_j);

clear pixel_i;
clear pixel_j;
clear XYt_averaged_Images;
disp('Case 6 finished, continuing with remaining cases');

%%CASE 7%%%%%%
[Image_Collection_Numbered, pixel_i, pixel_j] = ImageReading(
   first, FolderName, Case7(1), Case7(3), Case7(2), Case7(4));
Only_Green=Image_Collection_Numbered(:,:,2,:);
```

```
clear Image_Collection_Numbered;

Images_Time_Averaged=ImageTimeAverage(Only_Green);
clear Only_Green;

XYt_averaged_Images=XYRollingAverage(Images_Time_Averaged,
    pixel_i, pixel_j);
clear Images_Time_Averaged;
GreenpeakArrivalTime7=peakfinding(XYt_averaged_Images, pixel_i,
    pixel_j);

clear pixel_i;
clear pixel_j;
clear XYt_averaged_Images;
disp('Case 7 finished, continuing with remaining cases');

% %%%%%%%%%%%%%%%%%%%%%%%%%%%%%%%%%%%%%%%%%%%%%%%%% %
%Save workspace, just in case!
% %%%%%%%%%%%%%%%%%%%%%%%%%%%%%%%%%%%%%%%%%%%%%%%%% %
%create file name for saving
subfolder='Pre_Processing_Data';
saving_filename=[subfolder, '/', Videoname_no_extension,'.mat'];
if exist(subfolder, 'dir')
    disp('Saving to existing folder');
    save(saving_filename, '-v7');
```

```
    disp('File successfully saved!');

else
    disp('Saving to new folder');
    mkdir(subfolder);
    save(saving_filename, '-v7');
    disp('File successfully saved!');
end



% %%%%%%%%%%%%%%%%%%%%%%%%%%%%%%%%%%%%%%%%%%%%%%%%% %
%7th : Stitch together the Time Matrix
% %%%%%%%%%%%%%%%%%%%%%%%%%%%%%%%%%%%%%%%%%%%%%%%%% %
GreenpeakArrivalTime=NaN(Right_Bottom_Corner_Height-Left_Top_Corner_Height+1, Right_Bottom_Corner_Width-Left_Top_Corner_Width-1);
GreenpeakArrivalTime(1:Right_Bottom_Corner_Height-Left_Top_Corner_Height+1, 1:300)=GreenpeakArrivalTime1(:,1:300);
GreenpeakArrivalTime(1:Right_Bottom_Corner_Height-Left_Top_Corner_Height+1, 301:600)=GreenpeakArrivalTime2(:,1:300);
```

```
GreenpeakArrivalTime(1:Right_Bottom_Corner_Height-
    Left_Top_Corner_Height+1, 601:900)=GreenpeakArrivalTime3
    (:,1:300);
GreenpeakArrivalTime(1:Right_Bottom_Corner_Height-
    Left_Top_Corner_Height+1, 901:1200)=GreenpeakArrivalTime4
    (:,1:300);
GreenpeakArrivalTime(1:Right_Bottom_Corner_Height-
    Left_Top_Corner_Height+1, 1201:1500)=GreenpeakArrivalTime5
    (:,1:300);
GreenpeakArrivalTime(1:Right_Bottom_Corner_Height-
    Left_Top_Corner_Height+1, 1501:1800)=GreenpeakArrivalTime6
    (:,1:300);
GreenpeakArrivalTime(1:Right_Bottom_Corner_Height-
    Left_Top_Corner_Height+1, 1801:Right_Bottom_Corner_Width-1)=
    GreenpeakArrivalTime7(:,1:Right_Bottom_Corner_Width-1801);
% %%%%%%%%%%%%%%%%%%%%%%%%%%%%%%%%%%%%%%%%%%%%%%%%%% %
%8th : Save workspace again
% %%%%%%%%%%%%%%%%%%%%%%%%%%%%%%%%%%%%%%%%%%%%%%%%%% %
%create file name for saving
subfolder='Pre_Processing_Data';
saving_filename=[subfolder, '/', Videoname_no_extension,'.mat'];
if exist(subfolder, 'dir')
    disp('Saving to existing folder');
    save(saving_filename, 'GreenpeakArrivalTime', '-v7');
    disp('File successfully saved!');
```

```
else
    disp('Saving to new folder');
    mkdir(subfolder);
    save(saving_filename, 'GreenpeakArrivalTime', '-v7');
    disp('File successfully saved!');
end

toc
disp('Total Time');
disp('Code successfully executed');
```

Listing B.2: TLCCalibration.m

```
% %%%%     Post Processing TLC  %%%%%%%%%%%%%%%%%% %
% %         Marcel Otto, Gaurav Gupta, Jay Kapat  % %
% %  Sole Purpose of LAB and Experimental USAGE   % %
% %  Code is not to be comercialized              % %
% %%%%%%%%%%%%%%%%%%%%%%%%%%%%%%%%%%%%%%%%%%%%%%%%%% %

%TLC Calibration Code
tic
clc;
clear all;
%% %%%%%%%%%%%%USER VARIABLE%%%%%%%%%%%%%%%%%%%%%%
Videoname1='2019-10-22-Calibration.mp4'; %Video name including
   file extension
fps=29.98; %29.98 specify frames per second of recording
first = 1; %first image with data reading, let's not mess with it
    and consider the acutal time when converting time-step to
   seconds
% Curve fit values from excel Ax^2+Bx+C
A1=  1.5666897898E-06;
B1=4.4671955187E-04;
C1=5.4901036836E+01;

%green_threshold=100/255; %comes from calibration, for now
   defined as 86% of max intensity
```

```
%Please define the area of interest of the test. The imported images will
%be cropped to this size. The top left corner has the standard coord 0,0
Left_Top_Corner_Height1=504; %for actual TLC: 380
Left_Top_Corner_Width1=42; %for actual TLC: 1
Right_Bottom_Corner_Height1=813; %, %for actual TLC: 847,   338 for examply color circle import
Right_Bottom_Corner_Width1=1794;  % %for actual TLC: 1920,   640 for example
Calibration_Region1=[Left_Top_Corner_Height1, Right_Bottom_Corner_Height1, Left_Top_Corner_Width1, Right_Bottom_Corner_Width1];
%NotchLocations=[51, 481, 921, 1359, 1794];
NotchLocations=[51, 481, 921, 1359, 1794];

%%%%%%%%%%%END USER VARIABLE%%%%%%%%%%%%%%%%%%%%%%

%% %%%%%%%%%%%%%%%%%%%%%%%%%%%%%%%%%%%%%%%%%%%%%%%% %
%1st : Extract frames from video
% %%%%%%%%%%%%%%%%%%%%%%%%%%%%%%%%%%%%%%%%%%%%%%%%% %

disp('Start extracting Images from Video');
disp('Status: Running');
```

```matlab
%ExtractFramesFromVideo(Videoname); %only on pause that images are not imported over and over
Videoname_no_extension1=Videoname1(1:end-4);
FolderName1=sprintf(['Frames_', Videoname_no_extension1]);

%Output some info text about progress
disp('Finished extracting Images from Video');
disp(' ');

%% %%%%%%%%%%%%%%%%%%%%%%%%%%%%%%%%%%%%%%%%%%%%%%%% %
%2nd : Read frames into one Array
% %%%%%%%%%%%%%%%%%%%%%%%%%%%%%%%%%%%%%%%%%%%%%%%%% %
%for Case 1%

%Output some info text about progress
disp('Start importing Images to Matlab, Case1');
disp('Status: Running');

%calling user funtion to import frames into matlab. All frames are stored
%in Image_Collection_Numbered which has the structure (i location , j
%location, RGB layers, frame_number); The import is limited to the area of
%interest as defined in the USER VARIABLE Section
```

```
% Before importing calibration images, make sure the first image
   in the
% folder is the background, meaning no colors on the surface.
   Otherwise all
% color information will be lost during import

% % Check if calibration has been done already
Calibration_Name1=[Videoname_no_extension1,'.mat'];
if exist(fullfile(pwd, Calibration_Name1))==2;
    load(Calibration_Name1);
    disp('Calibration Data successfully loaded');
else
    disp('Calibration Data did not exist. Creating Look up Table!
       ');
    [Image_Collection_Numbered1, pixel_i1, pixel_j1] =
       ImageReading(first, FolderName1, Calibration_Region1(1),
       Calibration_Region1(3), Calibration_Region1(2),
       Calibration_Region1(4));
%clear Image_Collection_Numbered;
%Output some info text about progress

%% %%%%%%%%%%%%%%%%%%%%%%%%%%%%%%%%%%%%%%%%%%%%%% %
%3rd : Average value for each pixel from all imported images (
   average over
%time series
```

```
% %%%%%%%%%%%%%%%%%%%%%%%%%%%%%%%%%%%%%%%%%%%%%%%%% %
    Averaged1=[];
    for i=1:pixel_i1
        for j=1:pixel_j1
            Averaged1(i,j,1) = mean(Image_Collection_Numbered1(i,
               j,1, 2:end))+0.05;
            Averaged1(i,j,2) = mean(Image_Collection_Numbered1(i,
               j,2, 2:end))+0.05;
            Averaged1(i,j,3) = mean(Image_Collection_Numbered1(i,
               j,3, 2:end))+0.05;
        end
    end
    clear Image_Collection_Numbered;
    save(Calibration_Name1);

    disp('Calibration Images were processed and saved!');
end
disp('Finished importing Images to Matlab');
disp(' ');

%% %%%%%%%%%%%%%%%%%%%%%%%%%%%%%%%%%%%%%%%%%%%%%%%% %
%4th : apply filter matrix to smooth pixels

tic
```

```
%Original=Images_Time_Averaged(:,:,:,:);  %if averaging in space first, than time: replace Images_Time_Averaged with Image_Collection_Numbered and timestep_number with pic_number
FilterMatrix=[0.05 0.05 0.05; 0.05 0.6 0.05; 0.05 0.05 0.05];
    XY_averaged_Image1(:, :,1)=imfilter(Averaged1(:,:,1), FilterMatrix); %note the one at the RGB location, even though Green is 2, it is changed to 1 as only Green is imported during ImageRead
    XY_averaged_Image1(:, :,2)=imfilter(Averaged1(:,:,2), FilterMatrix); %note the one at the RGB location, even though Green is 2, it is changed to 1 as only Green is imported during ImageRead
    XY_averaged_Image1(:, :,3)=imfilter(Averaged1(:,:,3), FilterMatrix); %note the one at the RGB location, even though Green is 2, it is changed to 1 as only Green is imported during ImageRead
toc
disp('Time for x y Averaging');

disp('Importing Temperature Table');

%% %%%%%%%%%%%%%%%%%%%%%%%%%%%%%%%%%%%%%%%%% %
%5th : read excel file with temp readings / actually never mind. We don't
```

```
%have the curve fit tool box. So instead we import the curve fitting params
%from excel
% % read Excel file as specified above %%%
TC_Locations=[NotchLocations(1), ...                                % TC location 0
    NotchLocations(2), ...                                          % TC location 3
    floor(NotchLocations(2)+(NotchLocations(3)-NotchLocations(2))/6*3), ...    % TC location beginning 4.5
    floor(NotchLocations(2)+(NotchLocations(3)-NotchLocations(2))/6*4), ...    % TC location beginning 5        % TC location beginning
    floor(NotchLocations(2)+(NotchLocations(3)-NotchLocations(2))/6*5), ...    % TC location beginning 5.5
    NotchLocations(3), ...                                          % TC location beginning 6
    floor(NotchLocations(3)+(NotchLocations(4)-NotchLocations(3))/6*1),...     % TC location beginning 6.5
    floor(NotchLocations(3)+(NotchLocations(4)-NotchLocations(3))/6*2),...     % TC location beginning 7
```

```
    floor(NotchLocations(3)+(NotchLocations(4)-NotchLocations(3))/6*3),...      % TC location beginning 7.5
    NotchLocations(4),...                                                        % TC location beginning 9
    NotchLocations(5)];                                                          % TC location beginning 12

%% Create temperature curve per pixel based on correlation
x_values=[1:pixel_j1];
Curvefitted_Temperatur1e=NaN(1,pixel_j1);
for k=1:length(Curvefitted_Temperatur1e)
    Curvefitted_Temperatur1e(k)=(x_values(k)*x_values(k)).*A1+x_values(k).*B1+C1;
end

%% plot intensity versus coordinate

row_number_for_plot1=170;
close all;
figure('PaperPosition', [0 0 8.75 5])
hold on
set(gcf, 'Position', get(0, 'Screensize'));
hold on
```

```
red1=XY_averaged_Image1(row_number_for_plot1,:,1);
green1=XY_averaged_Image1(row_number_for_plot1,:,2);
blue1=XY_averaged_Image1(row_number_for_plot1,:,3);
red_plot1 = plot( red1,'Color','r', 'LineWidth', 2);
green_plot1 = plot( green1,'Color','g', 'LineWidth', 2);
blue_plot1 = plot( blue1, 'Color','b', 'LineWidth', 2);
golay_length1=701;
golay_red1=sgolayfilt(red1,7,golay_length1);
golay_green1=sgolayfilt(green1,7,golay_length1);
golay_blue1=sgolayfilt(blue1,3,golay_length1);
%red_fitted_plot = plot( golay_red, ':', 'Color','r', 'LineWidth
   ', 2);
green_fitted_plot1 =plot( golay_green1, ':', 'Color','g', '
   LineWidth', 2);
%blue_fitted_plot =plot( golay_blue, ':',  'Color','b', '
   LineWidth', 2);
[peaks1, locations1]=findpeaks(golay_green1, 'SortStr', 'descend'
   );
marker1=scatter(locations1(1), peaks1(1), 180, 'v', 'filled', '
   MarkerFaceColor', 'g' );
xlim([0 length(green1)]);
ylim([0 max(green1)+0.2]);

greenPeak_line1=line([locations1(1) locations1(1)], [0 peaks1(1)
   ]);
```

```
greenPeak_line1.LineWidth=2;
greenPeak_line1.LineStyle=':';
greenPeak_line1.Color='black';
hXLabel = xlabel('Pixel Location');
set(hXLabel, 'FontName', 'Times New Roman','FontSize', 16);
set(gca, 'FontName', 'Times New Roman', 'FontSize', 16);
hYLabel = ylabel('Color Intensity');
set(hYLabel, 'FontName', 'Times New Roman','FontSize', 16);
ax=gca;
ax.FontSize = 16;
ax.TickDir = 'in';
ax.LineWidth=2;

Image_savename1=['Intensity_per_Pixel_' Videoname_no_extension1 '
    .png'];
saveas(gcf, Image_savename1)

close all
hold off


hold on
%% plot intensity versus Temperature

close all;
```

```
figure('PaperPosition', [0 0 8.75 5])
hold on
set(gcf, 'Position', get(0, 'Screensize'));
hold on
red1=XY_averaged_Image1(row_number_for_plot1,:,1);
green1=XY_averaged_Image1(row_number_for_plot1,:,2);
blue1=XY_averaged_Image1(row_number_for_plot1,:,3);
red_plot1 = plot(Curvefitted_Temperatur1e, red1,'Color','r', 'LineWidth', 2);
green_plot1 = plot(Curvefitted_Temperatur1e, green1,'Color','g', 'LineWidth', 2);
blue_plot1 = plot(Curvefitted_Temperatur1e, blue1, 'Color','b', 'LineWidth', 2);
golay_length1=701;
golay_red1=sgolayfilt(red1,7,golay_length1);
golay_green1=sgolayfilt(green1,7,golay_length1);
golay_blue1=sgolayfilt(blue1,3,golay_length1);
%red_fitted_plot = plot( golay_red, ':', 'Color','r', 'LineWidth', 2);
green_fitted_plot1 =plot(Curvefitted_Temperatur1e, golay_green1, ':', 'Color','g', 'LineWidth', 2);
%blue_fitted_plot =plot( golay_blue, ':',  'Color','b', 'LineWidth', 2);
[peaks1, locations1]=findpeaks(golay_green1, 'SortStr', 'descend');
```

```
marker1=scatter(Curvefitted_Temperatur1e(locations1(1)), peaks1
    (1), 180, 'v', 'filled', 'MarkerFaceColor', 'g' );
xlim([55 62]);
ylim([0 0.4]);

GreenPeakTemperature1=Curvefitted_Temperatur1e(locations1(1));


greenPeak_line1=line([Curvefitted_Temperatur1e(locations1(1))
    Curvefitted_Temperatur1e(locations1(1))], [0 peaks1(1)]);
greenPeak_line1.LineWidth=2;
greenPeak_line1.LineStyle=':';
greenPeak_line1.Color='black';
hXLabel = xlabel('Temperature C');
set(hXLabel, 'FontName', 'Times New Roman','FontSize', 16);
set(gca, 'FontName', 'Times New Roman', 'FontSize', 16);
hYLabel = ylabel('Color Intensity');
set(hYLabel, 'FontName', 'Times New Roman','FontSize', 16);
ax=gca;
ax.FontSize = 16;
ax.TickDir = 'in';
ax.LineWidth=2;
% textfield=text(100,100,['\downarrow Green Peak Temperature',
    char(GreenPeakTemperature), ' deg C'])
```

```
% text(100,100, ['Green Peak Temperature' char(
   GreenPeakTemperature)])
set(gca, 'XTick', unique([GreenPeakTemperature1, get(gca, 'XTick'
   )]));
Image_savename1=['Intensity_per_Temperature_'
   Videoname_no_extension1 '.png'];
saveas(gcf, Image_savename1)


disp('and here is the green peak temperature in C')
disp(GreenPeakTemperature1)
```

Listing B.3: PlayVideo.m

```
% %%%%%     Post Processing TLC  %%%%%%%%%%%%%%%%%% %
% %         Marcel Otto, Gaurav Gupta, Jay Kapat  % %
% %  Sole Purpose of LAB and Experimental USAGE   % %
% %  Code is not to be comercialized              % %
% %%%%%%%%%%%%%%%%%%%%%%%%%%%%%%%%%%%%%%%%%%%%%%%%% %
function PlayVideo(Videoname);
t = timer('StartDelay',10,...
    'TimerFcn',@(~,~)delete(findall(groot,'WindowStyle','modal')));
start(t)
answer = questdlg('Would you like to play the video? For example to check for quality, if correctly cropped, etc? You have 10 seconds to decide or otherwise video playback will be skipped automatically.',    'Video');
% Handle response
if answer==1

        workspace;  % Make sure the workspace panel is showing.
        folder = fullfile(pwd, 'Videos'); %location of the video file relative to the working directory
        movieFullFileName = fullfile(folder, Videoname); %name of the video

        if ~exist(movieFullFileName, 'file')
```

```
        strErrorMessage = sprintf('File not found:\n%s\nYou can choose a new one, or cancel', movieFullFileName);
        response = questdlg(strErrorMessage, 'File not found', 'OK - choose a new movie.', 'Cancel', 'OK - choose a new movie.');
        if strcmpi(response, 'OK - choose a new movie.')
            [baseFileName, folderName, FilterIndex] = uigetfile('*.*');
            if ~isequal(baseFileName, 0)
                movieFullFileName = fullfile(folderName, baseFileName);
            else
                return;
            end
        else
            return;
        end
    end

    try
        implay(movieFullFileName)



```

```
            end

else

        disp([answer 'No video will be shown. Continue with
           algorithm'])

end

close all;  % Close all figures (except those of imtool.)
imtool close all;  % Close all imtool figures.
```

Listing B.4: ExtractFramesFromVideo.m

```
% %%%%     Post Processing TLC  %%%%%%%%%%%%%%%%%% %
% %          Marcel Otto, Gaurav Gupta, Jay Kapat  % %
% %  Sole Purpose of LAB and Experimental USAGE   % %
% %  Code is not to be comercialized              % %
% %%%%%%%%%%%%%%%%%%%%%%%%%%%%%%%%%%%%%%%%%%%%%%%%%% %
function ExtractFramesFromVideo(Videoname)

tic


%clc;    % Clear the command window.
%close all;  % Close all figures (except those of imtool.)
%imtool close all;  % Close all imtool figures.
%clear;  % Erase all existing variables.
workspace;  % Make sure the workspace panel is showing.
fontSize = 14;


folder = fullfile(pwd, 'Videos'); %location of the video file
   relative to the working directory
movieFullFileName = fullfile(folder, Videoname); %name of the
   video

if ~exist(movieFullFileName, 'file')
```

```
		strErrorMessage = sprintf('File not found:\n%s\nYou can choose a new one, or cancel', movieFullFileName);
		response = questdlg(strErrorMessage, 'File not found', 'OK - choose a new movie.', 'Cancel', 'OK - choose a new movie.');
		if strcmpi(response, 'OK - choose a new movie.')
			[baseFileName, folderName, FilterIndex] = uigetfile('*.*');
			if ~isequal(baseFileName, 0)
				movieFullFileName = fullfile(folderName, baseFileName);
			else
				return;
			end
		else
			return;
		end
end


try
		videoObject = VideoReader(movieFullFileName)
		% Determine how many frames there are.
		numberOfFrames = videoObject.NumberOfFrames;
		vidHeight = videoObject.Height;
```

```
        vidWidth = videoObject.Width;

        numberOfFramesWritten = 0;
        % Prepare a figure to show the images in the upper half of the screen.
        figure;
        %       screenSize = get(0, 'ScreenSize');
        % Enlarge figure to full screen.
        set(gcf, 'units','normalized','outerposition',[0 0 1 1]);

                writeToDisk = true;

                % Extract out the various parts of the filename.
                [folder, baseFileName, extentions] = fileparts(movieFullFileName);
                % Make up a special new output subfolder for all the separate
                % movie frames that we're going to extract and save to disk.
                % (Don't worry - windows can handle forward slashes in the folder name.)
                folder = pwd;   % Make it a subfolder of the folder where this m-file lives.
                outputFolder = sprintf('%s/Frames_%s', folder, baseFileName);
```

```
		% Create the folder if it doesn't exist already.
		if ~exist(outputFolder, 'dir')
			mkdir(outputFolder);
		end


	% Loop through the movie, writing all frames out.
	% Each frame will be in a separate file with unique name.

	for frame = 1 : numberOfFrames
		% Extract the frame from the movie structure.
		thisFrame = read(videoObject, frame);

		% Display it
		hImage = subplot(2, 2, 1);
		image(thisFrame);
		caption = sprintf('Frame %05d of %d.', frame,
		   numberOfFrames);
		title(caption, 'FontSize', fontSize);
	axis off
		drawnow; % Force it to refresh the window.

		% Write the image array to the output file, if
		   requested.
		if writeToDisk
```

```
				% Construct an output image file name.
				outputBaseFileName = sprintf('Frame%05.5d.tiff', frame);
				outputFullFileName = fullfile(outputFolder, outputBaseFileName);

				% Stamp the name and frame number onto the image.
				% At this point it's just going into the overlay,
				% not actually getting written into the pixel values.
				%text(5, 15, outputBaseFileName, 'FontSize', 20);

				% Extract the image with the text burned into it.
				% frameWithText = getframe(gca);
				% frameWithText.cdata is the image with the text
				% actually written into the pixel values.
				% Write it out to disk.
				imwrite(thisFrame, outputFullFileName, 'tiff');
		end

```

```
			% Update user with the progress.  Display in the command window.
			if writeToDisk
				progressIndication = sprintf('Wrote frame %5d of %d.', frame, numberOfFrames);
			else
				progressIndication = sprintf('Processed frame %5d of %d.', frame, numberOfFrames);
			end
			disp(progressIndication);
			% Increment frame count (should eventually = numberOfFrames
			% unless an error happens).
			numberOfFramesWritten = numberOfFramesWritten + 1;


	end

close all;  % Close all figures (except those of imtool.)
imtool close all;  % Close all imtool figures.


```

```
catch ME
        % Some error happened if you get here.
        strErrorMessage = sprintf('Error extracting movie frames from:\n\n%s\n\nError: %s\n\n)', movieFullFileName, ME.message);
        uiwait(msgbox(strErrorMessage));
end

toc
```

Listing B.5: ImageReading.m

```
% %%%%%     Post Processing TLC  %%%%%%%%%%%%%%%%%% %
% %         Marcel Otto, Gaurav Gupta, Jay Kapat  % %
% %  Sole Purpose of LAB and Experimental USAGE   % %
% %  Code is not to be comercialized              % %
% %%%%%%%%%%%%%%%%%%%%%%%%%%%%%%%%%%%%%%%%%%%%%%%%% %



% % Sub-routine Image reading and storage % %

function [Image_Collection_Numbered, pixel_i, pixel_j] = ImageReading(first, FolderName, Left_Top_Corner_Height, Left_Top_Corner_Width, Right_Bottom_Corner_Height, Right_Bottom_Corner_Width)
    tic
        disp('We are in the image reading function');
    A=[];
    Image_Collection_Numbered=[];  %    Image_Collection_Numbered is the array which contains all data points combined with
                                        %    the following structure: (y_coord vertical, x_coord horizontal, RGB_plane number, picture number )
```

```
                                          %    in order to recall one full image:
                                          % Image_Collection_Numbered(:,:,:,number)


    picfolder = fullfile(pwd, FolderName); %location of the video file relative to the working directory
    display(picfolder);
    %Count how many pictures are in folder
    imagefiles = dir([FolderName '/*.tiff']);
    nfiles = length(imagefiles);

    %sets the pointer for image import to the correct maximum location if
    %the first image is not image number one
    last_image=nfiles-1+first;

   %loops through all images in the folder, starting by image first up to the last image in the folder
     for pic_number=first:last_image
   %does a background substraction, the first image in the time series is
   %stored and substracted from all following images
```

```

        if pic_number==first

           picfilenames=sprintf('Frame%05.5d.tiff', pic_number);
           picFullName=fullfile(picfolder, picfilenames);
           %[A, map] = imread(picFullName);

           A = imread(picFullName, 'PixelRegion',{[
              Left_Top_Corner_Height, Right_Bottom_Corner_Height
              ],[Left_Top_Corner_Width,
              Right_Bottom_Corner_Width]});
           %if ~isempty(map)
          %        A=ind2rgb(A, map);
         %         disp('conversion yes');
           %else
           %    im2double(A);
           %    disp('conversion no');
           %end
           A=double(A)/255;
           A_first=A;

           location=pic_number-first+1;
           Image_Collection_Numbered(:,:,:,location)=A-A_first;
              %maybe change that to only read green into file
              and automatically omit all other colors
```

```
            %B = uint8(Image_timehistory_in_picnumber(:,:,:,
               pic_number));
            %Image_timehistory_in_picnumber(:,:,:,pic_number)=B;
            resolution=size(A);
            pixel_i=resolution(1);
            pixel_j=resolution(2);
         else
            picfilenames=sprintf('Frame%05.5d.tiff', pic_number);
            picFullName=fullfile(picfolder, picfilenames);
            %[A, map] = imread(picFullName);

            A = imread(picFullName, 'PixelRegion',{[
               Left_Top_Corner_Height, Right_Bottom_Corner_Height
               ],[Left_Top_Corner_Width,
               Right_Bottom_Corner_Width]});
            %if ~isempty(map)
           %        A=ind2rgb(A, map);
          %         disp('conversion yes');
            %else
            %    im2double(A);
            %    disp('conversion no');
            %end
            A=double(A)/255;
            location=pic_number-first+1;
```

```
            Image_Collection_Numbered(:,:,:,location)=A-A_first;
               %maybe change that to only read green into file
               and automatically omit all other colors
            %B = uint8(Image_timehistory_in_picnumber(:,:,:,
               pic_number));
            %Image_timehistory_in_picnumber(:,:,:,pic_number)=B;
            resolution=size(A);
            pixel_i=resolution(1);
            pixel_j=resolution(2);
            if mod(pic_number,100)==0
                disp(pic_number)
         end

        end
end

   % experiment_length = (m-first+1) / fps;  % length of
      experiment based on number of images and sampling rate //in
       seconds
toc
disp('Time for Image Import');
% % end of function Image_Reading
```

Listing B.6: ImageTimeAverage.m

```
% %%%%%     Post Processing TLC  %%%%%%%%%%%%%%%%%% %
% %         Marcel Otto, Gaurav Gupta, Jay Kapat  % %
% %  Sole Purpose of LAB and Experimental USAGE   % %
% %  Code is not to be comercialized              % %
% %%%%%%%%%%%%%%%%%%%%%%%%%%%%%%%%%%%%%%%%%%%%%%%%% %


%time averaging of based on fps
function Images_Time_Averaged=ImageTimeAverage(Image_Collection)
tic

[Size_x_orig, Size_y_orig, Number_RGB_Channels_orig, Number_of_Frames]=size(Image_Collection);
timestep_number=1;
while timestep_number <= Number_of_Frames

    if timestep_number == 1 %first picture: only average image 1 and 2
        Images_Time_Averaged(:,:,1,timestep_number)=(Image_Collection(:,:,1,timestep_number+1)+Image_Collection(:,:,1,timestep_number))/2;
    elseif timestep_number == Number_of_Frames %last image: only average last and second last image
```

```
        Images_Time_Averaged(:,:,1,timestep_number)=(Image_Collection(:,:,1,timestep_number-1)+Image_Collection(:,:,1,timestep_number))/2;
    else      %for all other situations average this and the previous and next image
        Images_Time_Averaged(:,:,1,timestep_number)=(Image_Collection(:,:,1,timestep_number-1)+Image_Collection(:,:,1,timestep_number)+Image_Collection(:,:,:,timestep_number+1))/3;
    end;

    timestep_number=timestep_number+1;

end
toc
disp('Time for Time Averaging');
```

Listing B.7: XYRollingAverage.m

```
% %%%%     Post Processing TLC  %%%%%%%%%%%%%%%%%% %
% %         Marcel Otto, Gaurav Gupta, Jay Kapat  % %
% %  Sole Purpose of LAB and Experimental USAGE   % %
% %  Code is not to be comercialized              % %
% %%%%%%%%%%%%%%%%%%%%%%%%%%%%%%%%%%%%%%%%%%%%%%%%% %


%rolling average in x and y direction
    % the averaging consists of a 3x3 window that rolls over the
       original
    % image and write the results into a now file, here, the
       pixels
    % directly at the edge are lost. The average is a weighted
       average with
    % 60% of the center pixel and 40% of the surrounding pixels
function XY_averaged_Image=XYRollingAverage(Original, pixel_i,
   pixel_j)
tic

%Original=Images_Time_Averaged(:,:,:,:);  %if averaging in space
   first, than time: replace Images_Time_Averaged with
   Image_Collection_Numbered and timestep_number with pic_number
timestep_number=size(Original);
timestep_number=timestep_number(4);
FilterMatrix=[0.05 0.05 0.05; 0.05 0.6 0.05; 0.05 0.05 0.05];
```

```
for t=1:timestep_number
    XY_averaged_Image(:, :,1,t)=imfilter(Original(:,:,1,t),
       FilterMatrix); %note the one at the RGB location, even
       though Green is 2, it is changed to 1 as only Green is
       imported during ImageRead
end
toc
disp('Time for x y Averaging');
```

Listing B.8: peakfinding.m

```
% %%%%%     Post Processing TLC  %%%%%%%%%%%%%%%%%% %
% %         Marcel Otto, Gaurav Gupta, Jay Kapat  % %
% %  Sole Purpose of LAB and Experimental USAGE   % %
% %  Code is not to be comercialized              % %
% %%%%%%%%%%%%%%%%%%%%%%%%%%%%%%%%%%%%%%%%%%%%%%%%%%%% %

%% Script for finding the half max-full width of a normally distributed intensity curve
function GreenPeakArrivalTime=peakfinding(Intensity, pixel_i, pixel_j);

%step = 1e-2; %Can be used based on the resolution of time
[pixel_i, pixel_j, dummy_value, Experiment_length]=size(Intensity);

new_intensity=squeeze(Intensity);
for i=1:pixel_i
   for j=1:pixel_j
       one_vector=new_intensity(i,j,:);
       one_vector=squeeze(one_vector);
       gol=sgolayfilt(one_vector,7,201);
       [peaks, locations, width, proms]=findpeaks(gol, 'SortStr', 'descend');
%         if proms(1) > 2*proms(2)
%             if proms(2) < 0.05
```

```
                 GreenPeakArrivalTime(i,j)=locations(1);
%            else
%                 GreenPeakArrivalTime(i,j)=NaN;
%            end
%        else
%            GreenPeakArrivalTime(i,j)=NaN;
%        end
  end
end

%The following section is only to create a plot comparing the peak
%locations and showing the location of the peaks for a random point
%i=40;
%j=60;
i=185;
j=187;
new_intensity=squeeze(Intensity);
    one_vector=new_intensity(i,j,:);
    one_vector=squeeze(one_vector);
   gol=sgolayfilt(one_vector,7,201);
  figure('PaperPosition', [0 0 8.75 5])
  hold on
  not_fitted=plot(one_vector);
```

```
  [peaks, locations]=findpeaks(gol, 'SortStr', 'descend');
  find_peaks=plot(gol);
  marker=scatter(locations, peaks, 80, 'v', 'filled' );
  set(not_fitted, 'LineWidth', 2);
  set(find_peaks, 'LineWidth', 2);

hXLabel = xlabel('Frame # since Start of Recording');
set(hXLabel, 'FontName', 'Times New Roman','FontSize', 16)
set(gca, 'FontName', 'Times New Roman', 'FontSize', 16)
hYLabel = ylabel('Green Intensity');
set(hYLabel, 'FontName', 'Times New Roman','FontSize', 16)
hLegend = legend(...
[not_fitted, find_peaks, marker],...
'Raw Signal', 'Fitted Signal', 'Peaks', 'Location', 'NorthEast');
 set([legend, gca], 'FontName', 'Times New Roman', 'FontSize',
    16);
ax=gca;
ax.FontSize = 16;
ax.TickDir = 'in';
ax.LineWidth=2;
%set(gcf, 'PaperPositionMode', 'auto');
saveas(gcf, 'FittedSignalAndPeaks.png')
hold on

 set(gca, 'YLim', [0.05 0.2]);
```

```
  set(gca, 'XLim', [0 1000]);
saveas(gcf, 'FittedSignalAndPeaks_Zoom.png')
```

Listing B.9: ShowIntensityPlotPerPixel.m

```
%this function returns a plot of Green Intensity of a particular
   Pixel pair
%x,y
function ShowIntensityPlotPerPixel(Images)
    prompt = 'What is the desired x location?';
    testpixel_j=input(prompt);
    prompt = 'What is the desired y location?';
    testpixel_i=input(prompt);

timestep_number=size(Images);
timestep_number=timestep_number(4);
timestepvector=[1:timestep_number];
for t=1:timestep_number
    GreenValuesAtXY(t)=Images(testpixel_i, testpixel_j,[2],t);
end

figure
plot(timestepvector, GreenValuesAtXY, 'g');
str=sprintf('Green Intensity of x=%d and y=%d', testpixel_j,
   testpixel_i);
%title()
title(str, 'FontSize',16, 'FontWeight','bold')
xlabel('Time in s')
ylabel('Green Intensity % of 255')
```

Listing B.10: ShowGreenOnly.m

```
function only_green=IsolateGreen(Images);
only_green=[];
timestep_number=size(XYt_averaged_Images);
timestep_number=timestep_number(4);
    only_green=XYt_averaged_Images(:,:,:,:);
    only_green(:,:,[1 3],:)=0;
    %only_red=XYt_averaged_Images(:,:,:,:);
    %only_red(:,:,[2 3])=0;
    %only_blue=XYt_averaged_Images(:,:,:,:);
    %only_blue(:,:,[1 2])=0;
```

Listing B.11: stitchingtogether.m

```
% figure
% subplot(1,4,1);
% contour(GreenpeakArrivalTime1)
% subplot(1,4,2);
% contour(GreenpeakArrivalTime2)
% subplot(1,4,3);
% contour(GreenpeakArrivalTime3)
% subplot(1,4,4);
% contour(GreenpeakArrivalTime4)

GreenpeakArrivalTime=NaN(Right_Bottom_Corner_Height-
   Left_Top_Corner_Height+1, Right_Bottom_Corner_Width-
   Left_Top_Corner_Width-1);
GreenpeakArrivalTime(1:Right_Bottom_Corner_Height-
   Left_Top_Corner_Height+1, 1:300)=GreenpeakArrivalTime1
   (:,1:300);
GreenpeakArrivalTime(1:Right_Bottom_Corner_Height-
   Left_Top_Corner_Height+1, 301:600)=GreenpeakArrivalTime2
   (:,1:300);
GreenpeakArrivalTime(1:Right_Bottom_Corner_Height-
   Left_Top_Corner_Height+1, 601:900)=GreenpeakArrivalTime3
   (:,1:300);
GreenpeakArrivalTime(1:Right_Bottom_Corner_Height-
   Left_Top_Corner_Height+1, 900:Right_Bottom_Corner_Width-1)=
   GreenpeakArrivalTime4(:,1:Right_Bottom_Corner_Width-900);
```

```
% %%%%%%%%%%%%%%
% Unable to perform assignment because the size of the left side is 467-by-300
% and the size of the right side is 468-by-300.
%  }
% >>  {Unable to perform assignment because the size of the left side is 467-by-300
% and the size of the right side is 468-by-300.
%  }
% >>  {Unable to perform assignment because the size of the left side is 467-by-300
% and the size of the right side is 468-by-300.
%  }
% >>  {Unable to perform assignment because the size of the left side is 467-by-1021
% and the size of the right side is 468-by-1020.
% }
```

Listing B.12: CreateFilterMask.m

```
function CreateFilterMask(A);
clc
clear
load('CalibrationImage.mat');
[pixel_i pixel_j dummy]=size(A);
filtermatrix=ones(pixel_i,pixel_j-1);
for i=1:pixel_i
    for j=1:pixel_j-1
        if A(i,j) > 0.37
            filtermatrix(i,j)=0;
        end
    end
end

filtermatrix(:,1:250)=0;
filtermatrix(1:40,:)=0;
filtermatrix(450:pixel_i,:)=0;

for i=1:pixel_i
    for j=1:pixel_j-1
         if GreenPeakArrivalTime_in_seconds_masked(i,j) < 5
             filtermatrix(i,j)=0;
         end
     end
 end
```

```
A_filtered=A;
for i=1:pixel_i
    for j=1:pixel_j-1
        if filtermatrix(i,j)==0
            A_filtered(i,j,:)=NaN;
        end
    end
end

imshow(A_filtered)
save('filter_mask.mat', 'filtermatrix');
```

Listing B.13: ApplyMask.m

```
function A_filtered=ApplyMask(A);
[pixel_i pixel_j dummy]=size(A);
A_filtered=A;
load('filter_mask.mat');
for i=1:pixel_i
     for j=1:pixel_j
         if filtermatrix(i,j)==0
            A_filtered(i,j)=NaN;
        end
     end
 end


%imshow(A_filtered)
```

Listing B.14: GiveHTCValues.m

```
% %%%%     Post Processing TLC  %%%%%%%%%%%%%%%%%% %
% %         Marcel Otto, Gaurav Gupta, Jay Kapat  % %
% %  Sole Purpose of LAB and Experimental USAGE   % %
% %  Code is not to be comercialized              % %
% %%%%%%%%%%%%%%%%%%%%%%%%%%%%%%%%%%%%%%%%%%%%%%%%%% %


function [h_final, Tbulk]=GiveHTCValue(alfa, k, beta,
   GreenpeakArrivalTime, RHS, Ti, Tgp,
   Temperature_interpolated_in_space, Pixel_Location_of_TCs);
tic
disp('Calculating HTC Values');
disp('Status: Running');

% Tgp: Temperararature of green peak (comes from
% calibration/manufacturer manual)
% Ti: Intial temprature (measured at the start of experiment)
% Tb_x: Bulk temperature at streamwise location (comes from
% intrpolation between measured air temperatures at inlet and
   exit
% of the test section)
%% Load some stuff in memory from Input parameters
TimeA = GreenpeakArrivalTime;
[m,n] = size(TimeA);
%%
```

```
%A ssumed values for debugging the code
%Tgp = 55.0; % in degree C
%Ti = 25.0; % in degree C
%Tb_x_t = 70;
%Tb_x = 60:10:70;  % dummy bulk temperature values for each pixel in x-direction
%%

%%
h_final=NaN(m,n);
Tbulk=NaN(m,n);
 for i =1:m; % m: Number of pixels in x-direction
     for j = 1:n; % n: Number of pixels in y-direction
        displaystring=['Started pixels i=' sprintf('%g', i) ', j=' sprintf('%g', j)];
        disp(displaystring);
        % % check what is the local arrival time for that pixel pair i, j
        local_Green_Peak_Arrival_Time=TimeA(i,j);

        % % now check if pixel pair i, j is within the range of interest,
        % meaning if it has a local green peak arrival time, that the
```

```
    % arrival time is larger than 3 seconds (if not, good indiction
    % that this pixel escaped the filter, and if the pixel pair is
    % between the sheathed TCs and has temperature readings
    if ((~isnan(local_Green_Peak_Arrival_Time)) && (local_Green_Peak_Arrival_Time>3) && (j>=Pixel_Location_of_TCs(1)) && (j<=Pixel_Location_of_TCs(5)))
        % % extract the time series vector for the pixel pair and the time
        % steps
        Tb_x_t= Temperature_interpolated_in_space(2:end,[1 j+1]);
        time_interpolation_x_vector=Tb_x_t(:,1);
        time_interpolation_y_vector=Tb_x_t(:,2);
        Tb_interpolated=interp1(time_interpolation_x_vector, time_interpolation_y_vector, local_Green_Peak_Arrival_Time,'pchip', 'extrap');
        T_ratio = (Tgp-Ti)./(Tb_interpolated-Ti);
        Tbulk(i,j)=Tb_interpolated;
        % Time taken to reach the final temperature from start of
        % experiment for that pixel to reach 90% of the final
        % temperature
```

```
        Temp_for_ninety_percent=time_interpolation_y_vector(1)+0.99*(time_interpolation_y_vector(end)-time_interpolation_y_vector(1));
        for new_counter=3:length(time_interpolation_y_vector)
            if Temp_for_ninety_percent<=time_interpolation_y_vector(new_counter)
                new_time_interpolation_y_vector(1)=time_interpolation_y_vector(new_counter-2);
                new_time_interpolation_y_vector(2)=time_interpolation_y_vector(new_counter-1);
                new_time_interpolation_y_vector(3)=time_interpolation_y_vector(new_counter);
                new_time_interpolation_y_vector(4)=time_interpolation_y_vector(new_counter+1);
                new_time_interpolation_y_vector(5)=time_interpolation_y_vector(new_counter+2);

                new_time_interpolation_x_vector(1)=time_interpolation_x_vector(new_counter-2);
```

```
                    new_time_interpolation_x_vector(2)=
                       time_interpolation_x_vector(new_counter-1)
                       ;
                    new_time_interpolation_x_vector(3)=
                       time_interpolation_x_vector(new_counter);
                    new_time_interpolation_x_vector(4)=
                       time_interpolation_x_vector(new_counter+1)
                       ;
                    new_time_interpolation_x_vector(5)=
                       time_interpolation_x_vector(new_counter+2)
                       ;
                    break
                else
                    new_counter=new_counter+1;
                end
            end

            DTstep =interp1(new_time_interpolation_y_vector,
               new_time_interpolation_x_vector,
               Temp_for_ninety_percent,'pchip', 'extrap');

            if T_ratio < 1
                % for N = 1:NLUT;  % I guess, this for loop is
                   not needed!
```

```
                % NLUT: Number of points in the look-up table (= time steps * htc steps in conduction model)


                N=1;
%                 display(T_ratio)
%                 display(Ti)
%                 display(Tb_interpolated);

                while T_ratio > RHS(N)
                    % Finds RHS which is closer to Tratio
                    N = N+1;
                end
                RHS_final = RHS (N);
                beta_low = beta(N-1);
                beta_high = beta(N);
                a = sqrt(alfa)/k;
                %alfa: Thermal diffusivity; k: Thermal conductivity

                h_green = beta_low/(a* sqrt(local_Green_Peak_Arrival_Time));

                %% check if we are outside of the step function, then only this approach is valid
```

```
                if local_Green_Peak_Arrival_Time > DTstep

                    h_blue = beta_high/(a* sqrt((local_Green_Peak_Arrival_Time-DTstep)));

                    hstep =  0.01 * 0.5*(h_green+h_blue);
                    %Step size is 5% of average htc value, can be changed based on actual values

                    if (h_blue-h_green) < hstep;
                        h_final(i,j) = h_green;
                        %h_final: Final value of htc for that particular pixel
                    else
                         h = h_green:hstep:h_blue;
                         [r_h, c_h] = size(h);
                         for K = 1:c_h
                             sum = 0;
                             MTempStep = 10000;
                             DT = 1;
                            %for M = 1, MTempStep;
                            M = 1;
                            while M < MTempStep;
                                %MTempStep: Number of bulk temperature steps to reach
```

```
                %the final temeprature

                Time = M*(DTstep/MTempStep);
                %Time: Time at Mth temperature step from the start

                beta_new(M) = h(K)*a*sqrt(local_Green_Peak_Arrival_Time-Time);
                %beta(M): Value of beta during temperature transient

                RHS_new(M) = 1 - (exp(beta_new(M).^2).*(1-erf(beta_new(M))));


                sum = sum + RHS_new(M)*(DT/(Tb_interpolated-Ti));
                %DT(M): Bulk Temperature step in M-1-->M step,
                %value will come from the Time vs Tb_x curve during
                %measurement.
                M = M + 1;
                    if sum > T_ratio;
```

```
                                        %M = MTempStep+1;
                                        h_final(i,j) = h(K);
                                        break
                                    end
                                     continue

                                    sum_final = sum;

                            end
                         end
                    end
                else
                        %% here stats the other case if Green Peak arrival time is smaller than DT_Step
                        % the problem here is that there is no upper limit h_blue since it is a complex number
                        % SQRT of something smaller 0 gives complex number. So we have to start doing the duhamel
                        % in form of a while loop, approaching it from the
                        % bottom

```

```
%% define a new hstep size
hstep=0.01*h_green;

%% initialize right hand side solution
h_new=h_green;
%% set up condition for while loop
M = 1;
sum=0;
while sum < T_ratio
     sum = 0;
     MTempStep = 10000;
     DT = 1;
    %for M = 1, MTempStep;
    M = 1;
    while M < MTempStep;
        %MTempStep: Number of bulk temperature steps to reach
        %the final temeprature

        Time = M*(DTstep/MTempStep);
        %Time: Time at Mth temperature step from the start
        % DTstep/MTempStep is the Duhamel
        % discretization time
```

```
beta_new = h_new*a*sqrt(
    local_Green_Peak_Arrival_Time-
    Time);
%beta(M): Value of beta during
    temperature transient

RHS_new = 1 - (exp(beta_new^2)
    .*(1-erf(beta_new)));


sum = sum + RHS_new*(DT/(
    Tb_interpolated-Ti));
%DT(M): Bulk Temperature step in
    M-1-->M step,
%value will come from the Time vs
     Tb_x curve during
%measurement.
M = M + 1;
if sum > T_ratio;
        %M = MTempStep+1;
        h_final(i,j) = h_new;
        break
end
h_new=h_new+hstep;

```

```
                                    end
                               end
                         end
                    end
               end
          end
     end

toc



%              Temp_for_ninety_percent_2=time_interpolation_y_vector(1)+0.90*(time_interpolation_y_vector(end)-time_interpolation_y_vector(1));
%              for new_counter=3:length(time_interpolation_y_vector)
%                  if Temp_for_ninety_percent_2<=time_interpolation_y_vector(new_counter)
%                      new_time_interpolation_y_vector(1)=time_interpolation_y_vector(new_counter-2);
%                      new_time_interpolation_y_vector(2)=time_interpolation_y_vector(new_counter-1);
```

```
%                    new_time_interpolation_y_vector(3)=
   time_interpolation_y_vector(new_counter);
%                    new_time_interpolation_y_vector(4)=
   time_interpolation_y_vector(new_counter+1);
%                    new_time_interpolation_y_vector(5)=
   time_interpolation_y_vector(new_counter+2);
%
%                    new_time_interpolation_x_vector(1)=
   time_interpolation_x_vector(new_counter-2);
%                    new_time_interpolation_x_vector(2)=
   time_interpolation_x_vector(new_counter-1);
%                    new_time_interpolation_x_vector(3)=
   time_interpolation_x_vector(new_counter);
%                    new_time_interpolation_x_vector(4)=
   time_interpolation_x_vector(new_counter+1);
%                    new_time_interpolation_x_vector(5)=
   time_interpolation_x_vector(new_counter+2);
%                    break
%                else
%                    new_counter=new_counter+1;
%                end
%            end
%
%            DTstep_nintey =interp1(
   new_time_interpolation_y_vector,
```

```
new_time_interpolation_x_vector,  Temp_for_ninety_percent_2,'pchip', 'extrap');
%Code for plotting temperature curve and 99% Temp interval and 99% arrival time at given pixel i,j
%  figure('PaperPosition', [0 0 8.75 5])
%  hold on
%  TemperatureSeries=plot(time_interpolation_x_vector, time_interpolation_y_vector);
%           set(TemperatureSeries, 'LineWidth', 2);
% hXLabel = xlabel('Time in Seconds since Start of Recording');
% set(hXLabel, 'FontName', 'Times New Roman','FontSize', 16)
% set(gca, 'FontName', 'Times New Roman', 'FontSize', 16)
% hYLabel = ylabel('Temperature in C');
% set(hYLabel, 'FontName', 'Times New Roman','FontSize', 16)
% ax=gca;
% ax.FontSize = 16;
% ax.TickDir = 'in';
% ax.LineWidth=2;
% hline_ref=line([0 DTstep], [Temp_for_ninety_percent Temp_for_ninety_percent]);
```

```
% line2=line([DTstep DTstep ],[0 Temp_for_ninety_percent]);
% hline_ref.LineWidth=2;
% hline_ref.LineStyle=':';
% hline_ref.Color='black'
% text1=text(190,75, '99% Temperature Threshold');
% text2=text(25,70, '90% Temperature Threshold');
% set(text1, 'FontName', 'Times New Roman','FontSize', 16);
% set(text2, 'FontName', 'Times New Roman','FontSize', 16);
% line2.LineWidth=2;
% line2.LineStyle=':';
% line2.Color='black'
%
% hline_ref2=line([0 DTstep_nintey], [Temp_for_ninety_percent_2 Temp_for_ninety_percent_2]);
% line2=line([DTstep_nintey DTstep_nintey],[0 Temp_for_ninety_percent_2]);
% hline_ref2.LineWidth=2;
% hline_ref2.LineStyle=':';
% hline_ref2.Color='black'
% text3=text(190,10, 'Time to reach 99% Temperature');
% text4=text(25,10, 'Time to reach 90% Temperature');
% set(text3, 'FontName', 'Times New Roman','FontSize', 16);
% set(text4, 'FontName', 'Times New Roman','FontSize', 16);
% line2.LineWidth=2;
% line2.LineStyle=':';
```

```
% line2.Color='black'
%
% saveas(gcf, 'Pixel_Temperature_Profile.png')
```

Listing B.15: CreateLookUpTable.m

```
% %%%%%     Post Processing TLC  %%%%%%%%%%%%%%%%%% %
% %         Marcel Otto, Gaurav Gupta, Jay Kapat  % %
% %  Sole Purpose of LAB and Experimental USAGE   % %
% %  Code is not to be comercialized              % %
% %%%%%%%%%%%%%%%%%%%%%%%%%%%%%%%%%%%%%%%%%%%%%%%%%% %


%%
function [RHS, beta] = CreateLoopUpTable (alfa, k);
tic
a = sqrt(alfa)/k;
h = 0:0.1:300; % Heat transfer coefficient in W/m^-K
t = 0:0.1:1000; % Time in seconds
[r_pmax , c_pmax] = size(h);
[r_qmax , c_qmax] = size(t);
        for p = 1 : c_pmax
             for q = 1 : c_qmax
                 b(p,q)  = h(p)*sqrt(t(q));
                 beta(p,q)  = a.*b(p,q);
                 RHS(p,q)  = 1 - (exp(beta(p,q).^2).*(1-erf(beta(p
                    ,q))));
             end
        end
        RHS = RHS (:);
        beta = beta (:);
```

```
        save('LookUpTable.mat', 'RHS', 'beta');
toc
```

Listing B.16: HandleDAQReadings.m

```
% %%%%%     Post Processing TLC  %%%%%%%%%%%%%%%%%% %
% %         Marcel Otto, Gaurav Gupta, Jay Kapat  % %
% %  Sole Purpose of LAB and Experimental USAGE   % %
% %  Code is not to be comercialized              % %
% %%%%%%%%%%%%%%%%%%%%%%%%%%%%%%%%%%%%%%%%%%%%%%%%% %


   % % Code to import excel information from DAQ

function [T_initial, Temperature_Matrix_in_j]=HandleDAQReadings(Excelfile, Pixel_Location_of_TCs, pixel_j);
tic
disp('Importing Temperature Table');
% % read Excel file as specified above %%%%
TemperatureTable=readtable(Excelfile);
% % convert table to matrix
Temperature_Matrix=table2array(TemperatureTable);
% % find out time step of data acquistion
time_delta_weird_format=(Temperature_Matrix(2,1))-(Temperature_Matrix(1,1));
% % rewrite time column with new times, do some re-formatting of the time
% dispay etc, took me a while do deal with that stuff
for i=1:length(Temperature_Matrix)
```

```
    converted_time=datetime(time_delta_weird_format,'ConvertFrom'
       ,'datenum','Format','sss.SSSSSSSSSSSSSSSSSSSSSSSSSSS');
    time_delta=str2double(char(converted_time));
    Temperature_Matrix(i,1)=time_delta*(i-1);
end
clear TemperatureTable;

% % averaging the TC readings for each streamwise location, the
   structure
% of the new matrix is as following:
% Temperature_Matrix_averaged(1,:) is pixel_j location of the TCs
% Temperature_Matrix_averaged(:,1) is time in seconds since start
    of experiment
% Temperature_Matrix_averaged(:,2) reading of TCs after honeycomb
% Temperature_Matrix_averaged(:,3) reading of sheathed TCs before
    row 1
% Temperature_Matrix_averaged(:,4) reading of TCs after row 1
% Temperature_Matrix_averaged(:,5) reading of TCs after row 2
% Temperature_Matrix_averaged(:,6) reading of TCs after row 3
% Temperature_Matrix_averaged(:,7) reading of sheathed TCs after
   row 4
% Temperature_Matrix_averaged(:,8) reading of ambient temperature

Temperature_Matrix_averaged(:,1)=Temperature_Matrix(:,1);
```

```
Temperature_Matrix_averaged(:,2)=(Temperature_Matrix(:,2)+
   Temperature_Matrix(:,3)+Temperature_Matrix(:,4))./3;
Temperature_Matrix_averaged(:,3)=(Temperature_Matrix(:,5)+
   Temperature_Matrix(:,6)+Temperature_Matrix(:,7))./3;
Temperature_Matrix_averaged(:,4)=(Temperature_Matrix(:,8)+
   Temperature_Matrix(:,9)+Temperature_Matrix(:,10))./3;
Temperature_Matrix_averaged(:,5)=(Temperature_Matrix(:,11)+
   Temperature_Matrix(:,12)+Temperature_Matrix(:,13))./3;
Temperature_Matrix_averaged(:,6)=(Temperature_Matrix(:,14)+
   Temperature_Matrix(:,15)+Temperature_Matrix(:,16))./3;
Temperature_Matrix_averaged(:,7)=(Temperature_Matrix(:,17)+
   Temperature_Matrix(:,18)+Temperature_Matrix(:,19))./3;
Temperature_Matrix_averaged(:,8)=(Temperature_Matrix(:,20)+
   Temperature_Matrix(:,21))./2;
Temperature_Matrix_averaged=[NaN NaN Pixel_Location_of_TCs NaN;
   Temperature_Matrix_averaged ];
clear Temperature_Matrix;
[size1, size2]=size(Temperature_Matrix_averaged);
% % plot the surface plot of Temperature vs time vs downstream
   position
% surf(Temperature_Matrix_averaged(2:end,3:7));

% % average reading of all six sheathed thermocouples and average
    for initial
% temperature
```

```
T_initial=(Temperature_Matrix_averaged(2,3)+
   Temperature_Matrix_averaged(2,7))/2;

% % create a new dummy matrix to store linear interpolated values
    in j
% direction for each time step
Temperature_Matrix_in_j=NaN(size1+100, pixel_j+1);
Temperature_Matrix_in_j(1:size1,1)=Temperature_Matrix_averaged
   (:,1);
Temperature_Matrix_in_j(1:size1,Pixel_Location_of_TCs(1)+1)=
   Temperature_Matrix_averaged(:,3);
Temperature_Matrix_in_j(1:size1,Pixel_Location_of_TCs(5)+1)=
   Temperature_Matrix_averaged(:,7);
Temperature_Matrix_in_j(1,2:end)=1:1:pixel_j;
% % determine first and last point in j direction for
   interpolation, only
% information of sheathed TC will be used
input_x_vector=[Pixel_Location_of_TCs(1)+1,Pixel_Location_of_TCs
   (5)+1];

% % loop through all rows with temperatures and interpolate
   between the TCs
% before first row and after fourth row. As no TC information is
   available
% for the section before and after, the averaged readings of that
```

```
% particular row will be used for the upstream and downstream
    temperature,
% respectively.
% % create a matrix that has temperature values for every pixel
    in j direction
% interpolation is done in a linear fashion between first row and
     last row TCs

for row_number=2:size1
    input_y_vector=[Temperature_Matrix_averaged(row_number,3),
       Temperature_Matrix_averaged(row_number,7)];
    %figure
    % % the actual interpolation
    interpolation=interp1(input_x_vector, input_y_vector,
       input_x_vector(1):1:input_x_vector(2));
    %plot(input_x_vector, input_y_vector, 'o', input_x_vector(1)
       :1:input_x_vector(2), interpolation, ':.')

    % % write interpolation data into Matrix
    Temperature_Matrix_in_j(row_number,input_x_vector(1):
       input_x_vector(2))=interpolation;

    % % write upstream and downstream temperature approximation
       into matrix
```

```
    %Temperature_Matrix_in_j(row_number,2:input_x_vector(1)-1)= Temperature_Matrix_in_j(row_number,input_x_vector(1));
    %Temperature_Matrix_in_j(row_number,input_x_vector(2)+1:end)= Temperature_Matrix_in_j(row_number,input_x_vector(2));
end

% % prevent any missmatch between time matrix and green peak arrival time
% by adding steady state temperature information to the end
row_number2=size1;
Temperature_Matrix_in_j(row_number2,1)=Temperature_Matrix_in_j(row_number,1)+time_delta;

for row_number2=size1+1:size1+100
    Temperature_Matrix_in_j(row_number2,2:end) = Temperature_Matrix_in_j(row_number,2:end);
    Temperature_Matrix_in_j(row_number2,1)= Temperature_Matrix_in_j(row_number2 -1,1)+time_delta;
end

% % and add all j coordinates to top row


disp('Finished importing Temperature Table');
toc
```

Listing B.17: NusseltPlot.m

```
% %%%%%     Post Processing TLC  %%%%%%%%%%%%%%%%%% %
% %         Marcel Otto, Gaurav Gupta, Jay Kapat  % %
% %  Sole Purpose of LAB and Experimental USAGE   % %
% %  Code is not to be comercialized              % %
% %%%%%%%%%%%%%%%%%%%%%%%%%%%%%%%%%%%%%%%%%%%%%%%%%% %

function [Array_Mean, Nusselt_Number_Ames]=NusseltPlot(
   Nusselt_Number, Re, Error, PostProcfolder, NormBasis,
   already_normalized)
%Nusselt_Number=test_30k_mean;
% %Re=10;
% Re=30;
% Error=0;
Array_Mean=NaN;
[pixel_i,pixel_j]=size(Nusselt_Number);
NormBasisName='own';


%% convert i, j to x/D and z/D
% center_point_r_one=[238,663];
% center_point_r_two=[347,892];


center_point_r_one=[238,665];
center_point_r_two=[347,885];
```

```

% calculate scaling factors based on distance between to pin center points
factor_z_over_D=1.25/(center_point_r_two(1)-center_point_r_one(1)+5);
factor_x_over_D=2.5/(center_point_r_two(2)-center_point_r_one(2)+2);

% shift zero to center of first pin
x_over_D_vector=[1:1:pixel_j]-center_point_r_one(2);
z_over_D_vector=[1:1:pixel_i]-center_point_r_one(1);

% apply scale
x_over_D_vector=x_over_D_vector.*factor_x_over_D;
z_over_D_vector=z_over_D_vector.*factor_z_over_D;

%% Normalize Data for Nusselt Augmentation
% normalize for Ames compare
if ((NormBasis == 1) && (Error==0))
    if Re==10
        Nusselt_Number_Ames=Nusselt_Number./54.1; %10k
    elseif Re==30
        Nusselt_Number_Ames=Nusselt_Number./111.5; %30k
    else
```

```
        display('Please enter correct Reynolds number, either 10
           or 30')
    end
    NormBasisName='Ames';
elseif ((Error==0) && (already_normalized==0))
    Array_Mean=CalculateMean(Nusselt_Number)
    Nusselt_Number_Ames=Nusselt_Number./Array_Mean;
elseif already_normalized==1
   Nusselt_Number_Ames=Nusselt_Number;
else
    Nusselt_Number_Ames=NaN;
end

%% make all the plots
%% Ames case
if ((NormBasis == 1) && (Error==0))

    % plot it
    close all;
    figure('PaperPosition', [0 0 8.75 5])
    hold on
    set(gcf, 'Position', get(0, 'Screensize'));
    limits=[0,1.8];
```

```
    Nusselt_contour=contourf(x_over_D_vector, z_over_D_vector,
       Nusselt_Number_Ames, [limits(1):0.05:limits(2)], '
       LineColor', 'none');
    colormap('Jet');
    axis equal
    xlim([-1.25 8.75]);
    ylim([-2.5 2.5]);
    % make lines for reference
%     line([0 8.5], [0 0])
%     line([0 0], [-2.5 2.5])
%     line([2.5 2.5], [-2.5 2.5])
%     line([5 5], [-2.5 2.5])
%     line([7.5 7.5], [-2.5 2.5])
%     line([0 8.5], [1.25 1.25])
%     line([0 8.5], [-1.25 -1.25])
    hXLabel = xlabel('x/D');
    set(hXLabel, 'FontName', 'Times New Roman','FontSize', 16)
    set(gca, 'FontName', 'Times New Roman', 'FontSize', 16)
    hYLabel = ylabel('y/D');
    set(hYLabel, 'FontName', 'Times New Roman','FontSize', 16)
    ax=gca;
    ax.FontSize = 16;
    ax.TickDir = 'in';
    ax.LineWidth=2;
    hcb=colorbar;
```

```
    string=['Nusselt Augmentation Nu/Nu_{ave} at Re=' int2str(Re) 'k'];
    hcb.Label.String =string;
    set(hcb.Label, 'FontName', 'Times New Roman','FontSize', 20);
    set(hcb, 'Location', 'northoutside');
    hcb.Limits=[limits(1) limits(2)];
    Image_savename=[PostProcfolder '\NusseltDistribution_' int2str(Re) 'k_' char(NormBasisName) '.png'];
    saveas(gcf, Image_savename)
    close all
    hold off

    %% my case
elseif Error==0
    % plot it
    close all;
    figure('PaperPosition', [0 0 8.75 5])
    hold on
    set(gcf, 'Position', get(0, 'Screensize'));
    limits=[0,1.6];
    Nusselt_contour=contourf(x_over_D_vector, z_over_D_vector, Nusselt_Number_Ames, [limits(1):0.05:limits(2)], 'LineColor', 'none');
    colormap('Jet');
    axis equal
```

```
    xlim([-1.25 8.75]);
    ylim([-2.5 2.5]);
    % make lines for reference
%     line([0 8.5], [0 0])
%     line([0 0], [-2.5 2.5])
%     line([2.5 2.5], [-2.5 2.5])
%     line([5 5], [-2.5 2.5])
%     line([7.5 7.5], [-2.5 2.5])
%     line([0 8.5], [1.25 1.25])
%     line([0 8.5], [-1.25 -1.25])
    hXLabel = xlabel('x/D');
    set(hXLabel, 'FontName', 'Times New Roman','FontSize', 16)
    set(gca, 'FontName', 'Times New Roman', 'FontSize', 16)
    hYLabel = ylabel('y/D');
    set(hYLabel, 'FontName', 'Times New Roman','FontSize', 16)
    ax=gca;
    ax.FontSize = 16;
    ax.TickDir = 'in';
    ax.LineWidth=2;
    hcb=colorbar;
    string=['Nusselt Augmentation Nu/Nu_{ave} at Re=' int2str(Re) 'k'];
    hcb.Label.String =string;
    set(hcb.Label, 'FontName', 'Times New Roman','FontSize', 20);
    set(hcb, 'Location', 'northoutside');
```

```
    hcb.Limits=[limits(1) limits(2)];
    Image_savename=[PostProcfolder '\NusseltDistribution_'
       int2str(Re) 'k_' char(NormBasisName) '.png'];
    saveas(gcf, Image_savename)
    close all
    hold off

%% Coefficient of variation (standard deviation / mean)*100%
elseif Error==1
   % plot it
    close all;
    figure('PaperPosition', [0 0 8.75 5])
    hold on
    set(gcf, 'Position', get(0, 'Screensize'));
    limits=[0,15];
    Nusselt_contour=contourf(x_over_D_vector, z_over_D_vector,
       Nusselt_Number, [limits(1):limits(2)], 'LineColor', 'none'
       );
    colormap('Jet');
    axis equal
    xlim([-1.25 8.75]);
    ylim([-2.5 2.5]);
    % make lines for reference
%     line([0 8.5], [0 0])
%     line([0 0], [-2.5 2.5])
```

```
%     line([2.5 2.5], [-2.5 2.5])
%     line([5 5], [-2.5 2.5])
%     line([7.5 7.5], [-2.5 2.5])
%     line([0 8.5], [1.25 1.25])
%     line([0 8.5], [-1.25 -1.25])
    hXLabel = xlabel('x/D');
    set(hXLabel, 'FontName', 'Times New Roman','FontSize', 16)
    set(gca, 'FontName', 'Times New Roman', 'FontSize', 16)
    hYLabel = ylabel('y/D');
    set(hYLabel, 'FontName', 'Times New Roman','FontSize', 16)
    ax=gca;
    ax.FontSize = 16;
    ax.TickDir = 'in';
    ax.LineWidth=2;
    hcb=colorbar;
    string=['Coefficient of Variation in Percent at Re=' int2str(
       Re) 'k'];
    hcb.Label.String =string;
    set(hcb.Label, 'FontName', 'Times New Roman','FontSize', 20);
    hcb.Limits=[limits(1) limits(2)];
    set(hcb, 'Location', 'northoutside');
    Image_savename=[PostProcfolder '\COV_'  int2str(Re) 'k' '.png
       '];
    saveas(gcf, Image_savename)
    close all
```

```
    hold off

%% Standard Variation
elseif Error==2
   % plot it
    close all;
    figure('PaperPosition', [0 0 8.75 5])
    hold on
    set(gcf, 'Position', get(0, 'Screensize'));
    limits=[0,15];
    Nusselt_contour=contourf(x_over_D_vector, z_over_D_vector,
       Nusselt_Number, [limits(1):1:limits(2)], 'LineColor', '
       none');
    colormap('Jet');
    axis equal
    xlim([-1.25 8.75]);
    ylim([-2.5 2.5]);
    % make lines for reference
%     line([0 8.5], [0 0])
%     line([0 0], [-2.5 2.5])
%     line([2.5 2.5], [-2.5 2.5])
%     line([5 5], [-2.5 2.5])
%     line([7.5 7.5], [-2.5 2.5])
%     line([0 8.5], [1.25 1.25])
%     line([0 8.5], [-1.25 -1.25])
```

```
    hXLabel = xlabel('x/D');
    set(hXLabel, 'FontName', 'Times New Roman','FontSize', 16)
    set(gca, 'FontName', 'Times New Roman', 'FontSize', 16)
    hYLabel = ylabel('y/D');
    set(hYLabel, 'FontName', 'Times New Roman','FontSize', 16)
    ax=gca;
    ax.FontSize = 16;
    ax.TickDir = 'in';
    ax.LineWidth=2;
    hcb=colorbar;
    string=['Standard Variation at Re=' int2str(Re) 'k']
    hcb.Label.String =string;
    set(hcb.Label, 'FontName', 'Times New Roman','FontSize', 20);
    hcb.Limits=[limits(1) limits(2)];
    set(hcb, 'Location', 'northoutside');
    Image_savename=[PostProcfolder '\SV_'  int2str(Re) 'k' '.png'
       ];
    saveas(gcf, Image_savename)
    close all
    hold off

%% local error margin at 95% confidence interval
elseif Error==3
   % plot it
    close all;
```

```
    figure('PaperPosition', [0 0 8.75 5])
    hold on
    set(gcf, 'Position', get(0, 'Screensize'));
    limits=[0,15];
    Nusselt_contour=contourf(x_over_D_vector, z_over_D_vector,
       Nusselt_Number, [limits(1):1:limits(2)], 'LineColor', '
       none');
    colormap('Jet');
    axis equal
    xlim([-1.25 8.75]);
    ylim([-2.5 2.5]);
    % make lines for reference
%     line([0 8.5], [0 0])
%     line([0 0], [-2.5 2.5])
%     line([2.5 2.5], [-2.5 2.5])
%     line([5 5], [-2.5 2.5])
%     line([7.5 7.5], [-2.5 2.5])
%     line([0 8.5], [1.25 1.25])
%     line([0 8.5], [-1.25 -1.25])
    hXLabel = xlabel('x/D');
    set(hXLabel, 'FontName', 'Times New Roman','FontSize', 16)
    set(gca, 'FontName', 'Times New Roman', 'FontSize', 16)
    hYLabel = ylabel('y/D');
    set(hYLabel, 'FontName', 'Times New Roman','FontSize', 16)
    ax=gca;
```

```
    ax.FontSize = 16;
    ax.TickDir = 'in';
    ax.LineWidth=2;
    hcb=colorbar;
    string=['Local Margin of Error at Re=' int2str(Re) 'k at 95% Confidence Interval']
    hcb.Label.String =string;
    set(hcb.Label, 'FontName', 'Times New Roman','FontSize', 20);
    hcb.Limits=[limits(1) limits(2)];
    set(hcb, 'Location', 'northoutside');
    Image_savename=[PostProcfolder '\Margin_'  int2str(Re) 'k' '.png'];
    saveas(gcf, Image_savename)
    close all
    hold off
%% local error
elseif Error==4
   % plot it
    close all;
    figure('PaperPosition', [0 0 8.75 5])
    hold on
    set(gcf, 'Position', get(0, 'Screensize'));
    limits=[0,25];
```

```
    Nusselt_contour=contourf(x_over_D_vector, z_over_D_vector,
       Nusselt_Number, [limits(1):1:limits(2)], 'LineColor', '
       none');
    colormap('Jet');
    axis equal
    xlim([-1.25 8.75]);
    ylim([-2.5 2.5]);
    % make lines for reference
%     line([0 8.5], [0 0])
%     line([0 0], [-2.5 2.5])
%     line([2.5 2.5], [-2.5 2.5])
%     line([5 5], [-2.5 2.5])
%     line([7.5 7.5], [-2.5 2.5])
%     line([0 8.5], [1.25 1.25])
%     line([0 8.5], [-1.25 -1.25])
    hXLabel = xlabel('x/D');
    set(hXLabel, 'FontName', 'Times New Roman','FontSize', 16)
    set(gca, 'FontName', 'Times New Roman', 'FontSize', 16)
    hYLabel = ylabel('y/D');
    set(hYLabel, 'FontName', 'Times New Roman','FontSize', 16)
    ax=gca;
    ax.FontSize = 16;
    ax.TickDir = 'in';
    ax.LineWidth=2;
    hcb=colorbar;
```

```
    string=['Relative Local Error in Percent at Re=' int2str(Re)
       'k at 95% Confidence Interval']
    hcb.Label.String =string;
    set(hcb.Label, 'FontName', 'Times New Roman','FontSize', 20);
    hcb.Limits=[limits(1) limits(2)];
    set(hcb, 'Location', 'northoutside');
    Image_savename=[PostProcfolder '\LocalError_'  int2str(Re) 'k
       ' '.png'];
    saveas(gcf, Image_savename)
    close all
    hold off
else
    disp('No correct input for Error. If you want to plot
       Coefficient of Variation , enter 1, if Standard Deviation
       2, Marging of Error 3, otherwise 0')
end
```

APPENDIX C: ARDUINO CODES

The traverse system was operated by a stepper motor which itself was controlled via an Arduino micro controller. As discussed in the experimental setup, two different routines where used to continuously move the laser setup during calibration and to move to a specific location. Both source codes are listed below.

Listing C.1: GoContinous.ino

```
//#include <AccelStepper.h>

//AccelStepper stepper(AccelStepper::DRIVER, 8, 9);


const int STEP_PIN =   9;
const int DIRECTION_PIN = 8;
 unsigned long ddelay;
 boolean  stopmotion =true;
void setup()
{
  Serial.begin(9600);
  pinMode(STEP_PIN, OUTPUT);
  pinMode(DIRECTION_PIN, OUTPUT);
  digitalWrite(STEP_PIN, LOW);
  digitalWrite(DIRECTION_PIN, HIGH);
}

void loop()
{
```

```

  char c;
  if(Serial.available()) {

    c = Serial.read();
    if (c == 'f') {  // forward
      digitalWrite(DIRECTION_PIN, HIGH);
    }
    if (c == 'r') {  // reverse
     digitalWrite(DIRECTION_PIN, LOW);
    }

    if (c == '1') {  // super slow
      ddelay = 1500;
       stopmotion = false;
    }
    if (c == 's') {  // stop
      //ddelay = 0;
      stopmotion=true;
    }
    if (c == '2'){
      ddelay = 80; //fast
      stopmotion = false;
    }
   }
```

```
if (stopmotion == true)
{
}
  else{
     digitalWrite(STEP_PIN, HIGH);
      delayMicroseconds(ddelay);
      digitalWrite(STEP_PIN, LOW);
     delayMicroseconds(ddelay);


  }


}
```

Listing C.2: GoToPosZehner.ino

```
const int stepsPerRevolution = 200*16;  // change1 this to fit
   the number of steps per revolution
#include <AccelStepper.h>
// Define a stepper and the pins it will use
AccelStepper stepper(AccelStepper::DRIVER, 9, 8);


// before closing, always set back to postion 1
//number of steps to each position from 0
long pos0 = -9280;        //left wall
long pos1 = 0;    //calibration plate
long pos2 = 6976;   //50%
long pos3 = 3725;   //40%
long pos4 = 474;  //30%
long pos5 = -2778;  //20%
long pos6 = -6029;  //10%
long pos7 = -9280;  //left wall

void setup() {
  Serial.begin(9600);
  stepper.setMaxSpeed(2000);
  stepper.setAcceleration(500);
}

void loop() {
```

```
char c;
  if(Serial.available()) {

    c = Serial.read();

     if (c == '0') {  // position 0

stepper.moveTo(pos0);
Serial.println(at position 0 (left wall), move to 1 to close);
      }

    if (c == '1') {  // position 1

stepper.moveTo(pos1);
Serial.println(at position 1, ready to close);
      }


    if (c == '2') {

stepper.moveTo(pos2);
Serial.println(at position 2, move to position 1 before closing);
    }

```

```
    if (c == '3'){

stepper.moveTo(pos3);
Serial.println(at position 3, move to position 1 before closing);
      }

    if (c == '4'){

stepper.moveTo(pos4);
Serial.println(at position 4, move to position 1 before closing);
    }

    if (c == '5'){

stepper.moveTo(pos5);
Serial.println(at position 5, move to position 1 before closing);
    }


    if (c == '6'){

stepper.moveTo(pos6);
Serial.println(at position 6, move to position 1 before closing);
   }

```

```
    if (c == '7'){

stepper.moveTo(pos7);
Serial.println(at position 7 (left wall), move to position 1
   before closing);
   }

  }

stepper.run();

}







}
```

LIST OF REFERENCES

[1] D'Costa, V., 2018. Coal & natural gas power in the us, ibisworld industry report 22111a. Report, IBISWorld, 08/2018.

[2] Kalyani, D., 2018. Mining, oil & gas machinery manufacturing in the us, ibisworld industry report 33313. Report, IBISWorld, 10/2018.

[3] Spitzer, D., 2019. Aircraft, engine & parts manufacturing in the us, ibisworld industry report 33641a. Report, IBISWorld, 08/2019.

[4] Masters, N., 2019. Aircraft maintenance, repair & overhaul in the us, ibisworld industry report 48819. Report, IBISWorld, 05/2019.

[5] Ames, F. E., Nordquist, C. A., and Klennert, L. A., 2007. "Endwall heat transfer measurements in a staggered pin fin array with an adiabatic pin". *Proceedings of the Asme Turbo Expo 2007, Vol 4, Pts a and B*, pp. 423–432.

[6] Hutt, R. "What are the 10 biggest global challenges". In World Economic Forum. Last modified January, Vol. 21.

[7] Wilson, C., 2016. Siemens sets new performance and efficiency world record at düsseldorf power plant.

[8] Lechner, C., and Seume, J., 2010. *Stationäre Gasturbinen*. Springer-Verlag.

[9] BP, p., 2018. Bp statistical review of world energy 2018. Report.

[10] Gülen, S. C., 2018. "Beyond brayton cycle: It is time to change the paradigm". *Journal of Engineering for Gas Turbines and Power,* ***140***(11), p. 111703.

[11] Hada, S., Tsukagoshi, K., Masada, J., and Ito, E., 2012. Test results of the world's first 1,600 c j-series gas turbine. Report, 03/2012.

[12] Yuri, M., Masada, J., Hada, S., and Wakazono, U., 2017. Operating results of j-series gas turbine and development of jac. Report, 09/2017.

[13] NASA, 1998. 40 years of innovations. Report, NASA, Sep 01, 1998.

[14] Yuri, M., Masada, J., Tsukagoshi, K., Ito, E., and HADA, S., 2013. Development of 1600c class high efficiency gas turbine for power generation applying j-type technology. Report, 09/2013.

[15] Webb, R., and Eckert, E., 1972. "Application of rough surfaces to heat exchanger design". *International Journal of Heat and Mass Transfer,* ***15***(9), pp. 1647–1658.

[16] Chyu, M., Yen, C., and Siw, S., 2007. "Comparison of heat transfer from staggered pin fin arrays with circular, cubic and diamond shaped elements". In ASME Turbo Expo 2007: power for land, sea, and air, American Society of Mechanical Engineers, pp. 991–999.

[17] Gupta, G., Fernandez, E., Otto, M., and Kapat, J. S., 2019. "Experimental and numerical investigation of fully turbulent flow in a rectangular channel with dimples and protrusions". In AIAA Propulsion and Energy 2019 Forum, p. 4178.

[18] Bergman, T. L., Incropera, F. P., DeWitt, D. P., and Lavine, A. S., 2011. *Fundamentals of heat and mass transfer*. John Wiley & Sons.

[19] Pope, S. B., 2001. *Turbulent flows*. Cambridge University Press.

[20] Tennekes, H., and Lumley, J. L., 1972. *A first course in turbulence*.

[21] Žukauskas, A., 1972. "Heat transfer from tubes in crossflow". *Advances in heat transfer,* ***8***, pp. 93–160.

[22] Vanfossen, G. J., 1981. "Heat-transfer coefficients for staggered arrays of short pin fins". *Journal of Engineering for Power-Transactions of the Asme,* ***104***(2), pp. 268–274.

[23] Brigham, B. A., and Vanfossen, G. J., 1984. "Length to diameter ratio and row number effects in short pin fin heat-transfer". *Journal of Engineering for Gas Turbines and Power-Transactions of the Asme,* ***106***(1), pp. 241–245.

[24] Simoneau, R., and VanFossen, G., 1984. "Effect of location in an array on heat transfer to a short cylinder in crossflow". *Journal of Heat Transfer,* ***106***(1), pp. 42–48.

[25] Metzger, D., Shepard, W., and Haley, S., 1986. "Row resolved heat transfer variations in pin-fin arrays including effects of non-uniform arrays and flow convergence". In ASME 1986 international gas turbine conference and exhibit, American Society of Mechanical Engineers, pp. V004T09A015–V004T09A015.

[26] Chyu, M., Hsing, Y., and Natarajan, V., 1998. "Convective heat transfer of cubic fin arrays in a narrow channel". *Journal of Turbomachinery,* ***120***(2), pp. 362–367.

[27] Uzol, O., and Camci, C. "Elliptical pin fins as an alternative to circular pin fins for gas turbine blade cooling applications: Part 1—endwall heat transfer and total pressure loss characteristics". In ASME Turbo Expo 2001: Power for Land, Sea, and Air, American Society of Mechanical Engineers, pp. V003T01A056–V003T01A056.

[28] Chyu, M., and Goldstein, R., 1991. "Influence of an array of wall-mounted cylinders on the mass transfer from a flat surface". *International journal of heat and mass transfer,* ***34***(9), pp. 2175–2186.

[29] Chyu, M., Hsing, Y., Shih, T.-P., and Natarajan, V., 1999. "Heat transfer contributions of pins and endwall in pin-fin arrays: Effects of thermal boundary condition modeling". *Journal of Turbomachinery,* ***121***(2), pp. 257–263.

[30] Chyu, M., Ding, H., Downs, J., Van Sutendael, A., and Soechting, F., 1997. "Determination of local heat transfer coefficient based on bulk mean temperature using a transient liquid crystals technique". In ASME 1997 International Gas Turbine and Aeroengine Congress and Exhibition, American Society of Mechanical Engineers, pp. V003T09A085–V003T09A085.

[31] Hippensteele, S. A., Russell, L. M., and Stepka, F. S., 1981. "Evaluation of a method for heat transfer measurements and thermal visualization using a composite of a heater element and liquid crystals.[thermal performance of turbine blade cooling configurations]".

[32] Ames, F. E., Dvorak, L. A., and Morrow, M. J., 2005. "Turbulent augmentation of internal convection over pins in staggered-pin fin arrays". *Journal of Turbomachinery-Transactions of the Asme,* ***127***(1), pp. 183–190.

[33] Ames, F. E., and Dvorak, L. A., 2006. "Turbulent transport in pin fin arrays: Experimental data and predictions". *Journal of Turbomachinery-Transactions of the Asme,* ***128***(1), pp. 71–81.

[34] Uzol, O., and Camci, C. "Elliptical pin fins as an alternative to circular pin fins for gas turbine blade cooling applications: Part 2—wake flow field measurements and visualization using particle image velocimetry". In ASME Turbo Expo 2001: Power for Land, Sea, and Air, American Society of Mechanical Engineers, pp. V003T01A057–V003T01A057.

[35] Melville, B. W., and Coleman, S. E., 2000. *Bridge scour*. Water Resources Publication.

[36] Incropera, F., 1988. "Convection heat transfer in electronic equipment cooling". *Journal of heat transfer,* ***110***(4b), pp. 1097–1111.

[37] Peles, Y., Koşar, A., Mishra, C., Kuo, C.-J., and Schneider, B., 2005. "Forced convective heat transfer across a pin fin micro heat sink". *International Journal of Heat and Mass Transfer,* ***48***(17), pp. 3615–3627.

[38] Ligrani, P. M., Oliveira, M. M., and Blaskovich, T., 2003. "Comparison of heat transfer augmentation techniques". *AIAA journal,* ***41***(3), pp. 337–362.

[39] Won, S. Y., Mahmood, G. I., and Ligrani, P. M., 2004. "Spatially-resolved heat transfer and flow structure in a rectangular channel with pin fins". *International Journal of Heat and Mass Transfer,* ***47***(8-9), pp. 1731–1743.

[40] Delibra, G., Borello, D., Hanjalić, K., and Rispoli, F., 2009. "Urans of flow and endwall heat transfer in a pinned passage relevant to gas-turbine blade cooling". *International Journal of Heat and Fluid Flow,* ***30***(3), pp. 549–560.

[41] Rodi, W., 1997. "Comparison of les and rans calculations of the flow around bluff bodies". *Journal of Wind Engineering and Industrial Aerodynamics,* ***71***, pp. 55–75.

[42] Delibra, G., Hanjalić, K., Borello, D., and Rispoli, F., 2010. "Vortex structures and heat transfer in a wall-bounded pin matrix: Les with a rans wall-treatment". *International Journal of Heat and Fluid Flow,* ***31***(5), pp. 740–753.

[43] Otto, M., Hodges, J., Gupta, G., and Kapat, J. S., 2019. "Vortical structures in pin fin arrays for turbine cooling applications". In ASME Turbo Expo 2019: Turbomachinery Technical Conference and Exposition, American Society of Mechanical Engineers Digital Collection.

[44] Metzger, D., Berry, R., and Bronson, J., 1982. "Developing heat transfer in rectangular ducts with staggered arrays of short pin fins". *Journal of Heat Transfer,* ***104***(4), pp. 700–706.

[45] Metzger, D., Fan, Z., and Shepard, W., 1982. "Pressure loss and heat transfer through multiple rows of short pin fins". In Heat Transfer 1982, Volume 3, Vol. 3, pp. 137–142.

[46] Metzger, D., and Haley, S., 1982. "Heat transfer experiments and flow visualization for arrays of short pin fins". In ASME 1982 International Gas Turbine Conference and Exhibit, American Society of Mechanical Engineers, pp. V004T09A007–V004T09A007.

[47] Metzger, D., Fan, C., and Haley, S., 1984. "Effects of pin shape and array orientation on heat transfer and pressure loss in pin fin arrays". *Journal of Engineering for Gas Turbines and Power,* ***106***(1), pp. 252–257.

[48] Armstrong, J., and Winstanley, D., 1988. "A review of staggered array pin fin heat transfer for turbine cooling applications". *Journal of Turbomachinery,* ***110***(1), pp. 94–103.

[49] Lau, S., Kim, Y., and Han, J., 1987. "Local endwall heat/mass-transfer distributions in pin fin channels". *Journal of thermophysics and heat transfer,* ***1***(4), pp. 365–372.

[50] Lau, S., Han, J., and Kim, Y., 1989. "Turbulent heat transfer and friction in pin fin channels with lateral flow ejection". *Journal of Heat Transfer,* ***111***, p. 51.

[51] CHYU, M., and NATARAJAN, V., 1991. "Local heat/mass transfer distributions on the surface of a wall-mounted cube". *Journal of heat transfer,* ***113***(4), pp. 851–857.

[52] GOLDSTEIN, R., and KARNI, J., 1984. "The effect of a wall boundary layer on local mass transfer from a cylinder in crossflow". *Journal of heat transfer,* ***106***(2), pp. 260–267.

[53] Chyu, M., and Natarajan, V., 1996. "Heat transfer on the base surface of threedimensional protruding elements". *International Journal of Heat and Mass Transfer,* ***39***(14), pp. 2925–2935.

[54] Hwang, J. J., Lai, D. Y., and Tsia, Y. P., 1999. "Heat transfer and pressure drop in pin-fin trapezoidal ducts". *Journal of Turbomachinery-Transactions of the Asme,* ***121***(2), pp. 264–271.

[55] Hwang, J.-J., and Lu, C.-C. "Lateral-flow effect on endwall heat transfer and pressure drop in a pin-fin trapezoidal duct of various pin shapes". In ASME Turbo Expo 2000: Power for Land, Sea, and Air, American Society of Mechanical Engineers, pp. V003T01A040–V003T01A040.

[56] Chyu, M. K., Siw, S. C., and Moon, H. K., 2009. "Effects of height-to-diameter ratio of pin element on heat transfer from staggered pin-fin arrays". In ASME Turbo Expo 2009: Power for Land, Sea, and Air, American Society of Mechanical Engineers, pp. 705–713.

[57] Lawson, S. A., Thrift, A. A., Thole, K. A., and Kohli, A., 2011. "Heat transfer from multiple row arrays of low aspect ratio pin fins". *International Journal of Heat and Mass Transfer,* ***54***(17-18), pp. 4099–4109.

[58] Otto, M., Fernandez, E., Kapat, J. S., Ricklick, M., and Mhetras, S., 2017. "Rib turbulated pin fin array for trailing edge cooling". In ASME Turbo Expo 2017: Turbomachinery Technical Conference and Exposition, American Society of Mechanical Engineers Digital Collection, pp. V05AT16A001–V05AT16A001.

[59] Goldstein, R., Jabbari, M., and Chen, S., 1994. "Convective mass transfer and pressure loss characteristics of staggered short pin-fin arrays". *International Journal of Heat and Mass Transfer,* ***37***, pp. 149–160.

[60] Uzol, O., and Camci, C., 2005. "Heat transfer, pressure loss and flow field measurements downstream of staggered two-row circular and elliptical pin fin arrays". *Journal of Heat Transfer-Transactions of the Asme,* ***127***(5), pp. 458–471.

[61] Ligrani, P. M., Oliveira, M. M., and Blaskovich, T., 2003. "Comparison of heat transfer augmentation techniques". *Aiaa Journal,* ***41***(3), pp. 337–362.

[62] Anderson, C. D., and Lynch, S. P., 2016. "Time-resolved stereo piv measurements of the horseshoe vortex system at multiple locations in a low-aspect-ratio pin–fin array". *Experiments in Fluids,* ***57***(1), p. 5.

[63] Baker, C. J., 1980. "The turbulent horseshoe vortex". *Journal of Wind Engineering and Industrial Aerodynamics,* ***6***(1-2), pp. 9–23.

[64] Bělík, L., 1973. "The secondary flow about circular cylinders mounted normal to a flat plate". *The Aeronautical Quarterly,* ***24***(1), pp. 47–54.

[65] Dargahi, B., 1989. "The turbulent flow field around a circular cylinder". *Experiments in Fluids,* ***8***(1-2), pp. 1–12.

[66] AGUI, J., and ANDREOPOULOS, J., 1992. "Experimental investigation of a three-dimensional boundary layer flow in the vicinity of an upright wall mounted cylinder". *Journal of fluids engineering,* ***114***(4), pp. 566–576.

[67] Heseltine, J. L., 2003. "Flow around a circular cylinder with a free end". PhD thesis, University of Saskatchewan.

[68] Eisenlohr, H., and Eckelmann, H., 1989. "Vortex splitting and its consequences in the vortex street wake of cylinders at low reynolds number". *Physics of Fluids A: Fluid Dynamics,* ***1***(2), pp. 189–192.

[69] Sahin, B., Ozturk, N. A., and Gurlek, C., 2008. "Horseshoe vortex studies in the passage of a model plate-fin-and-tube heat exchanger". *International Journal of Heat and Fluid Flow,* ***29***(1), pp. 340–351.

[70] Kirkil, G., and Constantinescu, G., 2015. "Effects of cylinder reynolds number on the turbulent horseshoe vortex system and near wake of a surface-mounted circular cylinder". *Physics of Fluids,* ***27***(7), p. 075102.

[71] Devenport, W. J., and Simpson, R. L., 1990. "Time-depeiident and time-averaged turbulence structure near the nose of a wing-body junction". *Journal of Fluid Mechanics,* ***210***, pp. 23–55.

[72] Apsilidis, N., Diplas, P., Dancey, C. L., and Bouratsis, P., 2015. "Time-resolved flow dynamics and reynolds number effects at a wall–cylinder junction". *Journal of Fluid Mechanics,* ***776***, pp. 475–511.

[73] Umeda, S., and Yang, W.-J., 1999. "Interaction of von karman vortices and intersecting main streams in staggered tube bundles". *Experiments in Fluids,* ***26***(5), pp. 389–396.

[74] Ostanek, J. K., and Thole, K. A., 2012. "Wake development in staggered short cylinder arrays within a channel". *Experiments in fluids,* ***53***(3), pp. 673–697.

[75] Ames, F., and Dvorak, L., 2006. "The influence of reynolds number and row position on surface pressure distributions in staggered pin fin arrays". *ASME Paper No. GT2006-90170*.

[76] Schanderl, W., Jenssen, U., Strobl, C., and Manhart, M., 2017. "The structure and budget of turbulent kinetic energy in front of a wall-mounted cylinder". *Journal of Fluid Mechanics,* ***827***, pp. 285–321.

[77] Blevins, R. D., 1977. "Flow-induced vibration". *New York, Van Nostrand Reinhold Co., 1977. 377 p.*

[78] Ames, F., Dvorak, L., and Morrow, M. "Turbulent augmentation of internal convection over pins in staggered pin fin arrays". In ASME Turbo Expo 2004: Power for Land, Sea, and Air, American Society of Mechanical Engineers, pp. 787–796.

[79] Li, W., Ren, J., Hongde, J., Luan, Y., and Ligrani, P., 2016. "Assessment of six turbulence models for modeling and predicting narrow passage flows, part 2: Pin fin arrays". *Numerical Heat Transfer, Part A: Applications,* ***69***(5), pp. 445–463.

[80] Escauriaza, C., and Sotiropoulos, F., 2011. "Reynolds number effects on the coherent dynamics of the turbulent horseshoe vortex system". *Flow Turbulence and Combustion,* ***86***(2), pp. 231–262.

[81] Schanderl, W., and Manhart, M., 2016. "Reliability of wall shear stress estimations of the flow around a wall-mounted cylinder". *Computers & Fluids,* ***128***, pp. 16–29.

[82] Fröhlich, J., and Rodi, W., 2004. "Les of the flow around a circular cylinder of finite height". *International journal of heat and fluid flow,* ***25***(3), pp. 537–548.

[83] Kellner, T., 2017. An epiphany of disruption: Ge additive chief explains how 3d printing will upend manufacturing.

[84] Kellner, T., 2018. Fired up: Ge successfully tested its advanced turboprop engine with 3d-printed parts.

[85] Siebold, M., 2019. "Additive manufacturing for serial production of high-performance metal parts". *Mechanical Engineering Magazine Select Articles,* ***141***(05), pp. 49–50.

[86] Wimmer, T., Rühmer, T., Mick, Y., Wang, L., and Weigand, B., 2019. "Experimental and numerical investigation on an additively manufactured gas turbine ring segment with an in-wall cooling scheme". In ASME Turbo Expo 2019: Turbomachinery Technical Conference and Exposition, American Society of Mechanical Engineers.

[87] Ghosh, S., Mondal, S., Kapat, J. S., and Roy, A., 2019. "Parametric shape optimization of pin fin arrays using surrogate model based baysian methods". In 55st AIAA/SAE/ASEE Joint Propulsion Conference.

[88] Ghosh, S., and Kapat, J. S., 2019. "Topology optimization of serpentine channels for minimization of pressure loss and maximization of heat transfer performance as applied for additive manufacturing". In ASME Turbo Expo 2019: Turbomachinery Technical Conference and Exposition, American Society of Mechanical Engineers Digital Collection.

[89] Elmore, M., and Kapat, J., 2018. *Analysis of heat transfer on turbulence generating ribs using dynamic mode decomposition.* University of Central Florida.

[90] Blasius, H., 1913. "Das aehnlichkeitsgesetz bei reibungsvorgängen in flüssigkeiten". In *Mitteilungen über Forschungsarbeiten auf dem Gebiete des Ingenieurwesens*. Springer, pp. 1–41.

[91] Smith, C., Sabatino, D., and Praisner, T., 2001. "Temperature sensing with thermochromic liquid crystals". *Experiments in fluids,* ***30***(2), pp. 190–201.

[92] Ekkad, S. V., and Han, J.-C., 2000. "A transient liquid crystal thermography technique for gas turbine heat transfer measurements". *Measurement Science and Technology,* ***11***(7), p. 957.

[93] Hippensteele, S. A., Russell, L. M., and Stepka, F. S., 1983. "Evaluation of a method for heat transfer measurements and thermal visualization using a composite of a heater element and liquid crystals". *Journal of Heat Transfer,* ***105***(1), pp. 184–189.

[94] Ireland, P., and Jones, T., 2000. "Liquid crystal measurements of heat transfer and surface shear stress". *Measurement Science and Technology,* ***11***(7), p. 969.

[95] Abdullah, N., Talib, A. R. A., Jaafar, A. A., Salleh, M. A. M., and Chong, W. T., 2010. "The basics and issues of thermochromic liquid crystal calibrations". *Experimental Thermal and Fluid Science,* ***34***(8), pp. 1089–1121.

[96] Kakade, V., Lock, G. D., Wilson, M., Owen, J., and Mayhew, J., 2009. "Accurate heat transfer measurements using thermochromic liquid crystal. part 1: Calibration and characteristics of crystals". *International Journal of Heat and Fluid Flow,* ***30***(5), pp. 939–949.

[97] Tran, L. V., Kapat, J. S., Pham, A. L., Little, Z. D., and Tran, P. K., 2013. "Heat transfer measurements using the hybrid heat transfer technique with thermally adiabatic and participating ribs". In ASME Turbo Expo 2013: Turbine Technical Conference and Exposition, American Society of Mechanical Engineers Digital Collection.

[98] Tran, L., 2014. "Development of full surface transient thermochromic liquid crystal technique for internal cooling channels".

[99] dos Santos, W. N., Mummery, P., and Wallwork, A., 2005. "Thermal diffusivity of polymers by the laser flash technique". *Polymer testing,* ***24***(5), pp. 628–634.

[100] Carslaw, H. S., and Jaeger, J. C., 1959. "Conduction of heat in solids". *Oxford: Clarendon Press, 1959, 2nd ed.*

[101] Schneider, P. J., 1955. *Conduction heat transfer*. Addison-Wesley Pub. Co.

[102] Hahn, D. W., and Özisik, M. N., 2012. *Heat conduction*. John Wiley & Sons.

[103] Metzger, D., and Larson, D., 1986. "Use of melting point surface coatings for local convection heat transfer measurements in rectangular channel flows with 90-deg turns". *Journal of Heat Transfer,* ***108***(1), pp. 48–54.

[104] von Wolfersdorf, J., Hoecker, R., and Hirsch, C., 1998. "A data reduction procedure for transient heat transfer measurements in long internal cooling channels". *Journal of heat transfer,* ***120***(2), pp. 314–321.

[105] Goldstein, R., 2017. *Fluid mechanics measurements*. Routledge.

[106] Melling, A., 1997. "Tracer particles and seeding for particle image velocimetry". *Measurement Science and Technology,* ***8***(12), p. 1406.

[107] Adrian, R. J., 1991. "Particle-imaging techniques for experimental fluid mechanics". *Annual review of fluid mechanics,* ***23***(1), pp. 261–304.

[108] Adrian, R. J., 2005. "Twenty years of particle image velocimetry". *Experiments in fluids,* ***39***(2), pp. 159–169.

[109] George, W. K., Beuther, P. D., and Arndt, R. E. A., 1984. "Pressure spectra in turbulent free shear flows". *Journal of Fluid Mechanics,* ***148***, p. 155–191.

[110] Jones, W., and Launder, B. E., 1972. "The prediction of laminarization with a two-equation model of turbulence". *International journal of heat and mass transfer,* ***15***(2), pp. 301–314.

[111] Launder, B. E., and Sharma, B., 1974. "Application of the energy-dissipation model of turbulence to the calculation of flow near a spinning disc". *Letters in heat and mass transfer,* ***1***(2), pp. 131–137.

[112] Wilcox, D. C., et al., 1998. *Turbulence modeling for CFD*, Vol. 2. DCW industries La Canada, CA.

[113] Leonard, A., 1975. "Energy cascade in large-eddy simulations of turbulent fluid flows". In *Advances in geophysics*, Vol. 18. Elsevier, pp. 237–248.

[114] Smagorinsky, J., 1963. "General circulation experiments with the primitive equations: I. the basic experiment". *Monthly weather review,* ***91***(3), pp. 99–164.

[115] Germano, M., Piomelli, U., Moin, P., and Cabot, W. H., 1991. "A dynamic subgrid-scale eddy viscosity model". *Physics of Fluids A: Fluid Dynamics,* ***3***(7), pp. 1760–1765.

[116] Assael, M., Botsios, S., Gialou, K., and Metaxa, I., 2005. "Thermal conductivity of polymethyl methacrylate (pmma) and borosilicate crown glass bk7". *International Journal of Thermophysics,* ***26***(5), pp. 1595–1605.

[117] Manceau, R., and Hanjalić, K., 2002. "Elliptic blending model: A new near-wall reynolds-stress turbulence closure". *Physics of Fluids,* ***14***(2), pp. 744–754.

[118] Daly, B. J., and Harlow, F. H., 1970. "Transport equations in turbulence". *Physics of Fluids,* ***13***(11).

[119] Ahmed, L., 2018. "Detailed understanding of flow, heat transfer, and pressure drop behavior in a square channel with 45 deg ribs".

[120] Kline, S. J., 1953. "Describing uncertainty in single sample experiments". *Mech. Engineering,* ***75***, pp. 3–8.

[121] Moffat, R. J., 1988. "Describing the uncertainties in experimental results". *Experimental Thermal and Fluid Science,* ***1***(1), pp. 3–17.

[122] PTC 19.1 - 2018, 2019. Test uncertainty. Standard, American Society of Mechanical Engineers.

[123] Wieneke, B., 2015. "Piv uncertainty quantification from correlation statistics". *Measurement Science and Technology,* ***26***(7), p. 074002.

[124] Sciacchitano, A., Neal, D. R., Smith, B. L., Warner, S. O., Vlachos, P. P., Wieneke, B., and Scarano, F., 2015. "Collaborative framework for piv uncertainty quantification: comparative assessment of methods". *Measurement Science and Technology,* ***26***(7), p. 074004.

[125] Tran, P. K., Fernandez, E., and Kapat, J. S., 2019. "Investigation of unsteady flow structures in a rectangular channel with pin fin array". In AIAA Propulsion and Energy 2019 Forum, p. 4179.

[126] Jacob, M., 1938. "Heat transfer and flow resistance in cross flow of gases over tube bank". *Trans. ASME,* ***50***, pp. 384–386.

[127] Zdravkovich, M., 1985. "Flow induced oscillations of two interfering circular cylinders". *Journal of Sound and Vibration,* ***101***(4), pp. 511–521.

[128] Paul, S., Tachie, M., and Ormiston, S., 2007. "Experimental study of turbulent crossflow in a staggered tube bundle using particle image velocimetry". *International Journal of Heat and Fluid Flow,* ***28***(3), pp. 441–453.

[129] Iwaki, C., Cheong, K., Monji, H., and Matsui, G., 2004. "Piv measurement of the vertical cross-flow structure over tube bundles". *Experiments in Fluids,* ***37***(3), pp. 350–363.

[130] Norberg, C., 2003. "Fluctuating lift on a circular cylinder: review and new measurements". *Journal of Fluids and Structures*, ***17***(1), pp. 57–96.

[131] Lumley, J. L., and Newman, G. R., 1977. "The return to isotropy of homogeneous turbulence". *Journal of Fluid Mechanics*, ***82***(1), pp. 161–178.